The University of Nottingham

School of Pharmacy

Laboratory of Biophysics and Surface Analysis

CHARACTERISATION OF THE PHYSICO-CHEMICAL AND SOLID-STATE BEHAVIOUR OF DRUGS IN HFA-134 AND 227

Abdennour Bouhroum, M.Pharm (Honours)

Thesis submitted to the University of Nottingham for the degree of

Doctor of Philosophy, May 2011

“À l’amour de ma vie qui se reconnaitra,
pour être cette personne si chère *à mon cœur et que sans elle*
rien ne serai plus pareil.”

*“*Al amor de mi vida, que se reconocerá,
por ser esta la persona la más querida de mi corazón, y que sin ella
nada no sera *lo mismo.”*

ACKNOWLEDGEMENT

I would like to express my deepest gratitude to my supervisors, Prof. Clive Roberts, Prof. Phil Williams, Prof. Neil Champness, Dr. Richard Toon and Dr. Phil Jinks for their guidance and support throughout the course of this work. Special thanks to Prof. Clive Roberts for his continuous academic support and understanding during the length of my studies at the University of Nottingham. I would also like to thank Dr. Jonathan Burley for his valuable input.

I thank my colleagues at the Laboratory of Biophysics and Surface analysis especially; Jeff, Jagadeesh, Mathieu, Aalae and Matthew for their help and support. I would also like to thank my office colleagues at A03 for providing a peaceful and enjoyable working environment. I am particularly thankful to Prof. Xinyong Chen for his valuable discussions and input with AFM use. Many thanks to Dr. Emily Smith for her XPS training and Dr. Stephen Argent for his help in the clathrate synthesis.

My appreciation and gratitude go to the many friends I have met during my stay at Nottingham, for their encouragement and support. A special thanks to Al-Zaytouna Nottingham Dabka Group for all the enjoyable and very exciting time we had while performing our folkloric showcases for Palestine.

Special thanks to Dr. Ahmed Al-Jarro who has always been there for me with his enduring support and endless understanding.

This thesis is dedicated to my family members who have always been there for me and especially throughout the past eight years of my studies in the UK. To my father, Abdelhakim, who has been my prime inspiration, to my mother, Saïda, my brother Abdelraouf and my sister Yasmine for their unconditional love, affection and support.

Thank you for always being there and getting me to where I am today.

LIST OF ABBREVIATIONS

API	Active pharmaceutical ingredient
AFM	Atomic force microscopy
ATR-IR	Attenuated total reflection infra-red
BDP	Beclomethasone dipropionate
CSD	Cambridge structural database
CFCs	Chlorofluorocarbons
COPD	Chronic obstructive pulmonary disease
CSD	Cluster size distribution
cAMP	Cyclic adenosine monophosphate
mHFA	2H, 3H, decafluoropentane, model HFA propellant
DSC	Differential scanning calorimetry
DTA	Differential thermal analysis
DPIs	Dry powder inhalers
ESC	Electron spectroscopy for chemical analysis
EtOH	Ethanol
EPDM	Ethylene-propylene-diene monomer
FAT	Fixed analysed transmission
FEP	Fluorinated ethylene propylene
F_{adh}	Force of adhesion
HFA-227	1,1,2,3,3,3 Heptafluoroethane
HFAs	Hydrofluoroalkanes
IPA	Isopropyl alcohol
LSW	Lifshitz-Slyosov-Wagner
LS	Light scattering
MMAD	Mass median aerodynamic distribution
MDSC	Modulated temperature DSC
PSD	Particle size distribution
PET	Polyethylene terephthalate
pMDIs	Pressurized metered dose inhalers

RH	Relative humidity
RF	Resonance frequency
RMS	Root mean square
SEM	Scanning electron microscopy
SPM	Scanning probe microscopy
STM	Scanning tunnelling microscopy
DNP-S	Sharpened silicon nitride probe
SE	Surface energy
TMDSC	Temperature modulated DSC
HFA-134a	1,1,1,2 tetrafluoroethane
TGA	Thermogravimetric analysis
CFC-11	Trichlorofluoromethane
VT-Raman spectroscopy	Variable temperature Raman spectroscopy
VT-XRPD	Variable temperature X-ray powder diffraction
XPS	X-ray photoelectron spectroscopy
X-RPD	X-ray powder diffraction
W_a	Work of adhesion
W_c	Work of cohesion

ABSTRACT

Most drugs have a considerably low solubility in the environmentally friendly hydrofluoroalkane propellants (HFAs) currently used in pressurized metered dose inhalers (pMDIs). As a consequence, instability can occur from crystal growth and Ostwald ripening of the system altering the therapeutic performance of the pMDI. Understanding and being able to predict the behaviour of such drugs in the propellant will help in selecting the correct co-solvents and/or surfactants to increase the stability of such formulations. When anhydrous beclomethasone dipropionate (BDP) is suspended in tricholoromonofluoromethane (CFC-11) rapid crystal growth occurs, leading to the formation of a clathrate. Since chlorofluorocarbon (CFCs) propellants have been replaced by HFAs, many questions arose concerning the ability of BDP to form clathrates in the HFA and any stability issues that arise from such reformulation. Clathrates are crystalline compounds consisting of a lattice of one type of molecule that hosts a second type of "guest" molecule within its structure. Since the solid state chemistry can significantly alter the physical interactions within a suspension formulation, it is crucial to determine the most stable crystalline form in the presence of the propellant.

Successful formation of BDP CFC-11 clathrates were observed in this work as well as positive outcomes in terms of reduction in the surface energy and the force of adhesion within a model pMDI formulation (even after processing i.e. size reduction). Following this, HFA-134a and 227-ae were selected to

determine any potential clathrate formation and to monitor their stability within a pMDI formulation. The focus of this project was to determine the stability of BDP and budesonide in HFA propellants, as well as the appropriateness of each formulation for pMDI use. This project considered the potential use of complementary surface and solid-state analytical tools to provide fundamental understanding of clathrate formation and their physicochemical characteristics. A special interest in understanding the fundamentals behind the process of Ostwald ripening, a process that affects drug particle size and their related stability and hence ultimately dose consistency was also considered. Atomic force microscopy (AFM) was used in order to determine its applicability in studying Ostwald ripening and surface activity of the different APIs in model propellant. Furthermore, the effects of a range of parameters that included storage time, co-solvents and surfactants on Ostwald ripening were taken into account.

The work presented in this thesis has demonstrated that the formation of a propellant clathrate is favourable for APIs that to improve formulation stability through a reduction in particle surface energy. However, isolation and full characterisation of such HFA clathrates remains challenging due to their decreased stability when removed from the high pressure media of the pMDI device. This thesis shows that a combination of co-solvent and surfactant provides an effective reduction in instabilities due to Ostwald ripening of the pMDI formulation and a better control of particle size of the APIs within the formulation. This work provides a platform for future formulation development for pMDIs..

List of Publications

The following publications have arisen out of the work described in this thesis

1. An Investigation on the Use of Clathrates in Metered Dose Inhaler Formulations. **A. Bouhroum**, R. Toon, P. Jinks, N. Champness, P. Williams and C. Roberts. British Association for Crystal Growth (BACG), Loughborough, UK 2008.

2. An investigation into the use of clathrates in metered-dose inhaler formulations. **A. Bouhroum**, J. James, R. Toon, P. Jinks, N. Champness, P. Williams and C. Roberts. Journal of Pharmacy and Pharmacology 60 A21-A21 2008.

3. An investigation into the physical interactions of a model clathrate in a suspension metered dose inhaler formulation. **A. Bouhroum**, R. Toon, P. Jinks, N. Champness, P. Williams and C. Roberts. Drug Delivery to the Lungs (DDL 19), Edinburgh, UK, 2008.

4. Characterization of a propellant clathrate of beclomethasone dipropionate and its interactions within a model, pMDI formulation. **A. Bouhroum**, J. Burley R. Toon, P. Jinks, N. Champness, P. Williams and C. Roberts. Young Pharmaceutical Conference, Nice, France, 2009.

5. Crystal clear benefit for inhaler. **A. Bouhroum**, R. Toon, P. Jinks, N. Champness, P. Williams and C. Roberts. Manufacturing Chemist 8 (9) 67-69 2009.

6. Spectroscopic and structural characterisation of a beclomethasone dipropionate clathrate pre- and post-micronisation for inclusion in a pMDI formulation**. A. Bouhroum**, R. Toon, P. Jinks, N. Champness, P. Williams and C. Roberts. Journal of Pharmacy and Pharmacology 61 A82-A83 2009.

7. An assessment of beclomethasone dipropionate clathrate formation in a model suspension metered dose inhaler. **A. Bouhroum**, J. Burley, R. Toon, P. Jinks, N. Champness, P. Williams and C. Roberts. International Journal of Pharmaceutics 391 (1-2) 98-106 (2010).

8. An Investigation of Ostwald Ripening of Beclomethasone Dipropionate (BDP) in a Model Suspension Metered Dose Inhaler Formulation. **A. Bouhroum**, P. Jinks, N. Champness, P. Williams and C. Roberts. Respiratory Drug Delivery (RDD), Orlando, Florida, USA, 2010.

TABLE OF CONTENT

Chapter 1 Introduction

1.1 General Introduction

Inhaled medications have been in clinical use since earliest days of medical history. Their origin can be traced back 4000 years ago to India, where the leave of the Atropa Belladonna plant were smoked to suppress cough. In the 19th and early 20th centuries, cigarettes that contained stramonium powder mixed with tobacco were used to treat the symptoms experienced by asthmatic patients (Labiris and Dolovich, 2003b) and medication was added to boiling water for patients to breathe which showed to be quite effective. However, since this time, formulations and delivery devices of medications for inhalations have continually evolved (Anderson, 2001). Currently, the pulmonary route is widely accepted as being the optimal route for the first line the management of respiratory tract diseases such as asthma and chronic obstructive pulmonary disease (COPD) (Labiris and Dolovich, 2003a). Different devices have been developed in order to achieve effective delivery of active pharmaceutical ingredient (API) which are nebulizers, dry powder inhalers (DPIs) and pressurized metered dose inhalers (pMDIs) (Labiris and Dolovich, 2003b). Pressurized metered dose inhalers (pMDIs) are the most common devices used around the world for therapeutic aerosol delivery. pMDIs are believed to have an 80% market share of all inhaled therapeutic devices (Brindley, 1999). These devices operate by the emission a drug aerosol, driven by propellant in the case of pMDI that the patient is able to inhale and will be deposited into the lung

(Labiris and Dolovich, 2003b). The advantage of pulmonary delivery of drugs is that it provides higher drug concentrations delivered to the desired site of action which provides rapid clinical response. Furthermore, it minimizes the risk of systemic side effects that are usually associated with oral delivery which results in a decrease in patient morbidity and mortality along side with an increase in the patient quality of life (Labiris and Dolovich, 2003b). Due to all these advantages, a growing attention has been given to pulmonary drug delivery as a non-invasive administration for systemic delivery of therapeutic agents such as peptides and proteins for the treatment of for example, diabetes (Frijlink and DeBoer, 1994, Anderson, 2001). As a result of this, many efforts have focused towards the development of new inhaler devices that will make it possible to deliver larger drug doses to the airways to achieve greater deposition efficiency (Labiris and Dolovich, 2003a).

Compared to other routes of delivery, pulmonary delivery of drugs has certain advantages. One of the major advantages is that it is very convenient to patients as most of the devices available are portable hand-held systems that are relatively easy to use (Fink, 2000). Furthermore, it is a non-invasive method for drug delivery and provides a needle-free delivery system for the treatment of systemic diseases (Labiris and Dolovich, 2003a). The lung offers a large absorptive surface area (up to 100 m^2) with an extremely thin (0.1 µm – 0.2 µm) absorptive mucosal membrane and good blood supply (Patton, 1996). Thus an API can be delivered directly to the lungs for the treatment of respiratory disorders such as asthma, COPD and cystic fibrosis (Anderson, 2001). The thin layer of epithelial cells present in the lungs can allow for drug absorption from the lungs into

systemic circulation. The advantages of this include rapid onset of action and avoidance of first-pass metabolism by the liver and poor gastrointestinal absorption (Byron and Patton, 1994). Furthermore, the lung provides a low enzymatic environment and high solute permeability. Moreover, delivering of smaller doses to provide good therapeutic effect decreases the likelihood of unwanted side effects induced by using larger doses for systemic drug exposure. Also, the pulmonary route can be considered a potential delivery method of large molecules with very low absorption rates as these can be absorbed in significant quantities due to lung periphery providing prolonged residency (Dolovich, 1997). Furthermore, it will provide better drug delivery since oral administration of these macromolecules is difficult due to their poor intestinal membrane permeability and susceptibility to enzymatic degradation (Shoyele and Cawthorne, 2006). Also, inhaler therapy can be used for the specific targeting of specific lung cells in order to treat more localized diseases such as in the treatment of tuberculosis (Chellat et al., 2005).

1.1.1 Chapter Aims and Objectives

This chapter aims to give the reader an understanding of the issues surrounding pulmonary disorders and the general requirement for an effective drug delivery to the lung alongside the requirements of an inhaled delivery system as an effective and efficient therapeutic vehicle. In order to understand the importance of these devices in achieving a therapeutic effect, it is crucial to give a reader an appropriate background on the physiology and function of the lung. A short overview about the disorders affecting the lung as well as the treatments

available including the different inhaled delivery systems used nowadays will be covered. Particular attention will be given to pMDI devices, as these will be the focus of this project. Subsequently, the propellants commonly used in pMDI systems will be discussed. A particular focus will be made on the shift from ozone depleting propellant to the more environmentally friendly ones as this has raised stability issues with different APIs. Studies examining clathrate formation and assessing Ostwald ripening within a pMDI system will be reviewed. The use of atomic force microscopy (AFM) in determining the physico-mechanical properties of the APIs and surface-surface interactions within a pMDI formulation will be the main focus in studying pMDI formulation stability. Finally a general outline of the project will be given in terms of each chapter.

1.2 Physiology and Function of the Respiratory Tract

The lungs constitute an attractive route for drug delivery due to its advantages for both systemic and local applications as well as its non-invasive nature (Sung et al., 2007). The respiratory system works with the circulatory system to deliver oxygen from the lungs to the cells and remove carbon dioxide that is produced from cellular function and is returned to the lungs to be exhaled as a waste product (Smola et al., 2008).

The respiratory system consists of all the organs involved in breathing. It includes the respiratory airways leading into the lungs, the lungs and the structures of the thorax involved in producing movements of the air through the

airways into and out of the lungs (Sherwood, 2008). It can be divided into 3 main parts (Fig. 1-1):

- The upper respiratory tract, consisting of the nose, nasal cavity and the pharynx (Sherwood, 2008, Smola et al., 2008).
- The lower respiratory tract consisting of the larynx, trachea and bronchi.
- The lungs, which contain the respiratory bronchioles, alveolar ducts, alveolar sacs and alveoli.

When breathing, air enters through the nose and mouth and travels down the pharynx through the larynx and into the trachea before entering the lungs (Marieb and Hoehn, 2007, Sherwood, 2008). Therefore, the upper respiratory system is very important in providing air conditioning and air conduction as well contributing to the olfactory and speech function (Marieb and Hoehn, 2007). The lower respiratory system gives structural support and protection against inhaled particles as well as playing the major role in gas conduction and exchange at the alveolar region. The trachea, which begins at the edge of the larynx, divides into two bronchi and continues into the lungs. The bronchi themselves divide into smaller bronchioles which branch in the lungs forming passageways for the air that end with the alveolar sac where gases are exchanged between the air and blood (Bailey and Berkland, 2009). The alveoli are the functional units of the lungs and they form the site of gaseous exchanges (Marieb, 2005). The conducting airways are lined with ciliated columnar epithelium, which transition to a cuboidal shape approaching the distal airways. The bronchial airways lumen

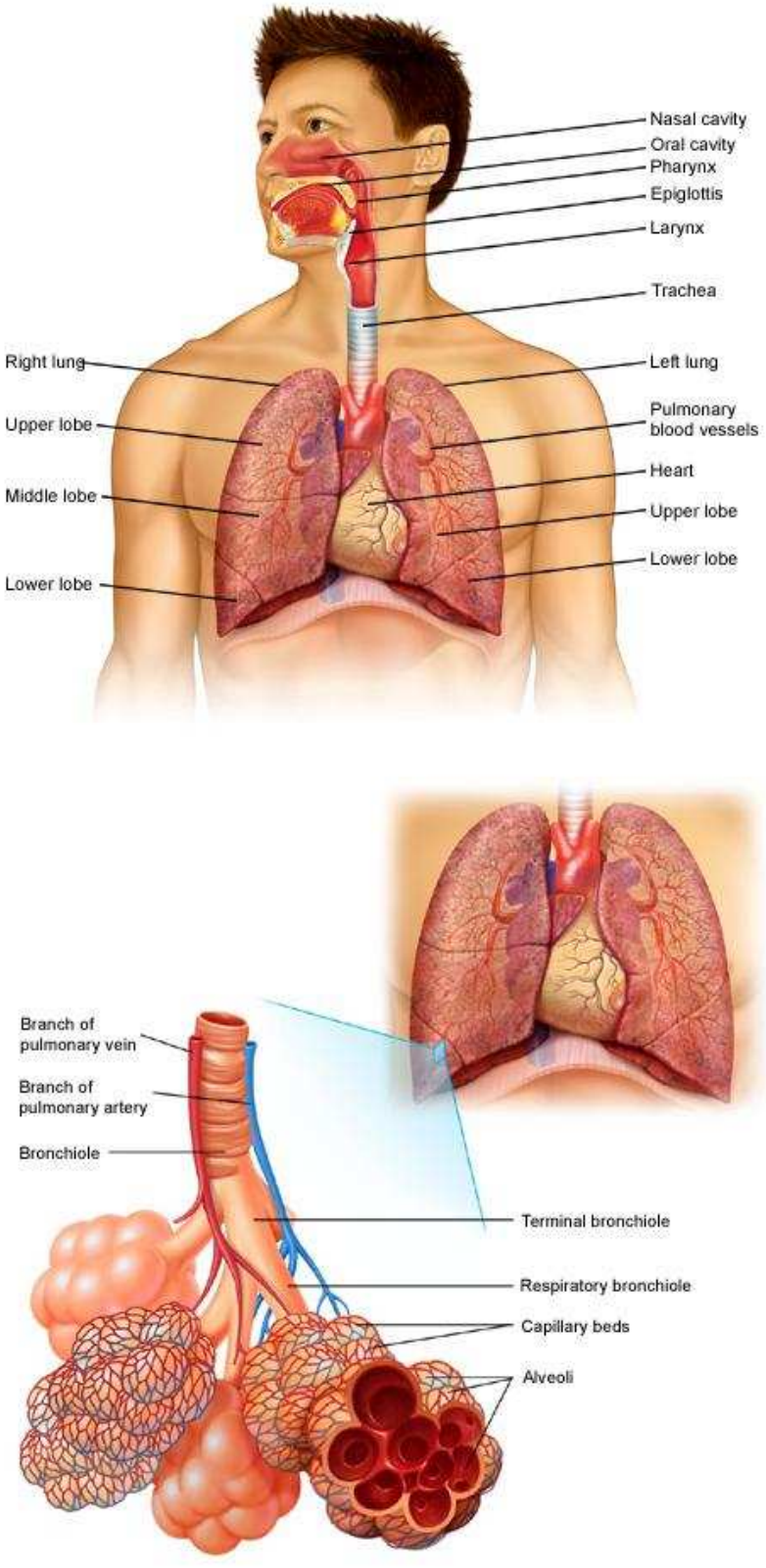

Figure 1-1: Diagram of the respiratory tract (Virtualmedicalcentre.com, 2010).

is covered with a thin layer of lumen (0.1 µm) that helps entrapment of inhaled particles.

At this area, the rhythmic beating of the celia cells helps moving the mucus up to the throat where it is swallowed. This process is known as the mucuscilary clearance and is a crucial method in the removal of inhaled particles from the respiratory system (Bailey and Berkland, 2009).

The combination of the large surface of the lungs that is greater than 100 m^2 which contains a high number of alveoli (approximately 300 million) with the very thin alveolar epithelium that have an extremely thin barrier of 0.1 µm between the pulmonary lumen and the capillaries, creates an excellent condition for efficient exchange between the external environment and the systemic circulation (Smola et al., 2008, Bailey and Berkland, 2009). The alveolar surface is composed of several types of pulmonary cells: Type I pneumocytes (small type A) are non-phagocytic and share a basement membrane with the pulmonary capillaries. Attached to the basement membrane are the larger alveolar cells (type II) that are responsible for producing the pulmonary surfactant fluid that lines the lung that is essential in alveolar repair and prevents alveolar collapse (Smola et al., 2008, Bailey and Berkland, 2009). The alveoli also contain macrophages which are phagocytic cells that are responsible for cleaning larger bodies and the removal of inhaled foreign particles (Bailey and Berkland, 2009).

1.3 Pharmacological Basis of Management of respiratory Tract Disorders

Pulmonary respiratory disorders include asthma, COPD and cystic fibrosis. The goals of treatment of these diseases are to improve the respiratory function and prevent any complications such as viral or bacterial infections. In the case of asthma, the treatment is divided into relief of symptoms which is achieved by bronchodilators which may reverse the early phase of asthma and prevention by using an-inflammatory agents (Randall and Neil, 2003). Bronchodilators include β_2-adrenoceptor agonists, muscarinic M-receptor antagonists and xanthines. Anti-inflammatory agents include corticosteroids. The focus on this project will be on corticosteroids. However, a brief description about the other APIs used in the treatment of asthma will be given.

- β_2-adrenoceptor agonists

These are the agents of first choice and act on β_2-adrenoceptor on the bronchial smooth muscle to increase cyclic adenosine monophosphate (cAMP), leading to rapid bronchodilations and reversal of the bronchospasms associated with the early phase. There are two types of β_2-adrenoceptor agonists. Short acting agents such as salbutamol and terbutaline which are used to relief the symptoms in the early phase and long acting β_2-adrenoceptor agonists such as formoterol and salmeterol which cause a prolonged and persistent bronchodilation and are used for prevention (Asthma, 2009).

- Muscarinic M-receptor antagonists

These agents such as ipratropium act by blocking the parasympathetic mediated bronchoconstriction with only limited side effects (Randall and Neil, 2003, Asthma, 2009).

- Anti-inflammatory agents - Glucocorticosteroids

Glucocorticoids have an anti-inflammatory action via activation of intracellular receptors, leading to altered gene transcription. This results in decreased cytokine production and the synthesis of lipocortin, which inhibits phospholipase A_2, and the production of the prostaglandins and leukotrienes (Asthma, 2009). Furthermore, they inhibit the influx of eosinophils into the lungs induced by allergen contact. Two glucocorticoids were used in this project and are detailed below:

- Beclomethasone Dipropionate

Beclomethasone dipropionate is a potent glucocortecoid used for the control of bronchial asthma in persons requiring continuous treatment. It is usually prescribed with a short acting β_2 agonist. It is used in a number of inhalation devices either as a suspension or a dry powder e.g. Beclozane® and Pulvinal® (BNF, 2009). Beclomethasone dipropionate is also used in oral therapies for the treatment of ulcerative colitis and as nasal sprays for the treatment of allergic and vasomotor rhinitis (BNF, 2009). Beclomethasone dipropionate undergoes 87% protein binding following conversion from a dipropionate to a monopropionate; it is metabolised via the hepatic route by esterase enzymes. It has a half life of

2.8 hours. However, the excretory route has not been characterised (British Pharmacopoeia, 2010).

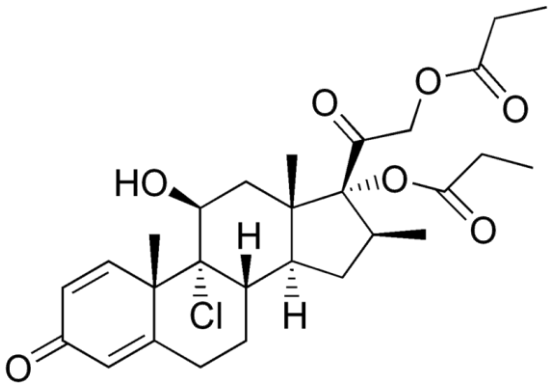

Figure 1-2: Chemical structure of beclomethasone dipropionate.

- Budesonide

Budesonide is prescribed for the prophylaxis treatment of asthma and the management of chronic asthma. It is formulated as an aerosol inhalation such as Pulmicort® or as a dry powder inhaler such as in Novolizer® (BNF, 2009). It is also used in oral therapy for the treatment of inflammatory bowel disease. Budesonide undergoes 85-90 % protein binding. It is metabolised by the hepatic route and is excreted in the urine and the faeces (British Pharmacopoeia, 2010).

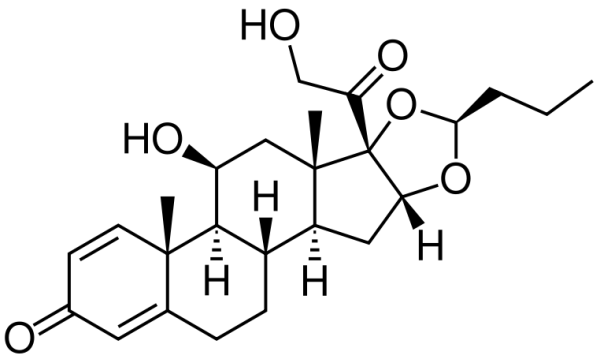

Figure 1-3: Chemical structure of budesonide.

1.4 Methods of Drug Delivery to the Lungs

The development of an efficacious inhalation thereby not only depends on the active pharmaceutical ingredient, but also on its formulation and a well designed delivery systems. At present, there are three different types of inhaler devices that are used for drug delivery to the lung: dry powder inhalers (DPIs), nebulisers and pressurised metered dose inhalers (pMDIs). A particular focus will be given to pMDI as this is the device that is dealt with in this project.

1.4.1 Dry Powder Inhalers (DPIs)

DPIs have seen an increased interest in the recent past due to their propellant free nature, high patient compliance, high dose capacity and drug stability (Chougule et al., 2007). DPIs (Fig. 4-1A) are devices that are used to deliver a dry powder formulation of an active drug for local or systemic effect via the pulmonary route. DPIs are formulated either as loose agglomerates of micronized drug particles or as carrier-based interactive mixtures where drug particles are adhered to the larger surface of carrier particles (Islam and Gladki, 2008). The medication is commonly held either in a capsule for manual loading or a proprietary form from inside the inhaler. DPIs were designed to eliminate the co-ordination difficulties experienced by the patients when using other devices such as pMDIs. However, DPIs are designed to maximise drug delivery at a relatively high inspiration rate which make them difficult to use for young children or patients with severely compromised airways. Therefore, their efficiency may vary between patients (Virchow et al., 2008). DPIs lung deposition varies among the

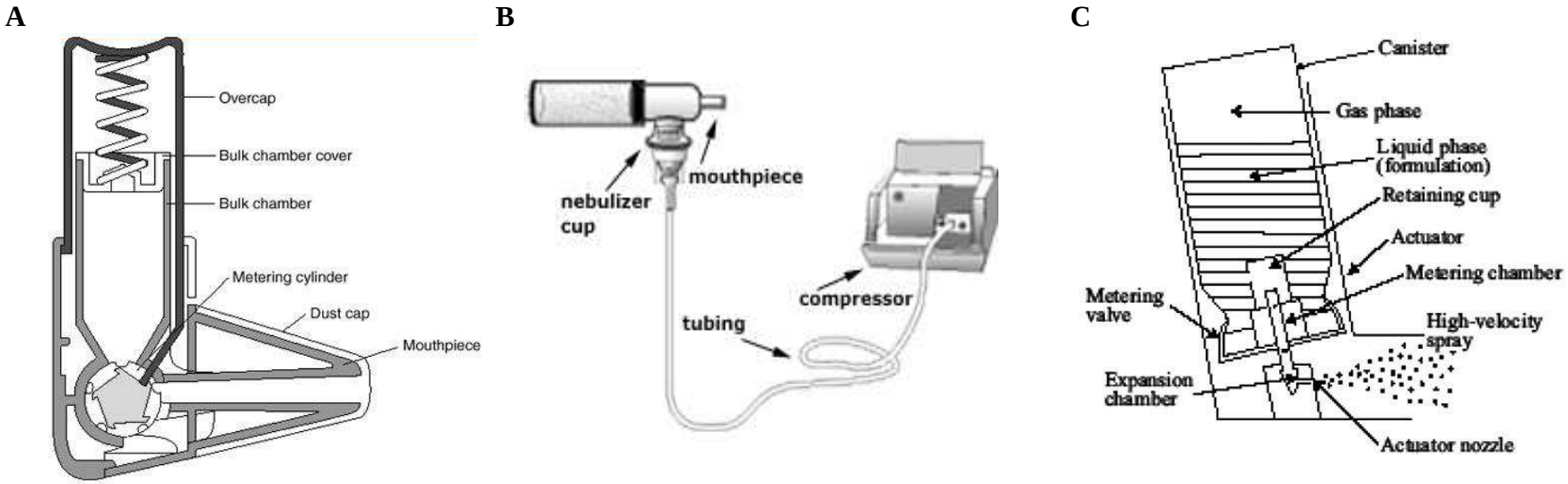

Figure 1-4: Schematic diagram of A- Dry powder inhaler (DPI) B- Nebulizer and C- pressurized metered dose inhaler (pMDI)

different DPI devices and is estimated to approximately 12-40% of the emitted dose delivered to the lungs with 20-25% of the dose still retained within the device (Labiris and Dolovich, 2003b).

1.4.2 Nebulisers

Nebulisers (Fig. 1-4B) have been used for many years to treat cystic fibrosis, asthma and other respiratory diseases. There are two basic types of nebulisers, jet and ultrasonic nebulisers which are non propellant alternatives for the delivery of inhaled therapeutics (Geller, 2005). They operate by pumping air or oxygen through a liquid formulation, which creates a vapour ready for inhalation by the patient. Nebulisers do not require a coordinated breathing manoeuvre or a strong respiratory effort; therefore, they can be used at any age, and for any disease severity or acuity (Anderson, 2001). Moreover, it is possible to mix more than one medication in a nebuliser and deliver them simultaneously as well as with very high drug doses. However, nebulisers are more time consuming than a DPI or an MDI with a large amounts of drug wastage of around 50% loss with continuously operated nebulisers (Labiris and Dolovich, 2003b). The physical properties of drug formulations such as viscosity, ionic strength, pH may prevent the nebulisation of some formulation and have an effect on the nebulisation rate and particle size (Labiris and Dolovich, 2003b). The nebulisers available in the market are quite expensive and larger in size than the portable DPI and MDI devices, however they are starting to become cheaper and more portable (Geller, 2005).

1.4.3 Pressurised Metered Dose Inhalers (pMDIs)

pMDIs are the most widely used device for drug delivery to the lungs. Over 70 million patients in the world use them (Terzano, 2001). The popularity of pMDIs with patients is due to their small size, portability, ease of use and low cost (Geller, 2005). However, the technique and coordination required for efficient MDI use can make it the most difficult of all the aerosol devices (Fink, 2000).

Little development has occurred on pMDIs since they were first discovered in 1950s (Terzano, 2001). The first pMDI was developed by Riker Laboratories (now owned by 3M Healthcare Ltd) after a suggestion from the 13-year-old daughter of Riker to change her leaky hand bulb nebuliser into a spray-can like the ones used for perfumes and hair sprays. The first pMDI prototype was made using empty soda bottle as a pressure container and a bottle capper containing a propellant and alcohol to dissolve the drug (Fink, 2000, Terzano, 2001). Nowadays, a pMDI is typically a pressurised canister containing a mixture of propellants, surfactants and co-solvents with approximately 1% of the total contents being active drug (Fink, 2000). The mixture is released from the canister through a metering valve and stem that fits into an actuator boot (Fig. 1-4C) (Clark, 1996). There are two types of pMDI, relating to their formulation characteristics – solution pMDIs where the API is dissolved in the propellant and suspension pMDIs where an API-propellant suspension exists (Terzano, 2001).

1.5 Propellants, Co-solvents and Surfactants Used in pMDI Formulation

Historically, pMDIs have used chlorofluorocarbons (CFCs) propellants as the energy source needed to disperse the formulation into respirable drug particles (Stein and Stefely, 2003). CFCs were used due to their chemical inertness, high vapour pressures and low toxicity (Smyth, 2003). CFC-containing formulations in general had the characteristics to produce effective aerosols for lung delivery. However, because of their potential zone deleting effect, CFCs have been banned as per the Montreal Protocol (Labiris and Dolovich, 2003b). The Montreal protocol was implemented in 1996 after evidence that CFCs were contributing to the ozone depletion which led to a ban of all common aerosols products using CFCs (Molina and Rowland, 1974). However, the Montreal Protocol still permits the use of CFCs under special circumstances where there are no alternative substitutes, if it crucial and necessary for the health and safety and if it is crucial for the normal functioning of the society (McDonald and Martin, 2000). The search for possible replacements for CFCs for pMDI was defined in terms of toxicity, flammability, chemical stability and physical properties as well as environmental compatibility. CFC-11, 12 and 114 (Fig. 1-5), the propellants that were already in use were taken as a template in order to synthesise newly emerging hydrofluoroalkane propellants (HFAs).

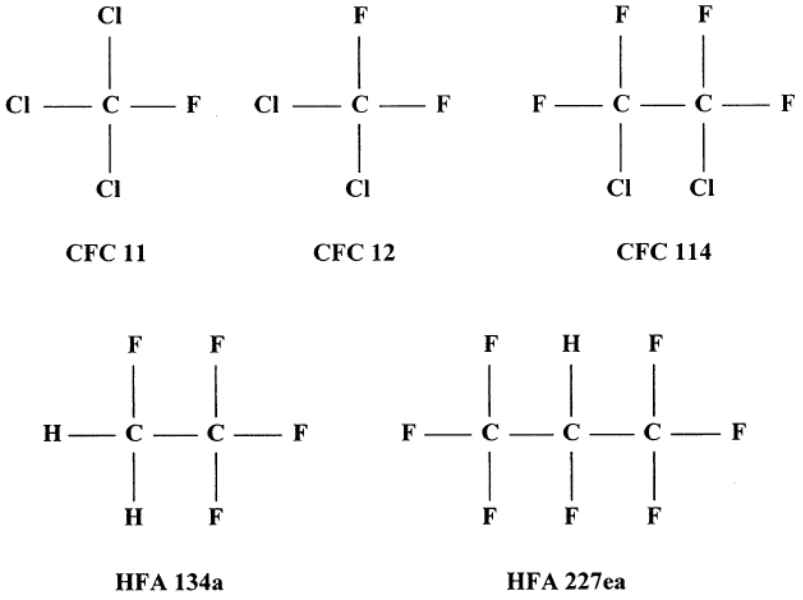

Figure 1-5: The chemical structures of common CFC and HFA propellants (Vervaet and Byron, 1999).

1.5.1 Hydrofluoroalkanes (HFAs)

Two propellants found to be effective substitutes for CFCs are hydrofluoroalkanes in nature (HFAs): tetrafluoroethane (HFA-134a) and heptafluoroethane (HFA-227) (Fig. 1-5) (Anderson, 2001). HFAs do not contain chlorine and thus have no ozone-depleting potential (Labiris and Dolovich, 2003b). Furthermore, HFAs are non-flammable and chemically stable propellant with suitable vapour pressures for pMDI use. HFA and CFC propellants possess different physical and chemical properties and are generally poor solvents for many anti-asthma drugs and excipients currently used in pMDIs (McDonald and Martin, 2000), thus the substitution to HFAs propellant changed the properties of some of the drugs delivered by CFC propellant systems and required reformulation of the drugs (Terzano, 2001).

The physical properties of the propellant (Table 1-1) can be related to details of the chemical structure and experimental investigations of propellant physicochemical behaviour. HFA 134a and 227 both have high vapour pressures and low boiling points (Vervaet and Byron, 1999). These properties are caused due to the enhanced electronegativity of the HFA molecules which created a distinct dipole on the hydrogen-carbon bonds in both propellants. These characteristics not only affect the physicochemical properties of the HFA propellants but also their water solubility as shown in Table 1-1 (Vervaet and Byron, 1999). The water solubility data indicates a very significant difference between CFC and HFA propellants which is due to the hydrofluoroalkane propellants' electropositive proton(s). These proton(s) act as sites for solute-solvent dipole-dipole attractive interactions which is carried through into HFA-ethanol blend. This implies that the dipolar interactions between HFAs and ethanol were not capable of completely displacing the HFA-water interactions in the liquid formulation (Vervaet and Byron, 1999). Therefore, this results in higher ingress rates of water into HFA formulation which may decrease in the formulation's shelf-lives and decrease product stability due to physical and chemical degradation (Williams, 1998). Thus the solvent properties of these propellants must be taken into account when moving from a CFC formulation to a HFA one especially when these are used with other co-solvent and other surfactants.

Table 1-1: Physicochemical properties and water solubility of the different pMDI propellants (adapted from (McDonald and Martin, 2000, Smyth, 2003)).

Property	CFC-11	CFC-12	CFC-114	HFA-134a	HFA-227ae
Boiling point (°C)	24	-30	4	-26	-16
Vapour pressure (kPa)	89	566	182	572	390
Density (g/cm^3)	1.49	1.33	1.47	1.23	1.42
Viscosity (mPa·s)	0.43	1.33	1.47	1.23	1.42
Water solubility (pure propellant) (ppm)	100	N/A	91	610	2220
Water solubility (propellant containing 10% (v/v) Ethanol) (ppm)	N/A	9900	N/A	11000	13500

N/A: Not Applicable

1.5.2 Surfactants and Co-solvents

Surfactants were traditionally used in CFC-based pMDIs for several reasons such as to stabilize the formulation and also to help solubilise drug and prevent crystal growth during the storage period in solution formulations (Smyth, 2003). Furthermore, surfactants were incorporated in CFC pMDIs in order to improve valve lubrication during the depression and release cycle associated with container emptying (Vervaet and Byron, 1999). Several surfactants are currently approved for use in pMDIs including oleic acid, sorbitan trioleate, and soya derived lecithin (McDonald and Martin, 2000). These surfactants are highly soluble in CFC but are not soluble in HFAs, hence, the requirement of a co-solvent to dissolve the surfactants in the HFA propellants (Vervaet and Byron, 1999). However, other approaches where adopted in which suspension formulations were developed where no other excipients were used other than the propellant (Cripps et al., 2000).

Ethanol is one of the most commonly used co-solvents in pMDI formulation. It is used in order to help lower the vapour pressure of HFA propellants which is required to produce smaller, more respirable drug fractions (Leach, 2005). However, ethanol can decrease the volatility and stability of the formulation which will have an effect of the efficiency of drug delivery (Stein and Stefely, 2003). Furthermore, ethanol can enhance the solubility of certain APIs which can lead to an increased crystal growth in some HFA systems (William III et al., 1999). Crystal growth in propellants may become a problem as it may involve a change of the physical form of the drug, modify the drug surface characteristics

which tend to retard the rate of dissolution (Vervaet and Byron, 1999). Moreover, the use of ethanol can increase the rate of Ostwald ripening, which is a phenomenon that arises due to surface area favouring dissolution of smaller micronized particles and drug recrystallization on larger particle (Vervaet and Byron, 1999, Smyth, 2003). This phenomenon will be discussed further in the next sections. A consequence of particle size changes is a general reduction in the stability and shelf life of the formulation as well as irregularities in the emitted doses due to the entrapment of the API in the pMDI device and hence affecting the amount of drug reaching the patient (Smyth, 2003). Ethanol also increases the chances of water ingress into the formulation. Water shows a high affinity to HFA propellants due to the presence of electropositive proton(s) as site for solute-solvent dipole-dipole attractive interactions which will result in a decreased solubilisation of the surfactant leading to a phase separation and precipitation of the drug (Vervaet and Byron, 1999, Smyth, 2003).

1.6 pMDI Formulation and Stability Issues

The use of co-solvents in HFA formulations is not always possible as these may trigger adverse effects in the formulation, such as a decrease in chemical and physical stability. Co-solvents may also lead to an increased tendency to crystal growth via Ostwald ripening. Changes in particle size distribution of aerosolized particles have an effect on the deposition profile in the lung following inhalation. Large particles of 5-10 μm will tend to be deposited in the mouth and the upper airway, while intermediate particle of 3-5 μm travel further down the airways and reach the bronchi and bronchioles. However, smaller particles of less than

0.5 μm might fail to be deposited in the deep lung due to being exhaled. Therefore, determining pMDI formulation stability is crucial as this will have an impact on dose uniformity and hence influence the dosage received by the patients.

1.6.1 Clathrates

Clathrates are a class of inclusion compound that generally consist of two molecular species that arrange themselves in space so that one molecule (host) entraps another molecule (guest) (Englezos, 1993). The host molecules are usually linked through hydrogen bonding to form a regular 3D structure from connected network (Plumridge and Waigh, 2002) and create cavities (host lattice) that can enclose a large variety of particles (guests) (Englezos, 1993).

1.6.1.1 Structural and Physicochemical properties of Clathrates

Clathrates are inclusion compounds of a guest molecule in a host lattice. The hypothetical lattice formed by the host molecules is known as the empty lattice. The formation of the lattice is due to the hydrogen bonding of the host molecules forming a network of polyhedral cavities (Englezos, 1993, Koh, 2002). The unfilled structure is thermodynamically unstable and is rendered stable when entrapping a molecular species under suitable pressure and temperature conditions (Englezos, 1993). Guest molecules occupy fully (hydrogen bonded to the host lattice) or partially the cages in the host framework made up of the host molecules (Patchkovskii and Tse, 2003). The thermodynamic stability of a

clathrate depends strongly on the size and shape of the guest molecules (Buffett, 2000). The guest molecules must be small enough to fit into the empty lattice but need to be large enough to provide stability to the structure (pseudo-close packing) (Buffett, 2000). The polyhedral cavities enclathrate small molecules, usually non-polar in nature (Plumridge and Waigh, 2002).

1.6.1.2 Kinetics of Clathrate Formation

The most challenging questions regarding clathrates concern the kinetic of their formation. Two fundamental questions have to be answered in the process of clathrate formation concerning the formation and the dissociation of these latter as well as the time it takes to start their formation at a certain temperature and pressure (Englezos, 1993, Dendy Sloan, 1998). The process of clathrate formation involves nucleation and growth. Nucleation has a key role in the crystallization and the stabilisation of clathrate (Rodriguez-Spong et al., 2004). Following this, a growth period might be associated with the formation of the first crystals (Englezos, 1993).

1.6.1.2.1 Clathrate Nucleation

In the first stage of clathrate formation, small clathrate crystals (i.e. nuclei) grow and disperse to achieve critical size for continued growth (Dendy Sloan, 1998). This stage is known as the nucleation process. Nucleation mechanisms can be divided into two main categories: homogeneous and heterogeneous nucleation (Rodriguez-Spong et al., 2004).

Homogeneous nucleation

Homogeneous nucleation involves the collision of many molecules simultaneously that will lead to a solidification in the absence of impurities (Dendy Sloan, 1998). During nucleation, a particle may either grow or dissolve depending on its radius until a critical size is reached (Fig. 1-6). When a particle attains a critical size, growth occurs.

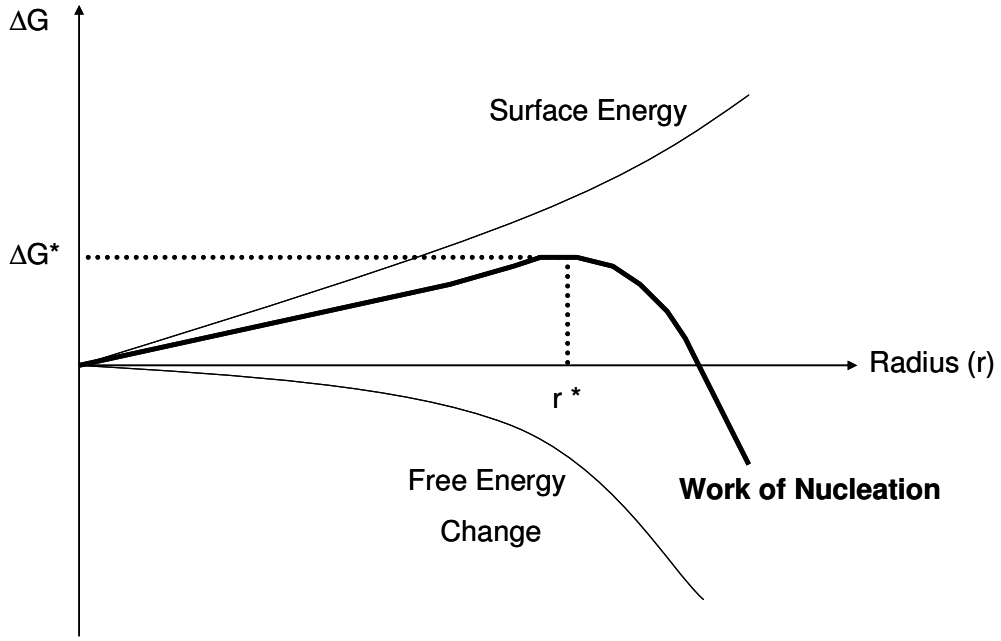

Figure 1-6: Homogenous nucleation: Any nuclei with a radius r>r* will grow while any nuclei with a r<r* will dissolve.

The thermodynamics of nucleation can be described by Gibbs free energy analysis in the following equation 1-1:

$$\Delta G = \Delta H - T\Delta S \qquad \textbf{Equation 1-1}$$

Where ΔG is the free energy change associated with the phase transition and ΔS is the entropy and ΔH is the enthalpy and T is the temperature (Rodriguez-Spong

et al., 2004). The rate of nucleation can be controlled by, molecular or ionic transport, viscosity, supersaturation, solubility, solid-liquid interfacial tension, and temperature (Rodriguez-Spong et al., 2004). Any increase in solubility will lead to an increase in the nucleation rate. This is due to a decrease in the interfacial energy and an increase the potential molecular collisions (Rodriguez-Spong et al., 2004).

Heterogeneous nucleation

Heterogeneous nucleation occurs due to the presence of a foreign particle or a surface that will promote nucleation(Dendy Sloan, 1998). The reactivity of solid surfaces as heterogeneous nucleants has significant consequences on the isolation of the desired solid-state (Rodriguez-Spong et al., 2004), since the foreign surface effectively lowers the free energy required for suitable growth (Dendy Sloan, 1998).

Nucleation times are stochastic and cannot theoretically be determined (Englezos, 1993). Formation of a clathrate typically occurs as heterogeneous nucleation at the vapour-liquid-interface, not only because the interface lowers the Gibbs free energy of nucleation, but also because the interface is the location of the required very high concentrations of host and guest molecules (Dendy Sloan, 1998).

1.6.1.2.2 Clathrate Growth

For the formation of a clathrate crystal, first the host matrix needs expansion and secondly the guest molecule must be incorporated into the cavities (Logvinenko et al., 2007). The first stage is an exothermic process, where there is a decrease in the entropy system, while the second stage is endothermic and leads to an increase in the entropy of the system (Logvinenko et al., 2007).

Barrer and Ruzicka suggested that growth rates were controlled by transport of the guest molecules to the surface of the clathrate (Barrer and Ruzicka, 1962a, Barrer and Ruzicka, 1962b, Dendy Sloan, 1998). Also, Graauw and Rutter determined that interfacial mass transfer was a rate limiting for step for clathrate formation and growth (Graauw and Rutten, 1970, Dendy Sloan, 1998). Englezos et al. based their clathrate model on homogeneous crystallisation that described growth throughout the bulk and not only restricted to the vapour-liquid interface as in heterogeneous nucleation. This model describes the initial growth period typically to be less than two hours (Englezos, 1993, Dendy Sloan, 1998). On a molecular level, clathrate growth can be considered to be a combination of two factors: 1) the kinetics of crystal growth at the clathrate surface and 2) mass transfer of components to the growing crystal surface (Dendy Sloan, 1998). Clathrate crystal growth occurring in the liquid phase is a first order irreversible homogeneous reaction (Koh, 2002). Rate of clathrate crystal nucleation and growth as well as their structural morphology is affected by supercooling, pressure and temperature, composition, and state of the clathrate-forming system (Englezos, 1993).

No models exist of the kinetic rate for clathrate growth, independent of mass transfer effects. All models of clathrate growth data have ignored heat transfer and assumed constant temperature systems (Dendy Sloan, 1998).

1.6.1.2.3 Clathrate Inhibition and Decomposition

Clathrate dissociation has only been determined and measured using thermal simulation (Englezos, 1993, Dendy Sloan, 1998). However, quantification studies using depressurisation as a mean of decomposing the clathrate is under investigation. In the thermal simulation studies of clathrate decomposition, pressure was kept constant and heat was applied in order to dissociate the clathrate structure (Dendy Sloan, 1998). The dissociation process of clathrates can divided into two different stages: 1) the removal of the guest molecule and 2) the collapse of the empty matrix (Logvinenko et al., 2007). Thermodynamically, the first stage is endothermic where entropy of the increases, while the second stage is an exothermic process, and the system entropy decreases (Logvinenko et al., 2007). The model for thermal simulation of clathrate dissociation assumes an instantaneous decomposition limited only the rate of heat transfer (Logvinenko et al., 2007).

1.6.1.2.4 Clathrate Stability

It is useful to know to what extent the guest-host molecule interaction contributes to the stability of clathrates (Schober et al., 2003). Clathrate are unstable and tend to dissociate rapidly from the cage like structure (Beauchamp, 2004). The addition of one or more guest molecules within the cavity can

stabilize the structure (Beauchamp, 2004). The guest molecules prevent the collapse of the open framework structure at higher temperatures due to their excluded-volume effect (Schober et al., 2003), and any removal needs structural reorganisation (Logvinenko et al., 2007). In fact, the interactions lower the free energy of the host molecules, making the clathrate structure stable when a sufficient number of cavities are filled (Buffett, 2000). The reduction in free energy of the host molecules depends only on the occupancy of the small and large cavities (Buffett, 2000). Ab initio geometry optimisation has been used to determine the effect of guest molecules on the stability of the clathrates and has shown that the guest atoms act as spacers preserving initial cage structure and that the specific configuration of a given cluster influences its stability (Schober et al., 2003).

1.6.2 Ostwald Ripening

The delivered dose and aerodynamic size distribution from a pMDI may change as a function of the number of doses used by the patient and storage time. Over longer storage times, changes in temperature and humidity may cause an increase in water content inside the containers. Such water ingress may cause aggregation of the suspension as well as crystal growth inside the pMDI due to the increased solubility of the APIs. This effect leads to changes in dose uniformity (Vervaet and Byron, 1999).

Crystal growth in the suspension is thermodynamically inevitable and, if uncontrolled, it may affect the emitted aerodynamic size distribution. This

phenomenon is of Ostwald ripening is due to entropy favouring the dissolution of micronized particles to contribute to the growth of a small number of larger more-ordered clusters. To avoid this, ideally, pMDI suspension should be formulated with drug substances which are insoluble in the continuous phase. However, if partially soluble micronized drugs are utilised, the addition of surfactants and co-solvents should be considered in order to reduce dissolution and drug solubility (Vervaet and Byron, 1999).

Ripening means that one single particle is growing at the expense of dissolving smaller particles. Therefore, clusters are either growing or dissolving at rates depending on their size as determined by the Kelvin equation (Equation 1-2) (Madras and McCoy, 2001). The competing growth and dissolution processes for a large and small clusters will lead to an increase in the size of large particles while smaller particles dissolve, and dissolution that decreases the number of clusters (Madras and McCoy, 2002b). The growth rate of a precipitate particle may be separated into two processes: First the transportation of molecules to the interface, which is controlled by diffusion of molecules through the solution to react at the cluster surface or rate of any stirring (Marqusee, 1983). The second stage is the incorporation of monomers into the precipitate particle that is driven by the surface free energy of the colloidal particle (Marqusee, 1983).

$$\ln \frac{p}{p_0} = \frac{-2\gamma V_m}{rRT}$$ **Equation 1-2**

Where p is the actual vapour pressure, p_0 is the saturated vapour pressure, γ is the surface tension, Vm is the molar volume, R is the universal gas constant, r is the radius of the droplet, and T is temperature.

The three basic processes in condensation (e.g.: vapour to liquid, liquid to solid) phase transition are nucleation, growth and ripening (Madras and McCoy, 2002c). These three processes are not really distinguishable, as they overlap during the evolution from a supersaturated phase to a single condensed ripened particle in equilibrium with a non-condensed phase. During nucleation, a new phase is formed out of a metastable phase, generating a large number of particles with a narrow distribution of sizes (Marqusee, 1983). The second stage consists of nuclei growing rapidly at the expense of the initial phase. Small particles generated in the nucleation phase may cause deposition on the nuclei and cause growth of clusters (Madras and McCoy, 2002c). Therefore, nucleation without accompanying growth is impossible (Madras and McCoy, 2002c). The nucleation phase is close but not equal to an equilibrium value. Ostwald ripening is the third and final stage of condensation (Madras and McCoy, 2003) where the phase evolves to minimise its surface free energy and it ends where there is complete phase separation (Marqusee, 1983). As growth and nucleation rates decline, the Gibbs-Thomson effect becomes significant, as large clusters grow due to their surface curvature at the expense of the smaller particles which will dissolve due to their thermodynamic instability on reaching their critical nucleus size leading to growth particle growth in the bulk (Madras and McCoy, 2002c, Madras and McCoy, 2003).

1.6.2.1 Theory of Ostwald Ripening

Ostwald ripening is the final stage of a first order transition for condensation of a metastable phase (Madras and McCoy, 2002b, Schober et al., 2003). It is generally thought to be a slow, diffusion-controlled process which occurs subsequent to phase separation under just under-saturation levels (Baldan, 2002). The driving force for this process is a decrease in the total surface free energy (Baldan, 2002, Madras and McCoy, 2003). Unlike simple crystal growth driven by supersaturation, this process occurs by dissolution of small clusters that give up their monomers to the growth of large particles (Baldan, 2002). An example of Ostwald ripening for a model bubble system is illustrated in Figure 1-7 (Mezzenga et al., 2005). Larger clusters accordingly will grow as supersaturation decreases during ripening. The explanation for such ripening is based on the Gibbs-Thomson relationship for interfacial and thermal energy that suggests that smaller clusters are more soluble than larger ones (Madras and McCoy, 2002b). The Gibbs-Thomson equation for a given supersaturation gives an expression for the critical nucleus size, where a cluster larger than the critical nucleus grows and those below will dissolve leading to a transfer of mass to the solution which is incorporated in to the larger cluster (Madras and McCoy, 2001, Madras and McCoy, 2002b). The growth of clusters might be influenced by different factors such as diffusion (Madras and McCoy, 2002b).

Different models have been proposed in order to explain this phenomenon. Some researchers included dissolution in their model (Madras and McCoy, 2002a), as dissolution can occur during growth and ripening when supersaturation decreases, causing an increase in the critical nucleus size. Therefore, any

particles smaller than critical nucleus size are unstable and instantly dissolve (Madras and McCoy, 2002a). Ultimately, Ostwald ripening should lead to the formation of one single condensed cluster containing all the available material; however, this does not occur due to the decrease in the growth rate as the size of the particle increases (Tadros et al., 2004).

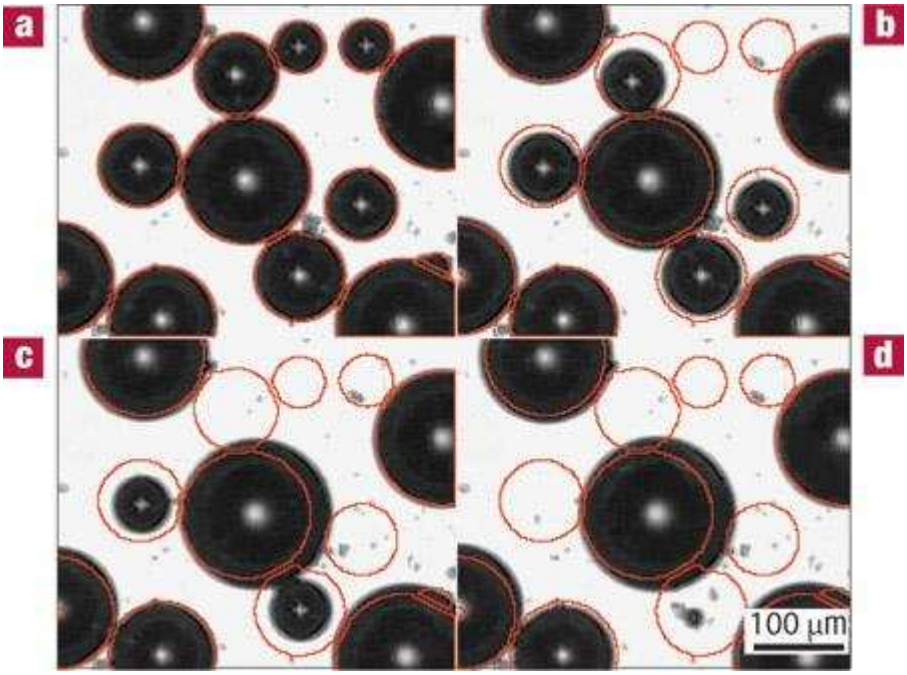

Figure 1-7: Bubble circumferences are drawn in red a, at the beginning of the experiment, and b–d, after 25, 50 and 75 minutes, respectively, showing the progressive loss of small bubbles due to gas diffusion towards big bubbles which progressively enlarge (Mezzenga et al., 2005).

1.6.2.2 Distribution Kinetics

Cluster size distribution (CSD) can be determined and expressed using the distribution kinetics approach that is generally applicable to growth, dissolution, or ripening. The CSDs can be influenced by the size-dependent rates for cluster growth and dissolution or the creation of new particles (Marqusee, 1983, Madras and McCoy, 2002b). Madras and McCoy defined CSD by c(x, t)dx, which

expresses the concentration of clusters at time t in the mass range (x,x+dx). The concentrations of the clusters are defined as integrals over the mass,

$$c^{(n)}(t) = \int_0^{\infty} c(x,t)\, x^n \, dx \qquad \text{(Madras and McCoy, 2001)} \qquad \textbf{Equation 1-3}$$

The deposition process where monomers are reversibly added to or dissociated from a cluster can be writer following this reaction,

$$\mathbf{C}(x) + \mathbf{M}(x') \underset{K_d(x)}{\overset{K_g(x)}{\rightleftharpoons}} \mathbf{C}(x + x') \qquad \text{(Madras and McCoy, 2001)}$$

where **C**(x) represents the cluster of mass x and **M**(*x'*) is the monomer. This process conserves mass. According to the molecularity equation 1-3, addition reactions are second order whereas dissociation reactions are first order (Madras and McCoy, 2002b). The growth rate k_g may be specific for a stirred system or may be related to the monomer diffusion coefficient in an unstirred system, and therefore, depends upon cluster mass and local thermodynamic conditions (Madras and McCoy, 2001).

1.6.2.3 Lifshitz-Slyosov-Wagner (LSW) Theory

In order to express the nucleation and growth with subsequent ripening a numerical solution is needed (Madras and McCoy, 2002c). In the early phase of the numerical model, the CSD is zero and nuclei are formed at their critical size.

At the second stage, the critical nucleus size grows leading to a reduced degree of metastabiltity, however the deposition of the monomer generated from the dissolving cluster have lead to the growth of larger clusters (Madras and McCoy, 2002c). The LSW theory is often used to describe and quantitatively assess the coarsening due to Ostwald ripening (Meinders and van Vliet, 2004). LSW theory allows an estimation of the rate of Ostwald ripening (Welin-Berger and Bergenstahl, 2000). The theory uses the following assumptions so that the rate of Ostwald ripening can be estimated (Madras and McCoy, 2003): a) the disperse phase particles are spherical and are fixed in space, b) the monomer atoms diffuse to the spherical particle in a continuous phase, c) there is no interaction between neighbouring particles d) the volume fraction of the dispersed phase in the continuous phase is infinitely dilute system and is constant except near the particle boundaries (Lifshitz and Slyozov, 1959, Welin-Berger and Bergenstahl, 2000, Baldan, 2002). However, by using all these assumptions quantitative conclusions are unaffected (Lifshitz and Slyozov, 1959). The LSW assumption is that growth of the cluster radius depends on a driving force related to the difference of the inverse radii of cluster and critical nucleus equation 1-5 (Berger, 2004),

$$\frac{dR}{dt} = K_{(LSW)}\left(\frac{1}{R}\right)\left(\frac{1}{R^*} - \frac{1}{R}\right) \qquad \textbf{Equation 1-4}$$

where R is the cluster radius, R* is the radius of the critical nucleus and $K_{(LSW)}$ is an empirical constant (Berger, 2004). dR/dt can be determined by the examination of the growth or dissolution of an isolated spherical particle in supersaturated media (Baldan, 2002). Therefore, the rate of Ostwald ripening is

directly proportional to the solubility of the disperse phase in the dispersion medium (Welin-Berger and Bergenstahl, 2000). Droplets with R>R* will grow while droplets with R<R* will dissolve (Fig. 1-8) (Lifshitz and Slyozov, 1959, Meinders and van Vliet, 2004). The critical size is governed not only by the initial supersaturation, but also by the number of clusters (where this can be considered a fixed quantity) (Lifshitz and Slyozov, 1959).

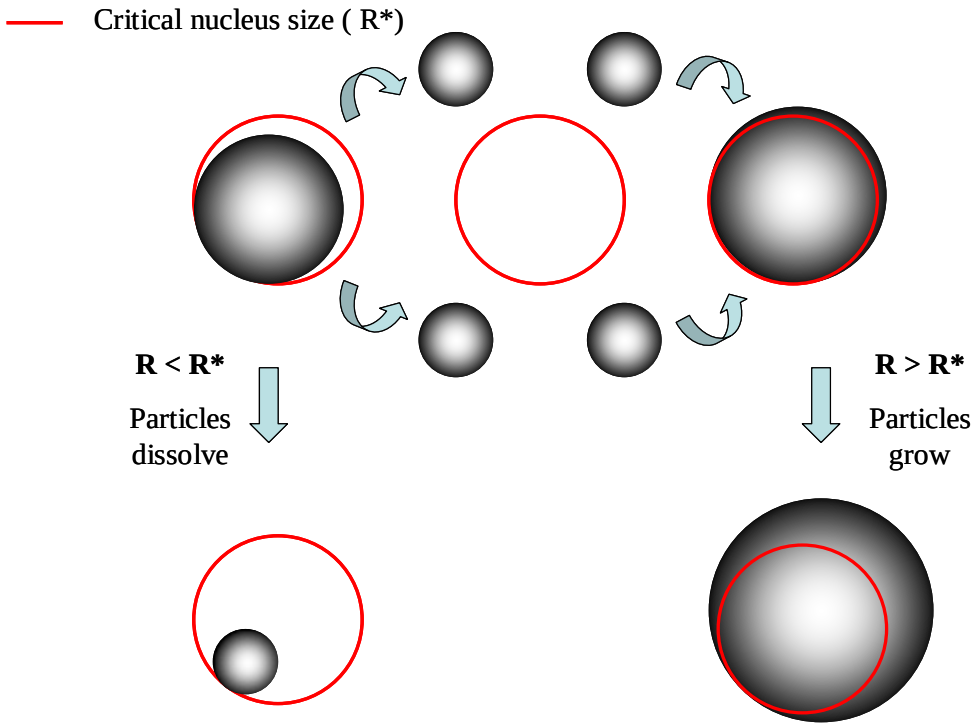

Figure 1-8: Schematic of the LSW theory.

The change in the particle radius following the LSW theory is time dependent and the average particle radius R(t) was found to increase with time as shown in equation 1-5:

$$R^3(t) = K_{LSW} \cdot t + R^3(0)$$ (Snyder, 2001) **Equation 1-5**

where R is the radius of the particles, K_{LSW} is the rate of Ostwald ripening and t is time.

As stated by Madras and McCoy, "the LSW theory yields only an asymptotic solution, valid in the limit of a zero volume fraction of a quasi-steady state after a long, unspecified period of time" (Madras and McCoy, 2003). Nevertheless, LSW theory has been widely adapted to determine the values of interfacial energy between the matrix and the dispersed phase (Baldan, 2002).

1.6.3 Material Properties Influencing Particle Interactions

There are several factors that influence particle interactions either with different materials or the particles with themselves. These factors are described below.

1.6.3.1 Surface Roughness

The principal interactions determining the adhesion between particles and surfaces are attractive van der Waal forces and electrostatic in case of charged particles (Eve et al., 2002). Elastic properties of the surface, surface morphology, particle shape and particle surface roughness is a main factor to consider in terms of adhesion and friction (Staniforth, 1995, Podczeck, 1998a). This is due to the degree of surface irregularities in the particle shape. Surface interactions will be diminished for spherical particles. Hence, any increase in irregularities in the particle shape will result in an increased interparticulate forces (Podczeck, 1998a). However, it has been shown that increasing surface roughness can be

used as a mean of significantly improving the adhesion properties between two surfaces at the nanoscale (Podczeck, 1998a, Rabinovich et al., 2000). This is due to decreasing contact area between the two surfaces with increasing roughness and hence less interaction between the two bulks and also to an increase in the distance between the bulk surfaces (Rabinovich et al., 2000). However, increased surface roughness can increase the adhesion between particles and surfaces if the particles are very small and thus can slip into the valleys between the asperities and have more contact with the surface (Fig. 1-9) (Podczeck, 1998b).

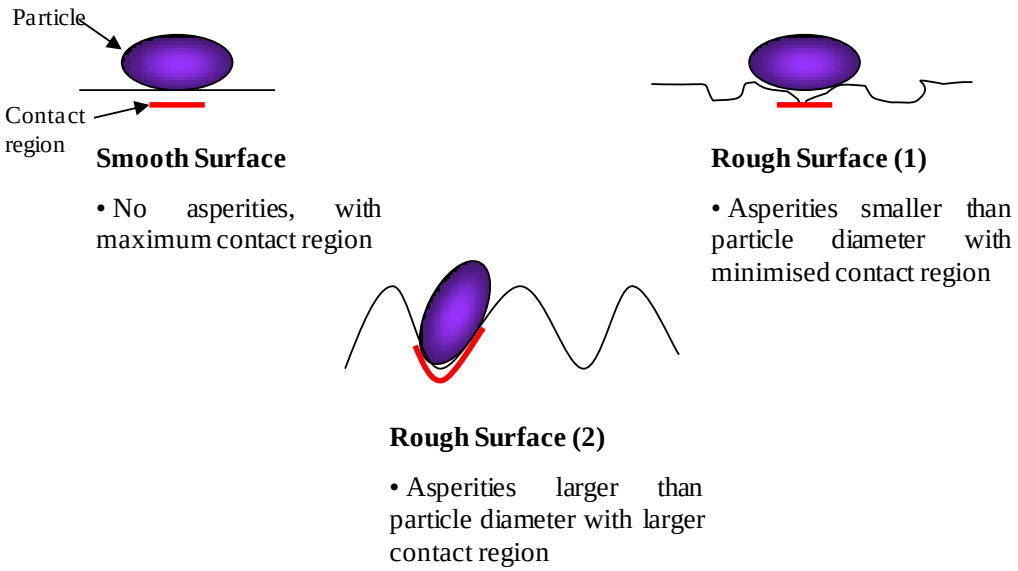

Figure 1-9: The relative effect of surface roughness on surface interactions.

1.6.3.2 Surface Energy

Surface free energy (γ) can be very closely related to the adhesion between two surfaces brought into contact. Therefore, a knowledge of surface energy is very useful in predicting and modelling the interactive behaviour between two different components of a pMDI formulation (Zhang et al., 2006). Surface

energy is defined as the free energy change during an increase in surface area by one unit in vacuum (Podczeck, 1998c). Surface energy can also be defined as the excess energy at the surface of the material compared to the bulk and it is derived from an unsatisfactory bonding potential at the surface of a material, resulting in free energy at the surface. Surfaces must be intrinsically less energetically favourable than the bulk of a material. However, this does not occur at a surface due to the exposure to different molecules. Therefore, the molecules will rearrange and react with the adjacent molecules to reduce their free energy. However, due to the lower strength of this interaction compared to the interaction with the surrounding molecules, there is an increased attraction of that molecule that will contract the material at the surface. Hence, the presence of surface tension at the surface of materials (Buckton, 1995).

The determination of surface energy of a pharmaceutical formulation is a recognized step in predicting a range of properties that may be displayed by a powder that include adhesion and its result on performance. For example, in a pMDI formulation, the surface energies of drug particles, excipients and the packaging materials can be used to predict the strength of interaction between each of these ingredients and hence help determine the suitability of the formulation and its stability (Davies et al., 2005, Zhang et al., 2006).

1.6.3.3 Adhesion Model

Different adhesion models theories are used in the literature to analyze pull-off force (Fig. 1-10). However, most models used to characterise particle

interactions use the "Hertz model of adhesion between contacting spheres" as their basis (Davies et al., 2005). Based upon the Hertz theory, two contact mechanics models were developed: Johnson-Kendall-Roberts (JKR) (Johnson et al., 1971) and Derjaguin-Muller-Toporov (DMT) (Derjaguin et al., 1975) and are frequently employed. The difference between these models is that the DMT theory calculates the force with the assumption that surface forces act outside the contact region (Johnson et al., 1971, Hooton et al., 2004). During this project, the JKR model has been followed and is described below.

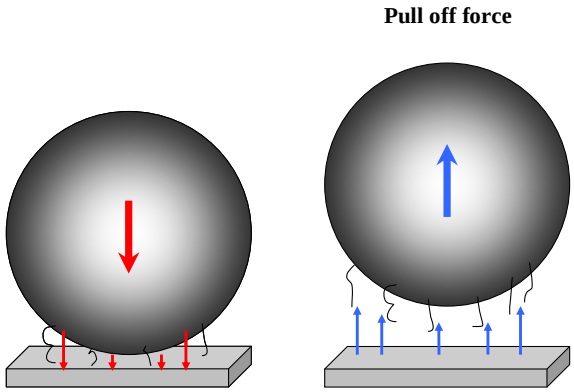

Figure 1-10: Schematic showing the pull off force

- The Johnson-Kendall-Roberts (JKR) Theory

The JKR model was developed by Johnson-Kendall-Roberts in 1971 and is the most used model for the determination of the adhesion between two materials (Johnson et al., 1971). The JKR theory calculates adhesion force (F_{adh}) by assuming that surface forces act only inside the contact region (Figure 1-11).

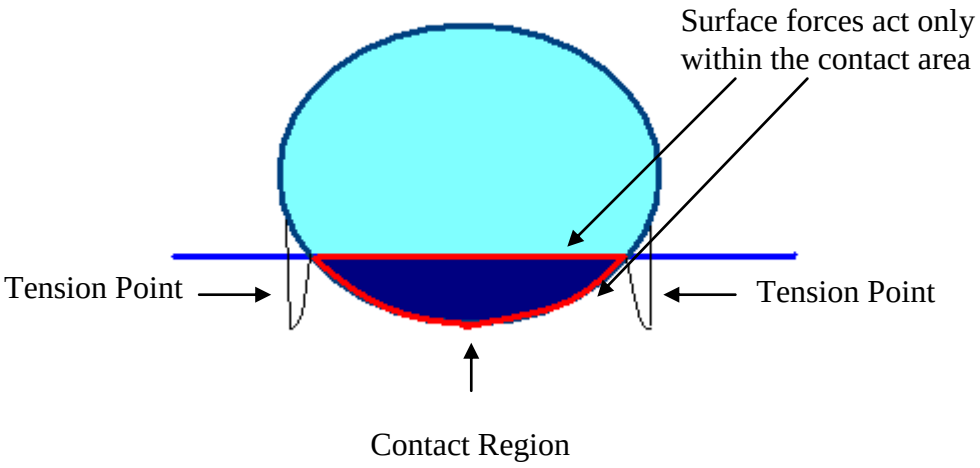

Figure 1-11: Applicability of the JKR model.

This model is based on the Hertz model and is described by the general Hertz Equation:

$$a_0^3 = \frac{3 R F_{on}}{4 E^*} \qquad \textbf{Equation 1-6}$$

Where a_0 is the contact radius, F_{on} is the loading force, R is the radius of the sphere and E* is the reduced Young's modulus of the system, which is calculated using the following equation:

$$\frac{1}{E^*} = \frac{1-\nu_1^2}{E_1} + \frac{1-\nu_2^2}{E_2} \qquad \textbf{Equation 1-7}$$

where E_1 and E_2 are the Young's modulus of the sphere and surface respectively, while ν_1 and ν_2 are the Poisson's ratios of the sphere and surface.

The fundamental principle on which the JKR model is based is a case where a smooth sphere, with elastic properties, contacts a flat substrate (Davies et al., 2005). The systems used throughout the project do not reflect this situation perfectly due to the use of different substrates with different surface characteristics. The JKR model is based upon the consideration that surface forces act inside the "neck" of the contact region and neglects any long-range force that might exist outside the contact region. Hence, it accounts for an infinite stress at the boundary of the contact zone as the load is reduced and the particle removed from contact (Hooton et al., 2003, Davies et al., 2005). The JKR model correlates the adhesion force (F_{adh}) with work of adhesion (W_a) through the following equation.

$$F_{adh} = 3/2\pi R W_a \qquad \textbf{Equation 1-8}$$

Where R is the radius of the sphere, F_{adh} is the force of adhesion and W_a is the work of adhesion. The work of adhesion can be calculated using the following equation;

$$W_a = 2\sqrt{\gamma_1\gamma_2} \qquad \textbf{Equation 1-9}$$

Where γ_1 and γ_2 are the dispersive components of the surface energy of particle and surface respectively. For work of adhesion between identical materials, the work of cohesion (W_c) is calculated following this equation;

$$W_C = 2\gamma \qquad \textbf{Equation 1-10}$$

1.7 Methods of Determining Particle-Surface Interactions

Different techniques can be used in order to study the interactions between particles and different surfaces. These techniques are vibration techniques, centrifugal techniques and scanning probe techniques (SPM). Atomic force microscopy (AFM) is a scanning probe technique that is now widely used for studying particle surface interactions. AFM is used during this project since it is the main technique used for studying particle surface interactions in different environment throughout the project.

1.7.1 Atomic Force Microscopy (AFM)

Atomic force microscopy (AFM) (Fig. 1-12) is a very high-resolution type of scanning probe microscopy (SPM). It was invented by Binnig, Quate, and Gerber in 1985. AFM imaging can be used to quantitatively determine surface topography and measure surface roughness with a nominal 5nm lateral and 0.01nm vertical resolution on all types of samples (Morris et al, 1999). The AFM works by scanning a probe over the sample surface, building up a map of the height and topography (Giessibl, 2003). A very sharp nanoscale tip, usually made from silicon or a nitrous silica compound, is used at the end of a flexible

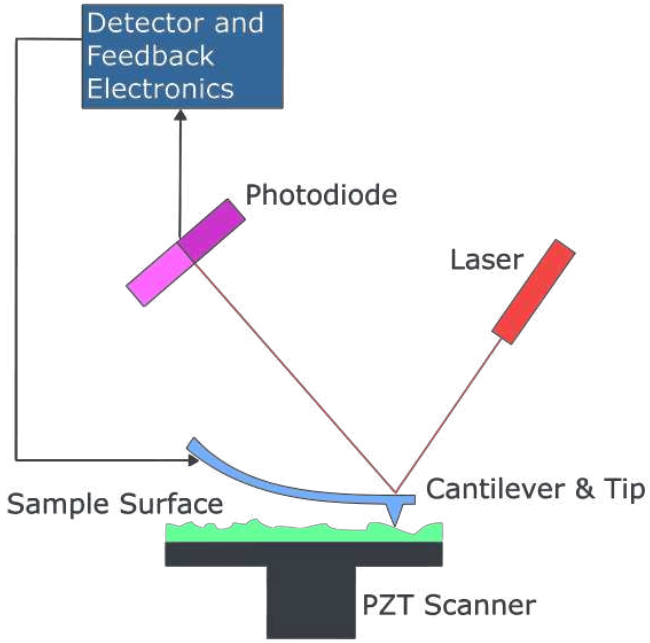

Figure 1-12: A Schematic diagram of an AFM (wikipedia.org, 2010).

cantilever and is scanned over a surface. The AFM utilizes an optical lever to monitor the motion of the tip mounted at the end of a reflective cantilever using a laser that is focused on the back of the cantilever (Morris et al., 1996). When scanning the surface sample, the tip undergoes upward and downward movements with the changes in the surface topography leading to the deflection of the laser into a segmented photodiode that traces the laser movement. The difference in light intensities between the upper and lower photo-detectors are monitored and converted into a voltage by the photo-detector (Morris et al., 1996). This latter generates a feedback mechanism that enables the piezo-ceramic transducers to maintain the tip at a constant force that allows real time determination of height information, or constant height to determine the deflection force above the sample (Giessibl, 2003). The images generated from the detector are three-dimensional topographical maps of the surface which are

constructed by plotting the local sample height versus horizontal probe tip position (Morris et al., 1996).

1.7.1.1 AFM Imaging Modes

The primary modes of operation are contact mode and tapping mode. In contact mode, the AFM tip is scanned across the sample whilst in constant contact with the sample surface (Morris et al., 1996). The tip deflection is monitored via a laser optical lever and used to generate a feedback signal. Because the measurement of a static signal is prone to noise and drift, low stiffness cantilevers are used to boost the deflection signal. However, close to the surface of the sample, attractive forces can be quite strong, causing the tip to 'snap-in' to the surface on approach. In contact mode, the force between the tip and the surface is kept constant during scanning by maintaining a constant deflection by the use of the feedback signal to control the piezo positioning. One of the main disadvantages of contact mode AFM is the unsuitability for soft or loose surfaces due to the deformations occurring to the surface due to the cantilever being dragged across the surface at constant and often relatively large force (especially lateral forces) (Morris et al., 1999). In addition to that, loose particles on the sample could be moved by the tip during imaging and thus giving a false surface topography imaging (Hooton et al., 2003).

In tapping mode, the cantilever is oscillated up and down at near its resonance frequency by a small piezoelectric element mounted in the AFM tip holder while being scanned across the sample surface. Upon contact with the sample surface,

changes in oscillation amplitude are detected and converted into a topographical image (Morris et al., 1996). A tapping AFM image is therefore produced by displaying an image of the feedback signal required to maintain constant amplitude of oscillation. This overcomes the problem of contact AFM related to sample damage due to lateral forces (Butt et al., 2005).

1.7.1.2 AFM Force Measurements Mode

In addition to these topographic measurements, the AFM can also provide much more information. As the AFM relies on the forces between the tip and the sample, it can be used to measure the long range attractive or repulsive forces between the probe tip and the sample surface at a single point or across a surface, elucidating local chemical and mechanical properties like adhesion and elasticity, and even molecular bond rupture strength (Butt et al., 2005a). The force is not measured directly, but calculated by measuring the deflection of the lever, and knowing the stiffness (spring-constant) of the cantilever following Hook's law (Equation 1-11)

$$F = -kz \qquad \textbf{Equation 1-11}$$

where F is the force, k is the spring constant (the stiffness of the lever), and z is the deflection distance of the cantilever.

Force curves (force-versus-distance curve) (Fig. 1-13) typically show the deflection of the free end of the AFM cantilever as the fixed end of the cantilever is brought vertically towards and then away from the sample surface.

Experimentally, this is done by applying a triangle-wave voltage pattern to the electrodes for the z-axis scanner. This causes the scanner to expand and then contract in the vertical direction, generating relative motion between the cantilever and sample. The deflection of the free end of the cantilever is measured and plotted at many points as the z-axis scanner extends the cantilever towards the surface and then retracts it again.

Similarly to the imaging mode, force measurements can be obtained for different surfaces under different conditions either in air or in liquid environment which is beneficial in terms of collecting data when particle-surface interactions are within a liquid environment such as in pMDI surface interactions where the APIs are suspended in the propellant.

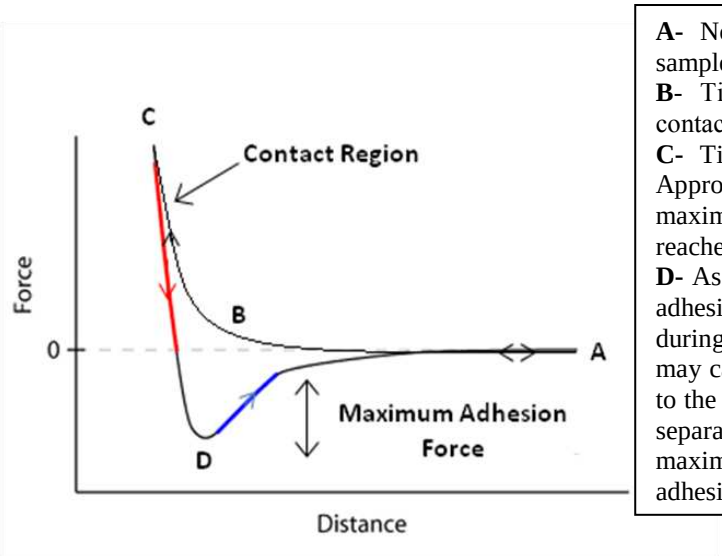

A- No contact between tip and sample
B- Tip and sample "jump into contact" due to attractive forces
C- Tip in contact with surface. Approach continues until the maximal nominal loading force is reached
D- As the cantilever is withdrawn, adhesion or cohesion formed during contact with the surface may cause the cantilever to adhere to the sample. The force needed to separate the tip and sample is the maximum force of adhesion/cohesion

Figure 1-13: Typical AFM force curve cycle (adapted from (Allen et al., 1998)).

1.7.1.3 AFM Use in Inhaled Particle Interactions

In recent years, many techniques have been developed in order to study and assess interparticulate interactions. AFM is one of the most utilized techniques in order to assess and quantify adhesion and cohesion between individual particles and sub-micron particle. Roberts highlighted how this technique could be used for the quantification of the adhesion forces and the significant potential of using AFM in formulation development (Roberts, 2005).

Several research groups used the potential of AFM in the area of inhalation where the knowledge of particle interactions and the components of the delivery device such as pMDI or DPI as well as with excipients. In one of his papers Ashayer et al. studied the forces of interaction between inhalable formoterol fumarate dehydrate particles and various components of a pMDI in the presence of a model HFA propellant and different surfactant polymers (Ashayer et al., 2004). Their studies were able to demonstrate a degree of instability of the formulation in a model HFA propellant in the presence and absence of polymers. Using AFM to determine the adhesion measurements, they also showed that the adhesion forces to the canister walls were diminished upon the addition of the surfactant polymers and that the use of block or comb copolymers may provide a better option in reducing the possibility of bringing interactions.

The effect of humidity on inhaled formulations has been the subject of a number of studies. Young et al. have demonstrated that the effect of an increase in the relative humidity may lead to an increase in drug cohesion in some materials and a decrease in drug cohesion for others (Young et al., 2004). Hooton et al. have

also showed that variation in particle contact morphology for the same material cause similar behaviour in terms of increased drug adhesion with increasing humidity (Hooton et al., 2004). Furthermore, they used AFM in order to investigate the effect of contact area acquired adhesion force measurements in a model pMDI propellant system, then relating those measurements to contact area and work of adhesion. Also, it was shown that it was possible to acquire three-dimensional representations of the area of contact of the particle and hence ability to compare different particles (Hooton et al., 2003). Moreover, Jones et al. demonstrated the ability of AFM in monitoring the recrystallization of amorphous regions in micronized particles in order to improve their processability and physico-chemical stability (Jones et al., 2008).

Williams and co-workers were able to show the use of AFM to study the delivery performance and the stability of pMDI formulation containing beclomethasone dipropionate (BDP) and triamicinolone acetonide (TAA) in HFA propellant in terms of particle crystal growth and also that the differences in the surface roughness of a pMDI canister were a function of the type of the propellant, temperature and storage conditions (Williams III et al., 2000). Ostwald ripening has also been studied by Madras and co-workers (Madras and McCoy, 2002c, Madras and McCoy, 2003). Sedimentation and creaming where studies in order to provide a better understanding of these phenomena and how these can be prevented (Jeelani et al., 2005, Watson et al., 2005).

1.8 Thesis Aims and Objectives

The work presented in this multi-disciplinary project aims to characterise and understand the physicochemical and solid state behaviour of drugs in HFA-134 and 227 propellants employed in metered dose inhaler devices. The project aims to investigate the long term stability of crystalline drugs in HFA-134 and 227 and the requirements for the formation of HFA clathrates in drug compounds for inhalation. The project will investigate several aspects contributing to the efficiency of a pMDI formulation such as:

- The physicochemical properties of a model CFC clathrate and HFA clathrates
- The surface characteristics of the different APIs and pMDI components
- The surface energy and forces of adhesion of the different APIs and their correspondent clathrates within a pMDI formulation
- The effect of size reduction on the surface energy and the force of adhesion of the different drug in a pMDI formulation
- Understand the process of Ostwald ripening and any effect of EtOH or surfactant on this phenomena in a pMDI formulation

In order to investigate these aims, the work will be detailed in the following manner;

Chapter 2 will cover the main materials and methods used to investigate and characterize clathrate formation and API-pMDI interactions and the process of Ostwald ripening.

Chapter 3 will investigate and characterise the physico-chemical properties of beclomethasone dipropionate (BDP) crystallized from trichloromonofluoromethane (CFC-11). Following the surface characterisation of the BDP CFC-11 clathrate, the effect of different BDP, CFC-11 concentrations will be used in order to determine their effect on the clathrate formation.

Chapter 4 will characterise and compare two different clathrates of BDP crystallized from HFA-134a and 227 and determine the effect of EtOH on their formation within a pMDI formulation. Surface characterisation and any polymorphic changes following heating will be determined in order to study the stability of BDP HFA propellant entities formed within a pMDI formulation.

Chapter 5 will capture the details of the study of the effect of size reduction on API interactions with different pMDI components. It will also determine the surface free energy (SE) and forces of adhesion (F_{adh}) of the different BDP entities used in this study with different pMDI components in a model propellant (decafluoropentane) and determine the effect of size reduction on the latter.

Chapter 6 aims to investigate and try to understand the process of Ostwald ripening for different BDP entities used during the project as well as budesonide

and determine the effect of ethanol and surfactant (oleic acid) on it within a pMDI formulation. Furthermore, AFM will be used in order to see any surface changes occurring during the process of Ostwald ripening and determine the effect of formulation excipients on these latter.

Chapter 7 will provide a brief summary of the findings of this project with an overview of the main conclusion obtained in each chapter and the general conclusion from the work. Furthermore, some suggested future work with respect to formulation-device interactions and other techniques that might be used to study Ostwald ripening process in a pMDI formulation.

1.9 References

ALLEN, S., CHEN, X., J., D., DAVIES, M. C., DAWKES, A. C., EDWARDS, J. C., ROBERTS, C. J., TENDLER, S. J. B. & WILLIAMS, P. M. (1998) The application of force microscopy to immunodiagnostic systems: imaging and biomolecular adhesion measurements. Applied Physics A Materials Science & Processing, 66**,** S255–S261.

ANDERSON, P. J. (2001) Delivery options and devices for aerosolized therapeutics. Chest, 120**,** 89S-93S.

ASHAYER, R., LUCKHAM, P. F., MANIMAARAN, S. & ROGUEDA, P. (2004) Investigation of the molecular interactions in a pMDI formulation by atomic force microscopy. European Journal Pharmaceutical Sciences, 21**,** 533-43.

ASTHMA (2009) British guideline on the management of asthma, SIGN and BTS.

BAILEY, M. M. & BERKLAND, C. J. (2009) Nanoparticle formulations in pulmonary drug delivery. Medicinal Research Review, 29**,** 196-212.

BALDAN, A. (2002) Progress in Ostwald ripening theories and their applications to nickel-base superalloys. Journal of materials science, 37**,** 2171-2202.

BARRER, R. M. & RUZICKA, D. J. (1962a) Non-Stoichiometric Clathrate Compounds of Water .3. Inclusion Energies and Constants in Small Cavities of Structure Ii. Transactions of the Faraday Society, 58**,** 2253-2261.

BARRER, R. M. & RUZICKA, D. J. (1962b) Non-Stoichiometric Clathrate Compounds of Water .4. Kinetics of Formation of Clathrate Phases. Transactions of the Faraday Society, 58**,** 2262-2271.

BEAUCHAMP, B. (2004) Natural gas hydrates: myths, facts and issues. Comptes Rendus Geoscience, 336**,** 751-765.

BERGER, A. (2004) An improved equation for crystal size distribution in second-phase influenced aggregates American Mineralogist, 89**,** 126-131.

BNF (2009) British National Formulary (BNF 58), BMJ Group and RPS Publishing.

BRINDLEY, A. (1999) The chlorofluorocarbon to hydrofluoroalkane transition: the effect on pressurized metered dose inhaler suspension stability. Journal of Allergy and Clinical Immunology, 104**,** S221-6.

BRITISH PHARMACOPOEIA, C. (2010) British Pharmacopoeia. British Pharmacopoeia 2010.

BUCKTON, G. (1995) Interfacial Phenomena in Drug Delivery and Targeting, Switzerland, Harwood Academic.

BUFFETT, B. A. (2000) Clathrate Hydrates. Annual Review of Earth and Planetary Science, 28**,** 477-507.

BUTT, H. J., CAPPELLA, B. & KAPPL, M. (2005a) Force measurements with the atomic force microscope: Technique, interpretation and applications. Surface Science Reports, 59**,** 1-152.

BUTT, H. J., CAPPELLA, B. & KAPPL, M. (2005b) Force measurements with the atomic force microscope: Technique, interpretation and applications. Surface Science Reports, 59**,** 1–152.

BYRON, P. R. & PATTON, J. S. (1994) Drug delivery via the respiratory tract. Journal of Aerosol Medicine, 7**,** 49-75.

CHELLAT, F., MERHI, Y., MOREAU, A. & YAHIA, L. (2005) Therapeutic potential of nanoparticulate systems for macrophage targeting. Biomaterials, 26**,** 7260-75.

CHOUGULE, M. B., PADHI, B. K., JINTURKAR, K. A. & MISRA, A. (2007) Development of dry powder inhalers. Recent Patents on Drug Delivery & Formulation, 1**,** 11-21.

CLARK, A. R. (1996) MDIs: physics of aerosol formation. Journal of Aerosol Medicine, 9 Suppl 1**,** S19-26.

CRIPPS, A., RIEBE, M., SCHULZE, M. & WOODHOUSE, R. (2000) Pharmaceutical transition to non-CFC pressurized metered dose inhalers. Respiratory Medicine, 94 Suppl B**,** S3-9.

DAVIES, M., BRINDLEY, A., CHEN, X., MARLOW, M., DOUGHTY, S. W., SHRUBB, I. & ROBERTS, C. J. (2005) Characterization of drug particle surface energetics and young's modulus by atomic force microscopy and inverse gas chromatography. Pharmaceutical Research, 22**,** 1158-66.

DENDY SLOAN, E. J. (1998) Clathrate hydrates of natural gases, Colorado, Marcel, Dekker, Inc.

DERJAGUIN, B. V., MULLER, V. M. & TOPOROV, Y. P. (1975) Effect of contact deformations on the adhesion of particles. Journal of Colloid and Interface Science, 53**,** 314-326.

DOLOVICH, M. B. (1997) Aerosols. IN BARNES, P. J. & GRUNSTEIN, M. M. (Eds.) Asthma. Philadelphia: Lippincott-Raven Publishers.

ENGLEZOS, P. (1993) Clathrate Hydrates. Industrial and Engineering Chemistry Research, 32**,** 1251-1274.

EVE, J. K., PATEL, N., LUK, S. Y., EBBENS, S. J. & ROBERTS, C. J. (2002) A study of single drug particle adhesion interactions using atomic force microscopy. International Journal of Pharmaceutics, 238**,** 17-27.

FINK, J. B. (2000) Metered-dose inhalers, dry powder inhalers, and transitions. Respiratory Care, 45**,** 623-35.

FRIJLINK, H. W. & DEBOER, A. H. (1994) Dry powder inhalers for pulmonary drug delivery. Expert Opinion on Drug Delivery, 1**,** 67-86.

GELLER, D. E. (2005) Comparing clinical features of the nebulizer, metered-dose inhaler, and dry powder inhaler. Respiratory Care, 50**,** 1313-21; discussion 1321-2.

GIESSIBL, F. J. (2003) Advances in atomic force microscopy. Reviews of Modern Physics, 75**,** 949-983.

GRAAUW, J. D. & RUTTEN, J. J. (1970). Dubrovnik, Proceeding of the Third International Symposium On fresh Water from the sea.

HOOTON, J. C., GERMAN, C. S., ALLEN, S., DAVIES, M. C., ROBERTS, C. J., TENDLER, S. J. & WILLIAMS, P. M. (2004) An atomic force microscopy study of the effect of nanoscale contact geometry and surface chemistry on the adhesion of pharmaceutical particles. Pharmaceutical Research, 21**,** 953-61.

ISLAM, N. & GLADKI, E. (2008) Dry powder inhalers (DPIs)--a review of device reliability and innovation. International Journal of Pharmaceutics, 360**,** 1-11.

JEELANI, S. A. K., BENOIST, G., JOSHI, K. S., GUNDE, R., KELLENBERGER, D. & WINDHAB, E. J. (2005) Creaming and aggregation of particles in suspensions. Colloids and Surfaces A: Physicochemical and Engineering Aspects**,** 263-379.

JOHNSON, K. L., KENDALL, K. & ROBERTS, A. D. (1971) Surface energy and the contact of elastic solids. Proceedings of the Royal Society of London, A324**,** 301-313.

JONES, M. D., YOUNG, P. M., TRAINI, D., SHUR, J., EDGE, S. & PRICE, R. (2008) The use of atomic force microscopy to study the conditioning of micronized budesonide. International Journal of Pharmaceutics, 357**,** 314-317.

KOH, C. A. (2002) Towards a fundamental understanding of natural gas hydrates. Chemical Society Reviews, 31**,** 157-67.

LABIRIS, N. R. & DOLOVICH, M. B. (2003a) Pulmonary drug delivery. Part I: physiological factors affecting therapeutic effectiveness of aerosolized medications. British Journal of Clinical Pharmacology, 56**,** 588-99.

LABIRIS, N. R. & DOLOVICH, M. B. (2003b) Pulmonary drug delivery. Part II: the role of inhalant delivery devices and drug formulations in therapeutic effectiveness of aerosolized medications. British Journal of Clinical Pharmacology, 56**,** 600-12.

LEACH, C. L. (2005) The CFC to HFA transition and its impact on pulmonary drug development. Respiratory Care, 50**,** 1201-8.

LIFSHITZ, I. M. & SLYOZOV, V. V. (1959) The kinetics of precipitation from supersaturated sold solutions. Journal of physical chemistry solids, 19**,** 35-50.

LOGVINENKO, V., DREBUSHCHAK, V., PINAKIV, D. & CHEKHOVA, G. (2007) Thermodynamic and kinetic stability of inclusion compounds under heating. Journal of thermal analysis and calorimetry, 90**,** 23-30.

MADRAS, G. & MCCOY, B. J. (2001) Distribution kinetics theory of Ostwald ripening. Journal of chemical physics, 115**,** 6699-6706.

MADRAS, G. & MCCOY, B. J. (2002a) Denucleation rates during Ostwald ripening: Distribution kinetics of unstable clusters. Journal of chemical physics, 117**,** 6607-6613.

MADRAS, G. & MCCOY, B. J. (2002b) Ostwald ripening with size-dependent rates: Similarity and power-law solutions. Journal of chemical physics, 17**,** 8042-8049.

MADRAS, G. & MCCOY, B. J. (2002c) Transition from nucleation and growth to Ostwald ripening. Chemical Engineering Science, 57**,** 3809-3818.

MADRAS, M. & MCCOY, B. J. (2003) Continuous distribution theory for Ostwald ripening: comparison with the LSW approach. Chemical Engineering Science, 58**,** 2903-2909.

MARIEB, E. N. (2005) The respiratory system. Essentials of human anatomy and physiology. 6th ed., Benjamin-Cummings Publishing company.

MARIEB, E. N. & HOEHN, K. (2007) Human anatomy & physiology, Pearson Education, Inc.

MARQUSEE, J. A. A. R., J. (1983) Kinetics of phase transitions: Theory of Ostwald ripening. Journal of chemical physics, 79**,** 373-378.

MCDONALD, K. J. & MARTIN, G. P. (2000) Transition to CFC-free metered dose inhalers - into the new millennium. International Journal of Pharmaceutics, 201**,** 89-107.

MEINDERS, M. B. & VAN VLIET, T. (2004) The role of interfacial rheological properties on Ostwald ripening in emulsions. Advances in Colloid and Interface Science, 108-109**,** 119-26.

MEZZENGA, R., SCHURTENBERGER, P., BURBIDGE, A. & MICHEL, M. (2005) Understanding foods as soft materials. Nature Materials, 4**,** 729-40.

MOLINA, M. J. & ROWLAND, F. S. (1974) Stratospheric sink for chlorofluoromethanes: chlorine atom catalysed destruction of ozone. Nature, 249**,** 810-812.

MORRIS, V. J., KIRBY, A. R. & GUNNING, A. P. (1996) Atomic force microscopy for beginners.

MORRIS, V. J., KIRBY, A. R. & GUNNING, A. P. (1999) Using Atomic Force Microscopy to Probe Food Biopolymer Functionality. Scanning, 21**,** 287–292.

PATCHKOVSKII, S. & TSE, J. S. (2003) Thermodynamic stability of hydrogen clathrates. Proceedings of the National Academy of Science. U S A, 100**,** 14645-50.

PATTON, J. S. (1996) Mechanisms of macromolecule absorption by the lungs. Advanced Drug Delivery Review, 19**,** 3-36.

PLUMRIDGE, T. H. & WAIGH, R. D. (2002) Water structure theory and some implications for drug design. Journal of Pharmacy and Pharmacology, 54**,** 1155-79.

PODCZECK, F. (1998a) Adhesion forces in interactive powder mixtures of a micronized drug and carrier particles of various particle size distributions. Journal of Adhesion Science and Technology, 12**,** 1323-1339.

PODCZECK, F. (1998b) Evaluation of the adhesion properties of salbutamol sulphate to inhaler materials. Pharmaceutical Research, 15**,** 806-8.

PODCZECK, F. (1998c) Particle-Particle Adhesion in Pharmaceutical Powder Handling, London, Imperial College Press.

RABINOVICH, Y. I., ADLER, J. J., ATA, A., SINGH, R. K. & MOUDGIL, B. M. (2000) Adhesion between Nanoscale Rough Surfaces. Journal of Colloid and Interface Science, 232**,** 10-16.

RANDALL, M. D. & NEIL, K. E. (2003) Disease Management, Pharmaceutical Press.

ROBERTS, C. J. (2005) What can we learn from atomic force microscopy adhesion measurements with single drug particles. European Journal of Pharmaceutical Sciences, 24**,** 153-157.

RODRIGUEZ-SPONG, B., PRICE, C. P., JAYASANKAR, A., MATZGER, A. J. & RODRIGUEZ-HORNEDO, N. (2004) General principles of pharmaceutical solid polymorphism: a supramolecular perspective. Advanced Drug Delivery Reviews, 56**,** 241-74.

SCHOBER, H., ITOH, H., KLAPPROTH, A., CHIHAIA, V. & KUHS, W. F. (2003) Guest-host coupling and anharmonicity in clathrate hydrates. The European physical journal. E, Soft matter, 12**,** 41-9.

SHERWOOD, L. (2008) Human Physiology: From Cells to Systems, Cossio, Y.

SHOYELE, S. A. & CAWTHORNE, S. (2006) Particle engineering techniques for inhaled biopharmaceuticals. Advanced Drug Delivery Reviews, 58**,** 1009-29.

SMOLA, M., VANDAMME, T. & SOKOLOWSKI, A. (2008) Nanocarriers as pulmonary drug delivery systems to treat and to diagnose respiratory and non respiratory diseases. International Journal of Nanomedicine, 3**,** 1-19.

SMYTH, H. D. (2003) The influence of formulation variables on the performance of alternative propellant-driven metered dose inhalers. Advanced Drug Delivery Reviews, 55**,** 807-28.

SNYDER, V. A., ALKEMPER, J. AND VOORHEES, P.W. (2001) Transient Ostwald ripening and the disagreement between steady-state coarsening theory and experiment. Acta Materials., 49**,** 699-709.

STANIFORTH, J. N. (1995) Performance-modifying influences in dry powder inhalation systems. Aerosol Science and Technology, 22**,** 346-353.

STEIN, S. W. & STEFELY, J. S. (2003) Reinventing metered dose inhalers; From poorly efficient CFC MDIs to highly efficient HFA MDIs. Drug Delivery Technology, 3**,** 45-51.

SUNG, J. C., PULLIAM, B. L. & EDWARDS, D. A. (2007) Nanoparticles for drug delivery to the lungs. Trends Biotechnology, 25**,** 563-70.

TADROS, T., IZQUIERDO, P., ESQUENA, J. & SOLANS, C. (2004) Formation and stability of nano-emulsions. Advances in Colloid and Interface Science, 108-109**,** 303-18.

TERZANO, C. (2001) Pressurized metered dose inhalers and add-on devices. Pulmonary Pharmacology and Therapeutics, 14**,** 351-66.

VERVAET, C. & BYRON, P. R. (1999) Drug-surfactant-propellant interactions in HFA-formulations. International Journal of Pharmaceutics, 186**,** 13-30.

VIRCHOW, J. C., CROMPTON, G. K., DAL NEGRO, R., PEDERSEN, S., MAGNAN, A., SEIDENBERG, J. & BARNES, P. J. (2008) Importance of inhaler devices in the management of airway disease. Respiratory Medicine, 102**,** 10-9.

VIRTUALMEDICALCENTRE.COM (2010) Respiratory System.

WATSON, A. D., BARKER, G. C. & ROBINS, M. M. (2005) Sedimentation in biodisperse and polydisperse colloids. Journal of Colloid and Interface Science, 286**,** 176-86.

WELIN-BERGER, K. & BERGENSTAHL, B. (2000) Inhibition of Ostwald ripening in local aesthetic emulsions by using hydrophobic excipients in the disperse phase. International Journal of Pharmaceutics, 200**,** 249-60.

WIKIPEDIA.ORG (2010) Atomic Force Microscopy.

WILLIAM III, R. O., ROGERS, T. O. & LIU, J. (1999) Study of Solubility of Steroids in Hydrofluoroalkane Propellants. Drug Development and Industrial Pharmacy, 25**,** 1227-1234.

WILLIAMS, G. (1998) Moisture transport into CFC-free MDIs. PMDIs in Transition: CFC to HFA Formulation. Drug Information Association, Arlington, VA.

YOUNG, P. M., PRICE, R., TOBYN, M. J., BUTTRUM, M. & DEY, F. (2004) The influence of relative humidity on the cohesion properties of micronized drugs used in inhalation therapy. Journal of Pharmaceutical Sciences, 93**,** 753-761.

ZHANG, J., EBBENS, S., CHEN, X., JIN, Z., LUK, S., MADDEN, C., PATEL, N. & ROBERTS, C. J. (2006) Determination of the surface free energy of crystalline and amorphous lactose by atomic force microscopy adhesion measurement. Pharmaceutical Research, 23**,** 401-7.

Chapter 2 Materials and Methods

2.1 Chapter Aims and Objectives

This chapter will provide the reader with a full knowledge of both the materials and the experimental procedures employed to produce the results detailed in this thesis. The active pharmaceutical ingredients, excipients, co-solvents and the model propellant used in this project will be presented and discussed. Subsequently the experimental protocols used to generate the results will be detailed. These techniques include scanning electron microscopy, atomic force microscopy, X-ray photoelectric spectrometry, differential scanning calorimetry and Raman spectroscopy, amongst others.

2.2 Materials

2.2.1 Active Pharmaceutical Ingredients

Two different pharmaceutical ingredients (APIs) were used throughout the course of this project. They are both widely used in pressurized metered dose inhalers and their formulation suffers some stability issues especially in the new hydrofluoroalkane propellants. These are as follow:

Beclomethasone Dipropionate:

Beclomethasone Dipropionate is a corticosteroid. It is a white/almost white crystalline powder, which is practically insoluble in water, soluble in acetone

while sparingly soluble in alcohol (96 per cent) (Figure 1-2, Chapter 1, Section 1.3) (British Pharmacopoeia, 2010).

Budesonide:

Budesonide is a corticosteroid. It is a white/almost white crystalline powder, which is partially soluble in water, freely soluble in methylene chloride, sparingly soluble in ethanol (96 per cent) (Figure 1-3, Chapter 1, Section 1.3) (British Pharmacopoeia, 2010).

2.2.2 Propellants

Trichlorofluoromethane (CFC-11) was used as a model for the initial phase of the project for the characterization of the clathrate, as it stable at ambient temperature and has been used previously used in pressurized metered dose inhalers before being replaced with 1,1,1,2-tetrafluoroethane (HFA-134a) and 1,1,1,2,3,3,3-heptafluoropropopane (HFA-227). HFA-134a and HFA-227ae were also used for the potential synthesis and characterisation of the API clathrate crystallized from the latter. 2H, 3H decafluoropentane was used as a model HFA propellant (referred to as mHFA therein after) as its properties are very similar to the more commonly used HFA-134a, HFA-227, but it is stable at ambient temperature and pressure and hence suitable for analysis where the pressure required to keep HFA's liquid cannot be applied. The chemical structures of the different propellants used in this study are shown in Figure 2-1.

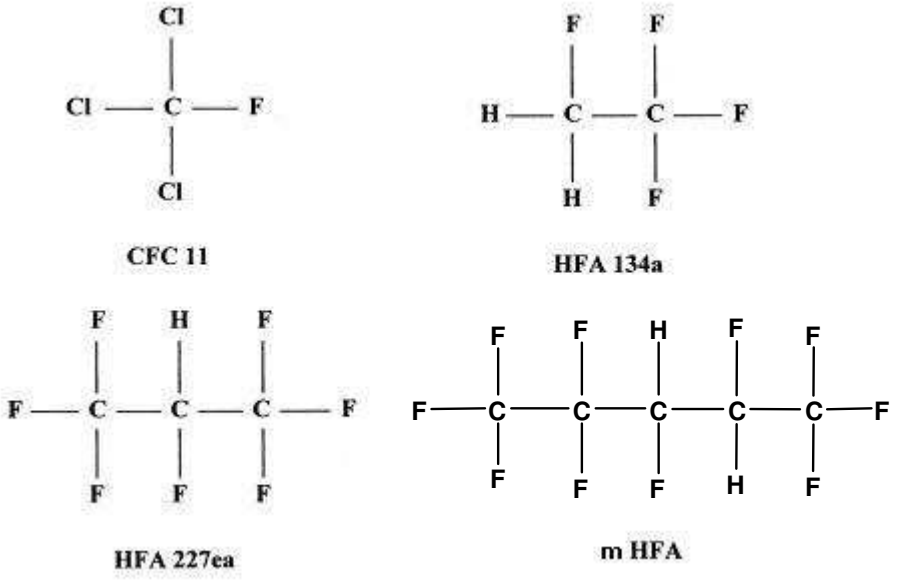

Figure 2-1 Chemical structure of the different propellants used in this study.

From Figure 2-1 we can observe that CFC-11 is completely halogenated and thus, the carbon backbone is shrouded entirely by large electronegative mantel atoms while the HFAs have one or two small, asymmetrically positioned, hydrogen atoms in their mantels (Vervaet and Byron, 1999). The enhanced electronegativity in the halogen mantel of the HFAs creates a distinct dipole on the hydrogen-carbon bonds in both propellants (Vervaet and Byron, 1999). mHFA is well characterised (Rogueda, 2003). The carbon backbone of mHFA is almost completely fluorinated, with the exception of two hydrogen atoms at positions 2 and 3 which make it structurally similar to the HFA 277 propellants. Therefore, it is believed to be a better model for the HFA 227 rather than HFA 134a (Rogueda, 2003, Selvam et al., 2006). The chemical properties of each HFA propellant are summarised in Table 2-1.

Table 2-1: The comparative properties of mHFA, CFC-11, HFA134a and HFA 227 (adapted from (Vervaet and Byron, 1999, Rogueda, 2003)).

	mHFA	CFC-11	HFA-134a	HFA-227
Molecular weight (g/mol)	252.05	137.37	170.03	102.03
Density (g/cm^3)	1.58	1.494	1.388	1.208
Boiling Point (°C)	53.6	23.77	-16.5	-26.3
Melting Point (°C)	-80	-110.48	-131	-101
Water Solubility (ppm)	390	100	610	2200
Surface Tension (mNm^{-1})	13.59	17.7	7.55	8.69
Dynamic Viscosity (mPa)	0.537	0.74	0.266	0.211
Dielectric Constant	15.05*	2.3	4.071	9.46

*at 18.06 Hz

2.2.3 Co-solvents

Ethanol (EtOH) and isopropyl alcohol (IPA) are used as a co-solvent in many HFA-containing pMDI suspension formulations in order to increase the solubility of APIs and certain surfactants in the propellant. The chemical structure of both ethanol and IPA is shown in Figure 2-2.

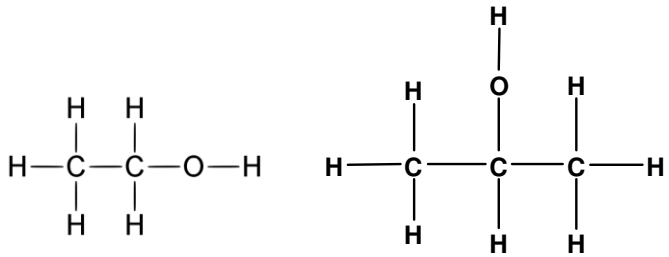

Figure 2-2: Chemical structure of ethanol and isopropyl alcohol.

Ethanol is a short chain alcohol, which has considerable solvent attributes, and is also non-toxic to humans in small volumes (Stein and Stefely, 2003). In contrast, IPA is used as co-solvent amongst other short alcohols with different APIs in pMDI formulation in order to form a crystalline solvate and thus lead to a more stable formulation (Jinks, 1989). The solubility of a drug in a solvent is reliant on its ability to form dipole-dipole interactions with the solvent (Vervaet and Byron, 1999). When one considers the small molecular size of these two alcohols, along with their dipole existence at the 'methyl-hydroxyl junction', their reason for use as a co-solvent in the new generation of HFA pMDI formulations is clear.

2.2.4 pMDI Components

Different pMDI components were utilized throughout this project, as a representation of the different components used in pMDI systems. These components were used for the assessment of the API-pMDI component adhesion. These are as follow:

Aluminium Canisters (non-coated) and Fluorinated Ethylene Propylene (FEP) Aluminium Canisters:

The pMDI canister is where the formulation resides. As a result, one would assume that most of the interactions between the API particles and the pMDI component will occur more frequently in this part of the pMDI. Stainless steel and aluminium canister have been developed due to the feature that they exhibit which are strengthened thicker walls and ellipsoidal base (Chan and Burt, 2009).

Aluminium canisters can be used as non-coated or FEP-coated with a submicron thick layer of a fluorinated polymer (Fig. 2-3) (Ashayer et al., 2004). This polymer is used reduce friction properties and improve non-reactivity (Ashayer et al., 2004). Throughout the different studies, both non-coated and FEP-coated aluminium canisters were used for direct assessment of API particle interactions. The non-coated aluminium canisters would assume a direct aluminium interaction with the API particles. However, fluorine, carbon and hydrogen will be predominantly interacting with the API particles in the case of the FEP-coated aluminium canister.

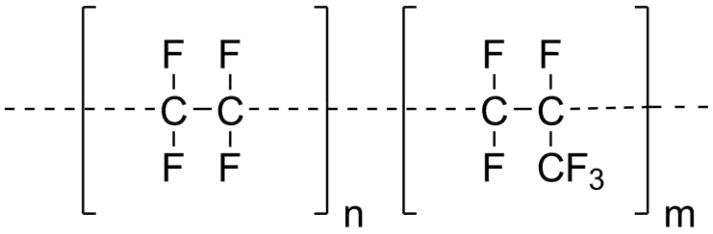

Figure 2-3: Chemical structure of Fluorinated Ethylene Propylene (FEP) molecule.

Ethylene-propylene-diene-monomer (EPDM) Valve Seal and Nitrile Valve Seal:

The pMDI valve seals are responsible for helping careful control of delivery of the metered dose during actuation and to provide precise through-life dose uniformity. Two commercially available seals are ethylene-propylene-diene monomer (EPDM) valve seals and nitrile valve seals. In this project, the two types were used and compared, with respect to adhesion to selected APIs. While both valve types are polyvinyl in nature, they have very different surface chemistries.

Stainless Steel Metering Chamber:

The metering chamber allows a metered quantity of the pMDI formulation to be dispensed or delivered with each actuation. The metering valve is required to retain and protect the contents of the canister while delivering a fixed volume (usually 25–100 ml) of the formulation accurately and reproducibly throughout use by the patient (McDonald and Martin, 2000). The metering chamber, along with other components including the valve seals make up most of the metering valve. At rest, the chamber is open to the bulk liquid. During actuation, the inner seal closes and outer opens so that only the contents of the chamber are discharged under the vapour pressure of the propellant. Therefore, there is the potential for significant API interactions with the metering chamber within the metering valve (McDonald and Martin, 2000). There are a number of commercially available metallic or polyvinyl valve components. For this study, metallic stainless steel valve components were used.

2.3 Methods

2.3.1 Scanning Electron Microscopy (SEM)

Scanning electron microscopy is a very powerful technique in terms of yielding information about the surface topography, morphology, composition and crystallographic information (Butt et al., 2004). SEM employs a beam of highly energetic electrons to examine objects on a sub-micron scale. A stream of electrons is generated by an electron gun in high vacuum (Egerton, 2005). This stream is accelerated towards the specimen by a high voltage (between 1 keV and

400 keV depending on the system) towards the sample. The sample is then irradiated by the beam and interactions occur inside the irradiated sample. The interaction of primary electrons with the sample surface results in the generation of lower-energy secondary electrons from the surface. These secondary and backscattered electrons are collected by a detector and subsequently the signal resulting from their emission is amplified and optimised in order to allow visualisation on a monitor (Egerton, 2005). A schematic diagram outlining the key components of an SEM is shown in Figure 2-4 with an example of a resultant image with respects to micronized particles in Figure 2-5.

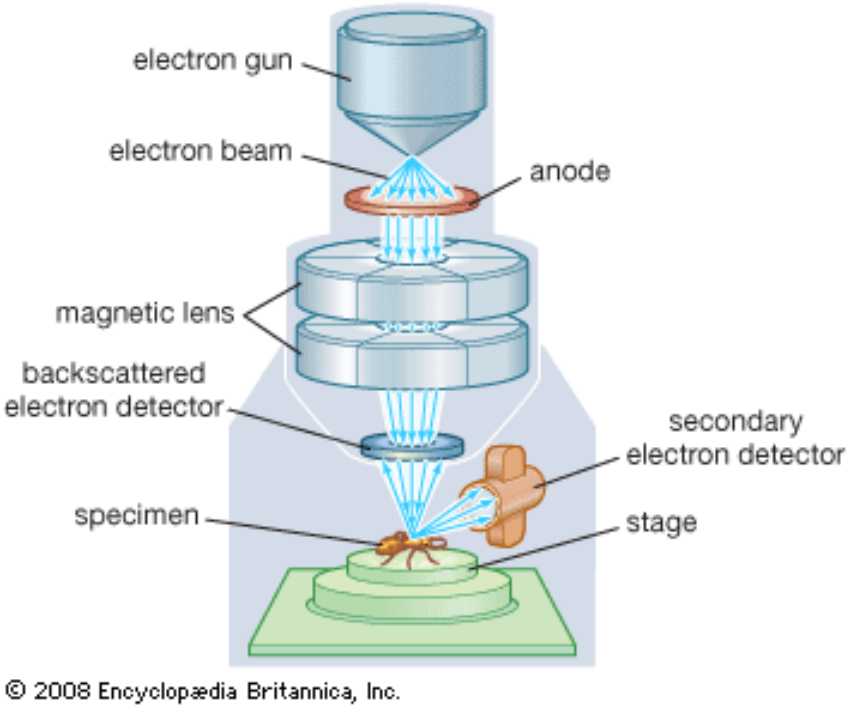

Figure 2-4: Schematic diagram of an SEM (Encyclopaedia and Britannica, 2008).

Due to the high vacuum and condition and the utilization of electrons to form an image, special preparations must be done to the sample. Non-conductive samples need to be made conductive by covering the sample with a thin layer of

conductive material (usually gold) so as to avoid charging the sample by the electron beam and subsequent distortion of the image.

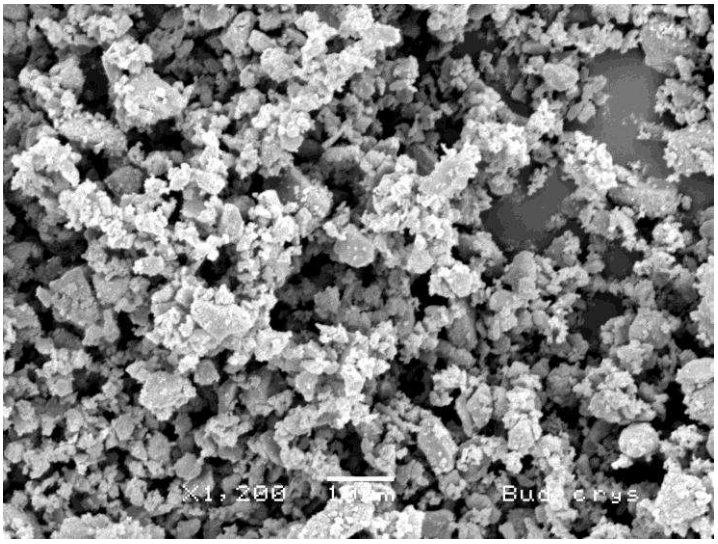

Figure 2-5: An example of an SEM image of micronized particles.

2.3.2 X-Ray Powder Diffraction (X-RPD)

X-ray powder diffraction (X-RPD) is a rapid analytical technique primarily used for phase identification of a crystalline material and can provide information about unit cell dimensions of a compound. X-ray diffraction is now a common technique for the study of crystal structures and atomic spacing. A schematic diagram of an X-Ray diffractometer is shown is Figure 2-6.

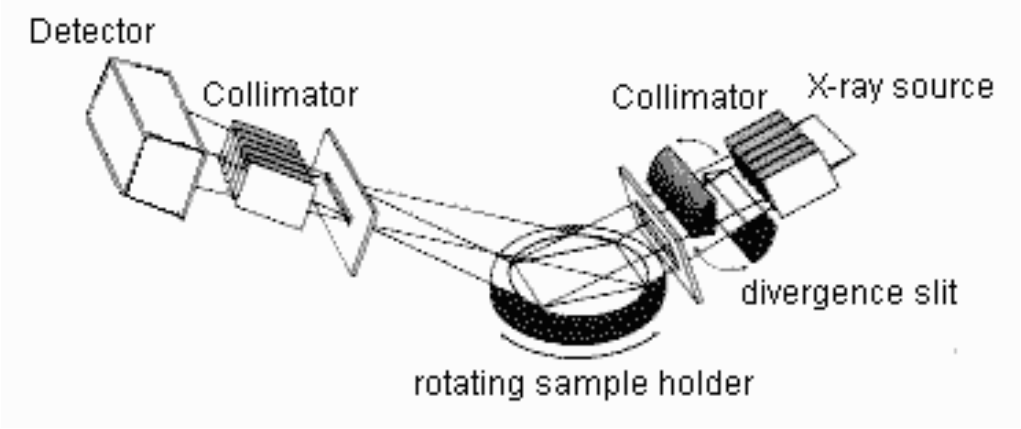

Figure 2-6: Schematic of an X-ray powder diffractometer (Chalupa, 2009).

X-ray diffraction is based on constructive interference of monochromatic X-rays and a crystalline sample. When a monochromatic X-ray is projected onto a crystalline material, diffraction occurs when the distance travelled by the rays reflected from successive planes differs by complete number n of wavelengths. By scanning the sample through a range of 2θ angles, all possible diffraction directions of the lattice should be attained due to the random orientation of the powdered material and the Bragg's Law conditions are satisfied ($n\lambda=2d \sin \theta$) (Warren, 1990). This law relates the wavelength of electromagnetic radiation (λ) to the diffraction angle (θ) and the lattice spacing (d) in a crystalline sample. Conversion of the diffraction peaks to d-spacing allows identification of the compound because each compound has a set of unique d-spacing. Typically, this is achieved by comparison of d-spacing with standard reference patterns (Warren, 1990). Where a mixture of different phases is present, the resultant diffractogram is formed by addition of the individual patterns. An example showing the X-RPD data for two polymorphs of paracetamol is shown in Figure 2-7.

During the course of this work, X-RPD will be used to characterise the crystalline nature of powder samples intended for analysis as well as solving the crystal structure of some of them.

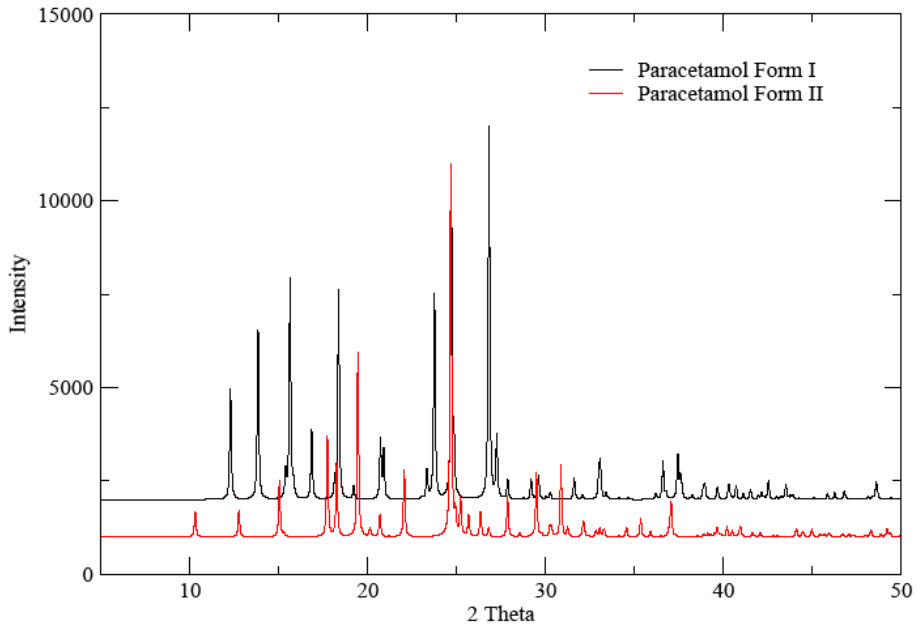

Figure 2-7: X-RPD pattern of paracetamol showing two different forms (Nichols and Frampton, 1998, Stone et al., 2009).

2.3.3 X-Ray Photoelectron Spectroscopy (XPS)

X-ray photoelectron spectroscopy (XPS) is a an extremely surface sensitive spectroscopic technique that provides quantitative information about the elemental composition (with exception of hydrogen and helium), empirical formula, chemical state and electronic state of the elements that exist on or near the surface of a material (Nefedov, 1988).

XPS provides quantitative compositional information from the top 10 atomic layers of a sample surface for the elements. The samples are irradiated with a monochromatic X-ray beam. XPS is based upon the photoelectric effect. The energy of the X-ray photon excites the surface and induces the escape and emition of the core electron from the atoms at the surface of the sample

(O'connor et al., 1992). The emitted electron have a specific kinetic energy related to its origin and is referred to as a photoelectron. The distribution of kinetic energies of the photoelectrons can be used to identify and quantify the amounts of elements and bonding environments on a sample due to the slight difference in binding energies (O'connor et al., 1992). A schematic representation of an XPS instrument is represented in Figure 2-8.

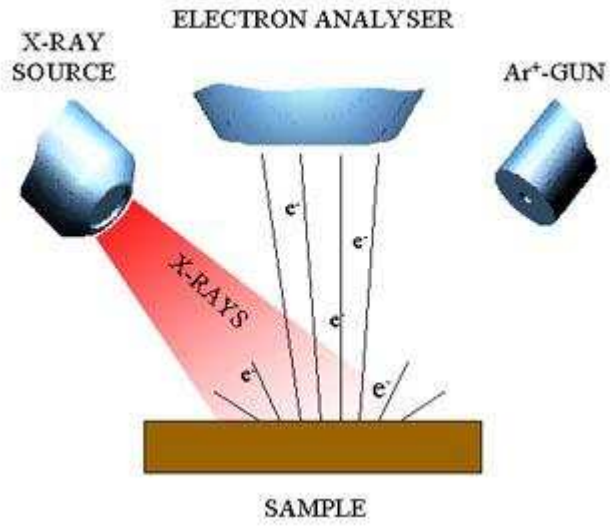

Figure 2-8: Schematic representation of an XPS instrument (SCK•CEN, 2004).

2.3.4 Differential Scanning Calorimetry (DSC)

The main application of DSC is in studying phase transitions, such as melting, glass transitions, or crystallization. These transitions involve heat capacity changes that can be detected by DSC with great sensitivity (Menczel et al., 2009). DSC is utilized to measure the temperature differences between the investigated sample and a reference samples as a function of temperature (Höhne et al., 2003). Both the sample and reference are maintained at nearly the same temperature throughout the experiment using constant heat flow rates. The

reference sample should have a well-defined heat capacity over the range of temperatures to be scanned.

The basic principle underlying this technique is the detection of changes in heat flow between the sample and the reference as the sample undergoes a physical transformation showing as endothermic or exothermic peaks (Sepe, 1997). By observing the difference in heat flow between the sample and reference, differential scanning calorimeters are able to measure the amount of heat absorbed or released during such transitions (Menczel et al., 2009). Calibration may be carried out using standards of known melting points such as sapphire or indium that are available as heat capacity standard. DSC curves can be used to calculate enthalpies of transitions. This is done by integrating the area under the curve corresponding to a given transition. It can be shown that the enthalpy of transition can be expressed using the following equation 2-1:

$$\Delta H = KA \qquad \textbf{Equation 2-1}$$

where ΔH is the enthalpy of transition, K is the calorimetric constant, and A is the area under the curve. The calometric constant will vary from instrument to instrument, and can be determined by analyzing a well-characterised sample with known enthalpies of transition (Menczel et al., 2009).

During the course of this work heat-flux DSC was used, a schematic representation of the DSC instrument is shown in Figure 2-9.

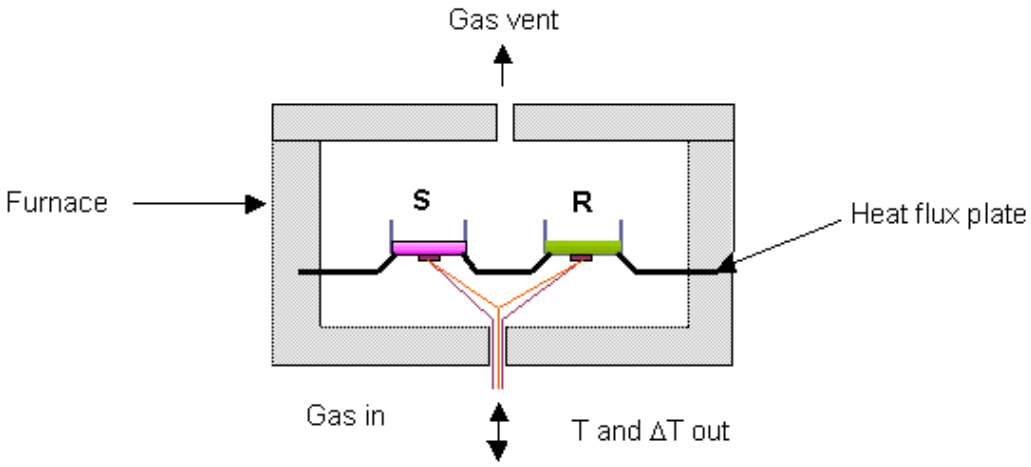

Figure 2-9: A schematic representation of a DSC instrument (R is the reference and S is the sample).

Temperature Modulate DSC (TMDSC) was also used during this work as complementary technique to conventional DSC. TMDSC is a modification of DSC which allows the differentiation of overlapping transitions. In TMDSC, a sinusoidal modulation is applied on top of the linear heating rate in order to measure the heat flow that responds to changing heating rates. This results in an improved resolution and sensitivity. Depending on the underlying heating rate, the period and amplitude of modulation, Fourier Transformation analysis is then used to separate the resulting raw experimental heat flow into the heat capacity related (reversible) and kinetic (non-reversible) heat flows.

2.3.5 Thermogravimetric Analysis (TGA)

Thermogravimetric analysis (TGA) is a thermal analysis techniques used to characterise a wide variety of materials. It provides complimentary characterisation information to the most commonly used thermal technique,

DSC. TGA measures the amount and rate of change in the mass of a sample as a function of temperature or time in a controlled atmosphere (Sepe, 1997).

The basic principle underlying this technique involves a continuous monitoring of changes in weight as a constant heating rate is applied to the sample in a TGA pan following a tare procedure. Typical weight changes results are analyzed for the amount or percent of weight change whether weight gain or loss at any given temperature, the amount or percent of non-combusted residue at some final temperature, and the temperatures of various sample degradation processes (Bruce Prime et al., 2009).

2.3.6 Raman Spectroscopy

Raman spectroscopy has become an important analytical and research tool used for a wide range of applications. It is a spectroscopic technique that is used to provide useful information used for chemical identification, characterization of molecular structures, effects of bonding, environment and stress on a sample.

Raman spectroscopy is based on inelastic scattering of a monochromatic light from a laser source. When light is scattered from a molecule most photons are elastically scattered due to the excited photons returning to the same vibrational state and thus, having the same energy and wavelength as the incident photons (Rayleigh effect). However, a small fraction of radiation is scattered inelastically at some different wavelengths (Stokes and Anti-Stokes Raman scattering) (Fig. 2-10) (Schrader and Bougeard, 1995). 1 in 10^7 photons is scattered at optical

frequencies different from, and usually lower than, the frequency of the incident photons. If a molecule is promoted from a ground to a virtual vibrational state and then returns back to a higher energy vibrational state then the resulting frequency is reduce and therefore have a longer wavelength. This is referred to as Stokes scattering. However, if the molecule at the time of interaction is already in a vibrational state then the scattered releases more energy and hence has a shorter wavelength as returning to the ground vibrational state. This phenomenon is referred to as anti-Stokes scattering (Schrader and Bougeard, 1995).

The Stokes and anti-Stokes scattered light will be shifted to an equal distance on opposite sides of the Rayleigh scattered light and is determined by the spacing between the vibrational states and the ground state. This shift provides information about vibrational, rotational and other low frequency transitions in molecules.

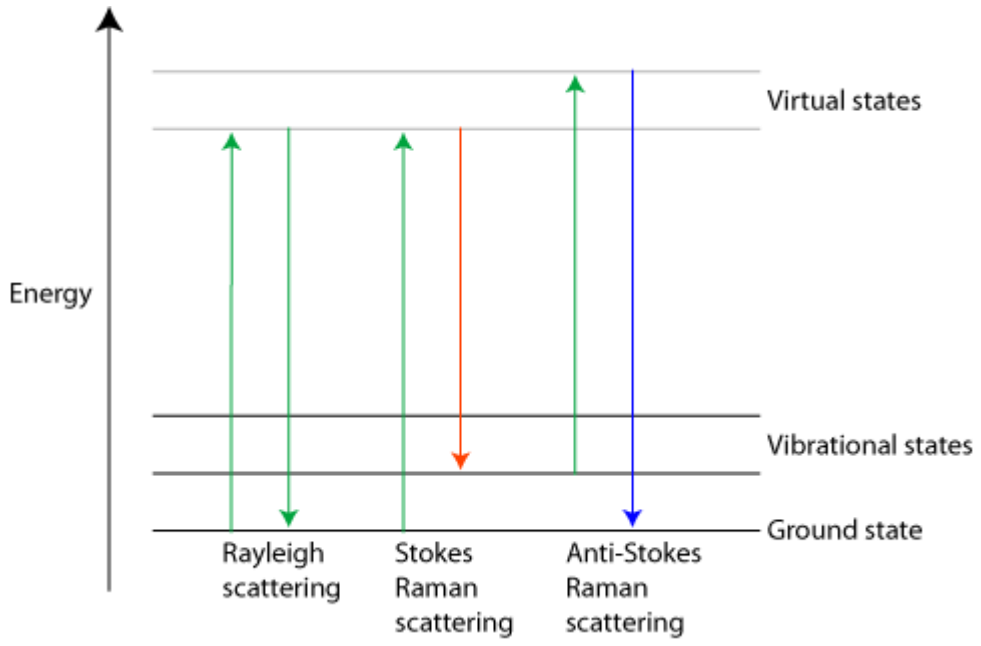

Figure 2-10: Energy level diagram for Rayleigh scattering and Raman scattering: Stokes Raman scattering and anti-Stokes Raman scattering.

Dispersive Raman has been used throughout this project. Dispersive Raman has become the largest and most widely used of the Raman systems, with an instrument typically consisting of a monochromator (spectrometer or spectrograph), a CCD detector, and various laser sources- ranging from UV to NIR. A microscope is often used to enable micron scale analysis (Fig. 2-11).

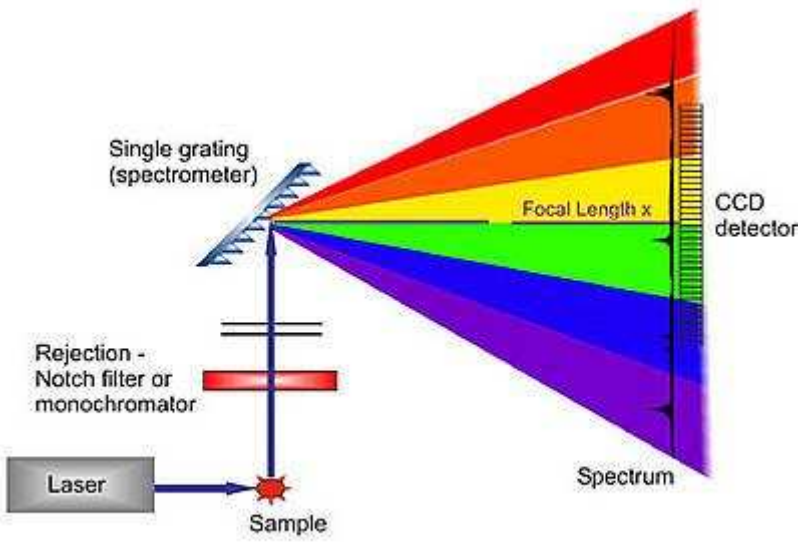

Figure 2-11: A schematic representation of a simplified Raman spectrometer (Sayfa, 2008).

Variable temperature Raman spectroscopy (VT-Raman spectroscopy) was also used during this work in order to study any potential polymorphic changes occurring to the different clathrates and APIs.

2.3.7 Atomic Force Microscopy (AFM)

2.3.7.1 Sample Preparation

API samples were placed onto an AFM stub. The API chosen was sprinkled across the top adhesive layer of a silicon wafer that was covered with a thin

sheen of epoxy resin (Loctite, Henkel Ltd, Hatfield, UK). Any excess API was removed by exposing the sample to a gentle stream of nitrogen for 30 seconds. When preparing samples of pMDI components, each sample was adhered directly onto an AFM stub using epoxy resin, and being allowed to dry at least 24 hours before use (Fig. 2-12).

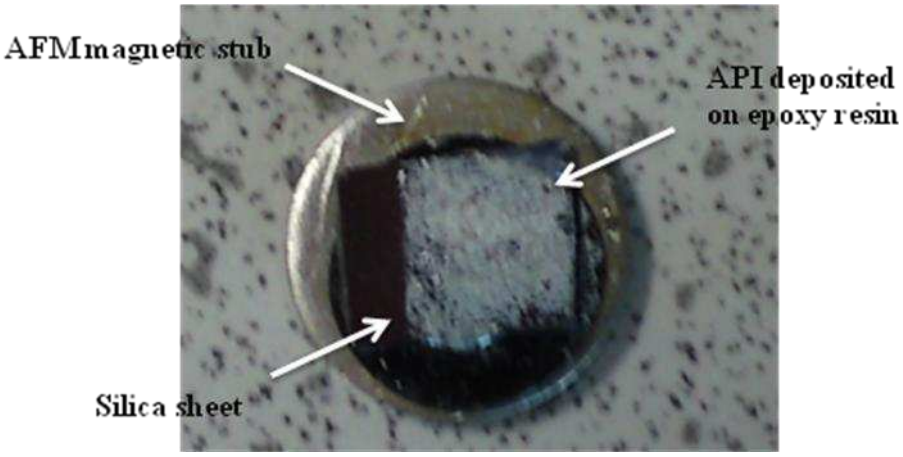

Figure 2-12: An example of an AFM stub sample preparation.

2.3.7.2 Topographical Imaging

Each of the pMDI components and the API samples were examined using AFM topographical imaging using an EnviroScope AFM (Veeco, Santa Barbara, CA, USA). Tapping mode was used for the acquisition of the images with NPS cantilevers (Veeco, Santa Barbara, CA, USA). A scan rate of 1.0 Hz was used over a 5 μm x 5 μm scan size for the pMDI and the API samples. A slow scan rate was employed in order to reduce the chances of any lateral movement of the sample. Topographical imaging also allowed for the determination of roughness parameters (the root mean square (RMS) roughness) of each sample. RMS was

achieved using the topographical software incorporated within the AFM system following equation 2-2:

$$R_{rms} = \sqrt{\frac{1}{n}\sum_{i=1}^{n} y_i^2} \qquad \textbf{Equation 2-2}$$

where n is the number of points in the topography profile, i is the asperities and y_i is the distance between the asperities. A typical 3D-processed AFM image is shown in Figure 2-13.

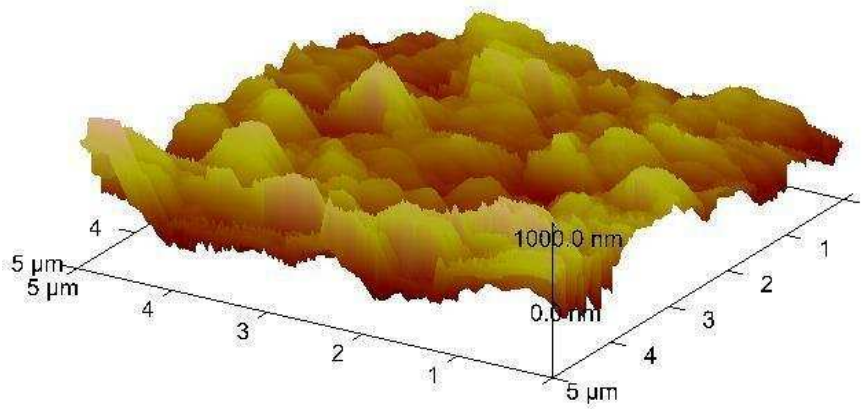

Figure 2-13: An example of a 3D-processed AFM Image of a 5 x 5 micron surface

2.3.7.3 Colloid Probe Preparation

The force measuring principle of colloid probe AFM is identical to that of a standard AFM (Kappl and Butt, 2002) but particles of each API material were attached to AFM cantilevers and challenged against each pMDI component surface (Davies et al., 2005) (Figure 2-14). Sharpened Silicon Nitride Probe .

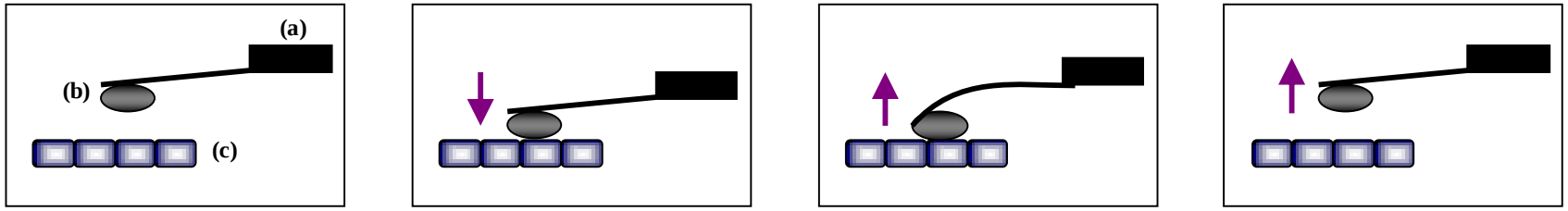

(a) AFM Cantilever

(b) Attached API particle

(c) Substrate, e.g. pMDI component surface of corresponding API particles

Colloid probe brought into contact with substrate

Colloid probe retracted from contact with substrate but adhesive force between tip and substrate maintains their contact

Colloid probe brought out of contact with substrate at the point where force of retraction equals the maximum adhesion force

Figure 2-14: The AFM colloid probe technique.

(DNP-S, V-shaped) cantilevers were used for this procedure. The spring constant of each lever, the resonant frequency (RF) and Q values of each tip were determined using the AFM before they were functionalized with an API particle and the spring constants calculated by Saders method (Sader et al., 1995). The spring constants for the V-shaped tips were between 0.3 and 0.5 Nm^{-1}. Each of the API particles was mounted onto the AFM cantilevers using the EnviroScope AFM. A black card was attached to a metal stub using a carbon stub where a thin line of glue was spread in the middle of the black card surface.

A sacrificial tip was used to draw thin perpendicular lines of the adhesive glue from bulk glue in order to enable the functionalization of the tip. This tip was then replaced with a silicon V-shaped cantilever of known spring constant for the functionalization, and the cantilever tip was then approached to the thinner line of the glue, to enable the coating of the tip with the glue. Immediately after coating the tip with the glue, the resin substrate was then removed and replaced with the appropriate powder sample. Using the optical view of the AFM system, small individual powder particles/crystals were identified and aligned with the position of the tip. The cantilever was then positioned over a single API particle and carefully lowered manually onto a single particle. Enough pressure was maintained to all the attachment of the API particle onto the tip. On retraction of the cantilever, the particle was adhered to the tip, and this 'colloid probe' was left to dry for a minimum of 24 hours before further use. Each API probe was produced in triplicate. Correct positioning of the particle on the cantilever was verified using SEM before and after AFM analysis. Samples were not gold coated, as this will render the tips unsuitable for force determination. The colloid

probes were mounted to carbon disks attached to aluminium stubs suitable for SEM use, then imaged using an acceleration voltage of 2.5 kV and a spot size of 45mm. Other parameters were adjusted in order to achieve better resolution images. An example of a SEM image of a colloid probe is shown in Figure 2-15.

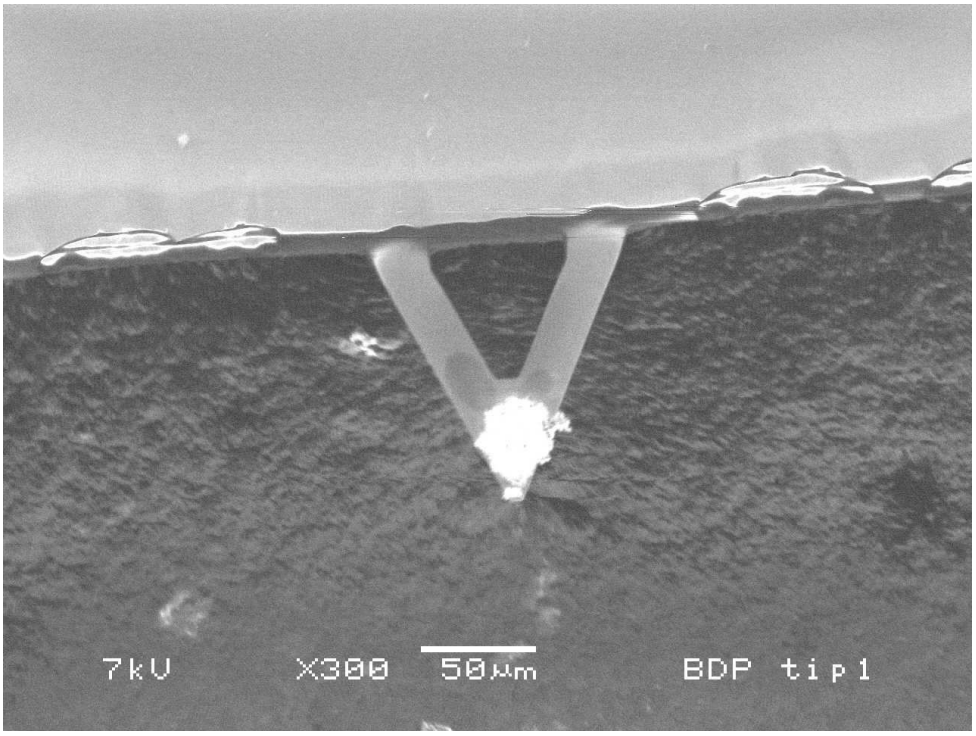

Figure 2-15: SEM image of a colloid probe (drug particle attached to an AFM cantilever) suitable for subsequent AFM analysis.

2.3.7.4 AFM Tip Characterization

Preceding any force measurement analysis, each of the colloid probes was imaged using an AFM tip-characterisation method. Tip characterisation was performed using an EnviroScope AFM (Veeco, Santa Barbara, CA, USA) and a tip characterization grid (TGT01; NT-MDT, Moscow, Russia), which is composed of a series of repeating sharp spikes, using a method detailed elsewhere (Hooton et al., 2004). To summarize the method for characterizing the tip, a topographical image of the particle surface is produced as the colloid probe

is scanned over the nanoscaled spike. The resulting topographical image is due to the spike being sharper than the asperities present on the surface and hence leading to an inverse imaging of the colloid particle rather than the surface of the grid (Williams et al., 1996). This approach allows the visualisation of any morphological changes occurring to the colloid probe particle following adhesion measurements. Furthermore, it allows the determination of the contact radius and contact area between the particle and a surface.

2.3.7.5 AFM Force Measurements

Each pMDI component stub or API stub was placed in a glass sample chamber to undertake AFM force measurements using an EnviroScope AFM (Veeco, Santa Barbara, CA, USA). Each colloid probe was inserted into a cantilever holder suitable for liquid AFM work. This latter was then placed onto the AFM and accurate laser alignment was established onto the tip of the colloid probe. The colloid probe was then lowered towards the surface until it was approximately 400 μm away from the surface. 20 ml of model propellant 2H, 3H decafluoropentane (referred to mHFA hereafter) (Apollo Scientific, Stockport, UK) were then added to the sample chamber that allowed the sample and the probe to be completely submerged in the propellant. A Laser re-alignment was performed, before approaching the surface and undertaking force measurements once contact had been made. One hundred force measurements were taken over a 5 μm x 5 μm area using each probe against each surface. The force measurements were conducted at 10°C and force data was calculated using custom software.

The force data is produced in the form of a force curve. If the cantilever and sample are kept in fixed lateral positions, the substrate (or cantilever) can be moved onto and off the cantilever (or substrate) by applying a voltage. When nearing contact the sample will very often attract the tip prior to a fixed level contact, causing a 'jump in' deflection (i.e. tip bends into contact with surface). The piezo input then continues the sample/cantilever movement until a pre-set value for the stage height (z-coordinate) is reached. The stage then reverses, and the sample and tip will separate. However this separation will occur only when the restoring force of the cantilever (spring constant) surpasses the interaction force of the tip and sample, and as such the negative deflection of the cantilever below the non-contact output can be used to quantify the interaction force described (Sindel and Zimmermann, 2001). By applying Hooke's law (Equation 2-3):

$$F_{adh} = -kz \qquad \textbf{Equation 2-3}$$

Where k is the spring constant of the cantilever and z is the cantilever deflection at the moment of separation, the interaction force F_{adh} can be calculated. This method of operation is called 'force' mode and Figure 2-16 shows a representation of the generation and interpretation of a single force curve and the relative deflection signals involved:

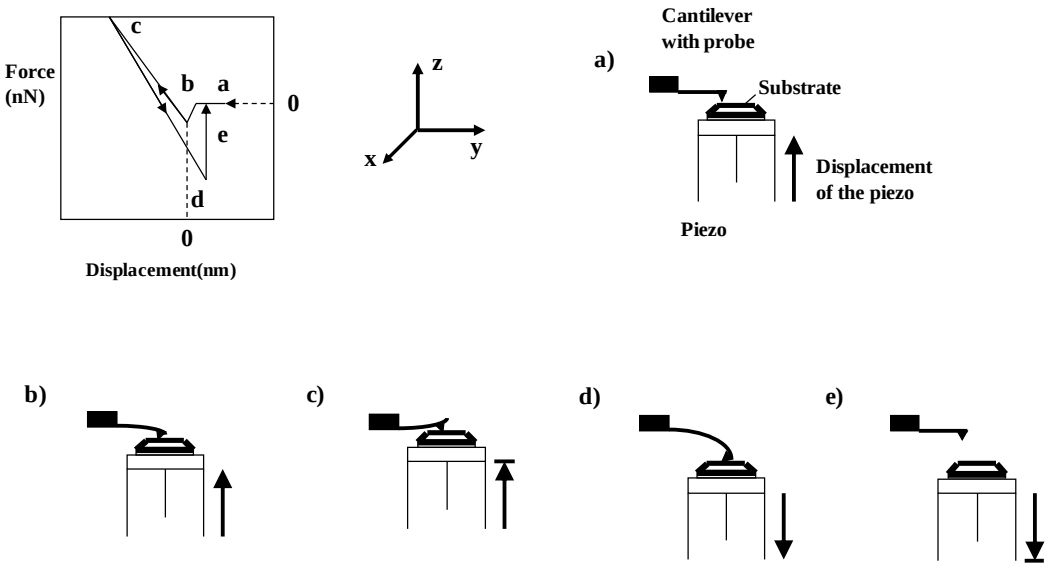

Figure 2-16: A typical AFM force curve cycle (Sindel and Zimmermann, 2001).

If a particle of interest (i.e. drug particle) is attached to the cantilever tip prior to force measurement, the force of interaction between that particle and the substrate can be measured (Ducker et al., 1991). While other techniques (centrifugation, tensiometry etc) may offer control over selected variables and bulk adhesion assessment (Salazar-Banda et al., 2007, Lohrmann et al., 2007), AFM offers the chance to manipulate several variables (temperature, humidity, force of contact etc.) without compromising other elements of the technique. Significantly this technique affords a method of experimentally determining the F_{adh} on a single particle level, and therefore a mean to explore the interfacial forces involved (Butt et al., 2005).

However, the use of real particles to probe surfaces has obvious problems associated with it. Most critically by using a 'real' particle, there is an almost complete loss of control of the morphology of the tip and hence the contact region with a substrate. Considering the importance of contact geometry upon

such fine scale interaction, as described above, this has rendered adhesion measurements made by this technique specific on a probe by probe basis. Hence, even adhesion measurements on the same substrate made with two different tips of the same material, may often exhibit huge differences in the forces calculated, and therefore it is very difficult to compare experimental data (Farshchi-Tabrizi et al., 2006). To ease any relative conclusions to be drawn between two sample materials, the same tip therefore needs to be employed for force measurement. This can be problematic in itself, as continued tip use can lead to wear of a particle and hence change in the contact area and potentially the form (Butt et al., 2005).

The calculated adhesion forces can be presented as a frequency distribution in order to illustrate the distribution of force measurements recorded during an experiment. If each set of force curves are normalised for contact radius, and are normally distributed, it follows that the data from different probes may be grouped together, allowing for the mean and the standard deviation to be calculated. Normally distributed force data is illustrated in Figure 2-17.

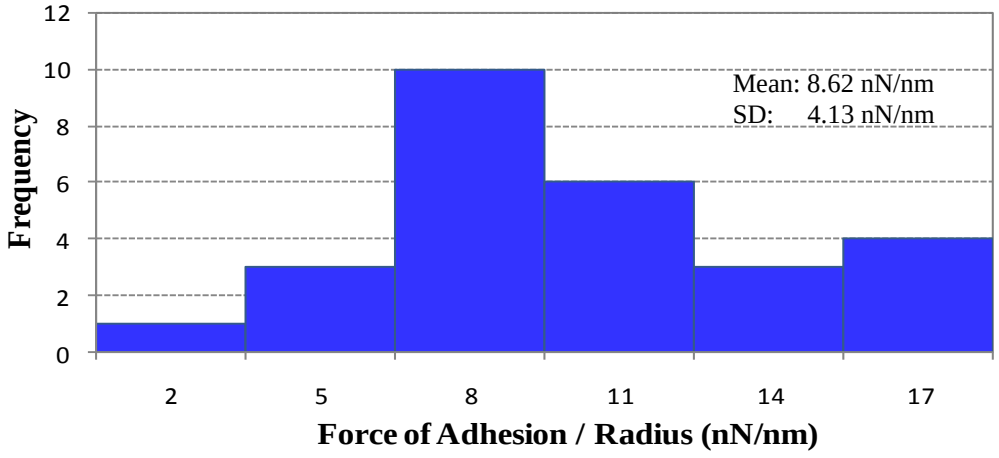

Figure 2-17: An example of a frequency distribution of normalised force of adhesion data.

2.3.8 Particle Size Determination

Particle size in inhaler formulation is critical as the size of the particles is very important for efficient drug delivery and successful therapy. This is because particles larger than a certain size tend to simply land in the mouth and throat and mostly do not enter into the lung. A similar problem arises if the particles are too small, as these will be exhaled or swallowed by the patient. Thus, IPAs are usually designed to produce drug particles of the specific size range suitable for lung delivery (ca. 1-5µm). Particles within a pMDI formulation can be subject to many different factors that would lead to changes in particle size within the formulation.

Light scattering (LS) is a phenomena that can be used to determine the size distribution profiles of particles in suspensions. It is one of the most popular methods used to determine the size of particles. In one approach, monochromatic light beam is scattered from "spherical" particles in Brownian motion causes a Doppler Shift and change in wavelength of the scattered light (Berne and Pecora, 2000). This change is related to the size of the particle. It is possible to compute the sphere size distribution and give a description of the particle's motion in the medium, measuring the diffusion coefficient of the particle and using the autocorrelation function.

In another approach (and as used here) particles passing through a laser beam will scatter light at an angle that is directly related to their size (Aubin et al., 2010). As particle size decreases, the observed scattering angle increases logarithmically. Scattering intensity is also dependent on particle size,

diminishing with particle volume. Large particles therefore scatter light at narrow angles with high intensity, whereas small particles scatter at wider angles but with low intensity (Berne and Pecora, 2000). It is this behaviour that instruments based on laser diffraction exploit in order to determine particle size. The dynamic range of the measurement is directly related to the angular range of the scattering measurement, with modern instruments making measurements from around 0.02 degrees through to beyond 140 degrees. The wavelength of light used for the measurements is also important, with smaller wavelengths (e.g. blue light sources) providing improved sensitivity to sub-micron particles (Agrawal et al., 1991).

Particle size distributions are calculated by comparing a sample's scattering pattern with an appropriate optical model. Traditionally two different models are used: the Fraunhofer Approximation and the Mie Theory. The Fraunhofer approximation assumes that the particles being measured are opaque and scatter light at narrow angles. As a result, it is only applicable to large particles and will give an incorrect assessment of the fine particle fraction (Xu, 2000, Malvern, 2010). Mie Theory predicts scattering intensities for particles, and provides a more rigorous solution for the calculation of particle size distributions from light scattering data. It is based on Maxwell's electromagnetic field equation. Mie theories assumes that the particle are spherical and are present in a dilute suspension (Aubin et al., 2010). Mie Theory allows for primary scattering from the surface of the particle, with the intensity predicted by the refractive index difference between the particle and the dispersion medium (Malvern, 2010). The

Mie theory is more appropriate for analysis of the diffraction patter of particles that less than 10 µm.

A Coulter LS 230 (Beckman, Coulter Corporation, USA) using Fraunhofer mode was used during this project. The Coulter LS 230 uses a laser of 750 nm and a double Fourier lens setup for focussing the scattered light on the ring-shaped detector setup (Fig. 2-18). The detection range (angles) for diffraction is 40 nm - 2000 µm, thus theoretically covering the size range expected here. The LS uses reverse Fourier lens optics incorporated in a patented binocular lens system. This enables the LS to optimize light scattering across the widest dynamic range in a single scan (Coulter, 2010). The detector segments are arranged in three main areas: a low-angle detector (L) with 62 detector elements, mid- (M) and high-angle (H) detector comprised of 32 elements each, allowing high-resolution of a wide particle size range (Pye and Blott, 2004). The amount of sample required is determined by the obstruction percentage of the laser beam through the sample

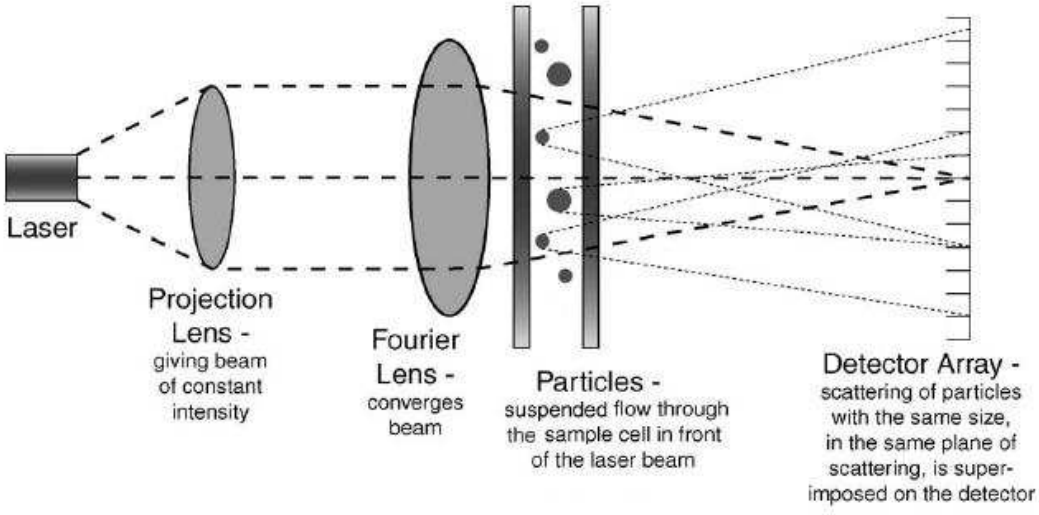

Figure 2-18: Schematic diagram of the LS 230 Coulter (adapted from (Pye and Blott, 2004)).

cell, with the recommended range between 8 and 12 %, which equates 5mg of API suspended in 10ml of the propellant. The suspension was sonicated for 5 minutes to allow disaggregation of the particles. 100 µl of the API suspension samples were diluted into 20 ml mHFA in the sample cell. Higher concentrations of API suspensions were used to achieve similar scattering intensities (about 4 ml into 20 ml).

2.3.9 Size Reduction

Size reduction is used widely throughout the pharmaceutical industry for the reduction of API particle size and size range. Size reduction is used to increase surface area and improve formulation properties and is used in inhaler formulation for the production of a particle size that is suitable for inhalation It is also used to maintain a consistent particle size distribution (PSD) for a formulation, thus allowing for a better quality mixture especially for powder when used in tablets and capsules. The primary benefit of size reduction in inhaler formulation is the increase in solubility/bioavailability due to the increase in surface area.

Size reduction on the different APIs used during this project was carried out by ball milling using a Restsch® MM 400 ball-miller (Restsch, Germany). The milling intensity was the maximum with a frequency of 30 Hz and was carried out for 2 hours on 500 mg of the each of the samples.

2.4 References

AGRAWAL, Y. C., MCCAVE, I. N. & RILEY, J. B. (1991) Laser Diffraction Size Analysis. IN SYVITSKI, J. P. M. (Ed.) Principles, Methods and Applications of Particle Size Analysis. Cambridge University Press.

ASHAYER, R., LUCKHAM, P. F., MANIMAARAN, S. & ROGUEDA, P. (2004) Investigation of the molecular interactions in a pMDI formulation by atomic force microscopy. European Journal of Pharmaceutical Sciences, 21**,** 533-43.

AUBIN, J., FERRANDO, M. & JIRICNY, V. (2010) Current methods for characterising mixing and flow in microchannels Chemical Engineering Science, 65**,** 2065-2093.

BERNE, B. J. & PECORA, R. (2000) Dynamic Light Scattering with Applications to Chemistry , Biology and Physics, Dover Publications, Inc.

BRITISH PHARMACOPOEIA, C. (2010) British Pharmacopoeia. British Pharmacopoeia 2010.

BRUCE PRIME, R., BAIR, H. E., VYAZOVSKIN, S., GALLAGHER, P. K. & RIGA, A. (2009) Thermogravimetric Analysis (TGA). IN MENCZEL, J. D. & BRUCE PRIME, R. (Eds.) Thermal Analysis of Polymers: Fundamentals and Applications.

BUTT, H.-J., CAPPELLA, B. & KAPPL, M. (2005) Force Measurements with the atomic force microscope: Technique, interpretation and applications. Surface Science Reports, 59**,** 1-152.

BUTT, H. J., GRAF, K. & KAPPL, M. (2004) Physics and Chemistry of Interfaces, Wiley-VCH Germany.

CHALUPA, G. (2009) X-ray powder diffraction analysis.

CHAN, S. & BURT, P. C. W. (2009) Canisters for Use in Metered Dose Inhalers. UK, Glaxo Group Limited

COULTER, B. (2010) LS 230 Multi-Wavelengthwith Dry Powder Module (DPM).

DAVIES, M., BRINDLEY, A., CHEN, X., MARLOW, M., DOUGHTY, S. W., SHRUBB, I. & ROBERTS, C. J. (2005) Characterization of drug particle surface energetics and young's modulus by atomic force microscopy and inverse gas chromatography. Pharmaceutical Research, 22**,** 1158-66.

DUCKER, W. A., SENDEN, T. J. & PASHLEY, R. M. (1991) Direct measurement of colloidal forces using an atomic force microscope. Nature, 353**,** 239-241.

EGERTON, R. F. (2005) The Scanning Electron microscope. Physical Principles of Electron Microscopy: An introduction to TEM, SEM, and AEM. Springer.

ENCYCLOPAEDIA & BRITANNICA (2008) Scanning Electron Microscope (SEM) (instrument). Encyclopaedia Britannica.

FARSHCHI-TABRIZI, M., KAPPL, M., CHENG, Y., GUTMANN, J. & BUTT, H.-J. (2006) On the Adhesion between Fine Particles and Nanocontacts: An Atomic Force Microscope Study. Langmuir**,** 2171-2184.

FERRARO, J. R., NAKAMOTO, K. & BROWN, C. W. (2003) Introduction to Raman spectroscopy, Elsevier Science (USA).

HÖHNE, G. W. H., HEMMINGER, W. F. & FLAMMERSHEIM, H., -J (2003) Differential Scanning Calorimetry, Springer-Verlag Berlin Heidelberg.

HOOTON, J. C., GERMAN, C. S., ALLEN, S., DAVIES, M. C., ROBERTS, C. J., TENDLER, S. J. & WILLIAMS, P. M. (2004) An atomic force microscopy

study of the effect of nanoscale contact geometry and surface chemistry on the adhesion of pharmaceutical particles. Pharmaceutical Research, 21**,** 953-61.

JINKS, P. A. (1989) Physically modified beclomethasone dipropionate suitable for use in aerosols. UK, Riker Laboratories.

KAPPL, M. & BUTT, H.-J. (2002) The Colloidal Probe Technique and its Application to Adhesion Force Measurements. Particle and Particle Systems Characterization, 19**,** 129-143.

LOHRMANN, M., KAPPL, M., BUTT, H. J., URBANETZ, N. A. & LIPPOLD, B. C. (2007) Adhesion forces in interactive mixtures for dry powder inhalers--evaluation of a new measuring method. European Journal of Pharmaceutics and Biopharmaceutics, 67**,** 579-86.

MALVERN (2010) Using Mie Theory and the Fraunhofer Approximation.

MCDONALD, K. J. & MARTIN, G. P. (2000) Transition to CFC-free metered dose inhalers - into the new millennium. International Journal of Pharmaceutics, 201**,** 89-107.

MENCZEL, J. D., JUDOVITS, L., BRUCE PRIME, R., BAIR, H. E., READING, M. & SWIER, S. (2009) Differential Scanning Calorimetry. IN MENCZEL, J. D. & BRUCE PRIME, R. (Eds.) Thermal Analysis of Polymers: Fundamentals and Applications. John Wiley and Sons Inc.

NEFEDOV, V. I. (1988) X-ray Photoelectron Spectroscopy of Solid Surfaces, VSP BV

NICHOLS, G. & FRAMPTON, C. S. (1998) Physicochemical Characterization of the Orthorhombic Polymorph of Paracetamol Crystallized from Solution. Journal of Pharmaceutical Sciences, 87**,** 684-693.

O'CONNOR, D. J., SEXTON, B. A. & SMART, R. C. (1992) Surface analysis method in materials science, Springer-Verlag, Heidelberg.

PYE, K. & BLOTT, S. J. (2004) Particle size analysis of sediments, soils and related particulate materials for forensic purposes using laser granulometry. Forensic Science International, 144**,** 19-27.

ROGUEDA, P. G. (2003) HPFP, a model propellant for pMDIs. Drug Development and Industrial Pharmacy, 29**,** 39-49.

SADER, J. E., LARSON, I., MULVANEY, P. & WHITE, L. R. (1995) Method for the calibration of atomic force microscope cantilevers. Review of Scientific Instruments, 66**,** 3789-3798.

SALAZAR-BANDA, G. R., FELICETTI, M. A., GONCALVES, J. A. S., COURY, J. R. & AGUIAR, M. L. (2007) Determination of the adhesion force between particles and a flat surface, using the centrifuge technique. Powder Technology, 173**,** 107-117.

SAYFA, S. (2008) Raman Spektroskopisi

SCHRADER, B. & BOUGEARD, D. (1995) Infrared and Raman Spectroscopy: Methods and Principals, VCH Publishers Inc.: New York.

SCK•CEN (2004) X-ray Photoelectron Spectroscopy at SCK•CEN.

SELVAM, P., PEGUIN, R. P., CHOKSHI, U. & DA ROCHA, S. R. (2006) Surfactant design for the 1,1,1,2-tetrafluoroethane-water interface: ab initio calculations and in situ high-pressure tensiometry. Langmuir, 22**,** 8675-83.

SEPE, M. P. (1997) Thermal Analysis of Polymers, Rapra Thechnology Ltd.

SINDEL, U. & ZIMMERMANN, I. (2001) Measurement of interaction forces between individual powder particles using an atomic force microscope. Powder Technology, 117**,** 247-254.

STEIN, S. W. & STEFELY, J. S. (2003) Reinventing metered dose inhalers; From poorly efficient CFC MDIs to highly efficient HFA MDIs. Drug Delivery Technology, 3**,** 45-51.

STONE, K. H., LAPIDUS, S. H. & STEPHENS, P. W. (2009) Implementation and use of robust refinement in powder diffraction in the presence of impurities. Journal of Applied Crystallography, 42**,** 385-391.

VERVAET, C. & BYRON, P. R. (1999) Drug-surfactant-propellant interactions in HFA-formulations. International Journal of Pharmaceutics, 186**,** 13-30.

WARREN, B. E. (1990) X-Ray Diffraction, Dover Publications, Inc.

WILLIAMS, P. M., SHAKESHEFF, K. M., DAVIES, M. C., JACKSON, D. E. & ROBERTS, C. J. (1996) Blind reconstruction of scanning probe image data. Journal of Vacuum Science and Technology, B 14**,** 1557-1562.

XU, R. (2000) Particle Characterization: Light Scattering Methods, Kluwer Academic Publishers.

Chapter 3 Physico-chemical characterization of a model propellant clathrate formed in a pressurized metered dose inhaler

3.1 General Introduction

The replacement of chlorofluorocarbon (CFC) with hydrofluoroalkane (HFA) propellants has challenged formulators of pressurized metered dose inhalers (pMDIs) in several major aspects. Due to the increased polarity of HFA, the use of alternative (soluble) surfactants or co-solvents along with traditional surfactants is required in order to stabilize pressurized suspension products. The surfactant type and composition, as well as drug concentration and particle size may have an effect on the solubility of an active pharmaceutical ingredient (API) and, also on any related crystal growth and consequently the efficacy of the formulation.

Drug particles used in the presence of CFC or HFA can have the tendency to form "clathrates" or molecular association of variable stoichiometry (Phillips and Byron, 1994). Clathrates are solid solutions consisting of polyhedral cavities (Koh, 2002) that arise from the API molecules being linked through hydrogen (Englezos, 1993). Host molecules are linked through hydrogen bonding to form a regular 3D structure in a connected network (Plumridge and Waigh, 2002) and create cavities (host lattice) that can enclose a large variety of other molecules (guests) (Englezos, 1993). Guest molecules occupy fully (hydrogen bonded to the host network) or partially (occupying void spaces) the cages in the host framework (Patchkovskii and Tse, 2003). Thermodynamic stability of clathrate

depends strongly on the size and shape of the guest molecules (Buffett, 2000) which must be small enough to fit into the cavities of the lattice but large enough to lend stability to the structure (Buffett, 2000). The area of crystal engineering provides insight into the physical and chemical properties of the new solid states formed by understanding the intermolecular interactions in the context of crystal packing (Desiraju, 2007). Different areas can be followed to determine the physicochemical characteristics of the clathrates that include: 1) the study of intermolecular interaction, 2) the study of packing modes and 3) the study of crystal properties (Englezos, 1993).

Beclomethasone dipropionate (BDP) is a widely used corticosteroid for the treatment of asthma. BDP is formulated in pMDIs in the presence of a propellant and other formulation ingredients (Millard and Myrdal, 2002). Since the solid state chemistry can significantly alter the therapeutic effect of the formulation, it is crucial to determine the most stable crystal form in the presence of the propellant. BDP crystallizes with a channel structure forming a clathrate with the propellant that allows the insertion of CFC-11/HFA-134a molecules. The structure is held together through hydrogen bonding (Harris et al., 2003). When BDP is suspended in a pMDI formulation containing CFC-11, rapid crystal growth occurs. This has been attributed to the association of BDP and CFC-11 to the formation of a clathrate. The formation of these crystals in the pMDI can be problematic especially if they are large, as upon inhalation, the particles will impact on the orapharynx rather than the bronchioles or pulmonary regions of the lung where they are required to exert their therapeutic effects. Furthermore, large particles may also disrupt the operation of the valve.

While the crystal structure of the BDP CFC-11 clathrate has been investigated with respect to resolving the structure (Vervaet and Byron, 1999a), to the author knowledge, there is little information on the physico-chemical characteristics of the BDP CFC-11 clathrate and its stability.

3.1.1 Chapter Aims and Objectives

This chapter will investigate and characterise the physico-chemical properties of beclomethasone dipropionate (BDP) crystallized from trichloromonofluoromethane (CFC-11). X-ray photoelectron spectroscopy (XPS) and X-ray powder diffraction (X-RPD) will be used to determine the surface chemistry and the purity of the samples. Additionally, thermal analysis will be used to determine the phase behaviour of the clathrate upon heating. Following the surface characterisation of the BDP CFC-11 clathrate, the effect of different BDP, CFC-11 concentration will be used in order to determine its influence on clathrate formation. Finally, Raman spectroscopy was used to determine the chemistry changes of the clathrate upon heating the clathrate to its melting point. From these results it may be possible to characterise the BDP CFC-11 clathrate and determine the effect of any changes on the chemistry of the latter on the potential interactions within a pMDI.

3.2 Materials and Methods

3.2.1 Materials

Anhydrous BDP (micronized) was purchased from Sicor (Italy) and CFC-11 was supplied by Arkerma (UK). All other chemicals were purchased from Sigma-Aldrich Company Ltd (UK), unless otherwise indicated. 3M Drug Delivery Systems (UK) supplied a micronized isopropyl alcohol (IPA) clathrate of BDP for investigation (EP 205530).

3.2.2 Methods

3.2.2.1 Isolation of BDP CFC-11 clathrate

Anhydrous BDP was suspended in CFC-11 in a pressure resistant vial. The concentrations of the API were, 0.1, 0.5, 1.67, 2, 2.5 and 3% w/w BDP in CFC-11. All formulations were shaken using a Stuart SF1 flask shaker (Barloworld Scientific Ltd, UK) for 2 hours at 800 oscillations per minute and stored at 5˚C for 24 hours. The material was isolated by vacuum filtration, using a glass filter, washed three times using the filtrate suspension, in order to filter as much as possible of the suspension. Excess propellant was then removed by evaporation for 24 hours under room temperature and pressure (Phillips and Byron, 1994). The extracted crystals were stored in glass vial under nitrogen after being sealed with a vial screw and Parafilm (Alcan, Neenah, WI, US), and stored in a fridge at 5°C prior to use.

3.2.2.2 Scanning Electron Microscopy (SEM)

The particle size and morphology of the synthesized clathrates were analysed by SEM using a JEOL JSM-6060LV (JEOL (UK) Ltd, Welwyn Garden City, UK) at various magnifications. The samples prepared, were mounted onto carbon stubs and then sputter coated with a thin layer of gold (20 nm thickness) in an argon atmosphere (50Pa) at 30 mA for 4 minutes for SEM analysis. SEM analysis was carried out at an appropriate accelerating voltage (between 1 keV and 10 keV) and a spot size between 48nm and 62 nm. These parameters were varied for each sample in order to optimise each particular image. For BDP CFC-11 clathrates, SEM images were taken before and after clathrate formation to determine whether any morphological changes occurring during the process.

3.2.2.3 X-ray Photoelectron Spectroscopy (XPS)

BDP and BDP CFC-11 clathrate samples were analysed using XPS in order to determine surface elemental composition using a Kratos AXIS ULTRA spectrometer (Kratos Analytical, Manchester, UK) with a mono-chromatic Al Kα X-ray source (1486.6eV) operated at 15mA emission current and 10kV anode potential. The ULTRA was used in fixed analysed transmission (FAT) mode, with pass energy of energy 20eV for high resolution scans. A wide survey scan and high resolution scans were performed on each sample. Wide scans were run for 5-10 minutes and high resolution scans for 10-30 minutes. Data analysis was carried out using CASAXPS software with Kratos sensitivity factors to determine the atomic percentage (atomic %) values from the peak areas. The irradiating X-rays were emitted at a take-off angle of 90 degrees.

3.2.2.4 X-ray Powder Diffraction (X-RPD)

X-RPD patterns were collected on a Bruker D8 diffractometer system (Bruker AXS, Madison, WI, USA), operating in a Debye-Scherrer geometry. A ceramic X-ray tube with a copper target, wavelength λ= 1.54059 Å, operated at 40 kV, 40 mA. A scintillation counter was employed. The scan rate was 2° / min and the chart speed was 1cm / min. The X-ray patterns were analysed using the Le Bail method (Le-Bail et al., 1988) to model the patterns obtained, based on the reported unit cell for the clathrate. All the patterns were collected straight after the formation of the crystals to determine the purity of the samples and its crystalline structure. Theoretical diffraction patterns were calculated using Mercury 1.4.2 software (The Cambridge Crystallographic Data Centre, Cambridge, UK)

3.2.2.5 Thermogravimetric analysis (TGA)

A SDT Q600 TGA/DSC was used to record the weight loss of the samples between 25˚C and 300˚C. Dry nitrogen gas was used as a purge and the scan speed was 10˚C/min. An isothermal period at 25˚C was run for 10 minutes prior to the measurements and any changes in weight during that period were monitored. In all measurements 6 to 7mg of sample was used in an open aluminium pan. The thermograms obtained from the TGA results were analysed using TA universal analysis -NT software.

3.2.2.6 Differential Scanning Calorimetry (DSC)

DSC experiments were carried out using a DSC 2920 Differential Scanning Calorimeter (TA Instruments, USA), with a constant 10˚C/min heating rate, from 0˚C to 300˚C in a dry nitrogen atmosphere. Non-sealed aluminium pans were used in order to allow propellant to escape during the desolvation phase. In all measurements 6 to 7mg of sample were used. When it was required, simultaneous TGA/DSC measurements were performed under identical conditions using a SDT Q600 TGA/DSC (TA instruments, USA). The thermograms obtained for the DSC results were analysed using TA universal analysis -NT software.

3.2.2.7 Variable Temperature X-Ray Powder Diffraction (VT-XRPD)

VT-XRPD patterns were collected on a Bruker D8 diffractometer system (Bruker AXS LTD., Coventry, UK) operating in a Debye-Scherrer geometry. X-ray radiation was generated inside a ceramic X-ray tube from an anode made of copper Cu in Kα spectral line at wavelength λ= 1.54059 Å. The diffractometer is equipped with a scintillation detector and Bruker Kristalloflex generator set on voltage 40kV and current 40mA. Samples were loaded in borosilicate glass capillary tubes BGCT with 0.7mm bore diameters (CTS Capillary Tube Supplies Ltd UK) and mounted on the goniometer in a preferable orientation. Samples were scanned from 2θ= 5˚ until 45˚ at a 1sec/step speed in increments of 0.02˚ stepwise. DIFFRACplus software package version 2.3 was used for data acquisition. Cryostream Plus controller (Oxford Cryosystems Ltd., Long Hanborough, Oxford, UK), a heating-cooling system was provided for VT-

XRPD which was controlled by a Cryopad PC programme for VT-XRPD scans. VT-XRPD scans were set from 2θ= 5˚ until 45˚ at a 1sec/step speed in increments of 0.02˚, acquired each 3˚ C from heated sample at a rate of 1˚ C/min starting from 20-221˚ C at a rate of a 3˚ C/min. All patterns were collected straight after the formation of the crystals to determine the purity of the samples and its crystalline structure and prevent any decomposition and/or contamination.

3.2.2.8 Modulated Temperature DSC (MDSC)

MDSC experiments were carried out using a DSC 2000 Differential Scanning Calorimeter (TA Instruments, USA). MDSC measurements were conducted using sine wave temperature programmes defined by underlying heating rate, amplitude and period. Samples of anhydrous BDP and BDP CFC-11 clathrates were equilibrated at and then kept at 25˚C for 1 minute; the samples were then heated at a rate of 1°C/min until melted. The temperature was oscillated at an amplitude of 0.5°C each 30 seconds. Non-sealed aluminium pans were used in order to allow the propellant to escape during the desolvation phase. In all measurements, accurately weighed 7±0.2mg of the samples were used. The temperature and the enthalpy were calibrated against an indium standard. The thermograms obtained for the DSC results were analysed using TA universal analysis -NT software.

3.2.2.9 Raman Spectroscopy

A small amount of anhydrous BDP and BDP CFC-11 crystals were spread on a microscope slide. Raman spectra were recorded with a Raman microscope (LabRam, Horiba Jobin Yvon, UK). Data processing was performed using LabSpec 5 (Horiba Jobin Yvon). The instrument conditions were: 200 µm wide confocal hole, 150 µm wide entrance slit, 600 gr/mm grating, and 100X LWD objective lens. Various exposure times (100, 300 and 900 ms) were used to a range of signal-to-noise ratios (S/N). An XYZ motorized stage (Marzhauzer) and a HeNe laser (783 nm) were used. Spectra were obtained using a near infrared diode laser operating at 783 nm working with a power source typically below 300 mW. The spectral range measured was 0 – 2000 cm^{-1}. Raman calibration was performed before acquiring Raman measurements. This was achieved on a standard silicon (Si) sample.

3.2.2.10 Variable temperature Raman spectroscopy

Small amounts of BDP CFC-11 crystals were spread on microscope slides. Samples were then heated at 1˚C/min using a XY manual cooling/heating stage (Linkam LTS350) with TMS94 temperature controlling programme and LNP94 cooling system with a 2 litres dewar for liquid nitrogen. Spectra were collected every 10˚C from 25˚C to 225˚C. The instrument parameters concerning the Raman microscope used were the same as above. The spectral range measured was 0 – 4000 cm^{-1}.

3.3 Results and Discussion

3.3.1 SEM Analysis

Anhydrous BDP suspended in CFC-11 showed a rapid growth of the crystals. SEM images of both anhydrous BDP and the crystals extracted from BDP CFC-11 suspension are shown in Figure 3-1. There are considerable differences in the morphology of the two different forms of BDP. Anhydrous BDP appear more spherical in comparison with the crystals from BDP CFC-11 suspension exhibiting a well-defined crystals with hexagonal morphology. The crystals are polydispersed, with a size range of 30 to 70 µm. The particles of anhydrous BDP observed using SEM (Fig. 3-1) showed round quasi-spherical particles of less than 5 µm in size.

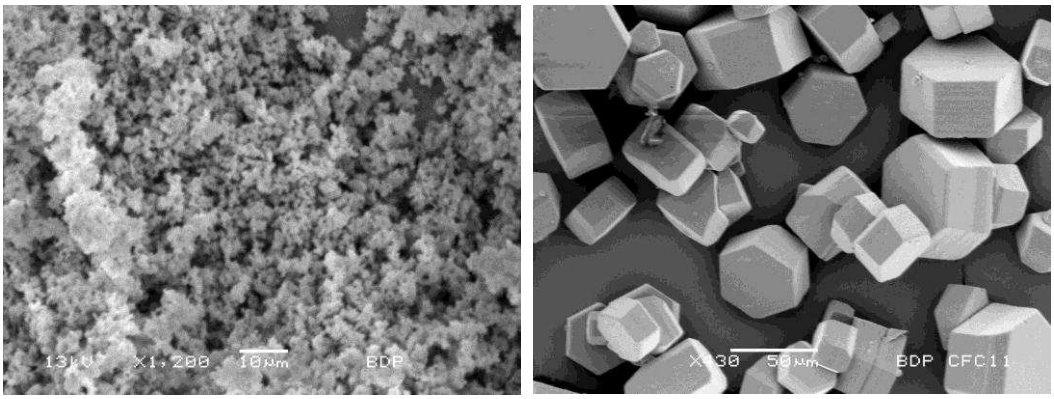

Figure 3-1: SEM images of anhydrous BDP (left) and Crystals from BDP CFC-11 suspension (right).

3.3.2 X-RPD results

Diffraction techniques are definitive tools for detecting and quantifying molecular order in a system (Shah et al., 2006). Four crystal structures have been reported and filed with the Cambridge Structural Database (CSD) for BDP

and its compounds: one for anhydrous BDP (Millard and Myrdal, 2002); one for BDP monohydrate (Duax et al., 1981); one for the HFA-134a clathrate (Harris et al., 2003); and one for the BDP ethanol clathrate (Kuehl et al., 2003). For the clathrates, only partial crystal structures are available: the guest molecules are disordered and only the atomic co-ordinates of the framework BDP molecules have been reported. The two reported clathrate structures are identical for all intents and purposes. The single-crystal derived structural data reported in the literature for these compounds were determined at 100 K, 271 K, 170 K and 170 K respectively.

For the sample of as-received anhydrous BDP, when the effects of thermal expansion were accounted for, we achieved an excellent match when comparing our room temperature data with a pattern calculated from the reported 100 K structure of BDP (ca. 4.5 % increase in volume at room temperature compared to 100 K). The Rietveld method was used to model the entire powder pattern profile and to calculate lattice parameters. The as-received material can therefore be unambiguously identified as identical with the previously reported anhydrous BDP (Millard and Myrdal, 2002), and our bulk sample is predominantly crystalline, and pure, within the limits of our data collection, analysis, etc.

A fair match was obtained for anhydrous BDP suspended in CFC-11 when comparing our data with patterns calculated based on the partial structures reported for the BDP HFA-134a and BDP ethanol clathrates (Fig. 3-2). The lack of an excellent match is expected given that the reported structures do not include the guest molecules.

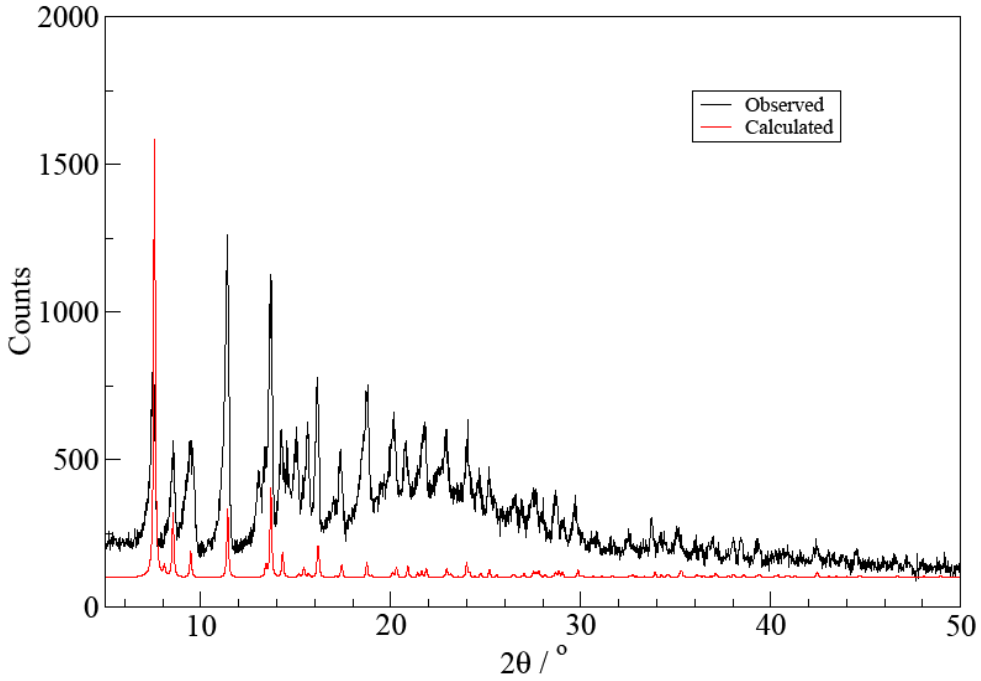

Figure 3-2: Superimposition of experimental BDP CFC-11 clathrate X-RPD pattern with that of the calculated BDP EtOH HFA-134a clathrate X-RPD pattern without the solvent.

A more rigorous comparison, using the Le Bail method (Le-Bail et al., 1988) to fit the observed pattern using the unit cell reported for the clathrate (and allowing for thermal expansion, ca. 1.5 % increase in volume at room temperature compared to 170 K) produces an excellent fit of the data, with no extra peaks present in the pattern. Particular care was taken to examine the regions of the pattern where peaks from anhydrous BDP might be observed. In addition to providing confidence that the bulk sample of anhydrous BDP suspended in CFC-11 is pure BDP CFC-11 clathrate (referred to it hereafter as BDP CFC-11 clathrate) (and has the clathrate unit cell), the Le Bail method allows us to estimate the "idealised" composition of the clathrate if space filling is assumed. Using the tabulated atomic volumes of Hofmann and Mighell (Hofmann, 2002, Himes and Mighell, 1987), a single BDP molecule is expected to occupy ca. 685 $Å^3$. Given that at room temperature the unit cell volume is 4959 $Å^3$ from our Le

Bail analysis, and that the unit cell of the clathrate contains six BDP molecules (Harris et al., 2003, Kuehl et al., 2003), there is 850 $Å^3$ of void space. If this void space is completely occupied by CFC-11 of approximate volume 100 Å3 per molecule, the overall stoichiometry for the CFC-11 clathrate is expected to be approximately BDP CFC-11 1:1.4. Likewise, for an EtOH molecule of approximate volume 70 $Å^3$, a stoichiometry of BDP EtOH of 1:2 is expected[1].

3.3.3 XPS results

Both anhydrous BDP and BDP CFC-11 clathrate were analysed using XPS and ATR-IR spectroscopy in order to determine the elemental composition of each of the compounds in particular CFC-11 inclusion. ATR-IR spectroscopy was performed on a small amount of the different concentrations of BDP CFC-11 clathrates (Fig. 3-3) in order to show the presence of fluorine on the clathrate crystal obtained. The spectra obtained showed very noticeable peak at a wavenumber of around 1000 cm^{-1}. This peak was ascribed to CFC-11 peak [Integrated Spectral Database System of Organic Compounds (SBDS)].

Wide scan XPS results obtained for the anhydrous BDP, BDP CFC-11 clathrate 0.5% w/w and BDP IPA clathrate are represented in Figure 3-4. The main peaks shown on the different scans are at 282, 530 and 197 eV which correspond to oxygen, carbon, and chlorine respectively. These elements constitute the backbone structure of BDP. A very small peak at 685 eV position can be seen in

[1] These stoichiometries are necessarily estimates. For comparison, the unit cell volume of anhydrous BDP is 2655.9 $Å^3$ from X-RPD, and 2680 $Å^3$ from the simple atomic volume calculation, which corresponds to a volume per BDP molecule of 664 $Å^3$ from X-RPD vs 670 $Å^3$ from the simple calculation.

the scan obtained for the BDP CFC-11 clathrate (Fig. 3-4B) which is ascribed to fluorine and hence is consistent with the formation of the clathrate.

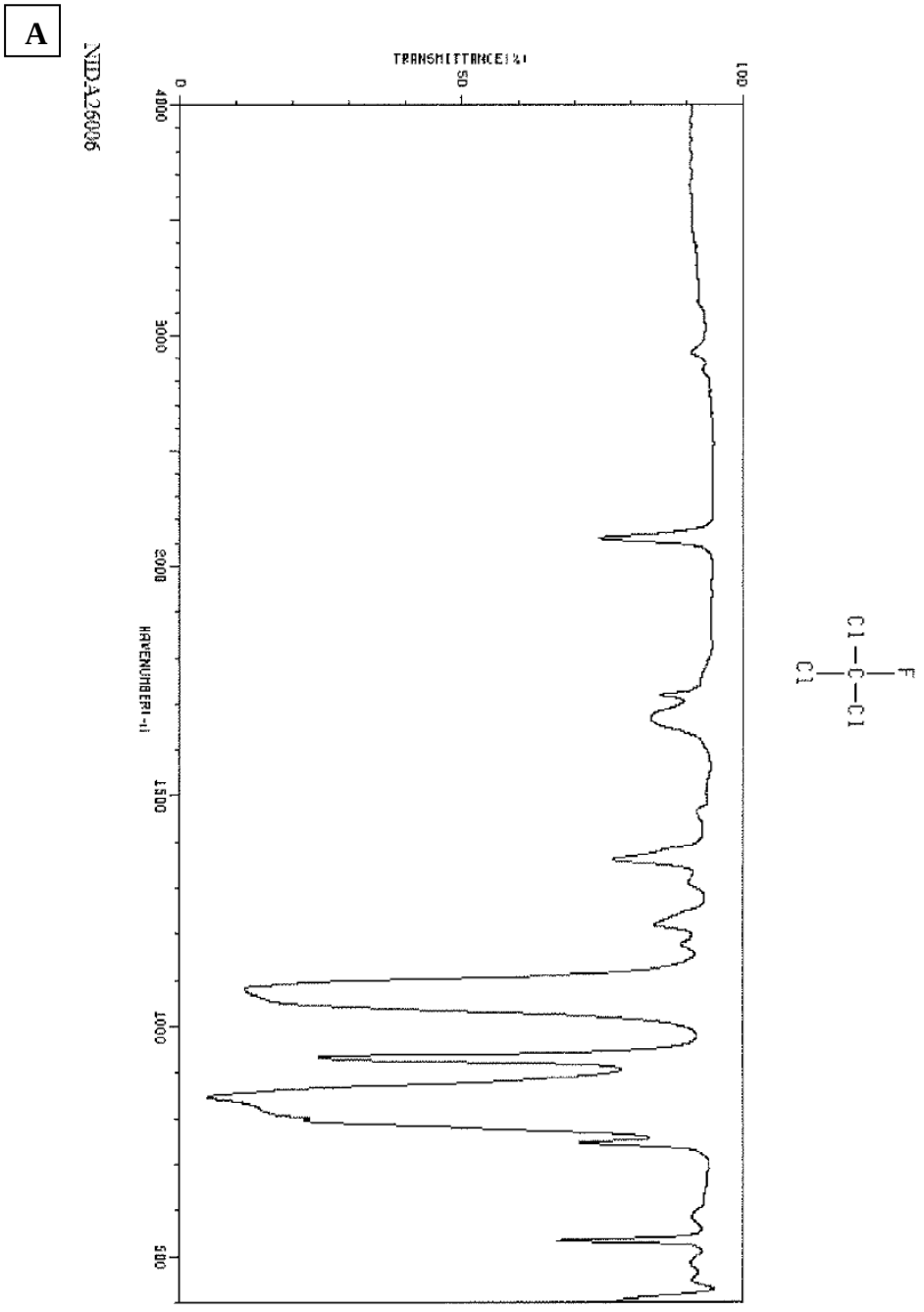

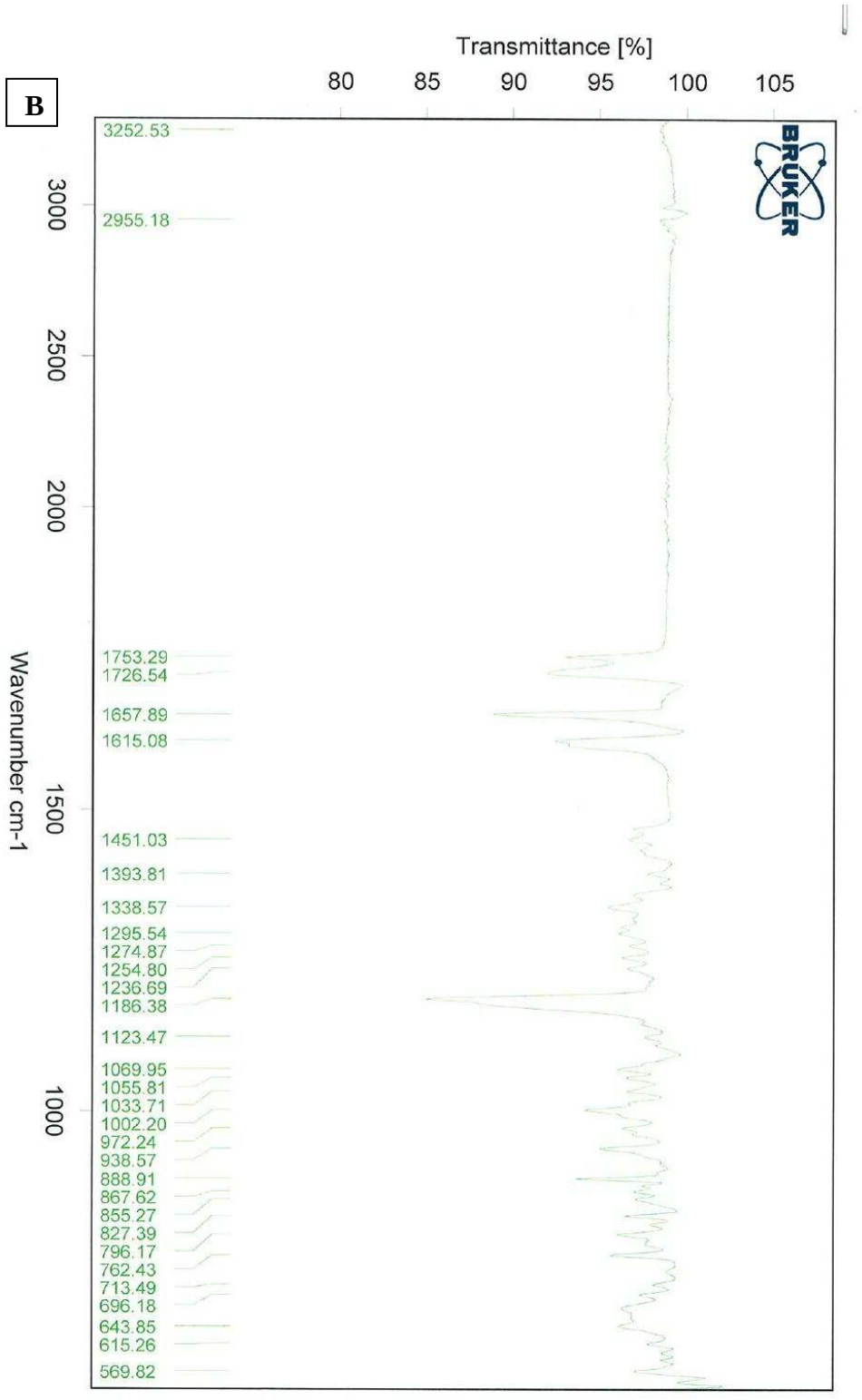
B
Transmittance [%]
80
85
90
95
100
105
Wavenumber cm-1
3000
2500
2000
1500
1000
3252.53
2955.18
1753.29
1726.54
1657.89
1615.08
1451.03
1393.81
1338.57
1295.54
1274.87
1254.80
1236.69
1186.38
1123.47
1069.95
1055.81
1033.71
1002.20
972.24
938.57
888.91
867.62
855.27
827.39
796.17
762.43
713.49
696.18
643.85
615.26
569.82
BRUKER

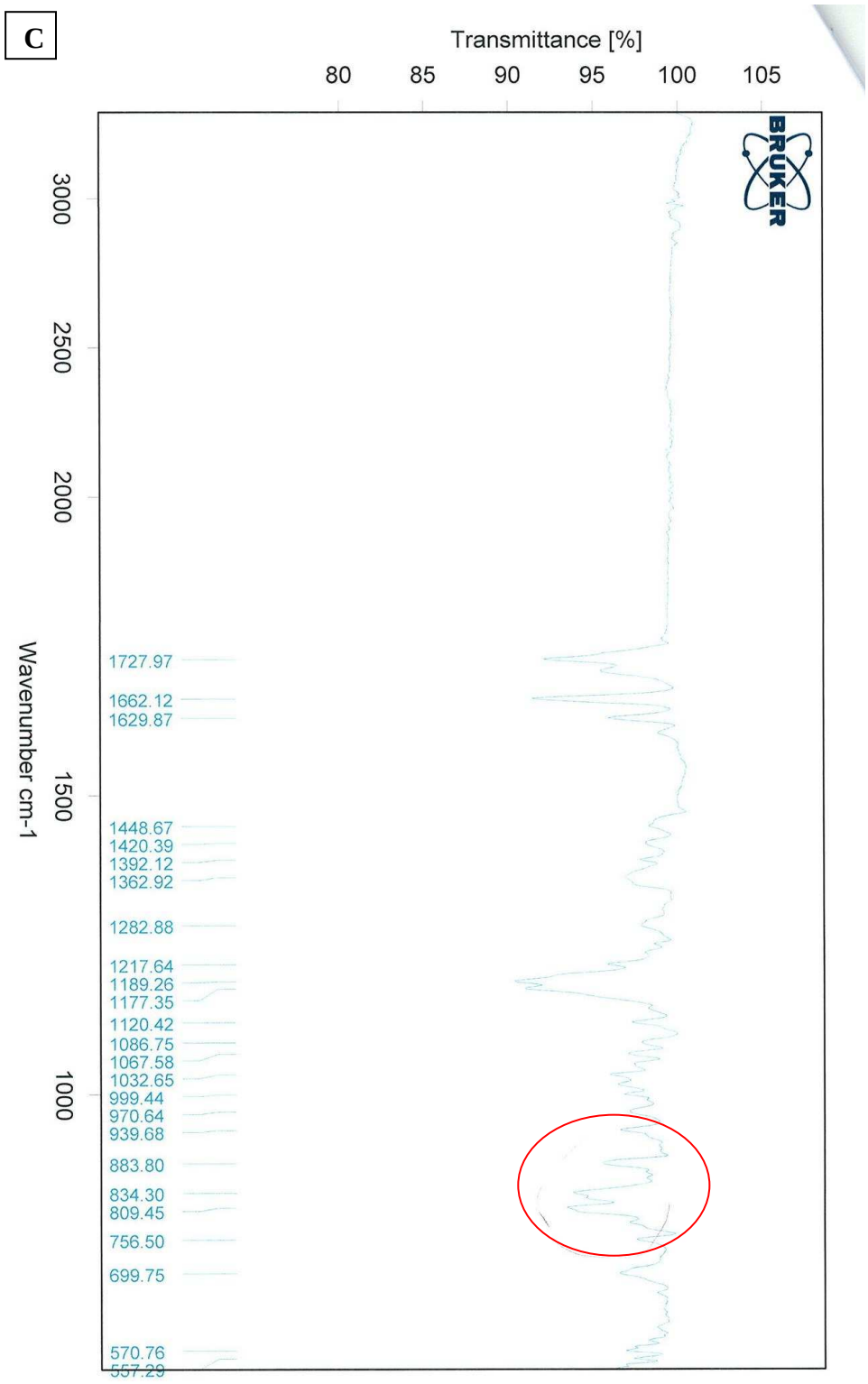

Figure 3-3: ATR-IR spectrum of A- CFC-11 as taken from the Integrated Spectral Database System of Organic Compounds (Data were obtained from the National Institute of Advanced Industrial Science and Technology (Japan)), B- Anhydrous BDP and C- BDP CFC-11 Clathrates.

The surface composition of both BDP CFC-11 clathrate at a concentration of 0.1% and 0.5% w/w BDP in CFC-11 did not show any significant changes in the atomic percentage of all the atoms present in the structure between the two different concentrations (Table 3-1). A very small change in the atomic percentage can be noticed for both anhydrous BDP and BDP IPA clathrate. The results obtained for both anhydrous BDP and BDP IPA clathrate (ratio of 1:1.5 BDP to IPA as IPA has a volume of approximately 94 $Å^3$) are quite consistent and comparable to the theoretical atomic percentage calculated (Table 3-1). However, for BDP CFC-11 clathrate, the results obtained seem quite different from the theoretical atomic percentage calculated for the 1:1.4 molar ratio of BDP to CFC-11. The results obtained showed a 1:0.4 molar ratio of BDP to CFC-11 for the two concentrations stated above. In order to confirm the molar ratio observed by XPS, a quantitative elemental analysis on the BDP CFC-11 clathrate of 0.1 and 0.5% w/w BDP in CFC-11 was performed. The analysis was accomplished via the combustion of the crystal and the collection of combustion product which is weighed and used in order to calculate the composition of the unknown samples. The results showed an average of 58.90% carbon and 6.48% hydrogen.

Table 3-1: Theoretical and measured atomic percentage of the surface analysis of anhydrous BDP, BDP CFC-11 (0.5 % w/w) and BDP IPA clathrate (n=3).

Atomic %	**Anhydrous BDP**		**BDP CFC-11 clathrate**		**BDP IPA clathrate**	
	Theoretical	**Measured**	**Theoretical**	**Measured**	**Theoretical**	**Measured**
C 1s	77.77	81.07 ± 1.21	68.37	75.1 ± 0.98	77.5	81.34 ± 0.72
O 1s	19.44	17.01 ± 0.75	16.28	18.54 ± 0.27	20	16.54 ± 0.2
Cl 2p	2.78	1.914 ± 0.54	12.09	5.43 ± 0.42	2.5	2.23 ± 0.35
F 1s	0	0	3.25	0.92 ± 0.12	0	0

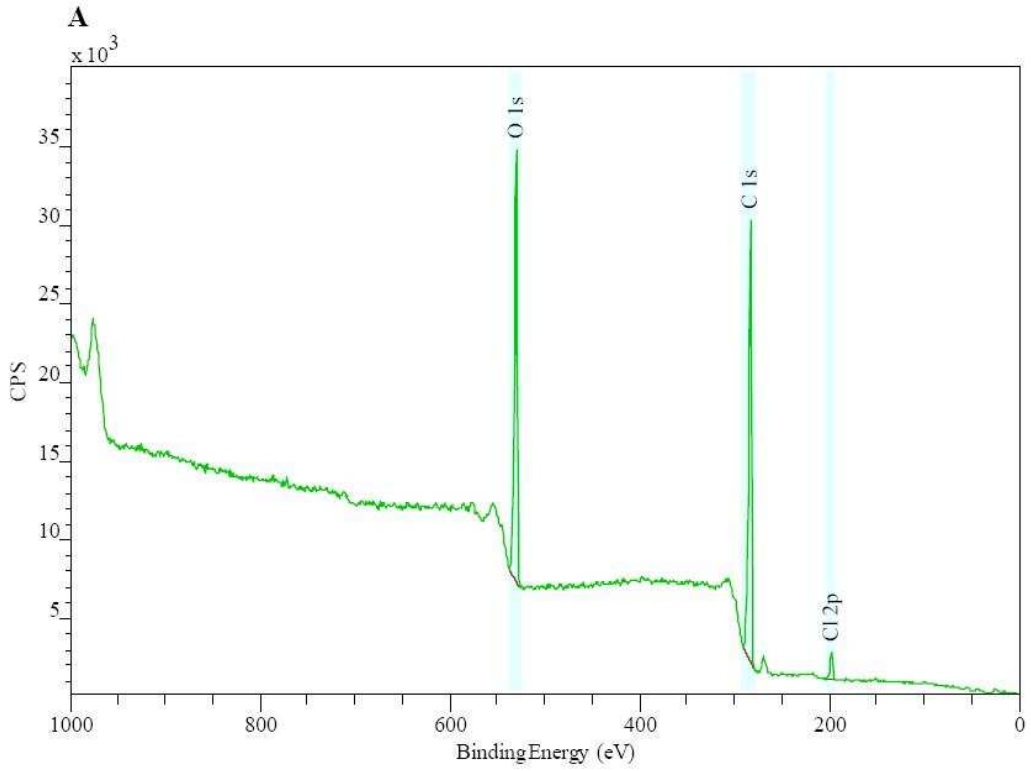
A
x 10^3
CPS
35
30
25
20
15
10
5
O 1s
C 1s
Cl 2p
1000
800
600
400
200
0
Binding Energy (eV)

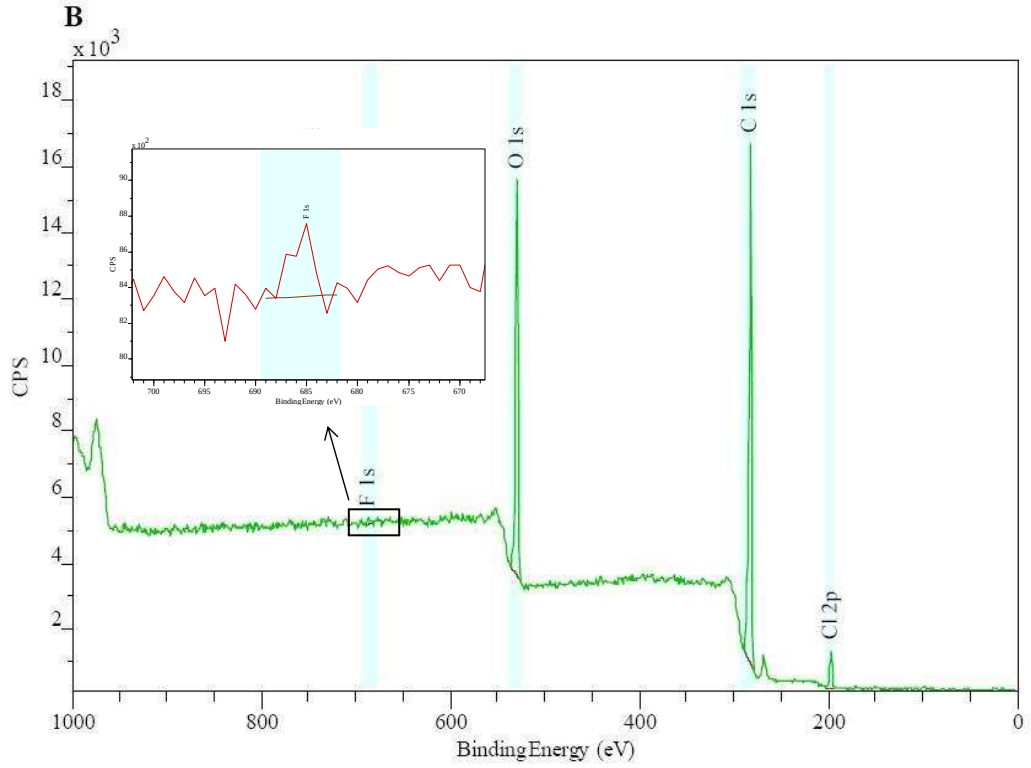
B
x 10^3
CPS
18
16
14
12
10
8
6
4
2
O 1s
C 1s
F 1s
Cl 2p
1000
800
600
400
200
0
Binding Energy (eV)

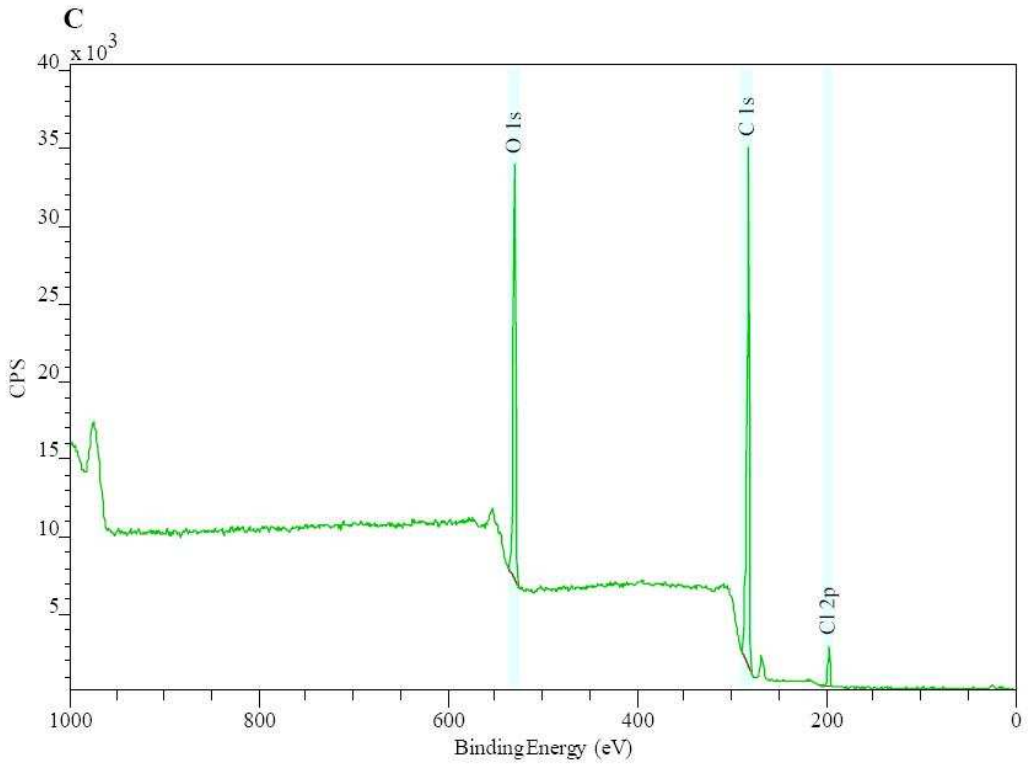

Figure 3-4: Wide survey scans of A- anhydrous BDP, B- BDP CFC-11 clathrate and C- BDP IPA clathrate using XPS.

To summarize, X-RPD, XPS and ATR-IR results show the successful formation of BDP CFC-11 clathrates.

3.3.4 Thermal Analysis

Analytical techniques based on the thermal energy principle have been widely used to characterise different amorphous and crystalline pharmaceutical systems (Shah et al., 2006, Hancock and Zografi, 1997). Crystallization and/or any solid state rearrangement can be induced by the thermo-analytical techniques to produce an exothermic or an endothermic change which then reveals the position of the transition (Shah et al., 2006). The two thermal techniques used to characterise the different compounds here were DSC and TGA.

3.3.4.1 TGA results

TGA relies on a high degree of precision in three measurements: weight, temperature, and temperature change (Shah et al., 2006). No weight loss was observed for anhydrous BDP between 0 and 212˚C (Fig. 3-5A). The weight loss observed after 212ºC (i.e. the melting point) is due to combustion of the sample (Fig. 3-5A). The loss of CFC-11 from the clathrate structure, observed at around 100˚C is confirmed by the TGA results and was observed with the different BDP CFC-11 clathrates over the range of concentrations used for the study. The results shown in Figure 3-5B are those observed for the highest weight loss of CFC-11 from the BDP CFC-11 clathrate. The loss of CFC-11 is expressed as 14.5% weight loss which corresponds to a 0.6:1 molar ratio of CFC-11 to BDP for a 1.67% w/w BDP in CFC-11 clathrate. Different samples of clathrates formed by using different concentrations of BDP in CFC-11 showed a different weight loss (Table 3-2). The percentage weight loss for this latter material also differs from the theoretical weight loss calculated for a molar ratio of 1.4:1 CFC-11 to BDP. All the measured weight losses of CFC-11 from the clathrates were lower than expected (Table 3-2). It was found from these results that CFC-11 was successfully included in the crystal structure for the different concentrations to form a clathrate. The TGA data for the BDP: EtOH solvate showed weight loss as soon as the samples were placed in the instrument, before and as soon as heating was applied (Fig. 3-5C). This loss of EtOH from the structure as soon as the heating was initiated is consistent with the results observed using DSC.

Table 3-2: Percentage weight loss of BDP CFC-11 Clathrate at different concentrations (n=3).

BDP CFC-11 clathrate concentration (% w/w)	0.1	0.5	1.67	2	2.5	3
Percentage weight loss (%)	3.79 ± 0.92	6.14 ± 1.98	13.8 ± 1.5	4.52 ± 0.12	8.39 ± 0.86	4.00 ± 1.77

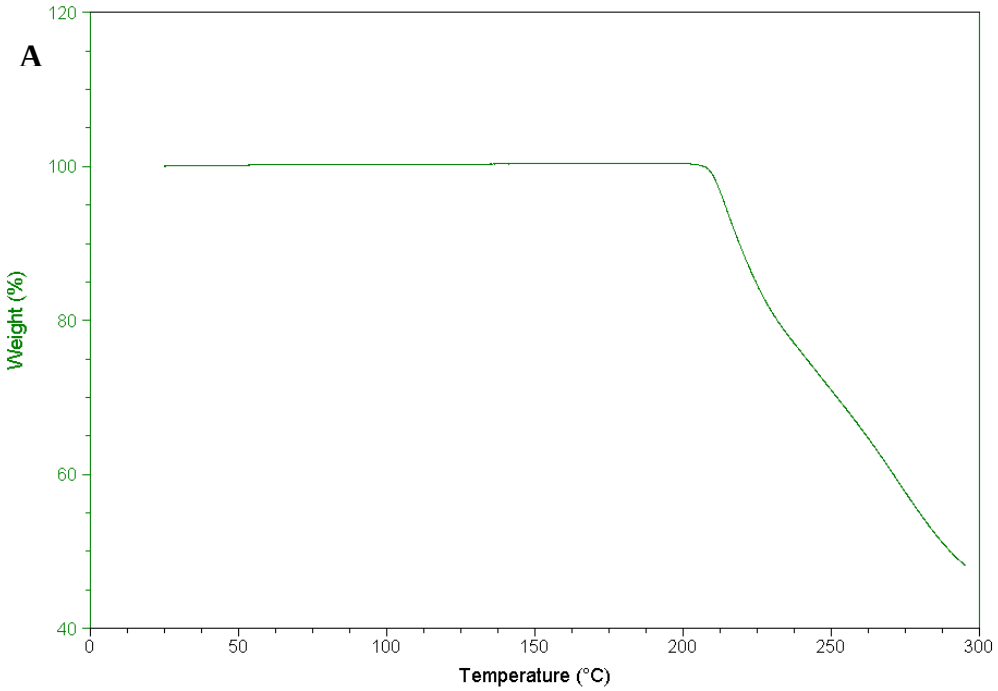
A
120
100
80
60
40
Weight (%)
0
50
100
150
200
250
300
Temperature (°C)

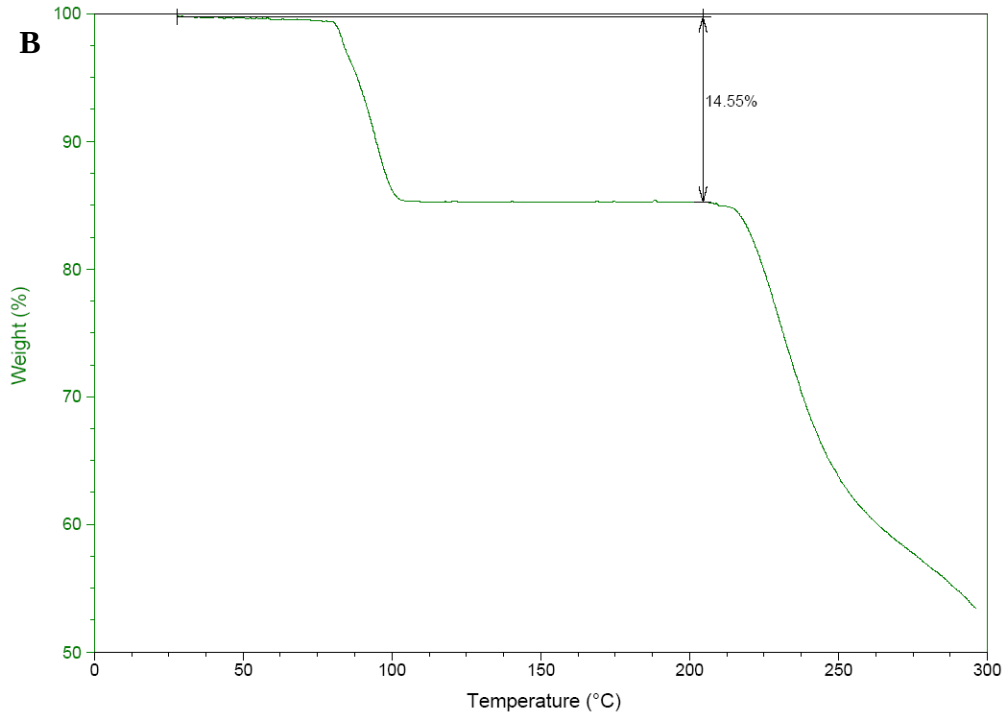
B
100
90
80
70
60
50
Weight (%)
14.55%
0
50
100
150
200
250
300
Temperature (°C)

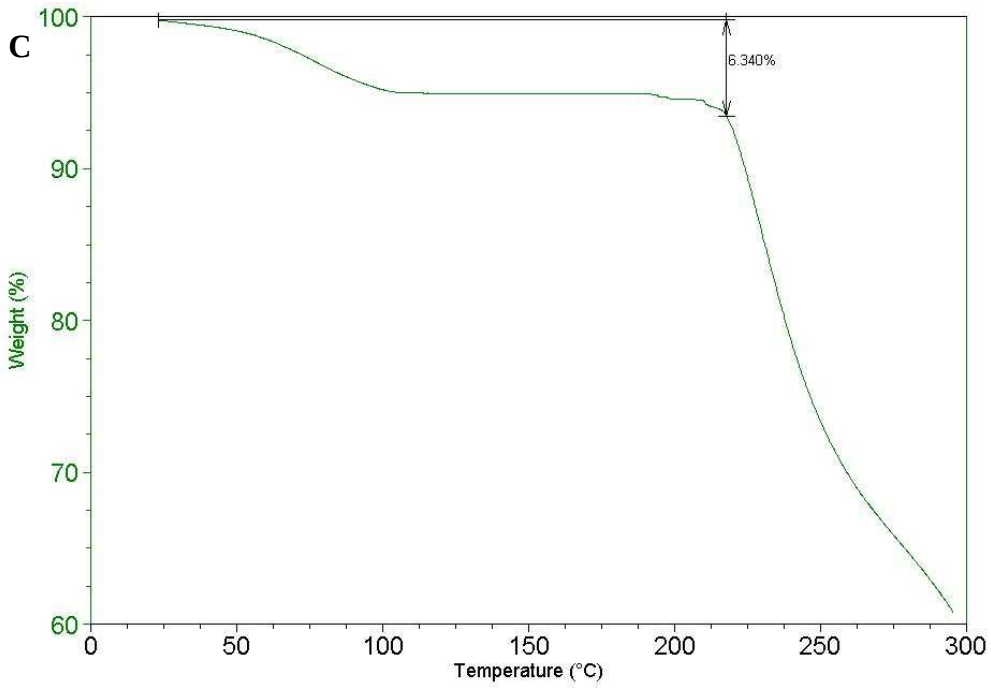

Figure 3-5: TGA curves of A- anhydrous BDP, B- BDP CFC-11 clathrate (1.67% w/w BDP in CFC-11) and C- BDP EtOH solvate. All samples were heated from 0˚C to 300˚C at a heating rate of 10˚C/min.

Furthermore, the measured weight loss was similar to the theoretical weight of BDP: EtOH solvate at a 2:1 molar of EtOH in BDP confirming the formation of a solvate (Table 3-3). BDP: IPA clathrate TGA results show similar results to BDP EtOH solvate without the initial weight loss observed at the beginning of heating (Table 3-3).

Table 3-3: The different crystal samples encountered together with experimental (TGA) and theoretical weight loss in weight % (n=3).

Samples	**% TGA Weight loss**	**Theoretical % weight loss**
BDP CFC-11 clathrate (1.67% w/w)	13.8 ± 1.5	19.72 (1:1.4 BDP to CFC-11)
BDP EtOH solvate	9.7 ± 0.78	8.19 (1:1 BDP to EtOH)
BDP monohydrate	----------	3.39 (1:1 BDP to H_2O)
BDP IPA clathrate	10.5 ± 1.04	18.7 (1:2 BDP to IPA)

Clathrates are described as crystalline solids in which guest molecules occupy cavities or channels in the host lattice that are formed upon crystallization (Vaidya, 2004). However, in non-clathrate crystal formation i.e. solvates, the individual molecules are tightly packed together, with intermolecular spaces between neighbouring entities (Vaidya, 2004). The intermolecular voids of the crystal are filled by a second, solvent-type molecule or used to complete a coordination sphere around a functional moiety. The solvent entities are rather loosely held in the lattice. The stoichiometric relationship between host and solvent are quite difficult to predict as it depends on the size of the voids and the actual size of the solvent and how these interact (Goldberg, 1988). Many of the solvates can therefore be considered as a special type of clathrate structure.

Stoichiometric analysis of the clathrates studied in this work showed a ratio of host to guest molecules slightly lower than would be expected. This indicates that all of the available cavities are not always filled. This can be explained by considering the process of clathrate formation where it is thought that clusters of host molecules begin to form in solution surrounding the guest molecules, when the agglomeration of host molecules reaches a critical size crystal growth begins. If the guest molecule is not correctly positioned or oriented at this point it will not be enclosed and thus some empty cavities are to be expected (Kuhs et al., 1997, Vaidya, 2004). In addition the level of cage occupation is thought to be influenced by the pressure and temperature at formation. It is also possible for each channel to contain multiple small guest molecules (Kuhs et al., 1997).

Table 3-4: Stoichiometric relationship of BDP CFC-11 clathrate using calculation of molar ratio of CFC-11 to BDP using results obtained from TGA (n=3).

Anhydrous BDP suspended in CFC-11 (% w/w)	0.1	0.5	1.67	2	2.5	3
Number of CFC-11 molecules in the channels	0.1 ± 0.02	0.4 ± 0.04	0.6 ± 0.037	0.35 ± 0.05	0.4 ± 0.02	0.15 ± 0.03

The TGA results were used to determine the number of CFC-11 molecules present in the channels of the clathrate structure and the EtOH molecules in the solvate structure. The results for the BDP: EtOH solvate showed a 1:1 molar ratio of BDP to EtOH. In contrast, the TGA data collected for the different concentration of BDP CFC-11 clathrates showed a different molecular ratio of CFC-11 to BDP with different concentrations of BDP CFC-11 clathrate (Table 3-4). The increasing then decreasing pattern of the number of molecules in the host crystal can be explained by the incorrect positioning or orientation of the guest molecules which will lead to molecules being not included and hence the formation of empty cavities (Kuhs et al., 1997, Vaidya, 2004). This process is influenced by the pressure and temperature at formation. The stoichiometric relationship is hence not clear but appears to show an increased molar ratio of CFC-11 to BDP with increasing concentration of BDP to CFC-11 during the conversion. At 1.67% w/w of BDP to CFC-11, it reaches its maximum with a 0.6:1 molar ratio of CFC-11 to BDP and then decreases as the concentration increases (Table 3-4).

3.3.4.2 DSC Results

DSC is widely used for investigating the phase behaviour of pharmaceutical solids and different methodologies based on instrument type can be utilized (Shah et al., 2006). Conventional DSC, as used here, is based on a linear heating rate of the sample through to its melting point (Shah et al., 2006). DSC data obtained for the different samples are shown in Figure 3-6.

Anhydrous BDP melts at about 212˚C (Fig. 3-6A) within limitations of data which corresponds to the literature value (Vervaet and Byron, 1999a). The thermogram for the BDP CFC-11 clathrate is illustrated in Figure 3-6B. A small exothermic onset is observed at about 99˚C, which may be due to a solid state rearrangement of the BDP CFC-11 clathrate structure. In addition, an endothermic transition is seen at about 100˚C. This is thought to be due to the release of CFC-11 from the tunnels of the clathrate structure. The melting point of BDP e after CFC-11 loss is seen at approximately 212˚C. The two different transitions for the release of the propellant from the structure are concomitant. The complex thermal events around the melting point observed in the different DSC curves of the different samples indicate that the BDP undergoes significant degradation during melting (Shah et al., 2006). Interestingly, the clathrate retains the solvent (CFC-11) until quite high temperatures are reached (100-120˚C).

A

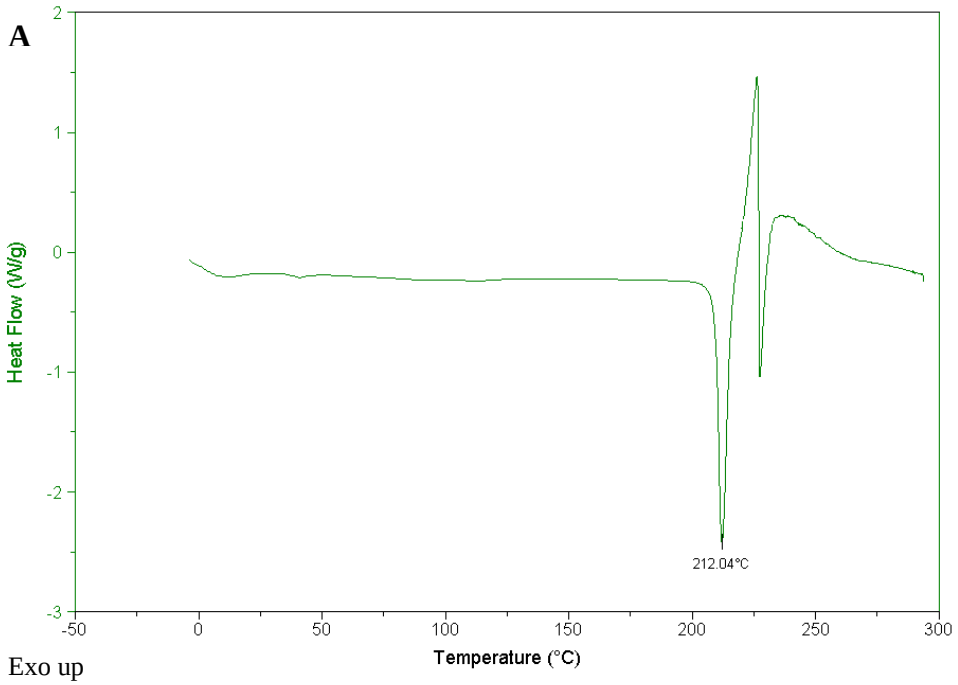

B

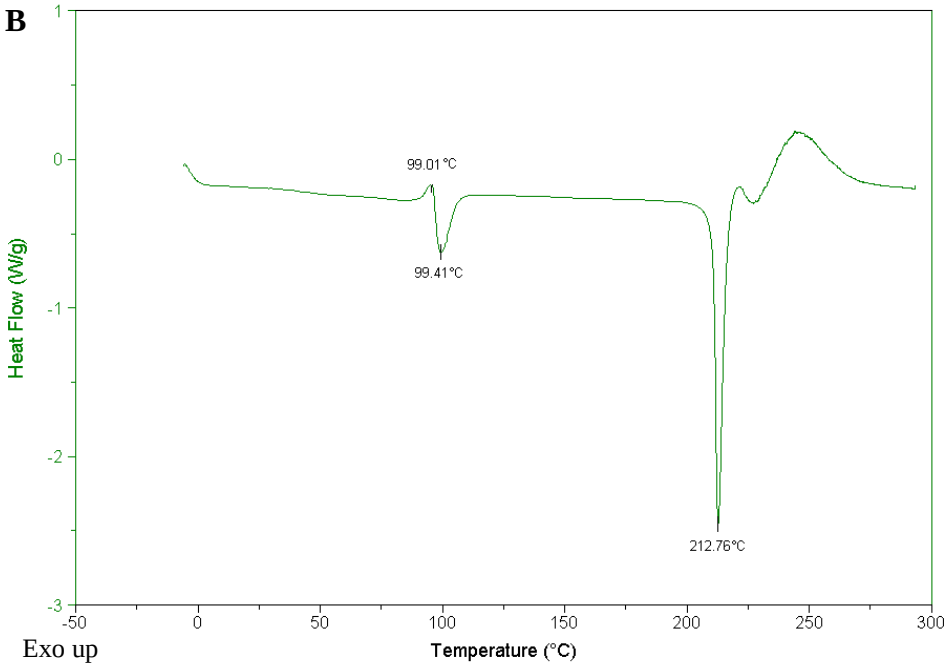
99.01°C
99.41°C
212.76°C
Heat Flow (W/g)
Temperature (°C)
Exo up

C

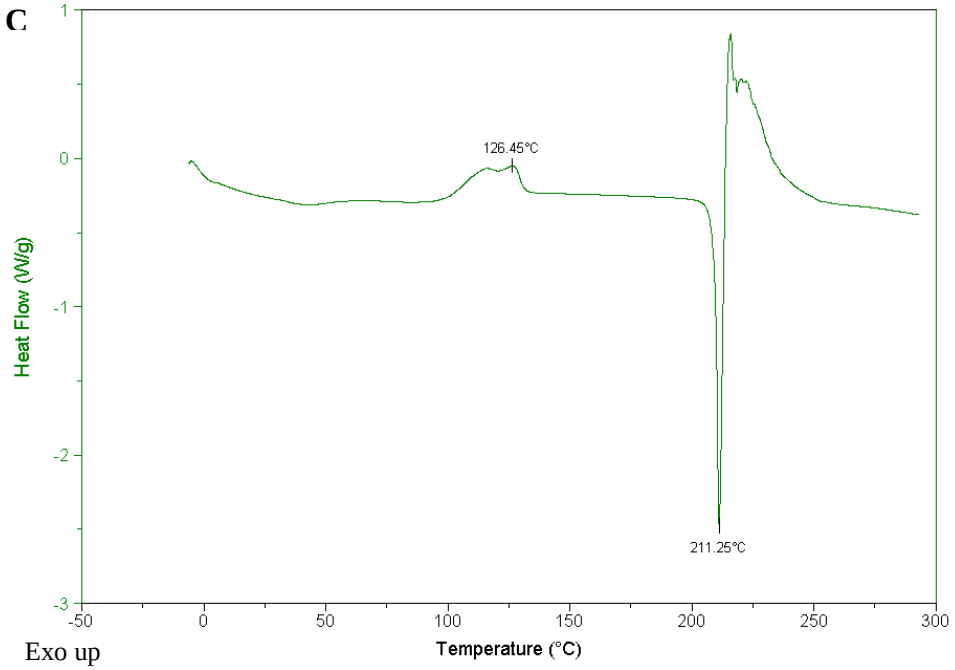
126.45°C
211.25°C
Heat Flow (W/g)
Temperature (°C)
Exo up

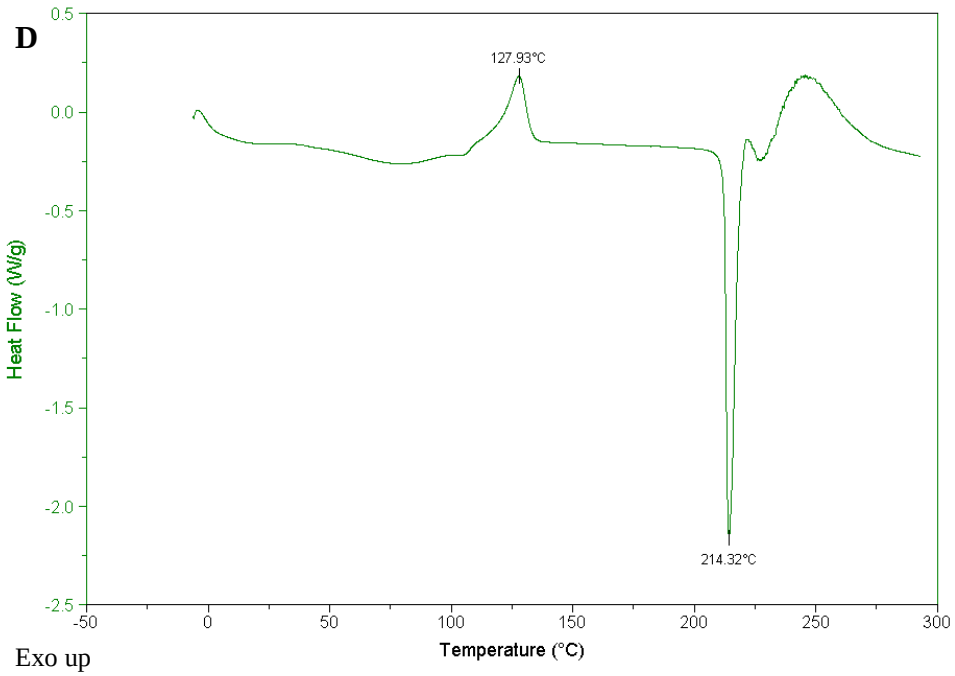

Figure 3-6: DSC curves of A- anhydrous BDP, B- BDP CFC-11 clathrate, C- BDP EtOH solvate, D- BDP IPA clathrate. All samples were heated from 0˚C to 300˚C at a heating rate of 10˚C /min.

The release of the CFC-11 propellant from the channels of the crystallized BDP can be thermodynamically described using the following Gibb's free energy equation 3-1:

$$\Delta G = \Delta H - T\Delta S \qquad \textbf{Equation 3-1}$$

where ΔG is Gibb's free energy (kJ mol^{-1}), ΔH is the enthalpy (J), T is the temperature (T) and ΔS is the entropy (JK^{-1}).

The process by which the guest molecule is released from the clathrate crystal is believed to consist of two stages represented by concomitant exothermic and endothermic events. The first step is indicated by a small exothermic event. As the temperature increases, ΔS must decrease.. This has been attributed to the

clathrate crystal undergoing solid state rearrangement/recrystallization. The second stage of clathrate decomposition or the desolvation of the clathrate is shown by a large endothermic event. A large decrease in heat flow indicates a large increase in entropy. This can be explained by the release of the guest molecules into the surrounding atmosphere (Vervaet and Byron, 1999). These two stages occur simultaneously and cannot be observed as distinct events. This is further addressed and investigated in the following modulated DSC section.

Thermograms were run in a cycle in order to check if the transitions were still present after heating. The cycle consisted of heating the samples from 0˚C to 150˚C and then recooling to 0˚C and reheating again to 300˚C. For all the samples studied here, the thermograms showed no presence of the transitions after initial heating to 150˚C. Therefore, the solid state rearrangement of the clathrate is irreversible and leads to a total loss of the solvent encaged in the channels.

The thermograms for both the BDP: EtOH solvate and BDP: IPA clathrate, showed an exothermic onset at about 110-135˚C and 115-145˚C respectively (Fig. 3-6C and D). The magnitude of the exothermic transition was slightly variable, due to the non-stoichiometric association of the drug with the solvent (Vervaet and Byron, 1999b, Kuehl, 2003) and represents the solid phase which is recrystallization followed by desolvation (Vervaet and Byron, 1999). This can be explained by a solid state rearrangement of the structure of the solvate/clathrate. A very broad endothermic peak is observed at about 60˚C which is variable

between the different batches synthesized and could be attributable to the excess EtOH on the samples or on the surface of BDP EtOH solvate.

3.3.5 MDSC Results

On standard DSC, heating anhydrous BDP to the melting point does not show any transition as shown previously. MDSC raw data is a complex heat flow signal which contains the reversing, non-reversing and phase information. Figure 3-7 shows a reversing, non-reversing and total heat flow signals of both anhydrous BDP and BDP CFC-11 clathrates. When heated, anhydrous BDP showed an endotherm in the total heat flow corresponding to the melting 207˚C (Fig. 3-7A). The melting point between standard DSC and MDSC are different in temperature due to the exposure of the BDP samples to higher temperature for longer time at lower heating rate leading to an earlier degradation. This also applies to the different transitions observed. The reversing and non-reversing components also follow this endotherm. It can be seen that the reversing signal shows a change in the heat capacity in the region of 56-75˚C. This transition is thought to be due to a solid state rearrangement on the crystal structure of BDP, which might confirm the rearrangement observed when CFC-11 was released from the clathrate structure upon heating. When looking at Figure 3-7B corresponding to the MDSC curve of BDP

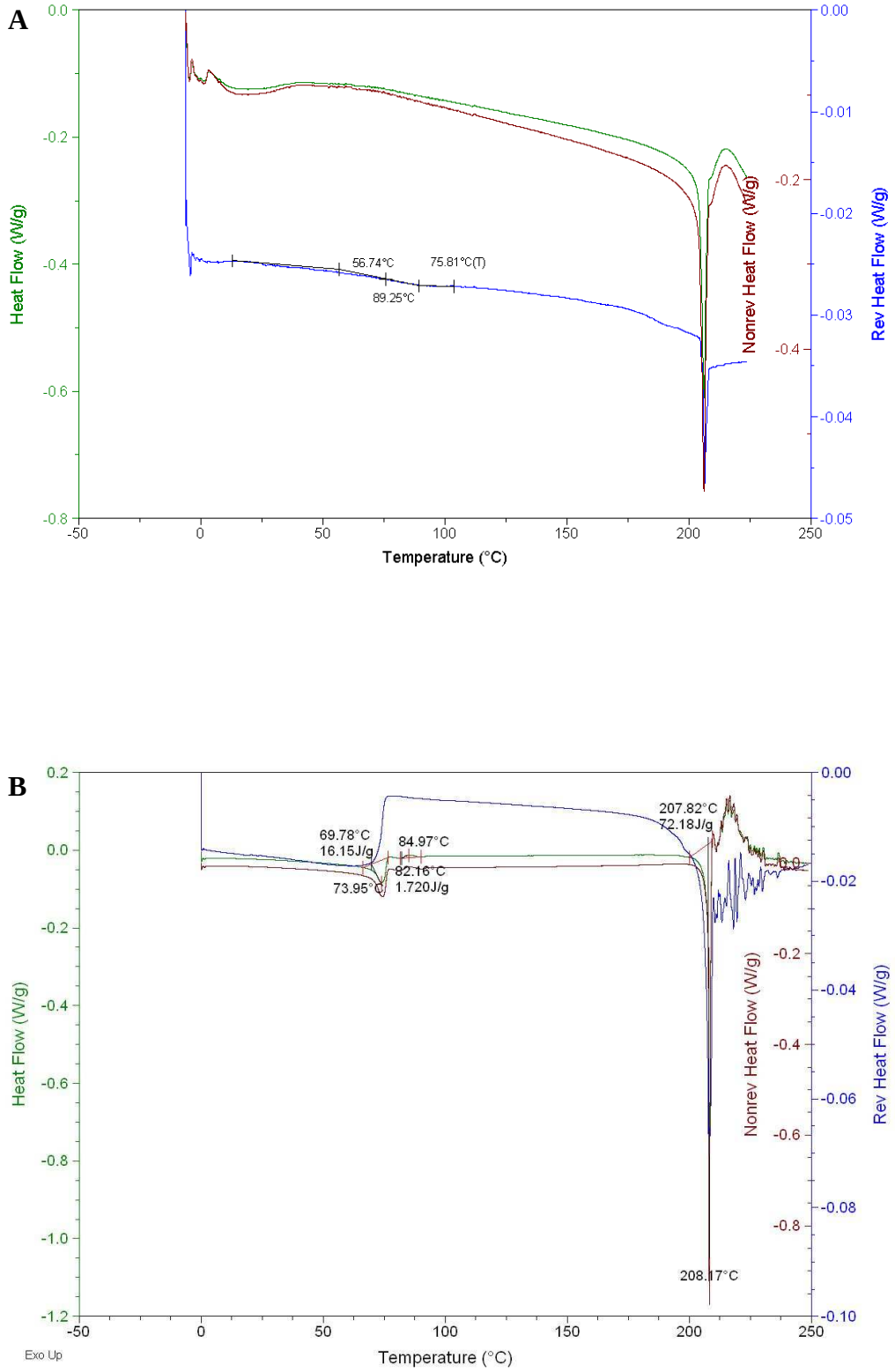

Figure 3-7: MDSC curves of A- Anhydrous BDP and B- BDP CFC-11 clathrate. All samples were heated to 250 °C.

CFC-11 clathrate, it can be seen that the heat flow curve shows the same transition as seen in standard mode DSC (Chapter 3, Section 3.3.4.2) with an exothermic peak at approximately 90 °C followed by an endothermic peak that confirms the release of CFC-11 from the crystal structure of the clathrate and then the last endothermic peak at 208 °C representing the melting of BDP. The non-reversing heat flow shows an endothermic onset followed by an exothermic onset at 80 °C. This shows a structural rearrangement/ recrystallization of the sample which is identical with the results obtained by conventional DSC (Chapter 3, Section 3.3.4.2).

In order to confirm that the release of the propellant from the clathrate structure is due to a structural rearrangement of the clathrate structure to the anhydrous from of BDP, an X-RPD pattern was taken after heating both anhydrous BDP and BDP CFC-11 clathrates to 150 °C as after this temperature both compound exhibit the same and only transition of melting. The X-RPD patterns obtained are shown in Figure 3-8 and compared to the calculated anhydrous BDP pattern. The crystal structural change was confirmed by X-RDP pattern obtained after heating BDP CFC-11 clathrate to 150 °C where the propellant was released from the crystal structure of the clathrate and these results showed that the compound present was pure anhydrous BDP due to the excellent match of both the obtained pattern of heated anhydrous BDP and BDP CFC-11 clathrate with the calculated pattern of anhydrous BDP. In conclusion from the results obtained in the sections above, the release of CFC-11 from the clathrate structure is undoubtly due to a structural rearrangement of clathrate structure to the anhydrous from of BDP that lead to the release of CFC-11.

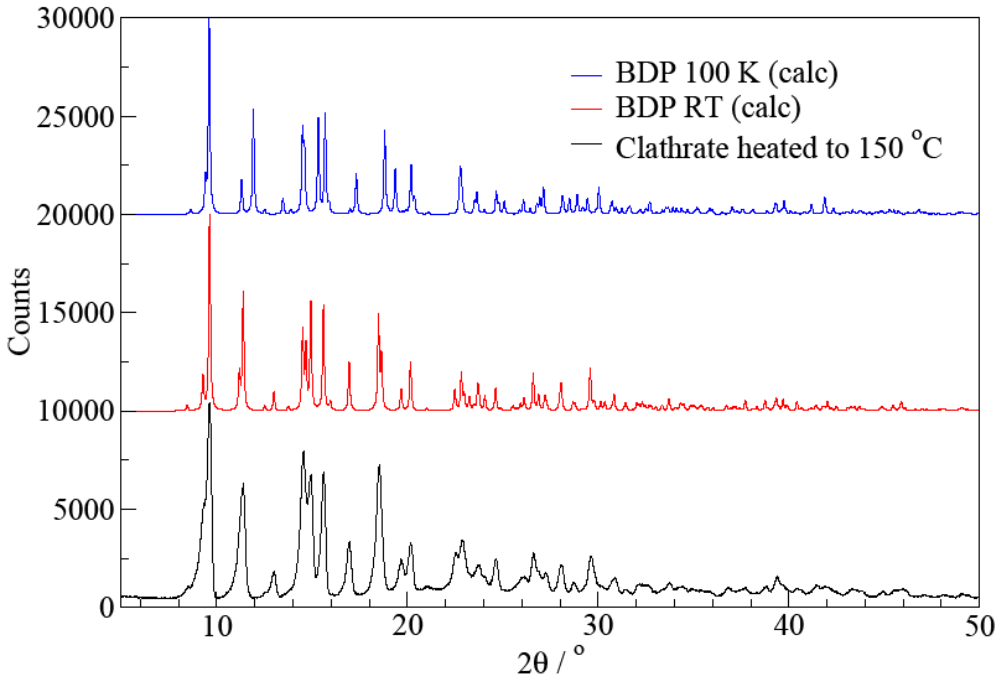

Figure 3-8: X-RPD patterns of heated anhydrous BDP and BDP CFC-11 clathrate.

3.3.6 VT-XRPD Results

Variable temperature XRPD analysis showed that the BDP CFC-11 clathrate entity was stable between room temperature and approximately 71 ºC (Fig. 3-9). No crystal transformation was observed between these temperatures. Further increases in temperature lead to transformation of BDP CFC-11 Clathrate to a different crystal form (Fig. 3-9A and 3-9B). The XRPD of this crystal form by heating BDP CFC-11 clathrate to >150ºC was comparable to the crystal structure of anhydrous BDP (Millard and Myrdal, 2002). Therefore, this confirmed the transformation of the clathrate to anhydrous BDP. The data in Figure 3-9 furthermore showed that melting and degradation process of BDP CFC-11 clathrate started at temperature approximately 210 °C. This degradation process was clearly illustrated by changes in the crystal structure observed at these

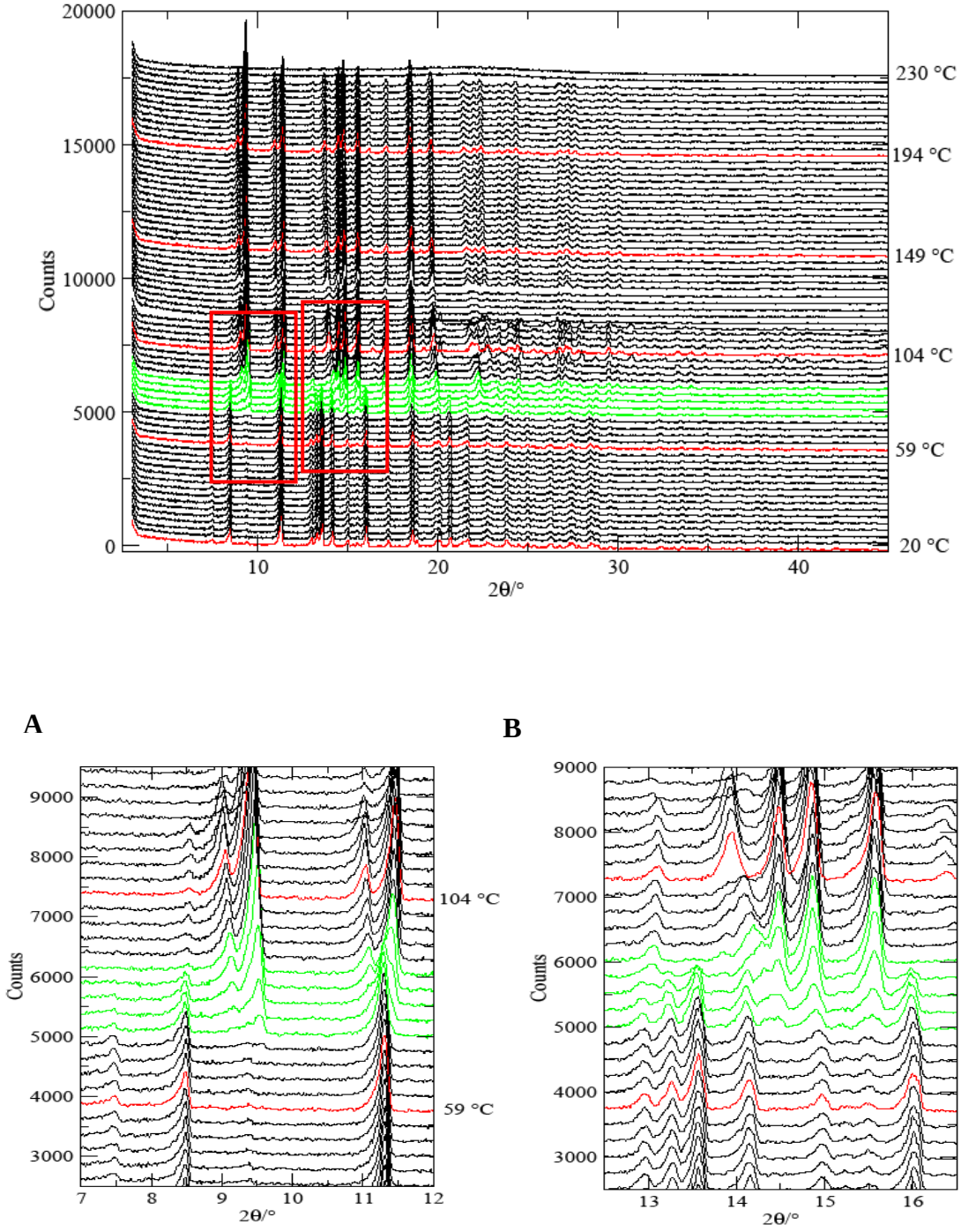

Figure 3-9: VT-XRPD patterns of BDP CFC-11 clathrates.. **A** and **B** are the magnified areas from lef to right respectively.

temperatures and by the formation of an amorphous form at higher temperatures (Fig. 3-9).

The pre-heated BDP CFC-11 clathrate heated to 150 ºC was analyzed upon a heating cycle consisting of cooling the entity to room temperature and then acquiring VT-XRPD patterns as described above. The results obtained are shown in Figure 3-10. The pattern confirmed the transformation of the clathrate to the anhydrous form of BDP upon heating to 150 ºC when comparing the XRPD pattern to the calculated pattern (Millard and Myrdal, 2002). Variable–temperature XRPD patterns obtained for the pre-heated clathrate indicated that the entity was stable through-out the heating cycle and that no crystal transformation was observed (Fig. 3-10). This confirms that the release of CFC-11 from the crystal structure of BDP CFC-11 clathrate and its subsequent transformation to the anhydrous BDP is an irreversible transformation and that no further transformation occurs with increasing temperatures. However, a slight shift of all the different peak of the patterns was observed to the left, an artefact due to thermal expansion. Figure 3-10 furthermore showed that melting and degradation process of BDP started at temperature above 226 ºC and illustrated the formation of an amorphous like crystal form at higher temperatures (Fig. 3-10).

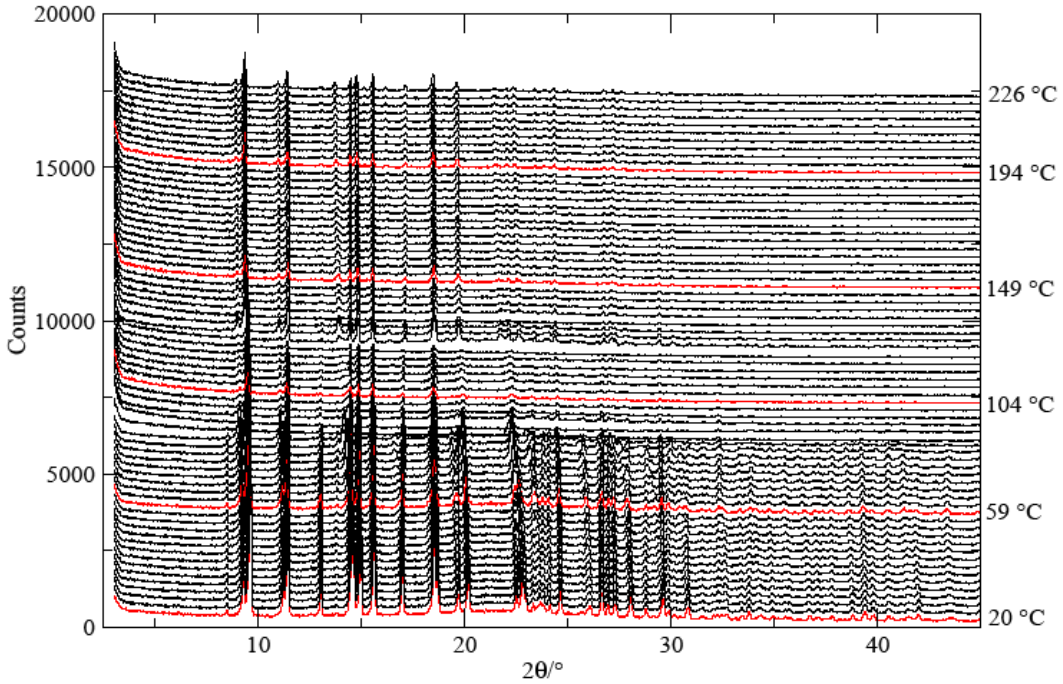

Figure 3-10: VT-XRPD patterns of BDP CFC-11 clathrate being heated to 150 ºC, cooled to room temperature and reheated to 250 ºC.

3.3.7 Raman Spectroscopy

Raman spectra of both anhydrous BDP and BDP CFC-11 clathrates were recorded in order to explore the potential of this technique in identifying clathrate formation and any structural changes accompanying the release of the propellant from the structure of the clathrate. Raman has recently intensively used as an analytical tool technology in identifying different analytical processes as well as different compounds (Jorgensen et al., 2002, Rantanen, 2007). Raman spectra for anhydrous BDP and BDP CFC-11 clathrate show a very different pattern (Fig. 3-11). The C-F peak for the BDP CFC-11 clathrate is shown at a Raman shift of 1005 cm^{-1}, which is not present in the anhydrous BDP spectra. Spectral differences between anhydrous BDP and BDP CFC-11 clathrates were also detected for the bands between 1600 and 1750 cm^{-1}. These can be assigned to the changes in the bonding structure of the carbonyl group in both anhydrous BDP and BDP CFC-11 clathrate as these are related to the interaction between the BDP molecules and the CFC-11 molecules within the clathrate structure proving that the carbonyl group is affected by the changes in the crystal packing. The intensity of peaks from 0-200 cm^{-1} (lattice vibration in crystals) show two different BDP entities with a high intensity for the BDP CFC-11 clathrate showing high crystallinity of the compound compared to the anhydrous BDP. These results confirm the formation of the clathrate and strengthen the results obtained using X-RDP due to the presence of the C-F peak confirming the enclathration and entrapment of the propellant molecules within the crystallized BDP molecules.

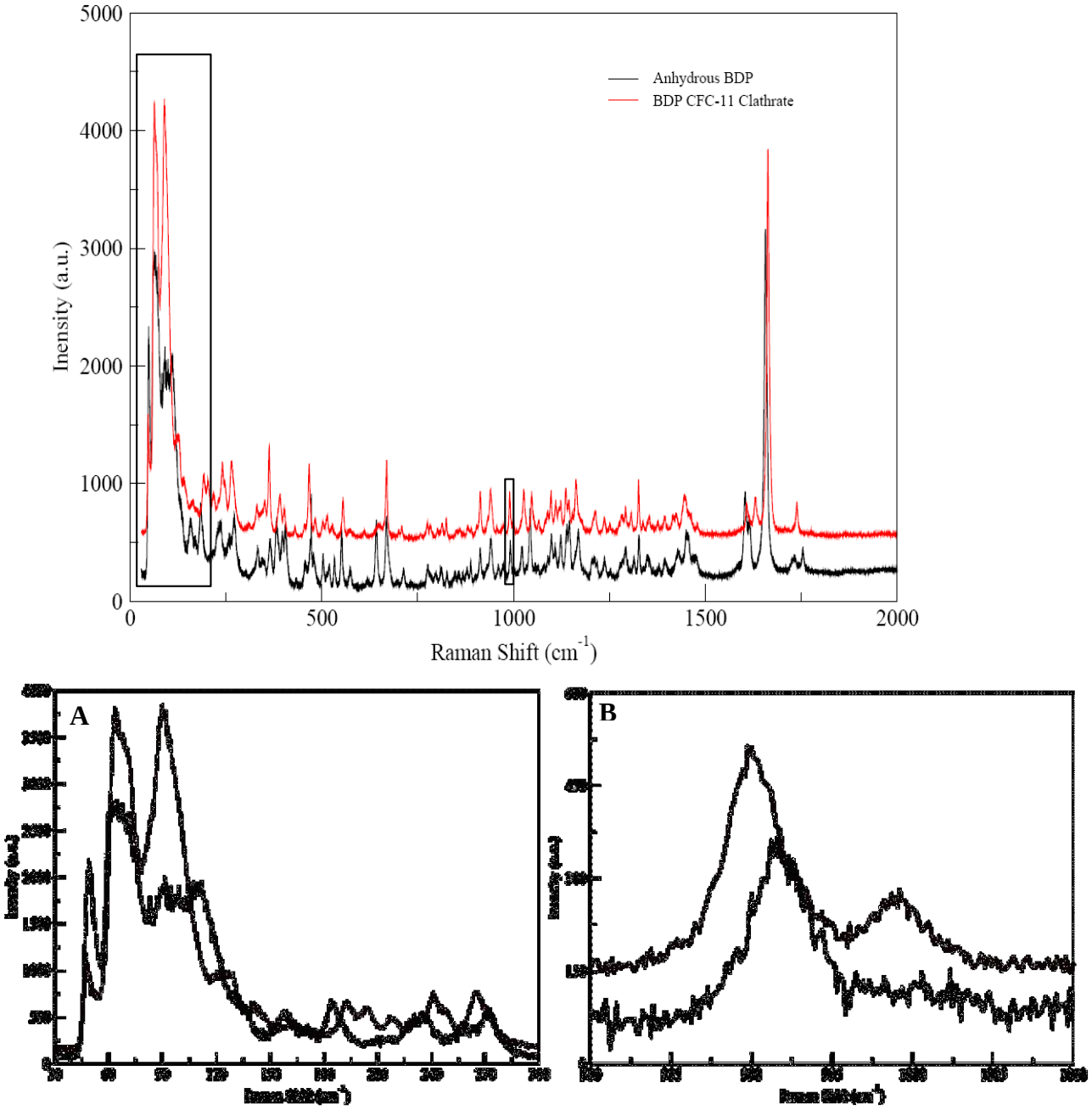

Figure 3-11: Raman spectrum of both anhydrous BDP and BDP CFC-11 clathrate A- Lattice vibration (0-200 cm^{-1}) and B- Fluorine Raman shift (980-1010 cm^{-1}).

3.3.8 Variable temperature Raman spectroscopy

From Figure 3-12 it can be observed that there are two different forms of the BDP before and after the temperature 90-100˚C. The initial material observed

corresponds to the BDP CFC-11 clathrate. Upon heating the Raman spectra obtained remained the same until reaching the region of 90-100ºC where a shift is observed as well as the removal of some peaks that were presents before reaching that temperature in the Raman spectrum.

Areas from the spectra (phonon, hydroxyl and carbonyl regions) were chosen separately in order to emphasis the different shifts observed when heating BDP CFC-11 clathrate (Fig. 3-12). The phonon region from 0-200 cm^{-1} showed a clear shift is observed at 90˚C showing a change in the nature of the crystal form of the BDP CFC-11 clathrate. An increase in intensity of the peaks in this region is also observed as well as peak splitting at 250 cm^{-1} and 350 cm^{-1} showing changes occurring to the vibrational stretching, hence, a change in the molecular bonding of the BDP CFC-11 clathrate molecules. The shifts are more pronounced at the carbonyl Raman shift at 1650 cm^{-1} and the hydroxyl Raman shift of 3000 cm^{-1} as these are involved in holding the clathrate structure via hydrogen bonding between the BDP molecules and the CFC-11. A peak that was present at 3500 cm^{-1} in the BDP CFC-11 clathrate spectra (hydroxyl region) disappeared after reaching 90˚C emphasising the structural changes in terms of molecular bonding occurring to the BDP CFC-11 clathrate upon heating and the subsequent removal of the CFC-11 propellant from within the crystal structure of the clathrate. These changes are also observed at the carbonyl region where a peak at 1600 cm^{-1} showed an increase in intensity after reaching 90˚C and the splitting of a peak that was observed at 1750 cm^{-1} Raman shift. The different changes in the Raman shifts can be attributed to structural rearrangement of the

crystal structures that result from the release of the CFC-11 molecules from the crystal structure of the crystallized BDP.

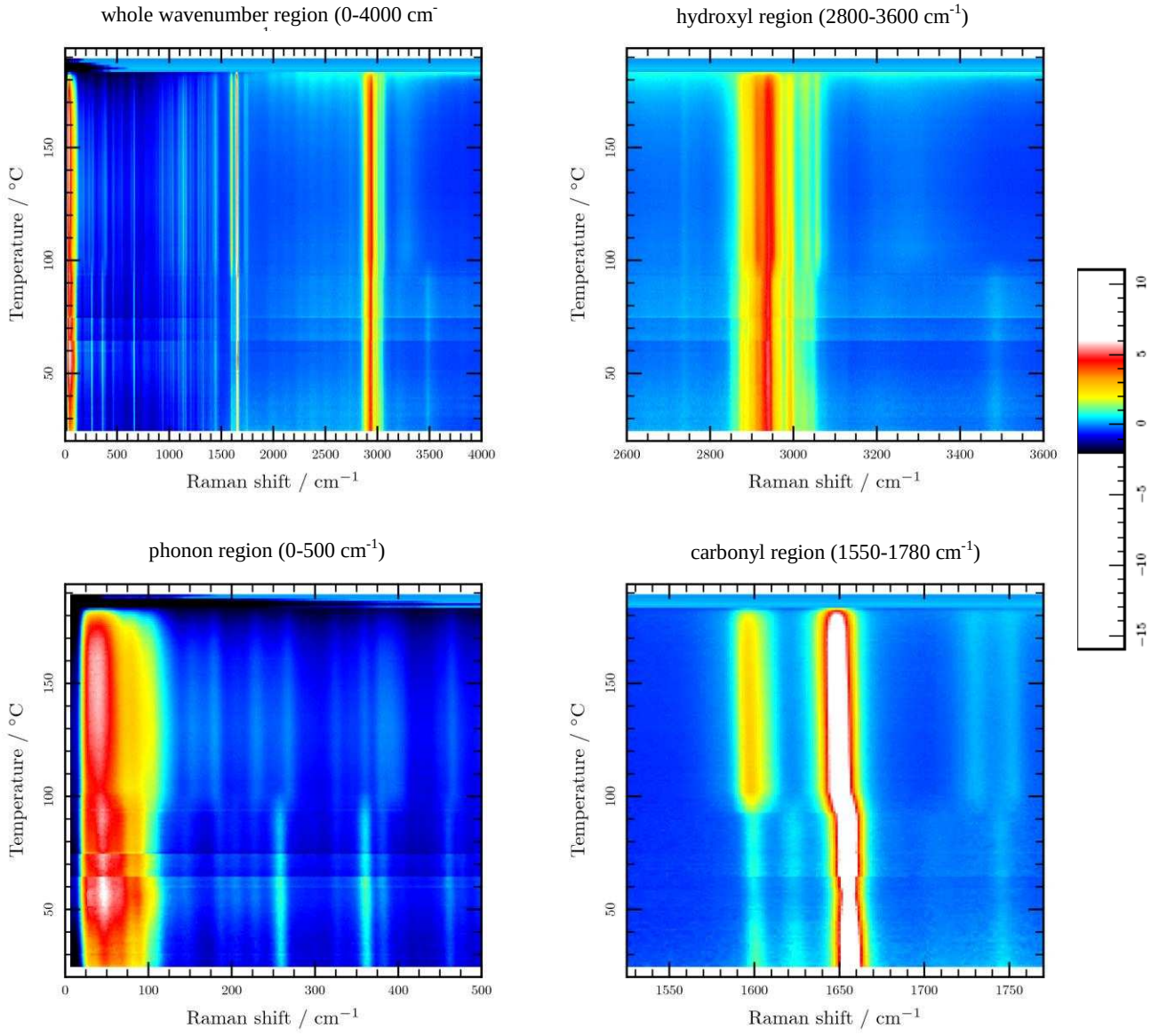

Figure 3-12: 3D plot of BDP CFC-11 clathrate spectra using hot stage VT-Raman spectroscopy

The carbonyl peak was chosen for further data interpretation showing change in Raman shift position as well as the width of peak as it is used as a H-bonding in the reported crystal structure (Harris et al., 2003). A shift is observed in the position of the carbonyl group between 90-100˚C as well as a change in the width of the peak (Fig. 3-13). The change in the carbonyl peak position is due a

solid state rearrangement of the structure which is in agreement with the results obtained with the thermal analysis techniques due to the removal of the CFC-11 propellant from within the crystal structure of the clathrate resulting in anhydrous BDP as an end product. The continuous change of peak width with temperature is due to dynamic disorder (vibrations of the molecules) which increases as the sample is heated.

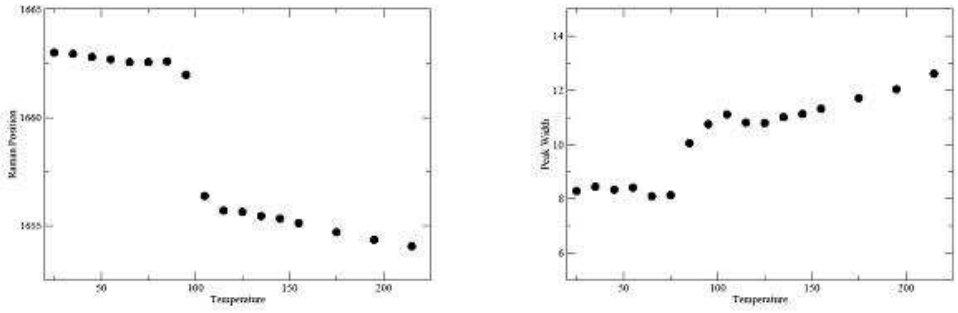

Figure 3-13: Changes in Raman shift and width of the carbonyl group peak of BDP CFC-11 clathrate with increased temperature using hot stage Raman Spectroscopy.

3.4 Conclusions

BDP CFC-11 clathrate has been synthesized and characterised in order to investigate the potential benefits of clathrate formation in metered dose inhaler formulations. The BDP CFC-11 clathrate was produced by suspending BDP in CFC-11 which led to a rapid formation of the clathrate. The results obtained using different techniques shows an efficient growth of the clathrate with the different concentrations used for the study. The highest molar ratio of CFC-11 to BDP was obtained with a 1.67% w/w BDP in CFC-11 and of 0.6:1 molar ratio. It is shown that the presence of a stoichiometric relationship can be observed. The release of the propellant from the structure was induced by heating which is

proposed to be due to a structural rearrangement of the clathrate. It is understood that this structural rearrangement induces changes in the hydrogen bonding holding the clathrate from collapsing or decomposing that leads to the release of the propellant from the tunnels constituting the structure of the clathrate.

3.5 References

BUFFETT, B. A. (2000) Clathrate Hydrates. Annual Review of Earth and Planetary Science, 28**,** 477-507.

DESIRAJU, G. R. (2007) Crystal Engineering: A Holistic View. Angewandte Chemie International Edition in English, 46**,** 8342-8356.

DUAX, W. L., CODY, V. & STRONG, P. D. (1981) Structure of the Asthma Drug Beclomethasone Dipropionate. Acta Crystallographica Section B-Structural Science, 37**,** 383-387.

ENGLEZOS, P. (1993) Clathrate Hydrates. Industrial & Engineering Chemistry Research, 32**,** 1251-1274.

GOLDBERG, I. (1988) The Significance of Molecular Type, Shape and Complementarity in Clathrate Inclusion. Topics in Current Chemistry, 149**,** 1-44.

HANCOCK, B. C. & ZOGRAFI, G. (1997) Characteristics and significance of the amorphous state in pharmaceutical systems. Journal of Pharmaceutical Sciences, 86**,** 1-12.

HARRIS, J. A., CARDUCCI, M. D. & MYRDAL, P. B. (2003) Beclomethasone dipropionate crystallized from HFA-134a and ethanol. Acta Crystallographica Section E, 59**,** 1631-1633.

HIMES, V. L. & MIGHELL, A. D. (1987) Nbs Crystal Data - Compound Identification and Characterization Using Lattice-Matching Techniques. Journal of Metals, 39**,** A29-A29.

HOFMANN, D. W. M. (2002) Fast estimation of crystal densities. Acta Crystallographica Section B-Structural Science, 58**,** 489-493.

JORGENSEN, A., RANTANEN, J., KARJALAINEN, M., KHRIACHTCHEV, L., RASANEN, E. & YLIRUUSI, J. (2002) Hydrate formation during wet granulation studied by spectroscopic methods and multivariate analysis. Pharmaceutical Research, 19**,** 1285-1291.

KOH, C. A. (2002) Towards a fundamental understanding of natural gas hydrates. Chemical Society Reviews., 31**,** 157-67.

KUEHL, P. J., GARDUCCI, M. D. & MYRDAL, P. B. (2003) An ethanol solvate of beclomethasone dipropionate. Acta Crystallographica Section E, 59**,** 1888-1890.

KUHS, W. F., CHAZALLON, B., RADAELLI, P. G. & PAUER, F. (1997) Cage occupancy and compressibility of deuterated N-2-clathrate hydrate by neutron diffraction. Journal of Inclusion Phenomena and Molecular Recognition in Chemistry, 29**,** 65-77.

LE-BAIL, A., DUROY, H. & FOURQUET, A. J. L. (1988) Ab-initio structure determination of $LiSbWO_6$ by X-ray powder diffraction. Material Research Bulletin**,** 447-452.

MILLARD, J. W. & MYRDAL, P. B. (2002) Anhydrous beclomethasone dipropionate. Acta Crystallographica Section E-Structure Reports Online, 58**,** O712-O714.

PATCHKOVSKII, S. & TSE, J. S. (2003) Thermodynamic stability of hydrogen clathrates. Proceedings of the National Academy of SciencesU S A, 100**,** 14645-50.

PHILLIPS, E. M. & BYRON, P. R. (1994) Surfactant promoted crystal growth of micronized methylprednisolone in trichloromonofluoromethane. Internation Journal of Pharmaceutics, 110**,** 9-19.

PLUMRIDGE, T. H. & WAIGH, R. D. (2002) Water structure theory and some implications for drug design. Journal of Pharmacy and Pharmacology, 54**,** 1155-79.

RANTANEN, J. (2007) Process analytical applications of Raman spectroscopy. Journal of Pharmacy and Pharmacology, 59**,** 171-177.

SHAH, B., KAKUMANU, V. K. & BANSAL, A. K. (2006) Analytical techniques for quantification of amorphous/crystalline phases in pharmaceutical solids. Journal of Pharmaceutical Sciences, 95**,** 1641-65.

VAIDYA, S. (2004) Clathrates - An Exploration of the Chemistry of Caged Compounds. Resonance, 9**,** 18 - 31.

VERVAET, C. & BYRON, P. R. (1999) Drug-surfactant-propellant interactions in HFA-formulations. International Journal of Pharmaceutics, 186**,** 13-30.

ZIMMERMANN, A., TIAN, F., LOPEZ DE DIEGO, H., FRYDENVANG, K., RANTANEN, J., RINGKJOBING ELEMA, M. & HOVGAARD, L. (2008) Structural Characterisation and Dehydration Behaviour of Siramesine Hydrochloride. Journal of Pharmaceutical Sciences, 98**,** 3596-3607.

Chapter 4 Physico-chemical characterization of hydrofluoroalkane propellant clathrate formed in a pressurised metered dose inhaler

4.1 General Introduction

The physicochemical properties of steroids are widely studied in pharmaceutical contexts. Steroids tend to crystallise fairly easily and often exhibit inclination to polymorphism as well as solvation and hydration depending on the media they are formed in. Such phenomena can have a drastic effect on product performance and on the nature of the formulation employed (Othman et al., 2008).

Metered dose inhalers can be formulated as either a suspension or a solution of drug in propellant, depending on the solubility of the active substance in the propellant-excipient mixture. Suspensions have the advantage of chemical stability and delivery of greater mass per unit volume compared to solutions. However, they have to be carefully formulated so that the physical stability is controlled throughout their lifetime. The potential for crystal growth, solvate formation or polymorph interconversion must be fully addressed early in the formulation development (Byron, 1992, McDonald and Martin, 2000).

Ethanol is a commonly used co-solvent in pMDI systems. It is employed to increase the solubility of several APIs otherwise insoluble in HFA propellants, hence, stabilizing the pMDI performance. Also, it used to help in the normal functioning of the valve. Ethanol has a number of advantages as a co-solvent

because it is cheap, slightly dipolar and fully miscible in HFA liquids (Smyth, 2003). The use of ethanol is most likely incompatible with HFA propellant suspension formulations as drug solubility will also be promoted (Smyth, 2003). The resulting increase in drug solubility can promote partial drug dissolution and crystal growth. Moreover, the raised API solubility may lead to an increase in the chemical instability of the API. Such induced crystal instability problems are often encountered during storage of suspension formulations and are to be controlled to ensure the performance and the quality of the pharmaceutical preparations (Vervaet and Byron, 1999a).

During a crystallisation process, solvent molecules may become incorporated into the crystal structure of APIs (Zimmermann et al., 2008). Changing the arrangement of the molecules in the crystal lattice generally alters solid state properties of APIs such as solubility and stability. The solubility of the different API will affect the bioavailability of the formulation as well as its stability and shelf life during storage.

As described in the literature and in Chapter 3, BDP crystallizes with a channel structure allowing the formation of clathrate with propellant molecules as well as co-solvent molecules if present within its crystal structure (Harris et al., 2003). The structure is held together through hydrogen bonding (Harris et al., 2003). It has been reported that a BDP clathrate from HFA-134a and ethanol was formed, when BDP was suspended in a pMDI formulation containing HFA-134a and ethanol as a co-solvent (Harris et al., 2003). Jones et al have reported that the solubility of the BDP to be 29.85 µg/g in HFA 134a (Jones et al, 2006). Thus,

the formation of such crystals can be problematic especially if the particle size changes in the pMDI canister, as well as in terms of their solubility and stability in the formulation and their long term stability. Thereby, previous knowledge of the possible solid forms of a drug is of vital importance in the development of pharmaceutical drug products and drug substances (Zimmermann et al., 2008).

4.1.1 Chapter Aims and Objectives

This chapter will investigate and characterise the physico-chemical properties of the resulting beclomethasone dipropionate crystals formed upon exposure of the latter to both 1,1,2,-tetrafluoroethane (HFA-134a) and 1,1,2,3,3,3-heptafluoropropane (HFA-227ae) propellants alone and in the presence of a co-solvent (ethanol). X-ray photoelectron spectroscopy (XPS) and X-ray powder diffraction (X-RPD) will be used to determine the surface chemistry and the purity of the samples. Additionally, thermal analysis will be used to determine the phase behaviour of the extracted crystals upon heating and any subsequent polymorphism. Finally variable temperature X-ray diffraction will be used to determine the chemistry changes on the clathrate resulting from heating the clathrate to its melting point. From these results, it will be possible to characterise the BDP clathrate and determine the effect of any changes on the chemistry and on the potential interactions within a pMDI.

4.2 Materials and Methods:

4.2.1 Materials

Anhydrous BDP (micronized) was purchased from Sicor (UK). 1,1,1,2-Tetrafluoroethane (HFA-134a) and 1,1,2,3,3,3-heptafluoropropane (HFA-227ae) were supplied by Dupont (UK). All other chemicals were purchased from Sigma-Aldrich Company Ltd (UK), unless otherwise indicated.

4.2.2 Methods

4.2.2.1 Isolation of Beclomethasone HFA Propellants Clathrate

4.2.2.1.1 BDP in HFA-134a

Beclomethasone dipropionate was suspended in HFA-134a (1.67 % w/w BDP in HFA-143a) in six clear PET vials (Precise Plastic Ltd, UK). BDP was weighed in each of the clear PET vials and a non-metering valve (3M Health Care Ltd, UK) was crimped in place in each of the vials. HFA-134a was then pressure transferred via a transfer button into each vial from a Trimline can (Crown Holdings Inc, UK) fitted with a 1-inch non-metering valve (Precision Valve Corporation, UK). The concentration of the API was 2% w/w BDP in HFA-134a. The six filled clear PET vials were stored in a desicator under no humidity for a period of six months. The crystals were then extracted by evaporating the propellant in a humidity controlled environment (RH = < 10%) at ambient pressure and room temperature. The extracted crystals were stored in glass vial

under nitrogen after being sealed with a vial screw and Parafilm (Alcan, Neenah, WI, US), and stored in a fridge at 5°C prior to use.

4.2.2.1.2 BDP in 20 %w/w EtOH and HFA-134a

BDP was suspended in HFA-134a (1.67 % w/w BDP in HFA-143a) with the addition of 20% w/w absolute anhydrous ethanol following the procedure described above.

4.2.2.1.3 BDP in HFA-227ae

BDP was suspended in HFA-227ae (1.67 % w/w BDP in HFA-227ae) as described in section 4.2.2.1.1.

4.2.2.1.4 BDP in 20% EtOH and HFA-227ae

BDP was suspended in HFA-227ae (1.67 % w/w BDP in HFA-227ae) with the addition of 20% w/w absolute anhydrous ethanol following the procedure described above in section 4.2.2.1.1.

4.2.2.2 Scanning Electron Microscopy (SEM)

The particle size and morphology of the synthesized BDP entities from the different HFA and HFA EtOH blends were analysed by SEM using a JEOL JSM-6060LV (JEOL (UK) Ltd, Welwyn Garden City, UK) at various magnifications. The BDP particles isolated as previously described were

mounted onto carbon stubs then sputter coated with a thin layer of gold (20 nm thickness) in an argon atmosphere (50Pa) at 30 mA for 4 minutes prior to SEM screening. SEM analysis was carried out at an appropriate accelerating voltage (between 1 keV and 10 keV) and a spot size between 48 nm and 62 nm. These parameters were varied for each sample in order to optimise each particular image.

4.2.2.3 X-ray Photoelectron Spectroscopy (XPS)

BDP HFA-134a, BDP HFA-227ae, BDP EtOH HFA-134a and BDP EtOH HFA-227ae samples were analysed using XPS in order to determine surface elemental composition using a Kratos AXIS ULTRA spectrometer (Kratos Analytical, Manchester, UK). The spectrometer is supplied with a mono-chromatic Al Kα X-ray source (1486.6eV) operating at 15mA emission current and 10kV anode potential. The ULTRA was used in fixed analysed transmission (FAT) mode, with a pass energy of 20eV for high resolution scans. A wide survey scan and high resolution scans were performed on each sample. Wide scans were run for 5-10 minutes and high resolution scans for 10-30 minutes. Data analysis was carried out using CASAXPS software with Kratos sensitivity factors to determine the atomic percentage (atomic %) values from the peak areas. The irradiating X-rays were emitted at a take-off angle of 90 degrees.

4.2.2.4 Thermogravimetric analysis (TGA)

A TGA Q500 (TA Instruments, USA) was used to record the weight loss of the samples between 20˚C and 250˚C at a scan speed of 10˚C/min under a constant purge of dry nitrogen. An isothermal period at 25˚C was run for 5 minutes prior to the measurements, during which any changes in weight were monitored. In all measurements, 6 to 7mg of sample was used. The thermograms obtained from the TGA results were analysed using TA universal analysis -NT software.

4.2.2.5 Differential Scanning Calorimetry (DSC)

DSC experiments were carried out using a DSC Q2000 Differential Scanning Calorimeter (TA Instruments, USA), with a constant 10˚C/min heating rate, from 25˚C to 250˚C in a dry nitrogen atmosphere. In all measurements 6-7mg of sample were used in pin-holed sealed non-hermetic aluminium pans to allow the escape of the propellant during the desolvation phase. The thermograms obtained for the DSC results were analysed using TA universal analysis -NT software.

4.2.2.6 X-ray Powder Diffraction (X-RPD)

X-RPD patterns were collected on a Bruker D8 diffractometer system (Bruker AXS, Madison, WI, USA), operating in a Debye-Scherrer geometry. A ceramic X-ray tube with a copper target, was used to generate x-ray radiation at wavelength λ= 1.54059 Å. The generator was set to operate at a voltage of 40 kV and current of 40 mA. A scintillation counter was employed. Samples were scanned from 2θ= 5˚ until 45˚ at a 1sec/step speed in increments of 0.02˚

stepwise. The X-ray patterns were analysed using the Le Bail method to model the patterns obtained, based on the reported unit cell for the clathrate. All the patterns were collected straight after the formation of the crystals to determine the purity of the samples and its crystalline structure.

4.2.2.7 Variable Temperature X-Ray Powder Diffraction (VT-XRPD)

VT-XRPD patterns were collected on a Bruker D8 diffractometer system (Bruker AXS LTD., Coventry, UK) operating in a Debye-Scherrer geometry. X-ray radiation was generated inside a ceramic X-ray tube from an anode made of copper Cu in Kα spectral line at wavelength λ= 1.54059 Å. The diffractometer is equipped with a scintillation detector and Bruker Kristalloflex generator set on voltage 40kV and current 40mA. Samples were loaded in borosilicate glass capillary tubes BGCT with 0.7mm bore diameters (CTS Capillary Tube Supplies Ltd UK) and mounted on the goniometer in a preferable orientation. Cryostream Plus controller (Oxford Cryosystems Ltd., Long Hanborough, Oxford, UK) a heating-cooling system was provided for VT-XRPD, was controlled by a Cryopad PC programme for VT-XRPD scans. VT-XRPD scans were set from 2θ= 5˚ until 45˚ at a 1sec/step speed in increments of 0.02˚, acquired each 3˚ C from heated sample at a rate of 1˚ C/min starting from 20-221˚ C at a rate of a 1˚ C/min. All the patterns were collected straight after the formation of the crystals to prevent any decomposition and/or contamination and to determine the purity of the samples and its crystalline structure.

4.3 Results and Discussion

4.3.1 SEM Analysis

Concerning the morphology of BDP HFA-134a crystals, the SEM images in Figure 4-1 show the formation of crystalline particles. The particles are mostly aggregated into small clusters and do not show significant poly-dispersity. The crystals particle size could not be really identified due to aggregation. However, the crystals seem to have a particle size of approximately 10µm. On the other hand, the particles obtained for BDP HFA-227ae suspension, had a size of less than 5 µm (Fig. 4-1).

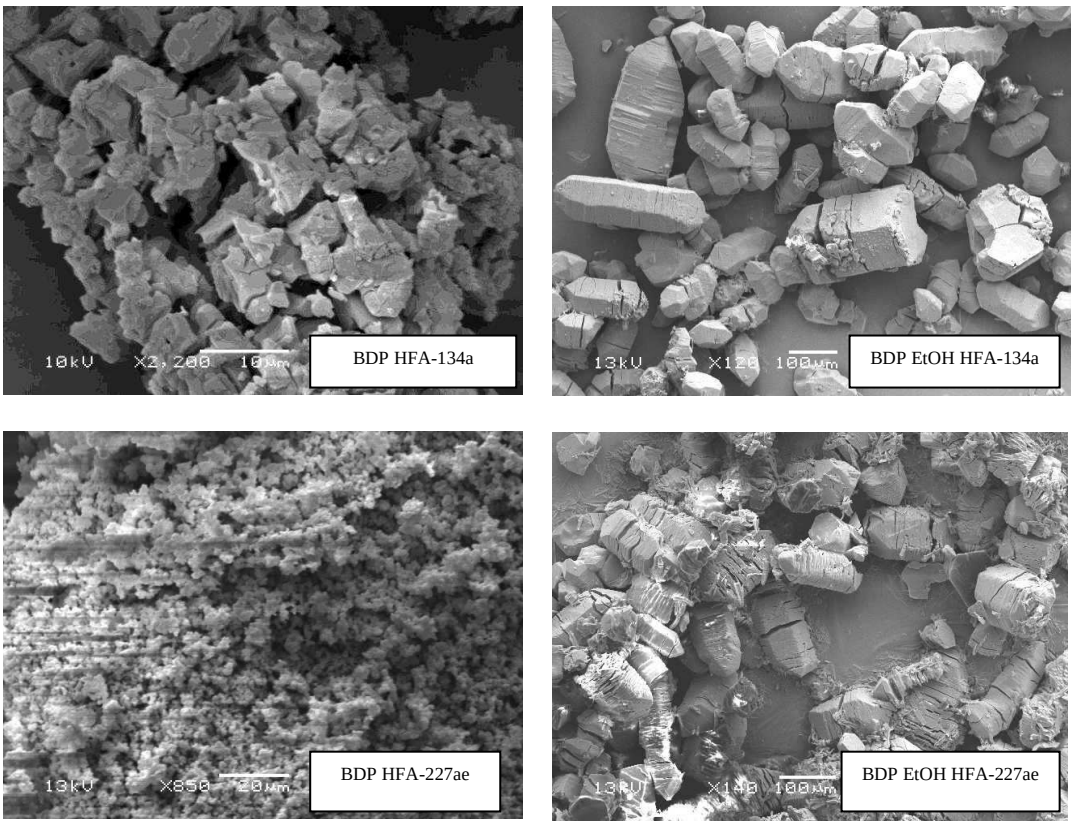

Figure 4-1: SEM images of BDP HFA-134a crystals, BDP EtOH HFA-134a crystals and BDP HFA-227ae crystals and BDP EtOH HFA-227ae crystals.

The crystals obtained from both suspensions of BDP EtOH HFA-134a and BDP EtOH HFA-227ae had an elongated hexagonal structure as seen in Figure 4-1. The particle size obtained for the crystals ranged between 50-100 µm. A feature that is only observed in these crystals is the crystal defects on the surface of the crystals as well as small cracks on the majority of the crystals. Such observations might be either due to decomposition of the crystals due to the exposure to the high vacuum medium during the gold coating and imaging with SEM or due to the collapse of the clathrate structure and the release of the propellant from the channels of BDP clathrates after the release from the pMDI canister.

4.3.2 XPS Results

The four different crystals extracted from the different BDP HFA and EtOH suspensions were analysed using XPS in order to determine the elemental surface composition of each of the compounds and in particular HFA/Ethanol inclusion. Wide scan XPS results obtained for the BDP HFA-134 in Figure 4-2, BDP HFA-227ae, BDP EtOH HFA-134a and BDP EtOH HFA-227ae crystals are shown in Appendix 1. The main peaks shown on the different scans at 282, 530 and 197 eV correspond to oxygen, carbon, and chlorine respectively. These elements constitute the backbone structure of BDP.

No fluorine peaks were observed in any of the different BDP HFA entities. This can be explained by either no formation of clathrate or instant decomposition of these after being at ambient pressure and room temperature. Another possible

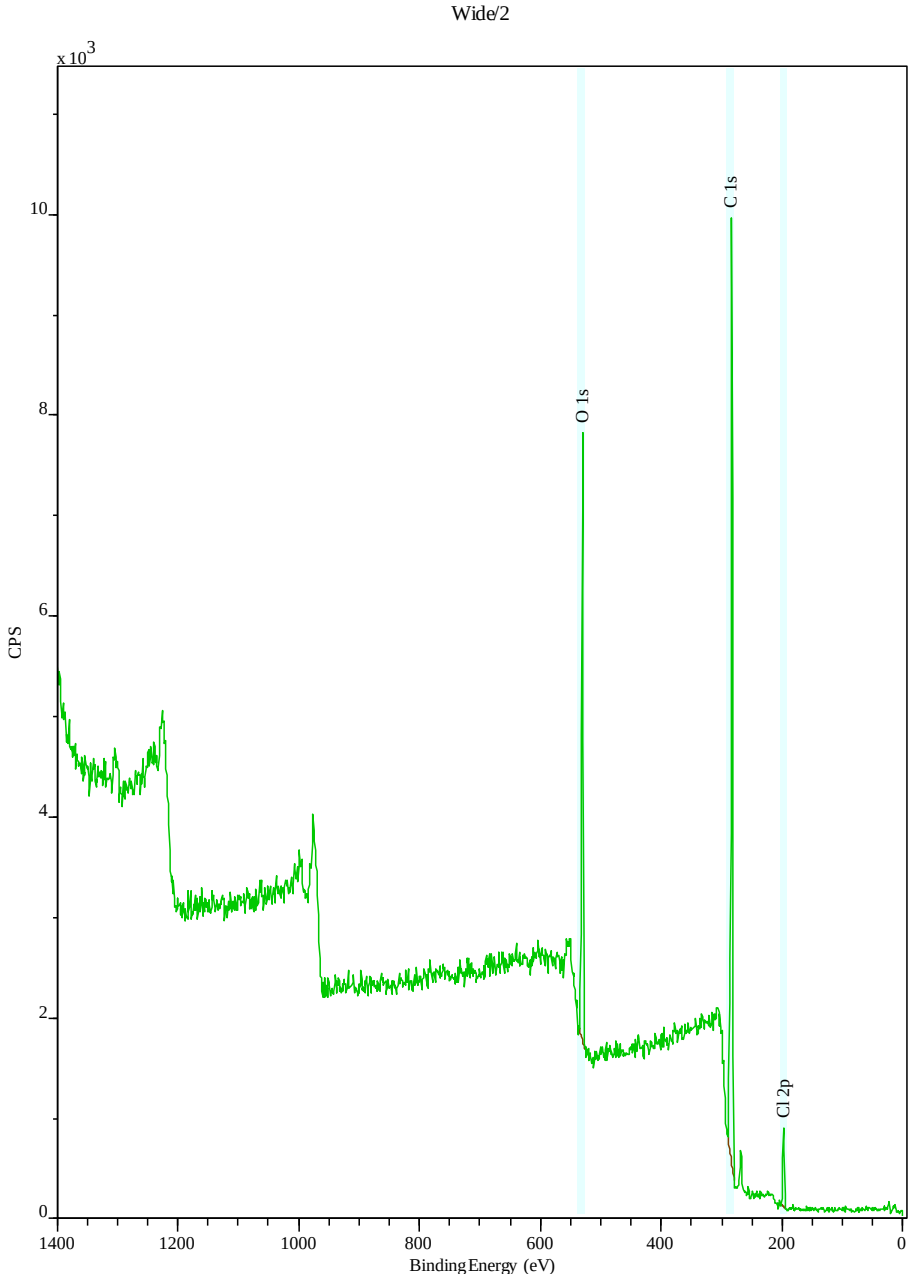

Figure 4-2: Wide survey scans of BDP HFA-134a crystals. (Similar patterns were obtained for the different BDP HFA/Ethanol propellants (Appendix 1)).

Table 4-1: Theoretical and measured atomic percentage of the surface analysis of BDP HFA-134a, BDP HFA-227ae, BDP EtOH HFA-134a and BDP EtOH HFA-227ae (n= 6).

Atomic %	**BDP HFA-134a**		**BDP HFA-227ae**		**BDP EtOH HFA-134a**		**BDP EtOH HFA-227ae**	
	Theoretical	**Measured**	**Theoretical**	**Measured**	**Theoretical**	**Measured**	**Theoretical**	**Measured**
C 1s	71.42	81.33 ± 0.7	67.38	81.08 ± 1	71.1	80.79 ± 0.75	67.34	81.42 ± 037
O 1s	16.16	16.52 ± 0.64	15.21	16.79 ± 0.21	17.77	16.94 ± 0.57	16.32	16.54 ±0.33
Cl 2p	2.38	2.15 ± 0.13	2.17	2.13 ± 0.21	2.22	2.28 ± 0.21	2.04	2.04 ± 0.1
F 1s	9.52	0	15.21	0	8.88	0	14.28	0

explanation might be that the HFA molecules are within different particles of the powder mixture and these could not have been detected by the instrument as it just detects up to 10 nm in depth of the structure. The surface composition of the different BDP HFA entities did not show any significant changes in the atomic percentage of all the atoms present in the structure between the different crystals (Table 4-1). Therefore, the two different HFA propellants may have not been included within the channels of the crystallized BDP. However, as observed with the different SEM images above, a possible structural change could have occurred due to the changes in the pressure. Also, the different atomic percentages observed for the different BDP HFA entities showed very close similarities to the percentage atomic composition of anhydrous BDP (Chapter 3). Therefore, these might suggest unsatisfactory results concerning the formation of possible clathrates from HFA propellants and ethanol HFA propellants.

4.3.3 Thermal Analysis

4.3.3.1 TGA Results

No weight loss was observed for anhydrous BDP between 0 and 212˚C (Fig. 4-3A). The weight loss observed after 212ºC (i.e. the melting point) is due to combustion of the sample in all the TGA curves. The total weight loss of the crystals extracted from the suspension of BDP in HFA-134a showed a total weight loss of approximately 13.25% as shown in Figure 4-3B. The weight loss is seen as three different phases that were observed using DSC and are going to be discussed further on the next section. The initial weight loss of approximately

6% was observed between 25 and 30 ºC which is believed to be an initial release of HFA-134a from the crystal structure of the BDP due to the high volatility of the propellant (-26.3 ºC boiling point) (Vervaet and Byron, 1999a, Millard and Myrdal, 2002, Harris et al., 2003). A second phase of weight loss of 5.5% was observed between 30 and 60 ºC which followed by the final phase of weight loss which ended at 125 ºC corresponding to a 2% weight loss. The two last phases of weight loss are thought to be due to the final release of HFA-134a from the crystal lattice of BDP leaving the entity as anhydrous BDP. The results observed using TGA suggest the formation of a crystalline clathrate from suspending BDP in HFA-134a. The TGA results were also used in order to determine the number of HFA-134a molecules in the crystal structure For BDP suspended in HFA-134a, it was calculated that the molecular ratio was of 0.75:1 HFA-134a to BDP. The molecular ratio of the calculated BDP HFA-134a clathrate is lower that the theoretical one. However, the percentage weight loss confirms the inclusion of the HFA-134a inside the crystal lattice of BDP.

When analysing the results from BDP suspended in HFA-227ae, Figure 4-3B shows no weight loss when heating the sample to 250 ºC apart from the weight loss seen after the melting point of BDP and at the point of combustion of the sample. Therefore, this shows that there is no transformation occurring within the structure of BDP when suspended in HFA-227ae and hence no clathrate or solvate formation as been achieved and the structure of BDP remains as anhydrous BDP.

A

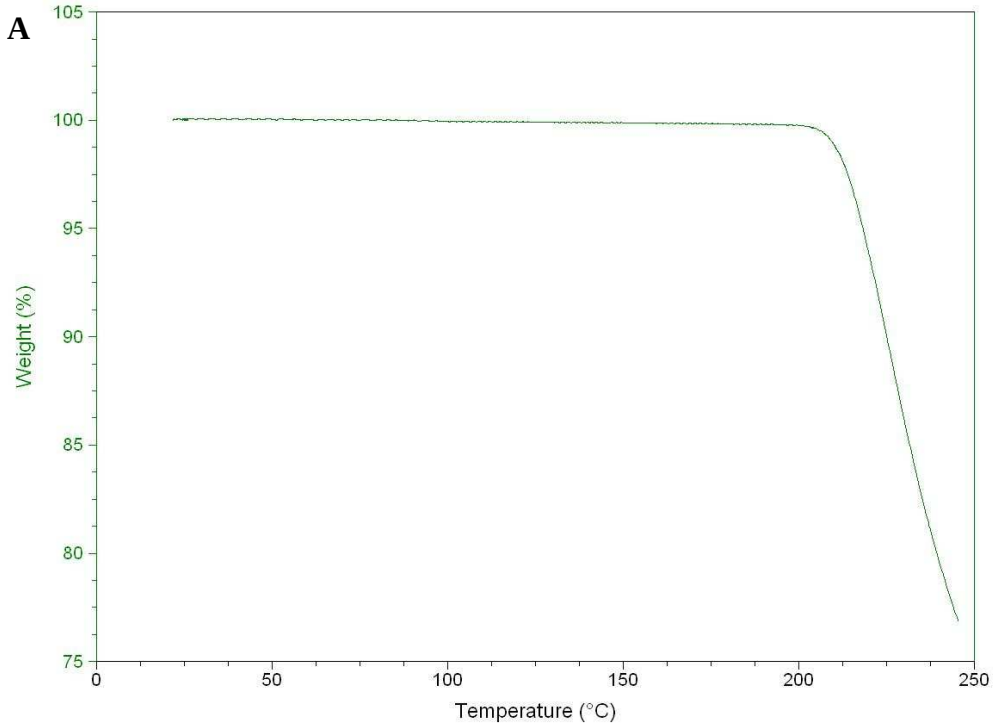
105
100
95
90
85
80
75
Weight (%)
0
50
100
150
200
250
Temperature (°C)

B

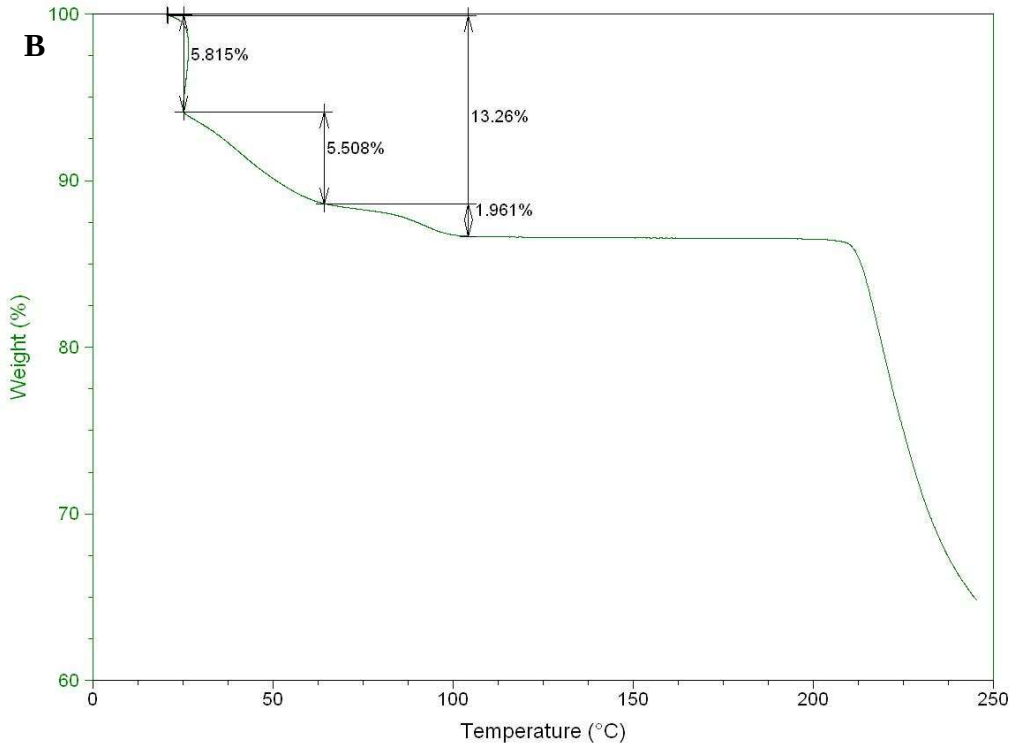
100
90
80
70
60
Weight (%)
5.815%
13.26%
5.508%
1.961%
0
50
100
150
200
250
Temperature (°C)

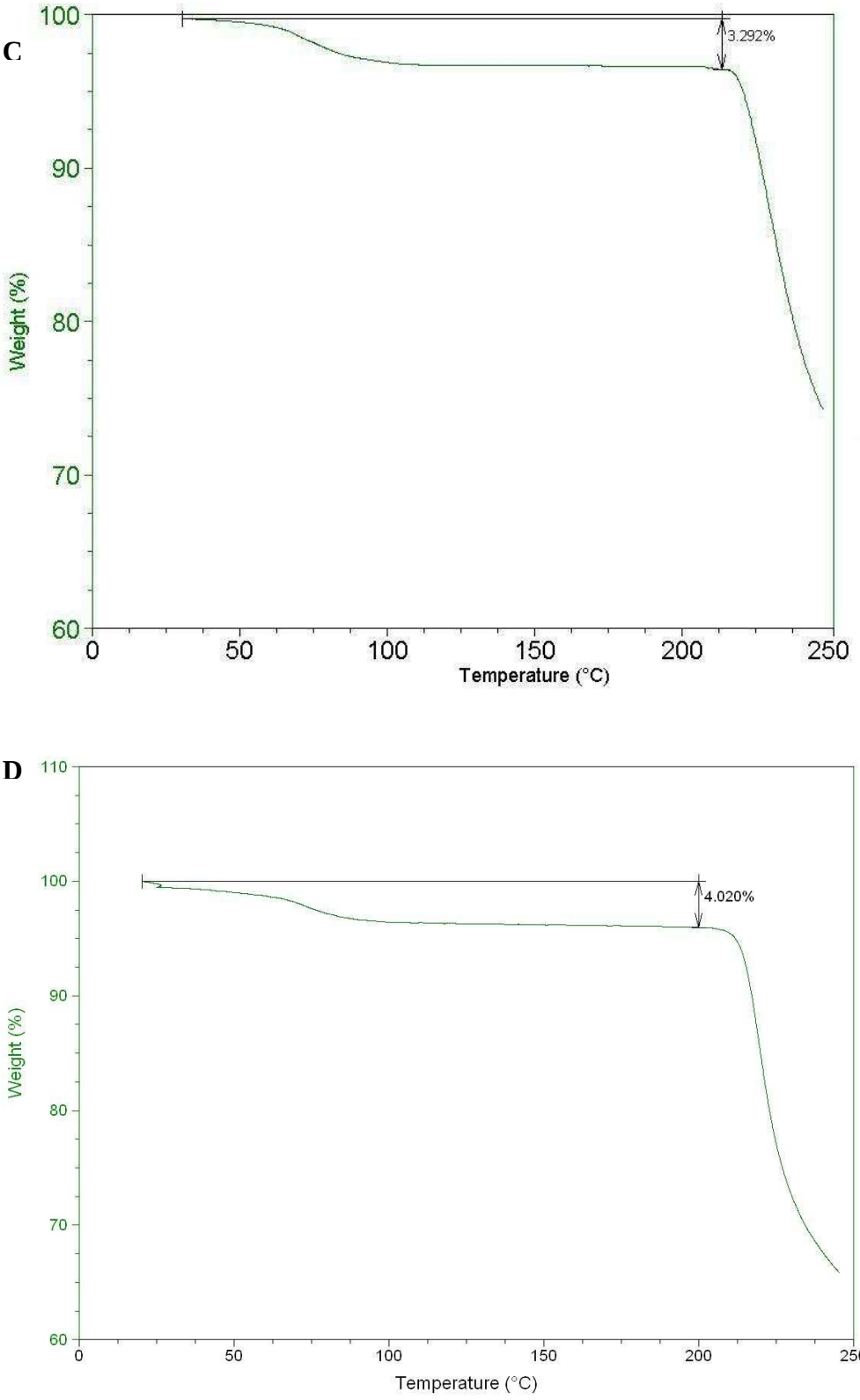

Figure 4-3: TGA curves of A- anhydrous BDP , B- BDP HFA-134a, B- BDP HFA-227ae, C- BDP EtOH HFA-134a and D- BDP EtOH HFA-227ae. All samples were heated from 20˚C to 250˚C at a heating rate of 10˚C/min.

The TGA results obtained for both BDP suspended in EtOH and HFA-134a/HFA-227ae show a similar pattern (Fig. 4-3C and 4-3D respectively). A total weight loss of approximately 4% was observed at an onset of 50 ºC and an ending of around 110 ºC. The total weight loss observed is extremely low and is 16.66% of the theoretical total weight loss (Table 4-1). The total weight losses observed corresponds to the calculated theoretical weight loss of water from the monohydrate (3.39% weight loss). Therefore, these results suggest the formation of a BDP monohydrate over the formation of a BDP EtOH propellant clathrate or a BDP EtOH solvate. The formation of the monohydrate is believed to be due to the residual water present in the anhydrous EtOH when used during the preparation that favours the formation of a monohydrate over the other solvate forms. Moreover, the high volatility of the HFA propellants may be the reason for the high instability of the crystal structure of the BDP clathrate which collapses when removed from the high pressure medium in the canister to the ambient pressure and temperature. These lead to rapid changes in the crystal structure after the evaporation of the excess propellant and the solvent and leads to the formation of a monohydrate.

Table 4-2: The different BDP entities encountered together with experimental (TGA) and theoretical weight loss in weight %.

Samples	% TGA Weight loss	Theoretical % weight loss
BDP HFA-134a	12.14 ± 1.58	16.37 (1:1 ratio)
BDP HFA-227ae	No weight loss	24 (1:1 ratio)
BDP EtOH HFA-134a	3.58 ± 0.57	22.42 (1:1:1 ratio)
BDP EtOH HFA-227ae	4.25 ± 1.23	29.24 (1:1:1 ratio)

4.3.3.2 DSC Results

Conventional DSC data obtained for the different samples are shown in Fig. 4-4 Anhydrous BDP melts at about 212˚C as shown previously, and which corresponds to literature (Nachiengtung, 1997, Vervaet and Byron, 1999a). The thermogram for BDP suspended in HFA-134a is shown in Figure 4-4A. An exothermic onset was observed after heating the sample to approximately 83 ˚C, which is believed to be due to a structural rearrangement of the clathrate structure. This exothermic peak is in agreement with the data obtained from the TGA analysis that showed an initial weight loss at this temperature. Therefore, this structural rearrangement leads to a very small loss of HFA-134a molecules from the crystal lattice of the

A

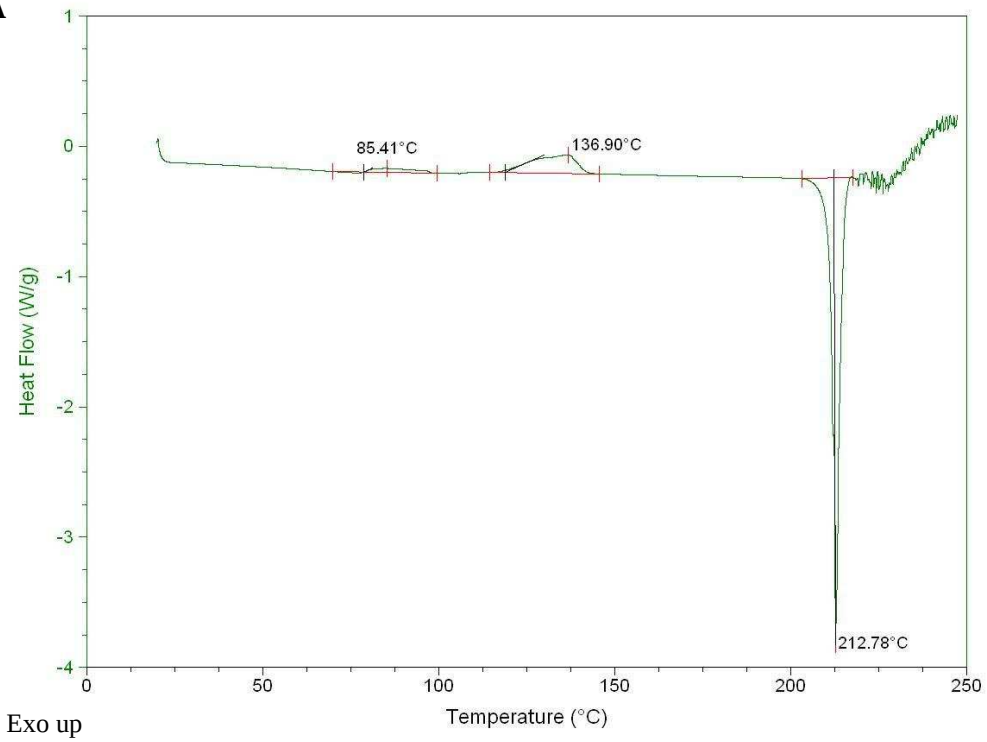

B

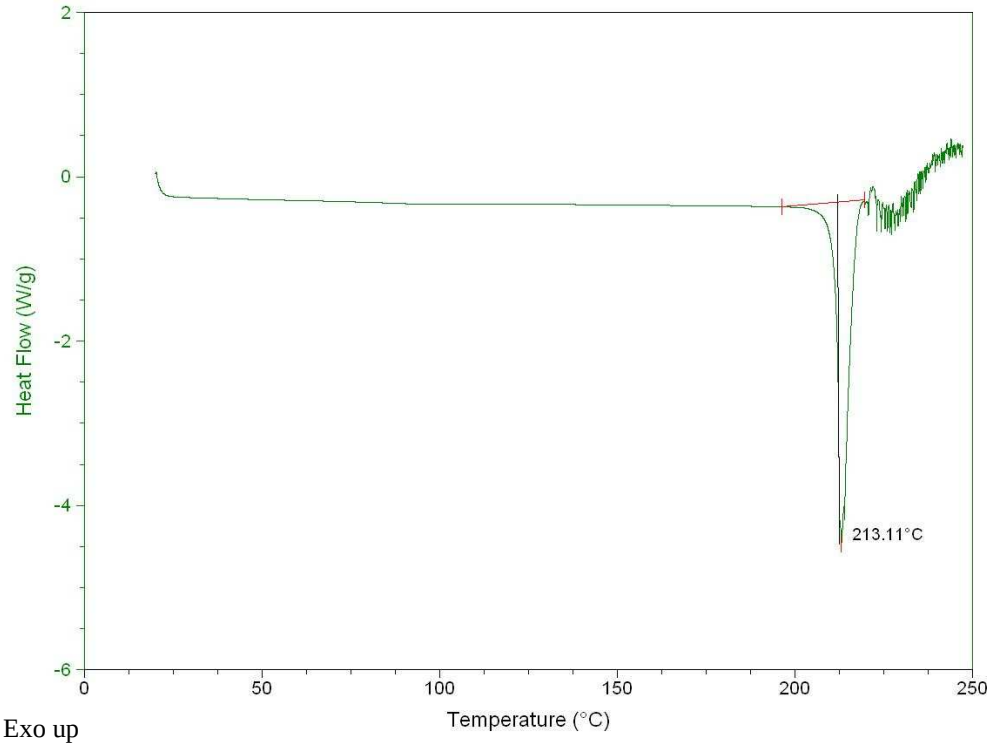
Heat Flow (W/g)
Temperature (°C)
213.11°C
Exo up

C

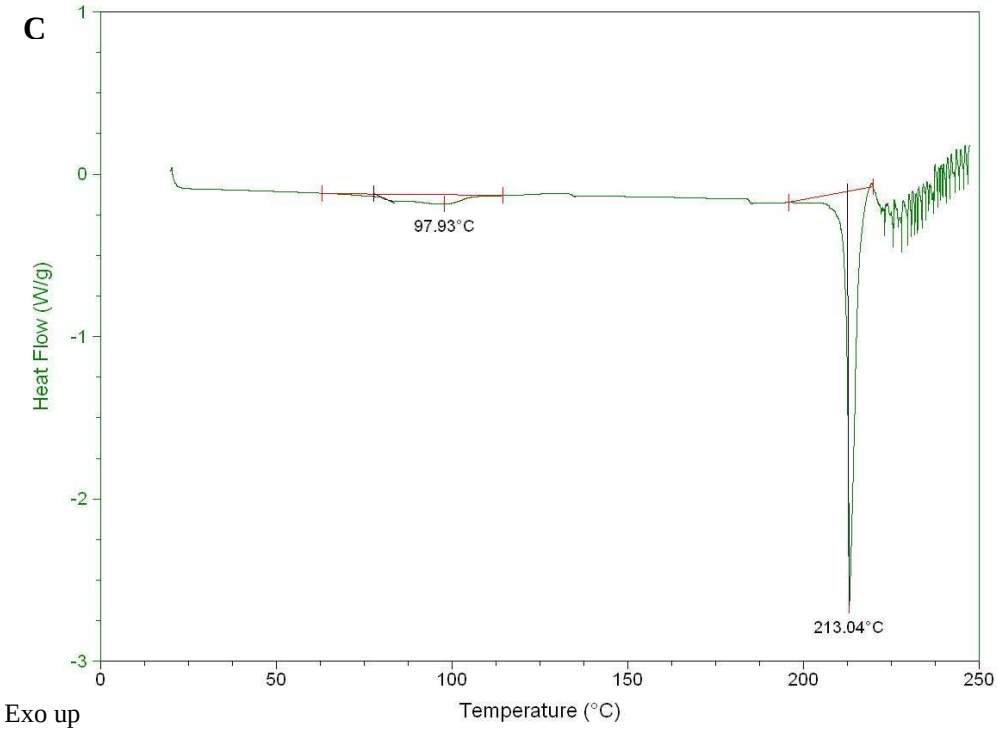
Heat Flow (W/g)
Temperature (°C)
97.93°C
213.04°C
Exo up

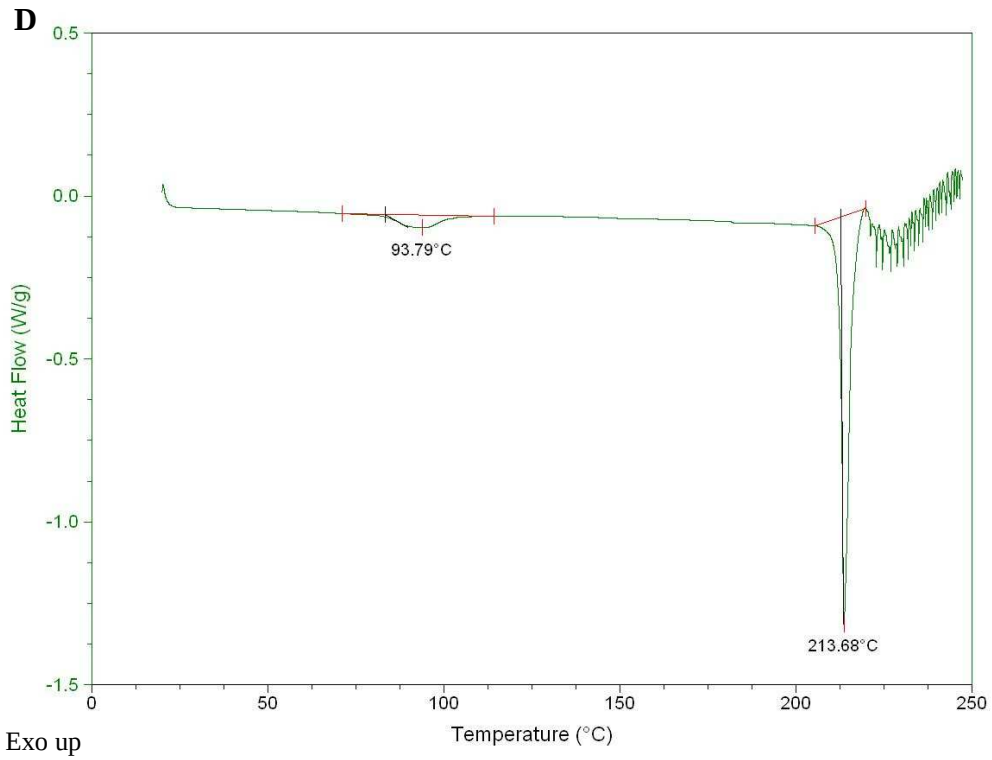

Figure 4-4: DSC curves of A- BDP HFA-134a, B- BDP HFA-227ae, C- BDP EtOH HFA-134a, D- BDP HFA-227ae. All samples were heated from 20˚C to 250˚C at a heating rate of 10˚C/min.

BDP HFA-134a clathrate. The total release of HFA-134a is thought to happen at an onset of 115 °C as shown by the second exothermic peak which is in agreement with TGA outcomes. The melting point of BDP HFA-134a clathrate after HFA-134a loss is seen at approximately 212˚C. The complex thermal events after the melting point observed in the different DSC scans of the different samples indicate that the BDP undergoes significant degradation during melting (Shah et al., 2006). Interestingly, the clathrate retains the propellant (HFA-134a) until quite high temperatures are reached (115 ˚C). The release of HFA-134a propellant molecules from the clathrate structure of the crystallized BDP can be explained thermodynamically by the Gibb's free energy equation

and follows the same principle as the release of CFC-11 from the clathrate structure of BDP CFC-11 clathrate as explained in Chapter 3, Section 3.3.4.2.

By looking at the thermogram obtained for the crystals extracted from the suspension of BDP in HFA-227ae, it can be observed that there is no transition when heating the crystals apart from the endothermic onset at 212 ˚C which represents the melting point of BDP (Fig. 4-4B). This result is in agreement with TGA where no weight loss was observed when heating the BDP HFA-227ae crystals to its melting point. Therefore, it can be concluded that suspending BDP in HFA-227ae does not result in crystallizing BDP to its clathrate form and hence it is not able to include the HFA-227ae into its crystal lattice to form the clathrate.

DSC scans for both BDP EtOH HFA-134a and BDP EtOH HFA-227ae suspensions (Fig. 4-4C and D respectively), showed an endothermic onset at 213 ˚C corresponding to the melting point of BDP (as reported previously by Saunders et al (Saunders, 2009). A broad endothermic peak was observed for both BDP entities starting at around 80 ˚C and ending at around 100 ˚C which is might be due to the release of water molecules as deducted from TGA results. These transitions are in total agreement with the results presented in literature by Saunders et al (Saunders, 2009). The magnitude of the endothermic transition was slightly variable, due to the non-stoichiometric association of the drug with the water molecules (Vervaet and Byron, 1999b, Kuehl, 2003). Therefore, combining both results obtained from DSC and TGA, suspending BDP in mixture of EtOH solvent and HFA propellant showed the formation of very

unstable crystals. These convert quite rapidly to the BDP monohydrate once removed from the pressurized mother liquor in the canister. The conversion might be due to the presence of water molecules in EtOH when preparing the suspensions. EtOH has a much higher boiling point (78.5 ˚C) (Wikipedia, 2010) than both HFA propellants, therefore, when extracting the crystals from the suspension, the high volatility of both HFA propellant leads to very rapid evaporation of the propellants when exposed to ambient conditions leaving the BDP crystals suspended in only EtOH. The crystals then might either transform to an EtOH solvate (not observed from TGA results) or a conversion to a monohydrate due to water molecules present in EtOH.

4.3.4 XRPD Results

4.3.4.1 BDP HFA-134a Suspension

The X-RPD pattern obtained from BDP HFA-134a samples was compared to the different patterns of BDP solid-state forms reported previously in the Cambridge Structural Database (CSD) as shown in Figure 4-5. The BDP HFA-134a pattern had peaks with an excellent match to the BDP CFC-11 clathrate and anhydrous BDP. Therefore, the sample is concluded to be a mixture of both anhydrous BDP and BDP HFA-134a clathrate. From Figure 4-5, it can be observed that the two initial peaks at a 7.5º and 8.3º from the BDP HFA-134a pattern are present in the experimental BDP CFC-11 clathrate pattern and these represent the two characteristic peaks in identifying BDP clathrate crystal structure. Hence, the partial formation of BDP HFA-134a clathrate can be confirmed from these results.

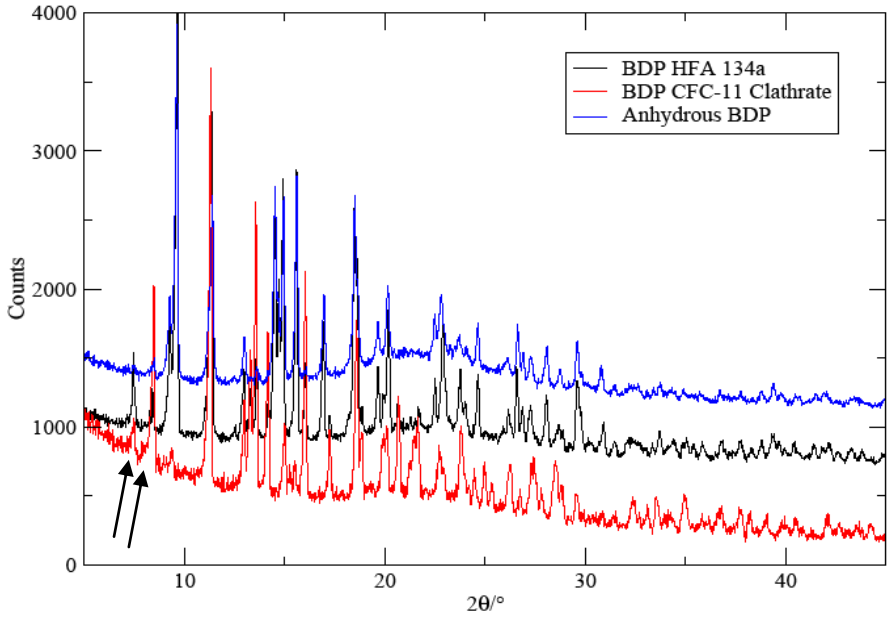

Figure 4-5: X-RPD patterns of BDP HFA-134a crystals compared to experimental BDP CFC-11 clathrate and anhydrous BDP.

On the other hand, the X-RPD pattern from 9.6º to 30º shows a very good match with the pattern obtained from anhydrous BDP with some small peaks matching those of the clathrate structure. The results observed in Figure 4-5 are in agreement with DSC and TGA results suggesting the formation of a clathrate. This is consistent with the slightly lower weight loss observed with the TGA results compared to the calculated theoretical weight loss, which is attributed to the non-stoichiometric nature of the clathrate.

4.3.4.2 BDP HFA-227ae Suspension

An excellent match was obtained for the X-RPD pattern of BDP HFA-227ae crystals when comparing the data with patterns from the experimental X-RPD pattern of the as received anhydrous BDP (Fig. 4-6). For the as-received

anhydrous BDP, when the effects of thermal expansion are accounted for, we achieve an excellent match when comparing the room temperature data with the calculated pattern from the reported 100 K structure of BDP (ca. 4.5 % increase in volume at room temperature compared to 100 K). The Rietveld method was used to model the entire powder pattern profile and to calculate lattice parameters. Therefore, these results complement the outcomes of thermal investigation as shown earlier using DSC and TGA. Hence, it was proven that the crystals extracted from suspending anhydrous BDP in HFA-227ae results in a crystalline anhydrous BDP with no subsequent formation of any BDP clathrate, BDP solvate or its monohydrate was observed.

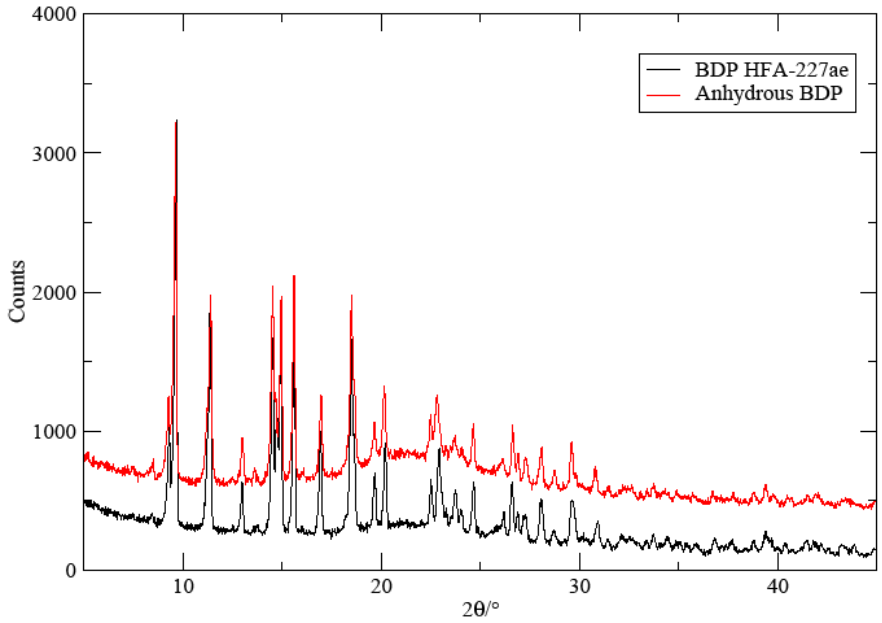

Figure 4-6: X-RPD patterns of BDP HFA-227ae crystals compared to experimental anhydrous BDP.

4.3.4.3 BDP EtOH HFA-134a Suspension

X-RPD data of the BDP EtOH HFA-134a crystals is shown in Figure 4-7. The experimentally obtained pattern when compared with the calculated pattern from single crystal diffraction of different BDP entities showed a good match with BDP monohydrates pattern in most of the peaks. However, small peaks can be observed indicating the presence of a small amount of anhydrous BDP crystals. As BDP EtOH HFA-134a clathrate is quite unstable when removed from its mother suspension at -50˚C and tends to convert more readily into the monohydrate form of BDP, it can be hypothesized that "BDP EtOH HFA-134a

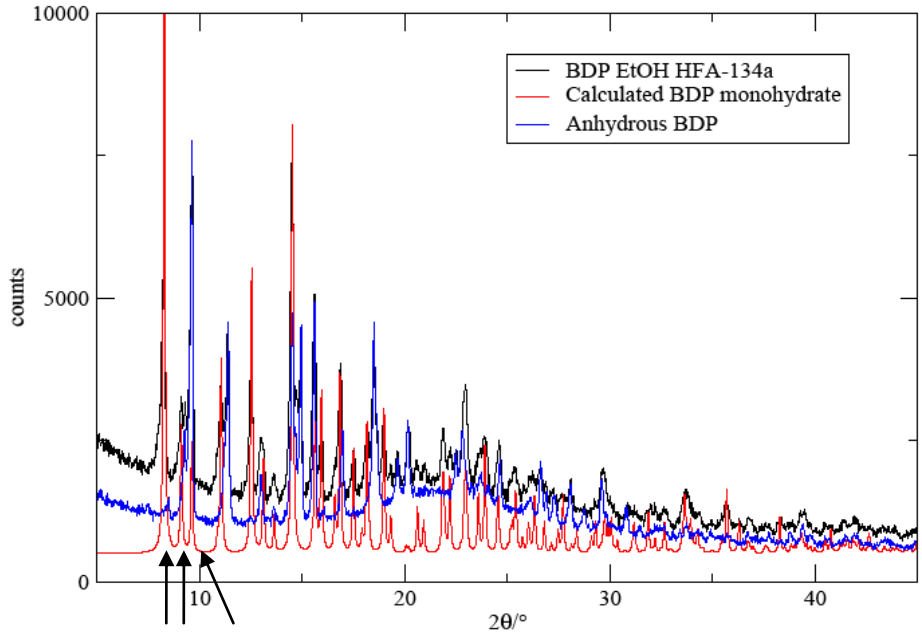

Figure 4-7: X-RPD patterns of BDP EtOH HFA-134a crystals compared to experimental anhydrous BDP and calculated BDP monohydrate.

clathrate" have been synthesized. However, due to the removal from the mother suspension to room temperature, the structure has decomposed quickly (cracks observed in the SEM images Figure 4-1) and converted rapidly to the

monohydrate form, which has been observed using both TGA results and DSC. The conversion of "BDP EtOH HFA-134a" to the BDP monohydrate is thought to be due to the presence of some water molecules in the anhydrous EtOH used during the preparation phase of the suspension or some humidity that is still present in the environment.

4.3.4.4 BDP EtOH HFA-227ae Suspension

Concerning the results obtained for the X-RPD pattern of BDP EtOH HFA-227ae crystals, similar results to BDP EtOH HFA-134a were obtained (Fig. 4-8). The X-RPD pattern showed an excellent match with the calculated pattern of BDP monohydrate with some peaks in common with anhydrous BDP at 19º and 20º. These results show that there is a mixture of two different forms of BDP. The presence of the monohydrate confirms and completes the results obtained by DSC and TGA that show a transition at around 93º C when being heated, which corresponds to the release of water molecules from the crystal structure. There were no apparent peaks that corresponded to any clathrate formation. There is a very small peak on the BDP EtOH HFA-227ae pattern at 7.5 º which can be attributed to the remaining parts of a potential formation of some BDP EtOH HFA-227ae.

As discussed in the previous section, the BDP EtOH HFA clathrate are very unstable when removed from the high pressure medium in the canister due to the very low boiling point of HFA propellants which leads to rapid decomposition and collapse of the clathrate structure when exposed to ambient pressure and

room temperature. This will lead to a rapid release of the propellant from the crystal structure and the conversion of the clathrate to the monohydrate due to

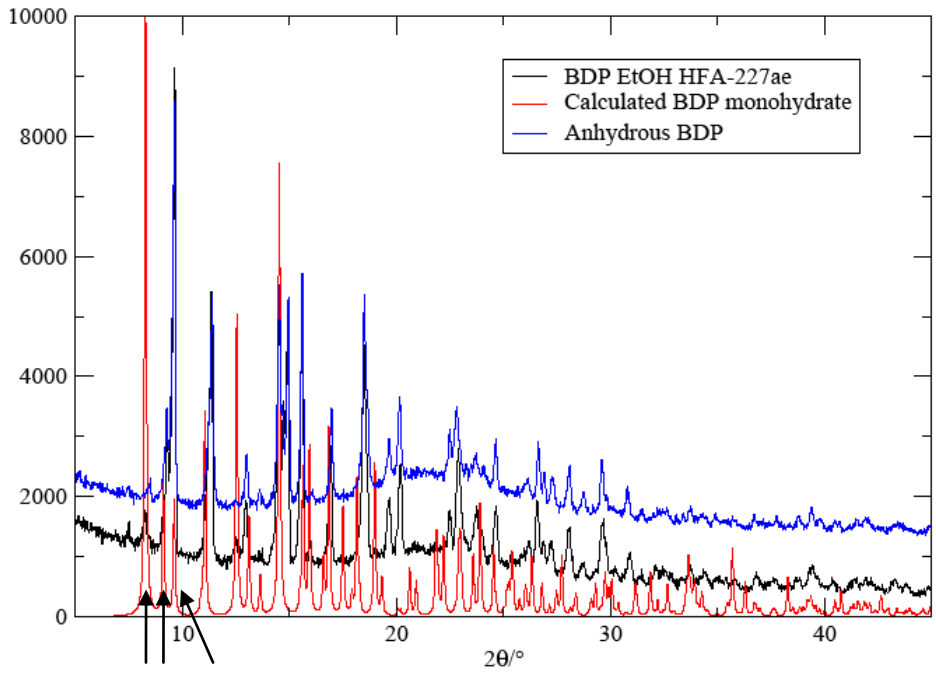

Figure 4-8: X-RPD patterns of BDP EtOH HFA-227ae crystals compared to experimental anhydrous BDP and calculated BDP monohydrate.

the presence of some water molecules in EtOH. Therefore, this increases the chances of conversion of the clathrate compound to either a BDP EtOH solvate or a monohydrate. BDP monohydrate is more easily obtainable due to the presence of some water molecules in the anhydrous EtOH (<0.005%) and also from the environment even at very low humidity levels. Hence, this leads to the formation of BDP monohydrate.

4.3.5 VT-XRPD Results

4.3.5.1 Anhydrous BDP

Figure 4-9 presents the measured VT-XRPD diffraction patterns for anhydrous BDP sample. The diffraction patterns of the anhydrous BDP sample did not change much during the heating from room temperature to 218 ºC indicating its stable crystal structure. The main changes in the VT-XRPD patterns were only observed in the intensities of the reflections due to the preferred orientation of the crystals. The reflections of the diffraction pattern showed a decrease in intensity and broadening of the peaks indicating the effects of melting on the crystal lattice at the temperature 217 °C and after which the melting of BDP was observed. Some peaks showed splitting starting from 86 ºC and being more defined with increasing temperature. These two peaks are presented at 2θ of 14º and 22.5º. The appearance of these peaks is due to the thermal expansion of the molecules due to heating and the change in the vibrational state of different parts of the BDP molecule due to heating. Thermal expansion is a fundamental physical property that reflects changes in the dimensions of the solid as a result of temperature variations which is a consequence of atomic vibrations within the molecules (Taylor and He, 1998, Abdullaev et al., 2001).

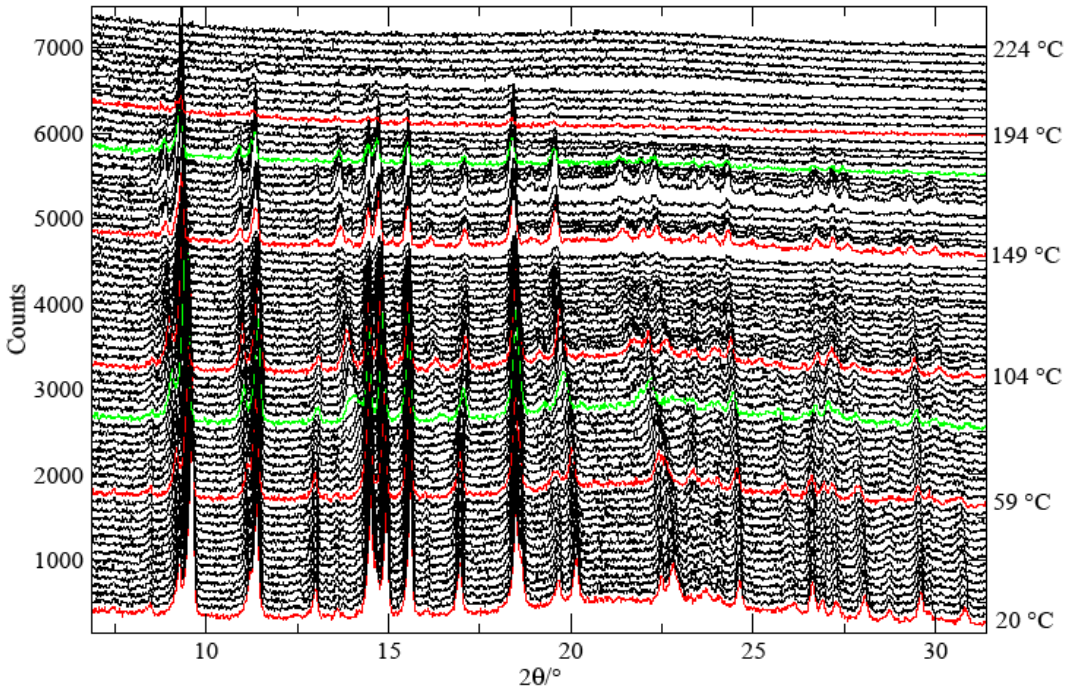

Figure 4-9: VT-XRPD patterns of anhydrous BDP.

4.3.5.2 BDP HFA-134a and 227ae Clathrates

Variable temperature X-RPD patterns obtained for BDP HFA-134a are presented in Figure 4-10. The pattern obtained at room temperature showed similar results to those discussed in the previous section where the compound showed a mixture of both anhydrous BDP and BDP HFA-134a clathrate. The clathrate peaks are quite distinctive and can be observed at a 2θ position of 6º and 12.5º; while the other peaks are distinctive of anhydrous BDP (Fig. 4-10). VT-XRPD analysis showed that the mixture was stable from room temperature to approximately 95 ºC (Fig. 4-10). A further increase in temperature led to the transformation of the clathrate part of the mixture to anhydrous BDP resulting in pure crystalline anhydrous BDP. This is shown by the disappearance of the reflection at a 2θ of 6º and 12.5º as well as two peaks from the triplet at 18.5º (2θ) leaving just a singlet (Fig. 4-10). This transformation of the crystal structure leading to the release of HFA-134a from within the channels formed from the clathrate is in consistent with the DSC and TGA data. A further increase in temperature showed no major changes in the different patterns and hence no crystal transformation was observed. However, as seen previously with the VT-XRPD of anhydrous BDP, some peaks splitting were observed starting at 122 ºC. The peak splitting is mostly observed at a 2θ of 14.5º and 22.5º. This is explained by the increased vibration with temperature of the side chain of the BDP molecules leading to these splitting due to an increased temperature. The intensities of the different patterns started to reduce in intensity from a temperature 215 ºC and finally melting at 224 ºC.

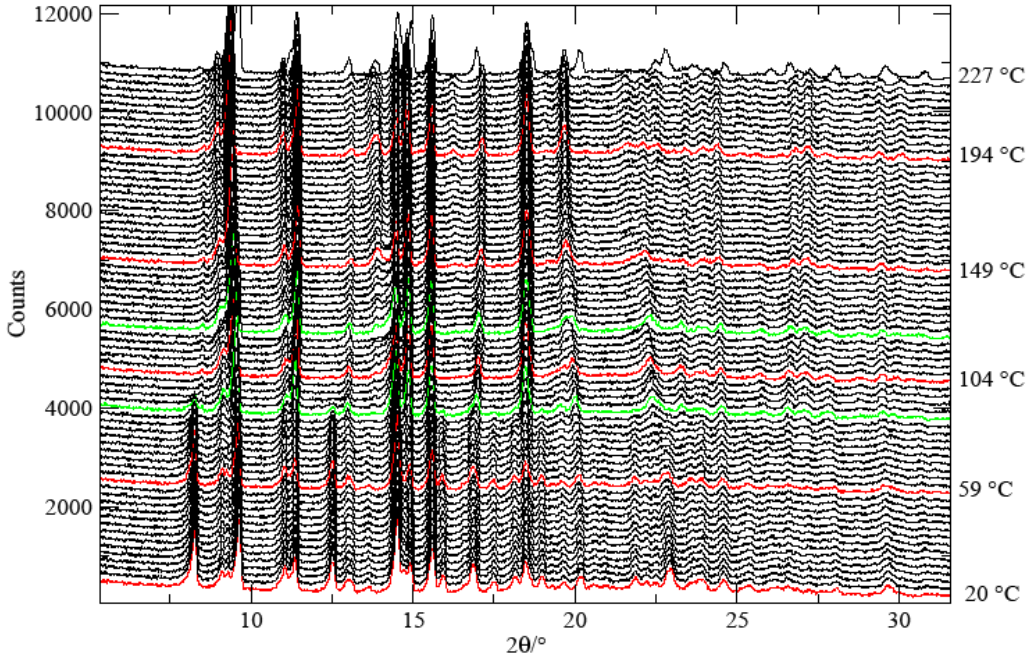

Figure 4-10: VT-XRPD patterns of BDP HFA-134.

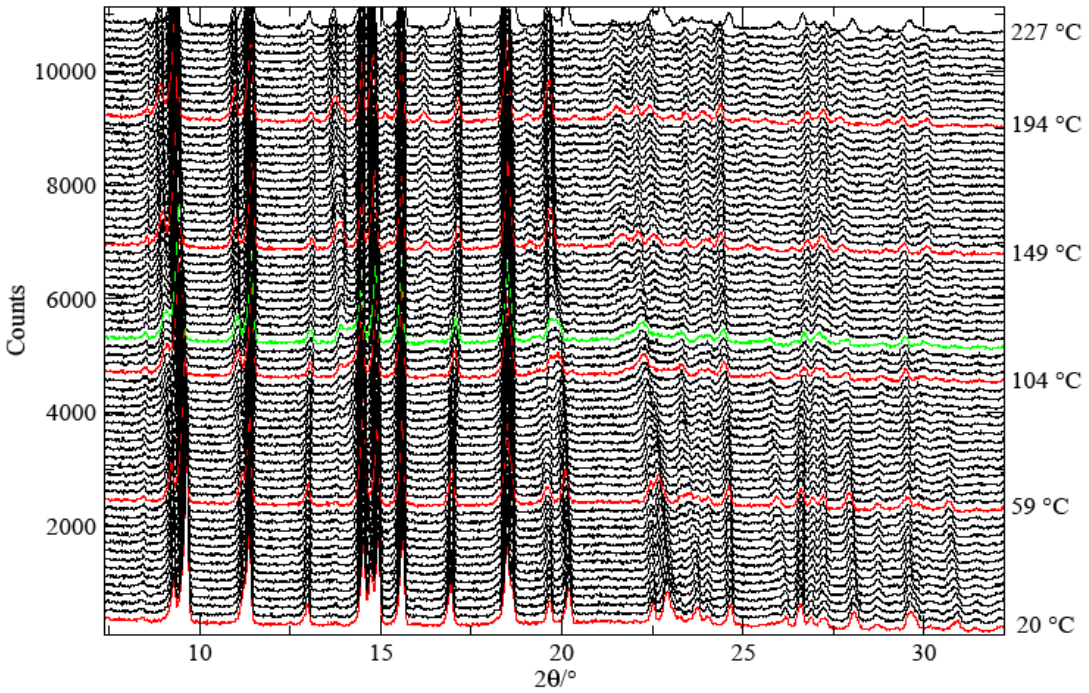

Figure 4-11: VT-XRPD patterns of BDP HFA-227ae.

The VT-XRPD patterns obtained for BDP HFA-227ae particles (Fig. 4-11), show no formation of clathrates as observed earlier as the pattern obtained at room temperature displays a perfect match with the reference pattern of anhydrous BDP (Millard and Myrdal, 2002). Furthermore, the different patterns obtained with increased temperature showed no crystal transformation and had a similar behaviour to the as received anhydrous BDP. The slight lower angle and the peak split at a 2θ position of 14.3º and 22.5º at a temperature above 104 ºC observed in the reflections were due to the thermal expansion of the molecule (Fig. 4-11). This split is due to the increased vibration of the side chains of the BDP molecules while increasing the temperature. The melting of the BDP HFA-227ae was detected at 227 ºC where the intensity of the different patterns decreased due to the melting of BDP

4.3.5.3 BDP EtOH HFA 134a and 227ae Clathrates

VT-XRPD was run on both BDP EtOH HFA-134a and BDP EtOH HFA-227ae crystals extracted from both BDP EtOH HFA-134a and 227ae suspensions. The results of these are presented in Figures 4-12 and 4-13 for BDP EtOH HFA-134a and BDP EtOH HFA-227ae respectively. The patterns observed for BDP EtOH HFA-134a show similar results to the ones observed earlier at room temperature (25 ºC) where it shows a mixture of both anhydrous BDP (mostly) and some peaks at a 2θ equal to 4.9º indicating the presence of BDP monohydrate when compared to the reference patterns (Duax et al., 1981, Millard and Myrdal, 2002) (Fig. 4-12). Furthermore, the results show that after heating the sample of BDP

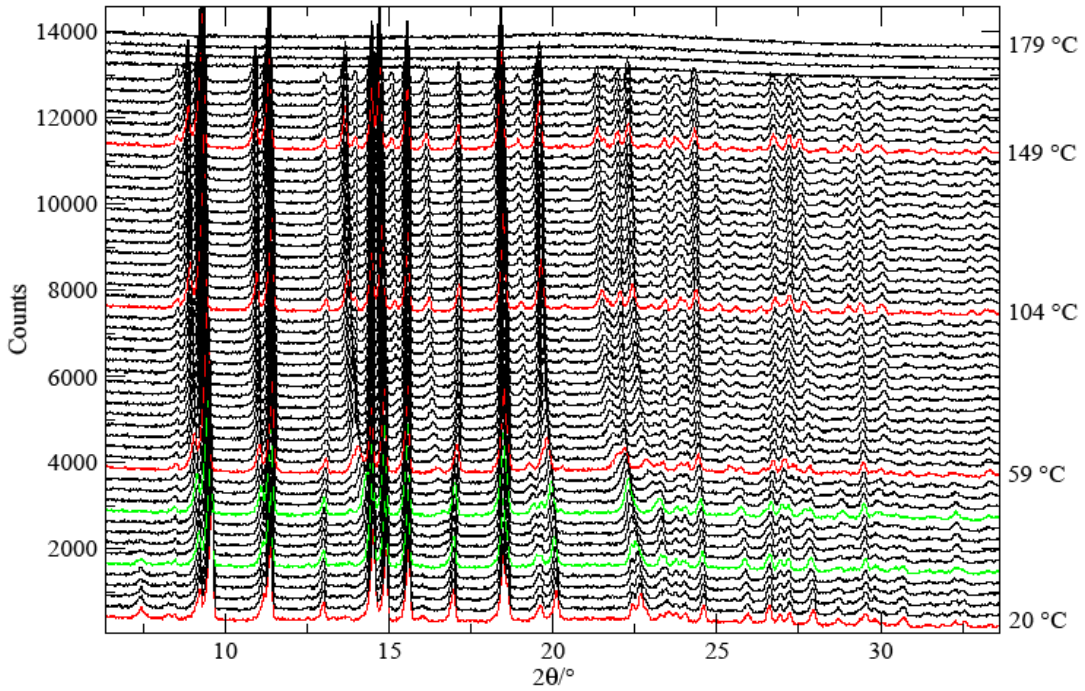

Figure 4-12: VT-XRPD patterns of BDP EtOH HFA 134a.

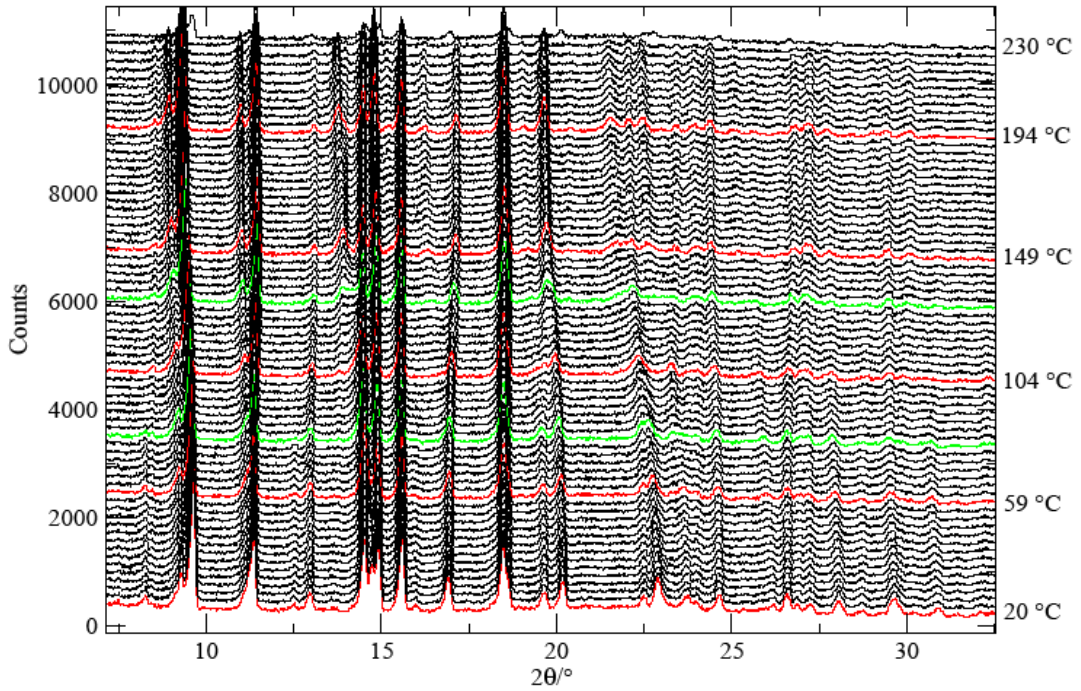

Figure 4-13: VT-XRPD patterns of BDP EtOH HFA-227ae.

EtOH HFA-134a particles to 35 ºC the first sign of a small transformation to anhydrous BDP appeared with the distinct fading of the reflections at 4.9º (2θ) and the appearance of a small reflection at 7.5º (2θ). The process of dehydration continues up to 53 ºC. This is in accordance with the findings observed using DSC and TGA experiments in the section 4.3.3.1 and 4.3.3.2. Since then, the diffraction patterns obtained did not change much during heating to about 194 ºC where the intensity of the different peaks diminished until disappearing completely as the samples melt at 216 ºC. A split in the peak at position 14º (2θ) was also observed starting at 59 ºC as observed for anhydrous BDP VT-XRPD patterns, which is due to the vibrations happening within the molecules of BDP. A shift to the left of the different reflections can also be noticed which is due to thermal expansion. Figure 4-13 presents the measured VT-XRPD diffraction patterns for BDP EtOH HFA-227ae from room temperature to 230 ºC. The pattern obtained at room temperature showed no clathrate formation and the pattern corresponded to the BDP monohydrate and anhydrous BDP when compared with the reference anhydrous BDP pattern and the monohydrate (Millard and Myrdal, 2002) as shown previously. As the temperature increased to 230 ºC, the different patterns exhibited similar results to those obtained earlier for anhydrous BDP, where no crystal transformation was observed with heating. A shift to the left was observed which is again attributed to thermal expansion of the molecules. Melting and degradation process of BDP started at temperature above 226.

4.4 Conclusions

Beclomethasone dipropionate is of a particular interest in pMDI formulation stability studies because of the existence of a range of solvates, clathrates with the solvent molecules incorporated into the channels. This situation has been reported in different papers (Duax et al., 1981, Kuehl et al., 2003, Harris et al., 2003, Othman et al., 2008) and in the work presented here.

The results showed the formation of a mixture of both crystalline anhydrous BDP and BDP HFA-134a clathrate when BDP was suspended in HFA-134a. The experimental approach based on DSC/TGA, XRPD showed evidence of the clathrate formation with HFA-134a. The crystals exhibited a transition when being heated to their melting point, which is considered to be due to the release of the HFA-134a from the channels constituting the crystal structure of the clathrate. This release is due to a structural rearrangement of the crystal structure leading to the formation of anhydrous BDP. The release of the propellant occurs at a temperature of 95 ºC as observed earlier for the BDP CFC-11 clathrates (Chapter 3). Furthermore, a rapid conversion of BDP EtOH HFA-134a clathrate to the monohydrate was observed when co-solvent was used which shows the instability of BDP EtOH HFA-134a clathrate when removed from the high pressure media of the pMDI system. This is due to the very low boiling point of HFA-134a and its high volatility at room temperature. In contrast, no clathrate formation was seen for BDP HFA-227ae which is due to the increased solubility of BDP in this propellant. The formation of monohydrate was observed when BDP was suspended in HFA-13a/ethanol and HFA-227ae/ethanol mixture

confirming the disability of forming a clathrate from these latter and a preferential monohydrate formation.

The polymorphic changes of beclomethasone HFA clathrates can be determined using VT-XRPD diffraction. VT-XRPD gives information about proportions of crystal structure of the polymorphic forms as well as crystallinity. It can be used effectively to characterize polymorphic changes during heating. The analysis of different BDP HFAs suspensions showed no formation of clathrates when anhydrous BDP was suspended in HFA-227ae and in HFA-227ae/ethanol mixture. The analysis showed that the crystals of pure anhydrous BDP which are due to the increased solubility of BDP in HFA-227ae do not allow further crystallisation at high pressure. The analysis showed that anhydrous BDP as received as well as the crystals obtained from suspending it in HFA-227a and HFA-227ae/ethanol mixture were stable and that its structure did not change as a function of temperature and hence no polymorphic transformations occurred. However, an increased vibration of different parts of the anhydrous BDP molecules especially the side chain showed some peak splitting from 84 ºC.

VT-XRPD showed that the mixture of anhydrous BDP and BDP HFA-134a clathrate was stable between room temperature and approximately 71 ºC. A further increase in temperature (to between 73 ºC and 90 ºC) leads to a transformation of BDP clathrate to the anhydrous form. This means that the formation of BDP HFA-134a is quite stable at room temperatures and that some clathrate channels retain the propellant to quite high temperatures. The same changes were observed using thermal analysis techniques. After 90 ºC, similar

behaviour to that observed in anhydrous BDP followed due to the increased vibration of the side chain of the BDP molecules.

4.5 References

ABDULLAEV, N. A., MAMEDOV, T. G. & SULEIMANOV, R. A. (2001) Thermal expansion of single crystals of the layered compounds TlGaSe2 and TlInS2. Low Temperature Physics, 27**,** 676-680.

BYRON, P. R. (1992) Towards the rational formulation of metered dose inhalers. Journal of Biopharmaceutical Sciences, 33**,** 001-009.

DUAX, W. L., CODY, V. & STRONG, P. D. (1981) Structure of the Asthma Drug Beclomethasone Dipropionate. Acta Crystallographica Section B-Structural Science, 37**,** 383-387.

HARRIS, J. A., CARDUCCI, M. D. & MYRDAL, P. B. (2003) Beclomethasone dipropionate crystallized from HFA-134a and ethanol. Acta Crystallographica Section E, 59**,** 1631-1633.

JONES, S. A., Martin, G. P. & Brown, M. C. (2006) Manipulation of beclomethasone–hydrofluoroalkane interactions using biocompatible macromolecules. Journal of Pharmaceutical Sciences, 95, 1060-1074.

KUEHL, P. J., GARDUCCI, M. D. & MYRDAL, P. B. (2003) An ethanol solvate of beclomethasone dipropionate. Acta Crystallographica Section E, 59**,** 1888-1890.

MCDONALD, K. J. & MARTIN, G. P. (2000) Transition to CFC-free metered dose inhalers - into the new millennium. International Journal of Pharmaceutics, 201**,** 89-107.

MILLARD, J. W. & MYRDAL, P. B. (2002) Anhydrous beclomethasone dipropionate. Acta Crystallographica Section E-Structure Reports Online, 58**,** O712-O714.

NACHIENGTUNG, N. (1997) Solid-state characterisation of beclomethasone dipropionate solvates and polymorphs. Phd thesis, Purdue University.

OTHMAN, A., RHARRIS, R. K. & HODGKINSON, P. (2008) Structural characterisation of two pharmaceutically important steroids by solid-state NMR. New Journal of Chemistry, 32**,** 1796-1806.

SAUNDERS, M., BUTTINI, F., GRAINGER, C., FORBES, B., ROYALL, P. G., LINCOLN, P & JONES, S. A. (2009) Characterisation of particles emitted from beclomethasone dipropionate solution metered dose inhalers. Proceedings to the Drug Delivery to the Lungs 19, UK.

SHAH, B., KAKUMANU, V. K. & BANSAL, A. K. (2006) Analytical techniques for quantification of amorphous/crystalline phases in pharmaceutical solids. Journal of Pharmaceutical Sciences, 95**,** 1641-65.

SMYTH, H. D. (2003) The influence of formulation variables on the performance of alternative propellant-driven metered dose inhalers. Advanced Drug Delivery Reviews, 55**,** 807-28.

TAYLOR, R. E. & HE, J. (1998) Thermal Expansion of Solids, ASM International, Materials Park, OH.

VERVAET, C. & BYRON, P. R. (1999a) Drug-surfactant-propellant interactions in HFA-formulations. International Journal of Pharmaceutics, 186**,** 13-30.

WIKIPEDIA.ORG (2010) Ethanol.

ZIMMERMANN, A., TIAN, F., LOPEZ DE DIEGO, H., FRYDENVANG, K., RANTANEN, J., RINGKJOBING ELEMA, M. & HOVGAARD, L. (2008) Structural Characterisation and Dehydration Behaviour of Siramesine Hydrochloride. Journal of Pharmaceutical Sciences, 98**,** 3596-3607.

Chapter 5 Effect of Size Reduction on API-Clathrate Surface Interactions

5.1 General Introduction

Micronisation is commonly used to reduce the particle size and size average of an active ingredient before it is dispersed in the propellant system for a suspension-based pressurized metered-dose inhaler (pMDI) formulation. Because the respirable fraction of the emitted aerosol of a pMDI formulation is largely dependent on the aerodynamic size of the bulk drug particles, the API usually requires significant size reduction to the range of 2 –5 µm by micronisation. The principal requirement for an effective delivery to the lung is that the mass median aerodynamic diameter of the particles generated from the device is in the range of 2 – 5 µm. A smaller particle size of 1.0 – 2.0 µm is required when the pulmonary route is being considered for a systemic drug administration and targeting the deep lung regions is required (Lucas et al., 1999). While the production of smaller particle size would enhance the respirability of drugs, the magnitude of their inherent surface electrostatic forces would produce more cohesive powder system or more adhesive to the different parts of the device (Lucas et al., 1999).

Size reduction techniques are used in order to produce smaller particles. Ball-milling, the technique used for size reduction during this project operates by retaining a bed of powder in a chamber in which the powder is comminuted by tumbling balls for an extended period of time. The residence time in the ball-mill

chamber depends on the degree of size reduction desired. The technique can produce final particles of less than 5 µm in diameter, primarily through impaction. As a result of the milling, the properties of the powder will change. The process of milling has been reported to result in particles becoming rounder and more spherical in shape due to the boundaries of the particles becoming smoother after micronisation (Akbarieh and Tawashi, 1987). The cohesiveness of the particles has been shown to increase with milling when compared to the non-milled form (Omelczuk et al., 1997). Furthermore, the surface energy of the powder has been shown to be affected by the process (Buckton et al., 1988) due to the potential changes in the orientation of the molecules on the surface of the powder particles or changes in form and hence orientation of the molecules at the surface of the powder (Briggner et al., 1994, Ahmed et al., 1996). For example, amorphous regions can form on a surface of the particles due to localized disorder introduced due to size reduction and hence becoming more prevalent than the occasional molecular dislocation (Ward and Schultz, 1995, Gerhardt et al., 1994). Amorphous regions are thermodynamically unstable and maintain a higher energy state compared to crystalline regions within a powder. Therefore, amorphous regions can significantly modify the behaviour of powders in pharmaceutical formulations, for example, by enhancing the dissolution rate (Burt and Mitchell, 1981), decreasing the chemical stability (Otsuka and Kaneniwa, 1990), and increasing the potential of polymorphic transition to a new crystalline state during storage (Kontny et al., 1987). Such changes in the physical properties of powders after the milling process can have an equally significant impact on aerosol formulations. The understanding of the influence of the milling process on the pMDI formulation would be greatly beneficial,

especially for the process of reformulating pMDIs with ozone-friendly propellants.

5.1.1 Chapter Aims and Objectives

This chapter will aim to study the effect of particle size reduction on API interactions with different pMDI components. The integrity of the structure of the clathrate following size reduction was determined using scanning electron microscopy (SEM), differential scanning calorimetry (DSC) and X-ray powder diffraction (X-RPD). Furthermore, the surface characterization of each of the BDP entities utilized during this study and different pMDI components was investigated. Following this, colloid probe AFM was be used to determine the adhesive interaction in a model propellant (mHFA). Additionally, the characteristics of AFM force curves was assessed and used to determine the surface free energy (γ) and the force of adhesion (F_{adh}) of the different BDP entities used in this study with different pMDI components in a model propellant (mHFA) and determining the effect of size reduction on the latter.

5.2 Materials and Methods

5.2.1 Materials

All of the chemicals used were the same as the ones stated in chapter 3, Section 3.2.1. Concerning the pMDI components and BDP IPA clathrates, both were all supplied by 3M Drug Delivery Systems (Loughborough, UK).

5.2.2 Methods

5.2.2.1 Preparation of mHFA Based Media for AFM Adhesion Experiments

To examine the effect of size reduction on different BDP entities surface interactions in mHFA, the following solutions were used:

Anhydrous mHFA: This medium was used throughout the project for the evaluation API-pMDI component interactions. A 2.5 litre batch of mHFA was placed into a clean, dry Duran bottle (Duran, Mainz, Germany). Approximately 100g of molecular sieves were added to the bottle, to remove any trace of water from the solution. The bottle was sealed with a screw-lid and Parafilm (Alcan, Neenah, WI, US), and stored in a fridge at 4°C prior to use.

5.2.2.2 Isolation of BDP CFC-11 Clathrate and BDP EtOH solvate

Anhydrous BDP was suspended in CFC-11 at a concentration of 1.67% w/w BDP in CFC-11. The same procedure as stated in Chapter 3, Section 3.2.2.1 was used to extract and store the clathrate crystals. Concerning BDP EtOH solvate crystals, these were extracted the ethanol solution with no propellant via rotary evaporation. The crystals were stored using the same conditions for the BDP CFC-11 clathrate as mentioned in Chapter 3, Section 3.2.2.1.

5.2.2.3 Size Reduction Using Ball-Milling

Size reduction on the BDP CFC-11 clathrate, BDP IPA clathrate and BDP EtOH solvate were carried out by ball milling using a Restsch® MM 400 ball-miller (Restsch, Germany). The milling intensity was the maximum with a frequency of 30 Hz and was carried out for 2 hours on 500 mg of the BDP CFC-11. The size and morphology of the ball-milled particles was studied by SEM. The samples were used for surface energy determination and force of adhesion with different pMDI components. The samples were stored in glass vial under nitrogen using after being sealed with a vial screw and Parafilm (Alcan, Neenah, WI, US), and stored in a fridge at 4°C prior to use.

5.2.2.4 Scanning Electron Microscopy (SEM)

The surface morphology of each of the BDP entities before and after milling, along with the different pMDI was investigated using SEM (JEOL (UK) Ltd, Welwyn Garden City, UK). The positioning of the API particle on the AFM cantilever were analysed before and after force data acquisition using SEM. SEM was carried out at an accelerating voltage (between 1 keV and 10 keV) and a spot size of between 48nm and 62 nm. These parameters were varied for each sample in order to optimise each particular image.

5.2.2.5 X-Ray Powder Diffraction (X-RPD)

Both crystalline and ball-milled samples of BDP CFC-11 clathrate were analyzed using X-RPD. X-RPD patterns were collected on a Bruker D8 diffractometer

system (Bruker AXS, Madison, WI, USA), operating in a Debye-Scherrer geometry. A ceramic X-ray tube with a copper target, wavelength λ= 1.54059 Å, operated at 40 kV, 40 mA. A scintillation counter was employed. The scan rate was 2° min^{-1}. The X-ray patterns were analysed using the Le Bail method (Le-Bail et al., 1988) to model the patterns obtained, based on the reported unit cell for the clathrate. All the patterns were collected straight after the formation of the crystals to determine the purity of the samples and its crystalline structure.

5.2.2.6 Differential Scanning Calorimetry (DSC)

Differences of phase behaviour between crystalline and ball-milled BDP CFC-11 clathrate were determined using DSC. DSC experiments were carried out using a DSC 2920 Differential Scanning Calorimeter (TA Instruments, USA), with a constant 10˚C/min heating rate, from 0˚C to 300˚C in a dry nitrogen atmosphere. Non-sealed aluminium pans were used in order to allow the escape of the propellant during the desolvation phase. In all measurements 6-7mg of sample were used. The thermograms obtained for the DSC results were analysed using TA universal analysis -NT software.

5.2.2.7 Thermogravimetric Analysis (TGA)

In order to determine whether the clathrate structure retained the propellant within the channels of the crystallized BDP after size reduction, TGA was performed on the ball-milled BDP CFC-11 clathrate. TGA of ball-milled BDP EtOH solvate and BDP IPA clathrate were also undertaken in order to determine the effect of size reduction on the solvates structure. An SDT Q600 TGA/DSC

was used to record the weight loss of the samples between 0˚C and 300˚C. Dry nitrogen gas was used as a purge and the scan speed was 10˚C/min. An isothermal period at 25˚C was run for 10 minutes prior to the measurements and any changes in weight during that period were monitored. In all measurements 6 to 7mg of sample was used. The thermograms obtained from the TGA results were analysed using TA universal analysis -NT software.

5.2.2.8 Atomic Force Microscopy (AFM) – Topographical Imaging Acquisition

Each material was topographically imaged in order to determine the root mean square (RMS) roughness of each BDP entity and pMDI component. Each sample was imaged using a Nanoscope IIIa MultiMode AFM (Veeco, Santa Barbara, CA, USA) in contact mode using NPS cantilevers (Veeco, Santa Barbara, CA, USA). A scan rate of 0.5 Hz was used over 5 µm x 5 µm scans. Three images were acquired from each pMDI component surface and the RMS roughness was calculated using software incorporated in the AFM system, via the following equation 5-1;

$$R_{rms} = \sqrt{\frac{1}{n}\sum_{i=1}^{n} y_i^2} \qquad \textbf{Equation 5-1}$$

where n is the number of points in the topography profile, i is the asperities and y_i is the distance between the asperities.

5.2.2.9 AFM – Surface Energy Determination

The surface energy of each material (Table 5-4) was determined using the blank AFM cantilever method where three Force Modulation Etched Silicon Probes (FESP) cantilevers (Veeco, Santa Barbara, CA, USA) were used to determine the F_{adh} from compacts of each clathrate and anhydrous BDP (Stegemann et al., 2007). In order to find out the flexibility (and hence exerted force) of each cantilever, the spring constants of these FESP cantilevers were determined using the Sader method prior to force data acquisition (Sader et al., 1995). The spring constants for the FESP tips were between 2.8 and 3.6 Nm^{-1}. The surface energies of the API materials were then determined based on the known surface energy of the silica probe (42.05 mJm^{-2}) and the measured adhesion to each API. Before force acquisition, each cantilever probe was cleaned using a UV ozone cleaner (Bioforce Nanosciences, Ames, IA, USA) for 20 minutes to remove organic contaminants on the probe surface. The force of adhesion (F_{adh}) measurements were then determined using an EnviroScope AFM (Veeco, Santa Barbara, CA, USA). The tests were conducted at ambient temperature (20°C) and less than 1 % relative humidity. A Triton Laboratory Instrument Control Application, version 1.0.32 (Triton Technology, Keyworth, UK) controlled and maintained the humidity within the chamber.

One hundred force measurements were recorded using each cantilever, employing a distance of 100 nm between sampling points. Force curves using each cantilever were also immediately collected against a freshly cleaned borosilicate glass cover-slip, before and after the F_{adh} measurements. The borosilicate cover slip was used as a non-indenting reference to determine the

sample deformation. The cover slip was cleaned, rinsed and dried using Piranha solution [a mixture of 30% H_2O_2 and 70% concentrated H_2SO_4 in water (1:4)], deionised water and nitrogen gas respectively. Before and directly after all force measurements, the tip radius of each single probe used was characterized by tip self-imaging in order to check the integrity of the tip throughout the studies (Davies et al., 2005).

5.2.2.10 AFM – Tip Characterization

AFM imaging was used in order to image the API particle on each probe, thus allowing the contact radius to be determined using a previously reported procedure (Hooton et al., 2004). Each colloid probe was imaged using an EnviroScope AFM (Veeco, Santa Barbara, CA, USA). A scan rate of 1.0 Hz was used over a 0.5μm x 0.5μm scan size.

5.2.2.11 AFM - Force of Adhesion Determination

AFM was used in order to measure the interactive forces between the anhydrous BDP, BDP CFC-11 clathrate, BDP IPA clathrate, ball milled BDP CFC-11 clathrate and chosen pMDI components. This was performed using the colloid probe technique, where particles of each API material were attached to AFM cantilevers (Davies et al., 2005). To summarise, single particles of each API were attached to individual cantilevers using epoxy resin. The spring constants for each cantilever (determined using the thermal method (Gibson et al., 2003)) ranged between 0.3 Nm^{-1} and 0.5 Nm^{-1}. Correct positioning of the particle on the cantilever was verified using SEM before and after AFM analysis (note: the

samples were not gold coated, as this would clearly render the tips unsuitable for use). Three probes were prepared for each API. Prior to force measurement analysis, each probe was imaged using a tip-characterisation method described elsewhere (Hooton et al., 2002). Imaging and force determination were performed using the EnviroScope AFM. One hundred force measurements were taken using each probe against the surfaces of anhydrous BDP, BDP CFC-11 clathrate, and BDP IPA clathrate in the presence of 20 ml of a model propellant 2H, 3H decafluoropentane (mHFA) (Sigma-Aldrich, UK). The measurements were conducted at 10°C and 25% relative humidity. The force data were integrated and calculated using custom software. The separation energy between each API and each pMDI surface was determined by integrating the area under each force curve, using in-house software.

Calculation of Results

F_{adh} between each probe and the substrate was determined using AFM. From these results, the Work of Adhesion (W_A) was calculated using the equation.

$$W_A = \frac{2F_{adh}}{3\pi R}$$ **Equation 5-2**

Where, R is equal to the radius of the hemispherical point of contact (assumed in accordance with the Johnson-Kendall-Roberts theory) determined by tip characterisation. Subsequently, the surface free energy of material was calculated using the formula:

$$\gamma_1 = \frac{W_A^2}{4\gamma_2}$$ **Equation 5-3**

In the case where blank cantilevers were used, γ_2 relates to the surface free energy of the silicon tip, which has a nominal value of 42 mJm^{-2}. Different publications have shown that the dispersive surface energy of silica determined using the contact angle technique, ranges from approximately 41 to 43 mJm^{-2} (Davies et al., 2005). The sample surface deformation (d) due to indentation was calculated from the difference in the gradient of the force - distance approach curve, subsequent to contact between the reference and sample surfaces. Following AFM measurements, the functionalised V-shaped cantilevers were analysed using SEM again to ensure that the imaging and force measurements had not changed the particle morphology or removed the particles completely from the apex of the AFM cantilever.

5.3 Results and Discussion

5.3.1 SEM Results

SEM images of the different BDP entities used in this chapter before and after ball-milling are shown in Figure 5-1. There are considerable changes that have occurred in the morphology of the BDP CFC-11 clathrate, changing from a well-defined hexagonal crystal structure to a more spherical structure of an average particle size of less than 10 µm in size. SEM images of the each pMDI component surfaces are shown in Figure 5-2. From these images, it can be seen

that the surface topographies can vary considerably between the different materials. For example, asperities can be seen on the surfaces of the valve seals, whilst striations are visible on the metering chambers. These features could be a result of manufacturing processes such as drawing for the springs and disk-pressing for the seals. Also, the surface of both EPDM valve seal and the Nitrile valve seal show a considerably higher surface roughness compared to the other pMDI components.

Both the SEM imaging and tip characterisation imaging of the cantilevers functionalised with drug particles, confirmed the integrity of the particles (Fig. 5-3). The drug particles were clearly proud of the cantilever surface and the morphologies of the particles were unchanged throughout the study.

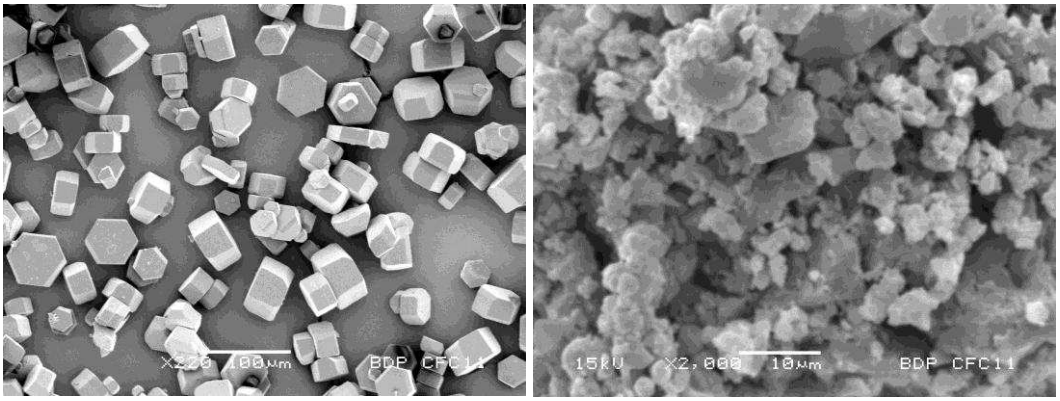

Figure 5-1: SEM photographs of crystalline BDP CFC-11 (left) and ball-milled BDP CFC-11 clathrate.

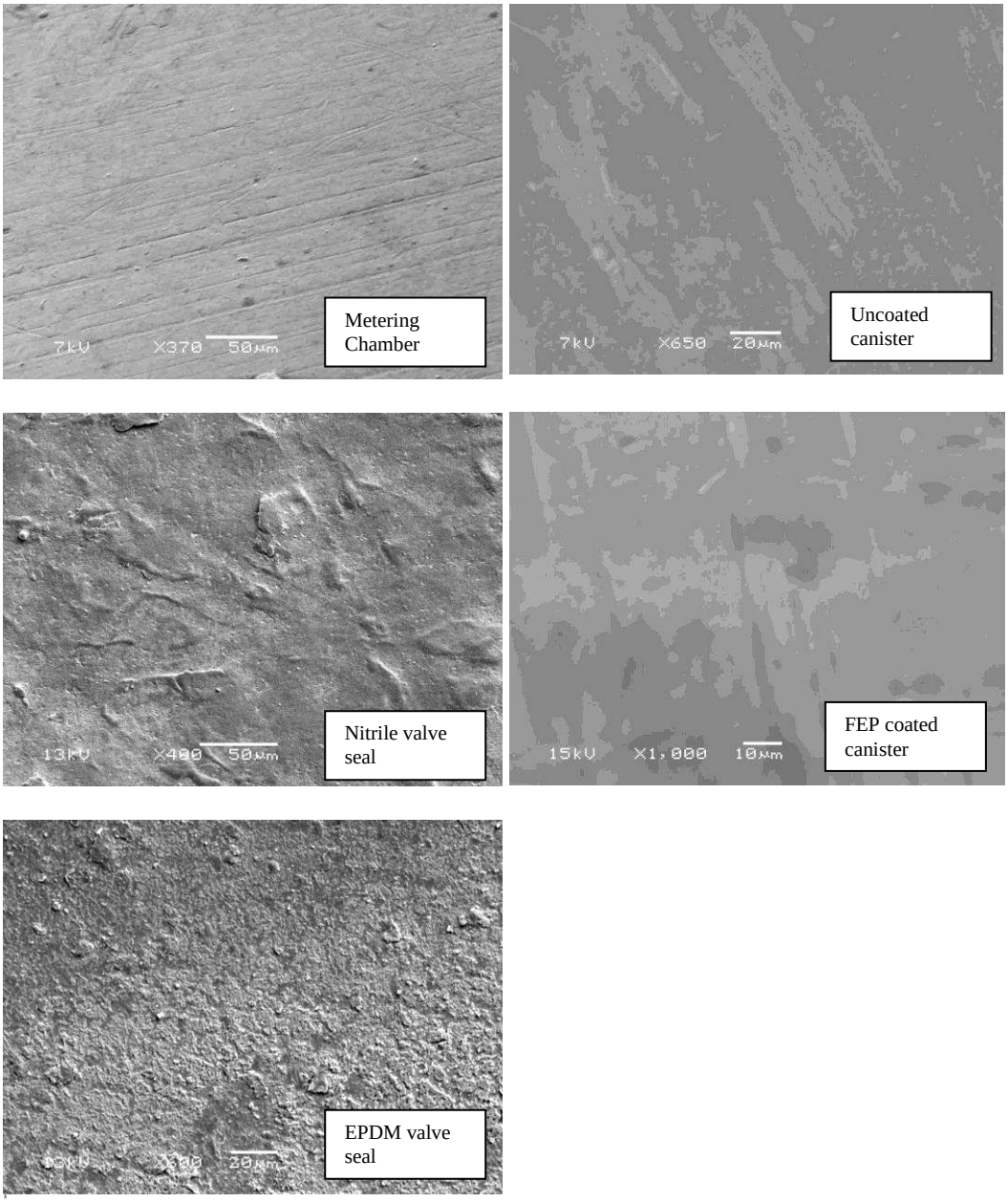

Figure 5-2: SEM images of selected pMDI components used in this study.

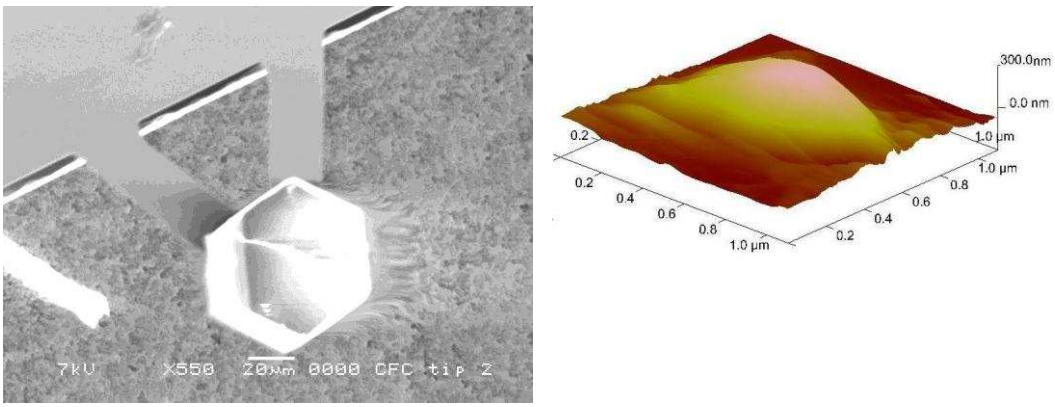

Figure 5-3: SEM Image of colloid probe (Left) and an AFM Image of API particle on probe (Right).

5.3.2 X-RPD Results

A reasonable match was obtained for ball-milled BDP CFC-11 clathrates when compared with patterns calculated based on the partial structures reported for the BDP EtOH HFA-134a clathrate (Fig. 5-4). The peak positions for the ball-milled BDP CFC-11 clathrate show a very good match with the characteristic peaks observed for the calculated clathrate pattern. These results confirm that the clathrate structure is retained and that there is no structural rearrangement or po-

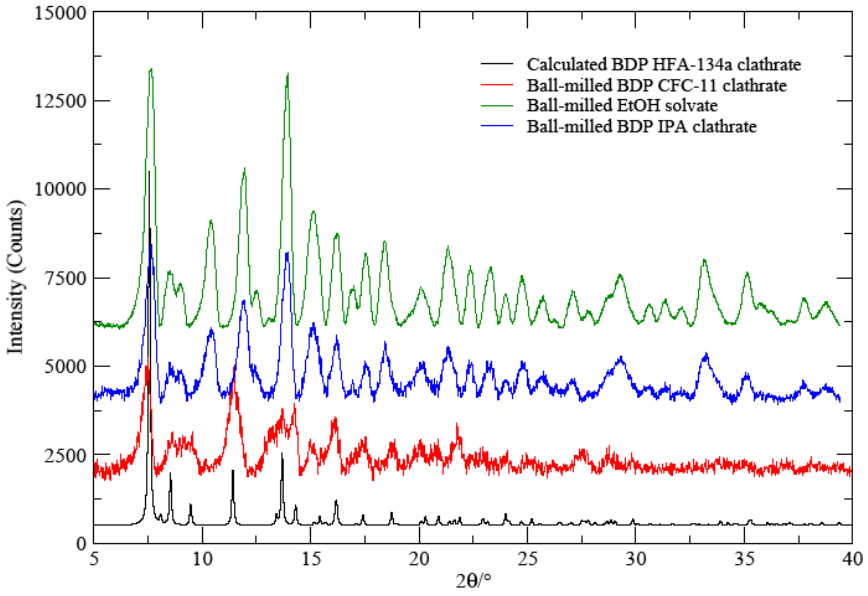

Figure 5-4: Superimposition of both ball-milled BDP CFC-11 clathrate and calculated BDP EtOH HFA-134a clathrate X-RPD patterns.

lymorphic changes in the crystal structure following size reduction. However, the characteristic peaks for the ball-milled BDP CFC-11 clathrate are broader and have less intensity compared to the crystalline structure. The decrease in the intensity of the peaks is due to the introduction of some amorphous regions upon milling. The amorphous regions are less ordered than the crystalline compound and therefore result in a broader, less sharp peaks with a lower intensity (Baites

et al., 2006). The same effect is observed for both ball-milled BDP EtOH solvate and ball-milled BDP IPA clathrate (Fig. 5-4)

5.3.3 TGA Results

The different BDP clathrates and solvates were heated to 300°C in order to investigate the total weight loss observed and determine if any structural changes in terms of the solvate/clathrate structure occurred after size reduction. The loss of CFC-11 molecules from the clathrate structure was observed between 85°C and 100° (Fig. 5-5) as was observed and reported in Chapter 3, Section 3.3.4.2. The weight loss is expressed by 11.61 ± 1.6 % which is 2% less than the non-milled BDP CFC-11 clathrate weight loss after heating. This is interpreted as the weight loss corresponding to the loss of CFC-11 from the crystal structure of the clathrates. The total weight loss for both the BDP EtOH solvate and the BDP IPA clathrate was expressed by 7.3 ± 0.65 % and 9.6 ± 1.36 % respectively as shown in Table 5-1. The weight loss of these two BDP entities also shows an approximate 2% decrease in weight loss when compared to the results obtained for the non-milled BDP EtOH solvate and the BDP IPA clathrate. From these results, it is demonstrated that the structure of both the solvate and the clathrate retains the propellant/solvent even after undertaking size reduction and that no significant loss of solvent/propellant is seen.

However, both TGA traces observed for ball-milled BDP EtOH solvate and ball-milled BDP IPA clathrate show a continuous and gradual weight loss that started as soon as the heating of the samples was initiated and continued until complete

Table 5-1: The different ball-milled crystal samples encountered together with experimental (TGA) calculated weight loss in weight %.

Samples (ball-milled)	% TGA weight loss (n=3)
BDP CFC-11 clathrate (1.67% w/w BDP in CFC-11)	11.61 ± 1.6
BDP EtOH solvate	7.3 ± 0.65
BDP IPA clathrate	9.6 ± 1.36

release of both solvents at approximately 120°C for the BDP EtOH solvate and 125°C for the BDP IPA clathrate as shown in Figure 5-5. The initial release of solvents is thought to be due to the evaporation of the excess solvent present on the surface of the ball-milled BDP EtOH solvate and the ball-milled BDP IPA clathrate. The presence of the solvent at the surface of the crystal samples is a result of the release of the solvent from the crystal structure of the crystallized BDP upon milling. The process of size reduction, will lead to some morphological changes as observed for the BDP CFC-11 clathrate on Figure 5-1 where the structure of the crystals becomes more rounded and spherical. Similar structures were observed for both ball-milled BDP EtOH solvate and BDP IPA clathrates (results not shown). These changes will result in the partial or complete destruction of the structure of some of the crystals leading to the release of the propellant/solvent from the unit cells constituting the crystal and therefore some reduction in the weight loss. As the solvent/propellant molecules are no longer entrapped within the crystal structure, they easily evaporate upon heating as shown in the results when the heating is initiated.

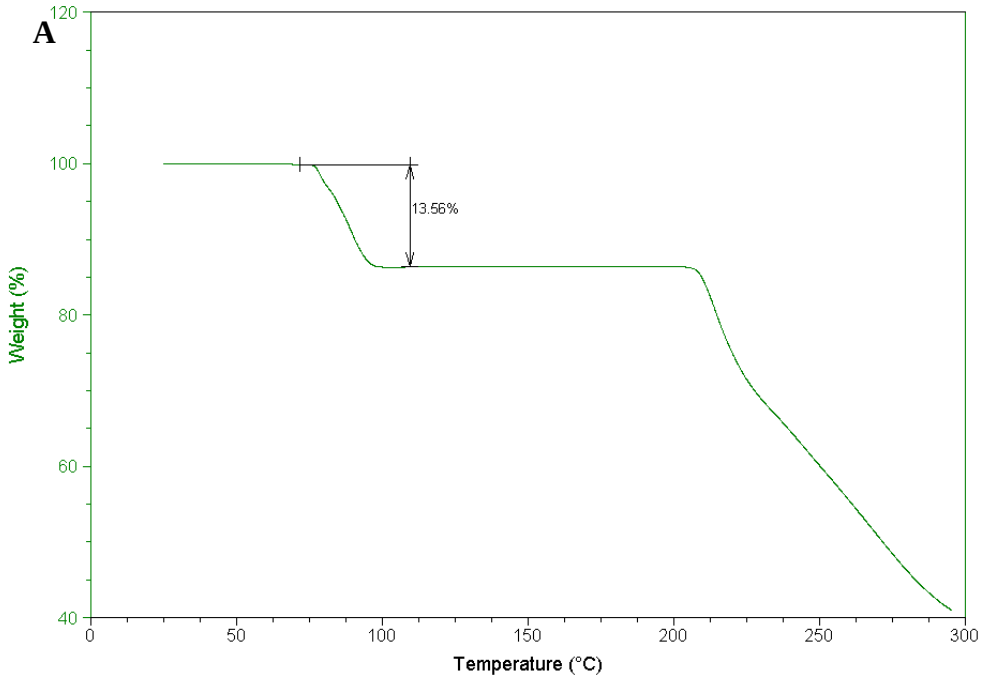
A
120
100
80
60
40
Weight (%)
13.56%
0
50
100
150
200
250
300
Temperature (°C)

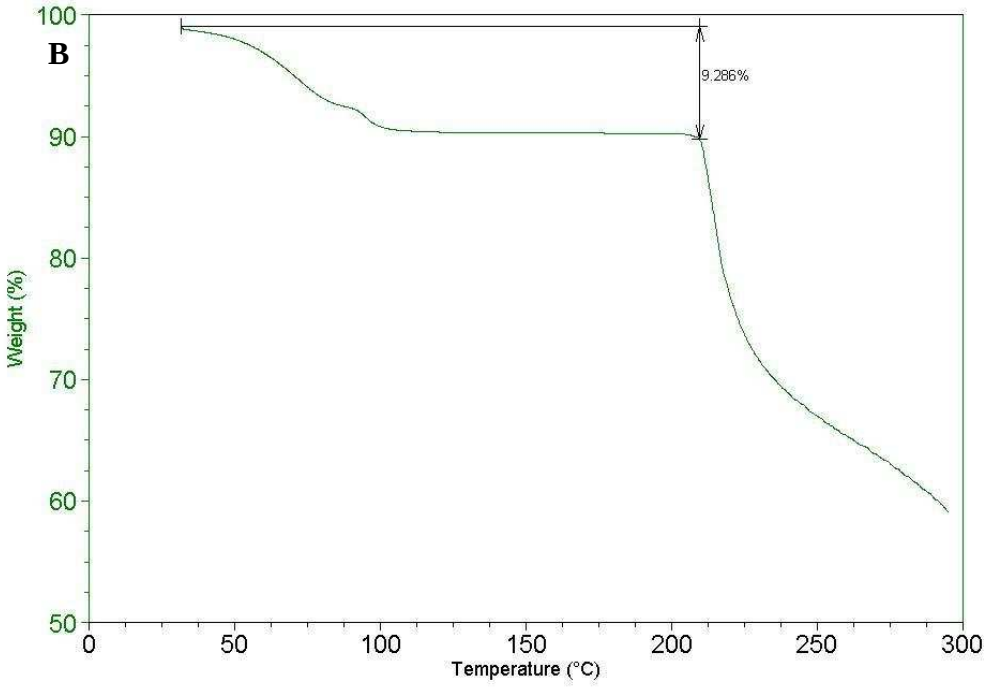
100
B
90
80
70
60
50
Weight (%)
9.286%
0
50
100
150
200
250
300
Temperature (°C)

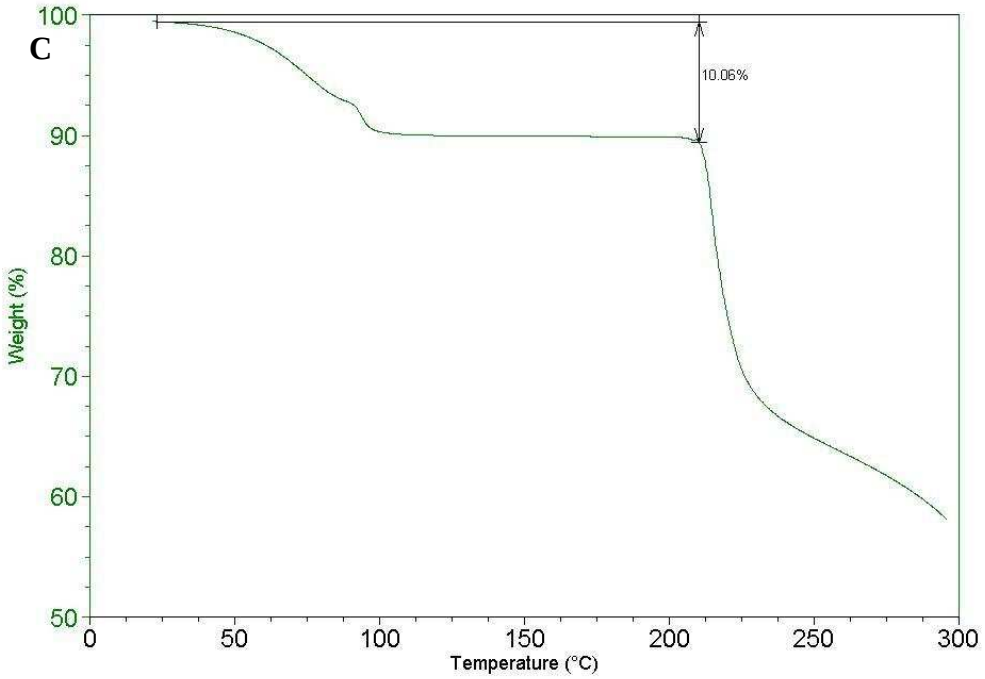

Figure 5-5: TGA curve of ball-milled: A- BDP CFC-11 clathrate, B- BDP EtOH solvate and C-BDP IPA clathrate. All samples were heated from 0°C to 300°C at a heating rate of 10°C/min.

5.3.4 Atomic Force Microscopy (AFM) – Topographical Imaging Acquisition

Two-dimensional and three-dimensional AFM images of various pMDI component surfaces (5 μm x 5 μm) are shown in Figure 5-6. From these images, it can be seen that the surface topographies can vary considerably between different materials. For example, the asperities seen on the non-coated pMDI canister are far less apparent on the FEP-coated canister. Meanwhile, striations are visible on the metering chamber and less-ordered surface roughness is observed on the valve stem and the valve seal. AFM images at this scale serve to further highlight that these features are more than likely attributed to manufacturing processes such as drawing coating and disk-pressing, as seem with the SEM images.

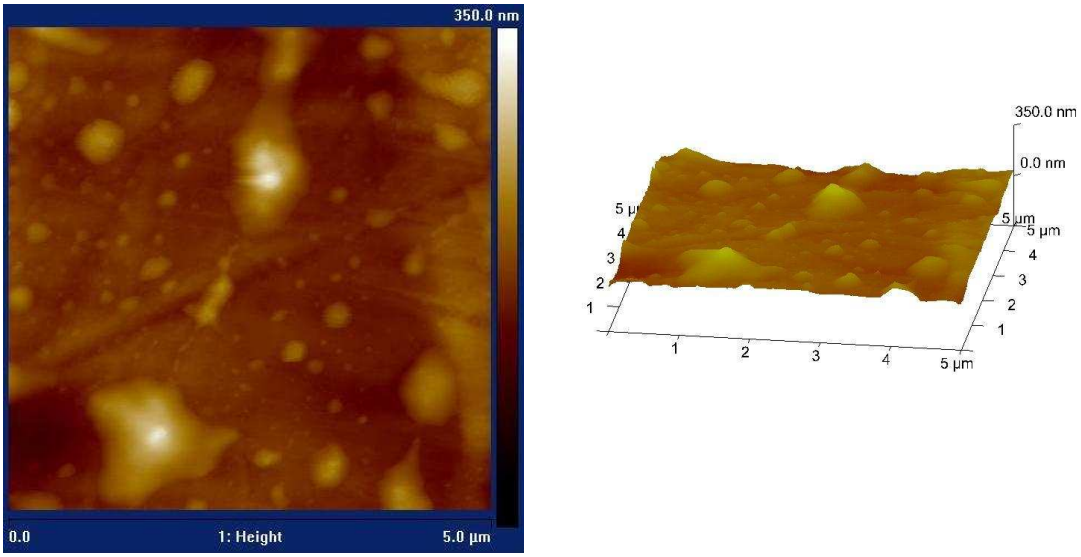

A- FEP Polymer Coated Aluminium Canister

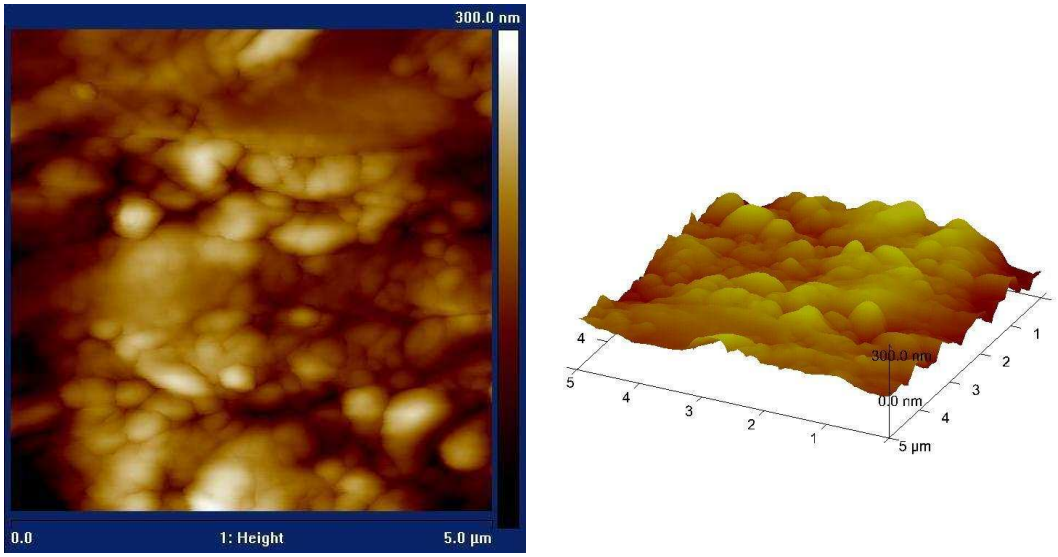

B- Uncoated Aluminium Canister

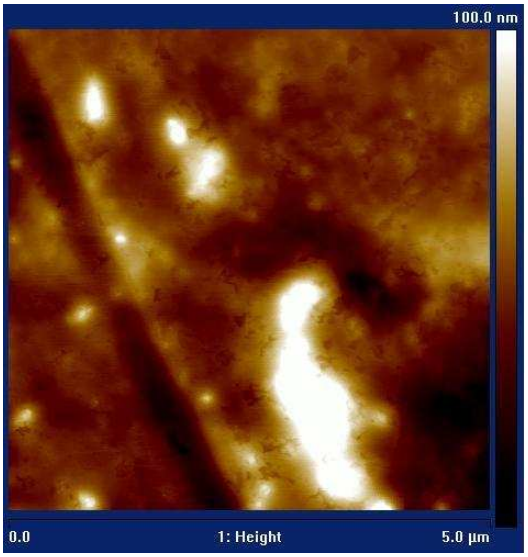

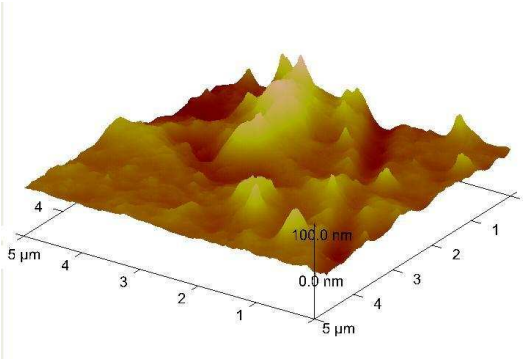

C- Stainless Steel Metering Chamber

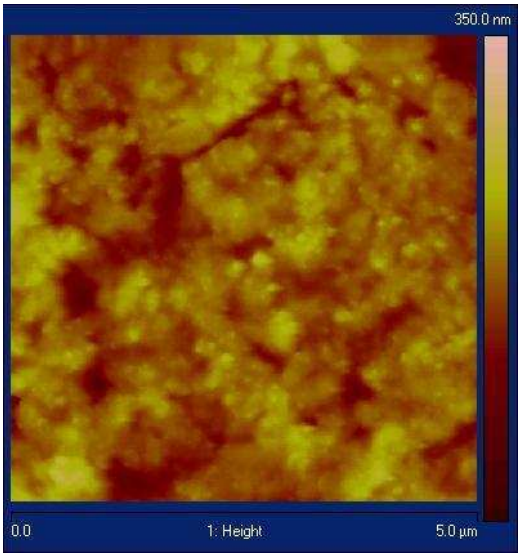

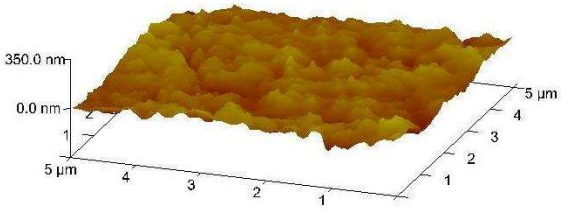

D- Nitrile Valve Seal

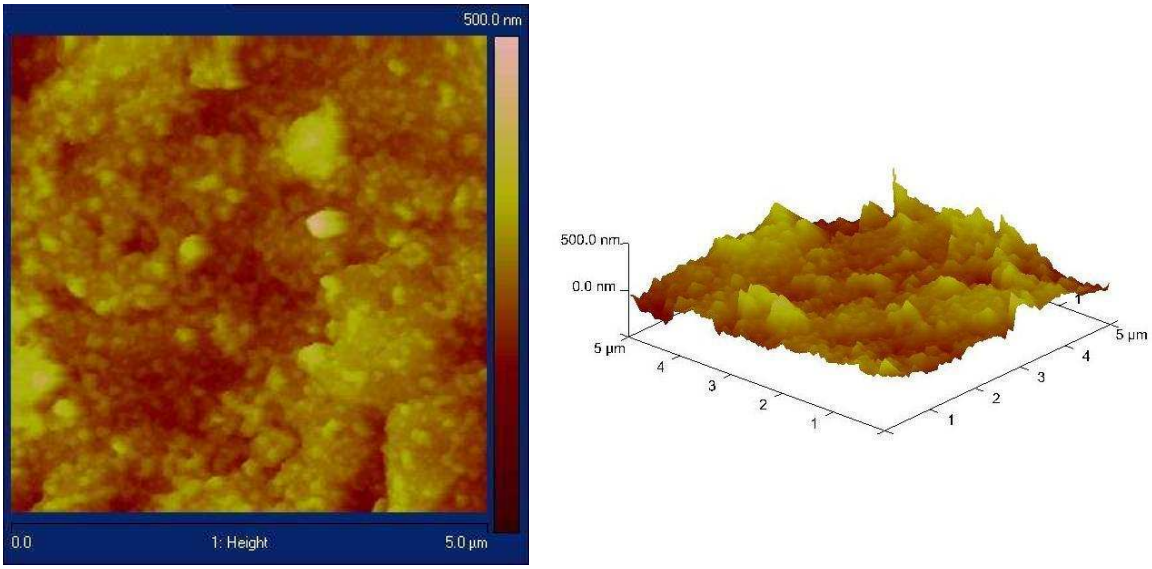

E- Ethylene Propylene Diene Monomer (EPDM) Valve Seal

Figure 5-6: 2D and 3D AFM images of various pMDI components (scale; 5 µm x 5 µm).

5.3.5 RMS Roughness Analysis

Table 5-2 shows the RMS roughness determined from individual particles for each of the API materials. The roughness of micronized anhydrous BDP is significantly higher compared to BDP IPA clathrate and BDP CFC-11 clathrate roughness values ($P < 0.05$). Ball-milling of the clathrate produced a significantly higher roughness value compared to the crystalline materials of the same compound ($P < 0.05$). In general, their relatively low levels of surface roughness are consistent with their crystalline nature. The increase in the surface roughness of the ball-milled BDP CFC-11 clathrates compared to the crystalline ones is due to the introduction of some irregularities on the surface of the ball-milled clathrate that resulted from the ball-milling process. However, the AFM images highlight irregular areas on some of the API crystals. These 'craters' could have been created due to particle-particle agitation during the post-manufacture storage and transit of these APIs. Therefore, for the AFM adhesion

experiments it was important to select visibly smooth surfaces from the more uniform-looking crystals.

Table 5-2: RMS roughness values for each of the BDP entities used in this study. Statistical significance was defined as $P < 0.05$ between anhydrous BDP and the rest of the BDP entities.

Active Pharmaceutical Ingredients	RMS Roughness (nm) (n=3)
Anhydrous BDP	117.6 ± 5.8
BDP IPA clathrate	29.5 ± 6.5 (**)
Ball-milled BDP IPA clathrate	98.76 ± 12.42
BDP CFC-11 clathrate	12.1 ± 4.4 (***)
Ball-milled BDP CFC-11 clathrate	94.2 ± 17.6
BDP EtOH Solvate	35.16 ± 8.9 (**)
Ball-milled BDP EtOH Solvate	101.84 ± 4.7

The SEM images highlight the difference in surface topography of each component. For example, asperities can be seen on the surfaces of the valve seals, whilst striations are visible on the metering chambers. These features could be a result of manufacturing processes such disk-pressing for the seals or polishing for the metering chamber. The RMS roughness calculations support the SEM data. Uncoated aluminium canisters have a significantly higher roughness value than the FEP coated aluminium canisters (Table 5-3) ($P < 0.05$). This is probably due to the FEP coating on the canisters. The roughness value of the stainless steel metering chamber is lower than both the aluminium canisters (Table 5-3), probably due to the polishing process of the chamber during the manufacturing process. Unlike the metallic component of the pMDI, both EPDM and nitrile seal shows a higher roughness value, which might be related to the nature of the material. Both the SEM images and RMS roughness data suggest irregular surface characteristics and prominent asperities for certain materials.

Table 5-3: RMS roughness values for each pMDI component used in this study. Statistical significance was defined as $P < 0.05$ between uncoated and FEP coated aluminium canister.

pMDI System Component	RMS Roughness (nm) (n=3)
Uncoated Aluminium Canister	40.0 ± 9.3
FEP Coated Aluminium Canister	24.7 ± 1.3
Stainless Steel Metering Chamber	22.8 ± 8.4
Ethylene Propylene Diene Monomer (EPDM) Valve Seal	47.5 ± 5.85
Nitrile Valve Seal	34.45 ± 3.5

5.3.6 AFM - Surface Energy Determination

The surface energy (γ) and work of adhesion (W_a) values determined using the AFM adhesion data for each BDP formulation using blank FESP tips are summarised in table 5-4. The observed ranges of W_a and γ values for each material indicate that the relative surface energies of the BDP formulations rank as follow: micronized BDP: IPA clathrate> micronized anhydrous BDP > ball-milled BDP EtOH solvate ball-milled BDP IPA clathrate > crystalline BDP EtOH solvate > crystalline BDP IPA clathrate > ball-milled BDP CFC-11 clathrate> crystalline BDP CFC-11 clathrate. The surface energy tip images obtained using AFM indicate that the structural integrity of each tip was maintained throughout the process of imaging and the force measurements.

Figure 5-7 highlights the significant reduction in surface energy on the clathrate and solvate forms of BDP compared to anhydrous BDP ($P < 0.001$). Expect for ball-milled BDP EtOH solvate and ball-milled BDP IPA clathrate (statistically similar to anhydrous BDP in terms of surface energy), ball-milling had no major effects on the surface energy of both clathrate forms of BDP. In addition, the

changes in surface energy accompanying the ball-milling show a significant increase in surface energy compared to the non-milled crystalline forms of the same material expect for BDP CFC-11 clathrates where ball-milling resulted in non significant change in surface energy ($P < 0.01 – 0.001$).

The higher surface energy observed for the BDP: IPA clathrate and BDP EtOH solvate is most likely attributable to its non-solvated nature, since the IPA and EtOH associated with the BDP could possibly promote hydrogen bonding (Fig. 5-7). Thus, the surface of the BDP may be more 'active' compared to anhydrous

Table 5-4: The mean force of adhesion, work of adhesion and surface free energy of the different BDP clathrates, determined using blank FESP cantilevers (n=100).

	Mean force of adhesion (F_{adh}) (nN)	**Mean work of adhesion (W_a) (mJm^{-2})**	**Mean surface energy (γ) (mJm^{-2})**
Anhydrous BDP	242.20 ± 16.37	88.52 ± 8.69	47.5 ± 4.9
BDP IPA clathrate	144.12 ± 22.38	52.69 ± 11.88	16.5 ± 6.7
Ball-milled BDP IPA clathrate	197.65 ± 23.06	72.06 ± 5.75	31.04 ± 4.86
BDP EtOH solvate	145.06 ± 11.85	53.38 ± 2.97	17.68 ± 1.88
Ball-milled BDP EtOH solvate	245.05 ± 3.44	90.43 ± 2.08	48.68 ± 1.2
BDP CFC-11 clathrate	120.62 ± 4.13	44.05 ± 0.77	11.3 ± 4.1
Ball-milled BDP CFC-11 clathrate	138.25 ± 22.77	50.85 ± 2.08	15.24 ± 1.26

BDP. The higher surface energy of the ball-milled BDP CFC-11 clathrate compared to the non-milled BDP CFC-11 clathrate may be due to either the formation of some amorphous material or the exposure of higher energy sites on the surface (Fig. 5-7). This has implications when considering interparticulate interactions, since a higher surface energy typically results in greater cohesive

and adhesive properties. The reduction in the dispersive surface energy suggests that the formation of the CFC-11 clathrate may have a positive effect in terms of reduced interaction within an MDI formulation.

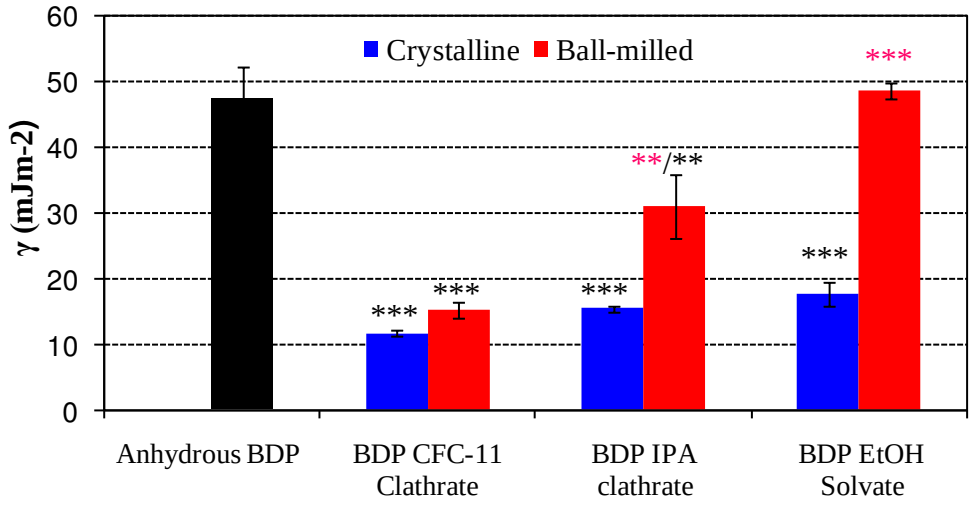

Figure 5-7: Surface energy of micronized anhydrous BDP, both crystalline and ball-milled BDP CFC-11 clathrate, BDP IPA clathrate and BDP EtOH solvate determined by AFM. Statistical significance was defined as $P < 0.05$ compared to anhydrous BDP, *** = $P < 0.001$, ** = $P < 0.01$. The significance between the crystalline and ball-milled entities was also defined as $P < 0.05$, *** = $P < 0.001$, ** = $P < 0.01$.

5.3.7 AFM – Force of Adhesion Determination

As stated previously, the force of adhesion between each BDP solid form and each pMDI component was determined using AFM. It is clear from Figure 5-8 that there are differences in the level of API adhesion to each pMDI material. There appears in general to be more API adhesion to the metallic components such as the metering chamber and to the valve seals. From this figure, it can be observed that the normalized force of adhesion is significantly highest for the anhydrous with the different pMDI components except for EPDM seal ($P < 0.05$-0.001). BDP CFC-11 clathrates showed the most significant reduction in F_{adh} compared to anhydrous BDP and BDP IPA clathrates within all the different

pMDI components ($P < 0.001$). Furthermore, ball-milling of the BDP CFC-11 clathrate does not seem to have any major effect in terms of adhesion to the different pMDI components as it showed only a slightly higher F_{adh} than the crystalline BDP CFC-11 clathrate. It can be seen from Figure 5-8, that the normalized F_{adh} for the four different BDP entities with the two types of aluminium canister are approximately the same with a slightly lower adhesion to the fluorinated ethylene propylene (FEP) coated aluminium canister. This is due to the FEP coated aluminium canister having a lower surface energy and a slightly smoother surface than the uncoated aluminium canister. Concerning the F_{adh} of the different BDP entities with the two seals, the results show a very large difference in the adhesive force. Higher normalized F_{adh} values were observed for the different BDP entities with the nitrile ring seal compared to the ethylene diene M-class rubber (EPDM) seal. However, BDP CFC-11 clathrate still show the lowest adhesion with both seals. The significantly high F_{adh} seen with the nitrile ring seal could be attributed to the roughness of the surface of the seal and the irregularities of the surface observed using AFM (Fig. 5-6). The data obtained for the F_{adh} measurements with of the APIs with the different pMDI components supports the results obtained with the surface energy obtained in Chapter 5, Section 5.3.6. Higher surface energies of the particles will automatically result in higher force of adhesion with other particles/surface or increase cohesion within the particles themselves. The higher surface energies observed with the micronized BDP resulted in higher adhesion with the different pMDI components. Similarly, the force of adhesion of ball-milled BDP CFC-11 clathrates showed higher force of adhesion to most of the pMDI component compared to the crystalline BDP CFC-11 clathrate which is in total agreement

with the results observed with the surface energy that showed a higher surface energy of the ball-milled clathrates compared to the crystalline ones.

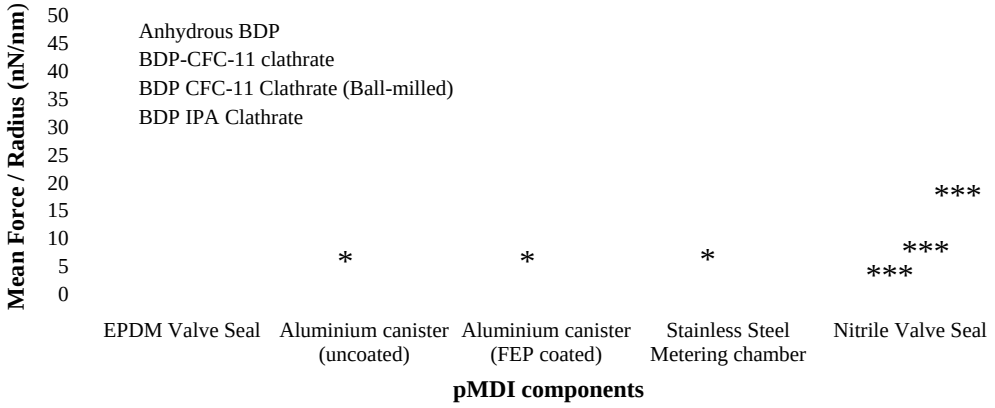

Figure 5-8: Normalized force of adhesion of anhydrous BDP, BDP IPA clathrate and BDP CFC-11 clathrate (crystalline and ball-milled) with different pMDI component. Statistical significance was defined as $P < 0.05$ compared to anhydrous BDP within the individual pMDI components, *** = $P < 0.001$, * = $P < 0.05$.

An important consideration when obtaining adhesion measurements from a number of different surfaces is the variation in the roughness of each surface, since roughness directly affects the degree of contact between the probe and the surface. Thus, it is undesirable for the surface roughness to be a major contributing factor in the adhesion forces measured. Previous studies have shown that significant surface roughness would results in a log-normal frequency distribution of adhesive force measurements, (Price et al., 2002, Young et al., 2004), whereas a smooth surface would result in a normally distributed frequency distribution of force measurements (Buckton et al., 1995, Price et al., 2002). Normal frequency distributions were obtained for all adhesion measurements; hence it can be assumed that surface roughness was not significant factor of the adhesion data produced here.

5.4 Conclusions

Surface roughness values for each BDP solid form were determined at sample sizes of 5µmx5µm. The different BDP entities ranked in terms of surface roughness as follow: anhydrous BDP > ball-milled BDP IPA clathrate > ball-milled BDP CFC-11 clathrate > BDP IPA clathrate > BDP CFC-11 clathrate.

It was possible to calculate the surface energy of the different material using single particle adhesion data. The surface free energies for anhydrous BDP (micronized), BDP CFC-11 clathrate (ball- milled for 2.5 hours) and the BDP CFC-11 clathrate (crystalline) were 47.5 ± 4.9 mJm^{-2}, 15.24 ± 1.26 mJm^{-2} and 11.27 ± 4.05 mJm^{-2} respectively. Normalised force of adhesion results measured in a model propellant showed that BDP CFC-11 clathrates had a lower F_{adh} compared to anhydrous BDP with the different pMDI components studied and that size reduction of the BDP CFC-11 clathrate did not have any major effect in terms of surface energy and F_{adh}. The adhesive interactions between the three different BDP entities and pMDI components in a model propellant had been characterised using AFM.

The results generally suggest that the in situ formation of a clathrate in a propellant formulation is beneficial in terms of a reduction the force of adhesion with different pMDI components. This could have implications for future HFA formulation development with APIs that are prone to the formation of propellant clathrates because BDP forms a clathrate with HFA 134a much more slowly (over a time scale of months), when the two materials are mixed in suspension formulations (Vervaet and Byron, 1999).

5.5 References

AHMED, H., BUCKTON, G. & RAWLINS, D. A. (1996) The use of isothermal microcalorimetry in the study of small degrees of amorphous content of a hydrophobic powder. International Journal of Pharmaceutics, 130**,** 195-201.

AKBARIEH, M. & TAWASHI, R. (1987) Morphic features of solid particles after micronization in the fluid energy mill. International Journal of Pharmaceutics, 35**,** 81-89.

BAITES, S., ZOGRAFI, G., ENGERS, D., MORRIS, K., CROWLEY, K. & AND NEWMAN, A. (2006) Analysis of Amorphous and Nanocrystalline Solids from Their X-Ray Diffraction Patterns. Pharmaceutical Research, 23**,** 2333-2349.

BRIGGNER, L. E., BUCKTON, G., BYSTROM, K. & DARCY, P. (1994) The use of isothermal microcalorimetry in the study of changes in crystallinity induced during the processing of powders. International Journal of Pharmaceutics, 105**,** 125-135.

BUCKTON, G., CHOULARTON, A., BEEZER, A. E. & CHATHAM, S. M. (1988) The effect of comminution technique on the surface energy of a powder. International Journal of Pharmaceutics, 47**,** 121-128.

BUCKTON, G., DARCY, P. & MCCARTHY, D. (1995) The Extent of Errors Associated with Contact Angles .3. the Influence of Surface-Roughness Effects on Angles Measured Using a Wilhelmy Plate Technique for Powders. Colloids and Surfaces a-Physicochemical and Engineering Aspects, 95**,** 27-35.

BURT, H. M. & MITCHELL, A. G. (1981) Crystal defects and dissolution. International Journal of Pharmaceutics, 9**,** 137-152.

DAVIES, M., BRINDLEY, A., CHEN, X., MARLOW, M., DOUGHTY, S. W., SHRUBB, I. & ROBERTS, C. J. (2005) Characterization of drug particle surface

energetics and young's modulus by atomic force microscopy and inverse gas chromatography. Pharmaceutical Research, 22**,** 1158-66.

GERHARDT, A. S., ANLNECK, C. & ZOGRAFI, G. (1994) Assessment of disorder in crystalline solids. International Journal of Pharmaceutics, 101**,** 237-247.

GIBSON, C. T., WEEKS, B. L., ABELL, C., RAYMENT, T. & MYHRA, S. (2003) Calibration of AFM cantilever spring constants. Ultramicroscopy, 97**,** 113-8.

HOOTON, J. C., GERMAN, C. S., ALLEN, S., DAVIES, M. C., ROBERTS, C. J., TENDLER, S. J. & WILLIAMS, P. M. (2004) An atomic force microscopy study of the effect of nanoscale contact geometry and surface chemistry on the adhesion of pharmaceutical particles. Pharmaceutical Research, 21**,** 953-61.

HOOTON, J. C., GERMAN, C. S., ALLEN, S., DAVIES, M. C., ROBERTS, C. J., TENDLER, S. J. B. & P.M., W. (2002) Characterization of Particle-Interactions by Atomic Force Microscopy: Effect of Contact Area. Pharmaceutical Research, 20**,** 508-514.

KONTNY, M. J., GRANDOLFI, G. P. & ZOGRAFI, G. (1987) Water Vapor Sorption of Water-Soluble Substances: Studies of Crystalline Solids Below Their Critical Relative Humidities. Pharmaceutical Research, 4**,** 104-112.

LE-BAIL, A., DUROY, H. & FOURQUET, A. J. L. (1988) Ab-initio structure determination of $LiSbWO_6$ by X-ray powder diffraction. Material Research Bulletin**,** 447-452.

LUCAS, P., ANDERSON, K., POTTER, U. J. & STANIFORTH, J. N. (1999) Enhancement of small particle size dry powder aerosol formulations using an ultra low density additive. Pharmaceutical Research, 16**,** 1643-7.

OMELCZUK, M. O., WANG, C. C. & POPE, D. G. (1997) Influence of micronization on the compaction properties of an investigational drug using tableting index analysis. European Journal of Pharmaceutics and Biopharmaceutics, 43**,** 95-100.

OTSUKA, M. & KANENIWA, N. (1990) Effect of grinding on the crystallinity and chemical stability in the solid state of cephalothin sodium. International Journal of Pharmaceutics, 62**,** 65-73.

PRICE, R., YOUNG, P. M., EDGE, S. & STANIFORTH, J. N. (2002) The influence of relative humidity on particulate interactions in carrier-based dry powder inhaler formulations. International Journal of Pharmaceutics, 246**,** 47-59.

SADER, J. E., LARSON, I., MULVANEY, P. & WHITE, L. R. (1995) Method for the calibration of atomic force microscope cantilevers. Review of Scientific Instruments, 66**,** 3789-3798.

STEGEMANN, B., BACKHAUS, H., KLOSS, H. & SANTNER, A. E. (2007) Spherical AFM Probes for Adhesion Force Measurements on Metal Single Crystals. Modern Research and Educational Topics in Microscopy**,** 820-827.

VERVAET, C. & BYRON, P. R. (1999) Drug-surfactant-propellant interactions in HFA-formulations. International Journal of Pharmaceutics, 186**,** 13-30.

WARD, G. H. & SCHULTZ, R. K. (1995) Process-induced crystallinity changes in albuterol sulfate and its effect on powder physical stability. Pharmaceutical Research, 12**,** 773-9.

YOUNG, P. M., PRICE, R., TOBYN, M. J., BUTTRUM, M. & DEY, F. (2004) The influence of relative humidity on the cohesion properties of micronized drugs used in inhalation therapy. Journal of Pharmaceutical Sciences, 93**,** 753-761.

Chapter 6 Investigation of Ostwald Ripening of Beclomethasone Dipropionate and Budesonide in a Model pMDI System

6.1 Introduction

The general environmental issues related to the use of chlorofluorocarbons (CFCs) and their replacement hydrofluoroalkanes (HFAs) are well known and following the advent of the Montreal Protocol in 1989, this has led to the phasing out of CFCs and alternative MDI systems containing HFAs have needed to be developed. The new MDI systems are being investigated for delivery of small molecule drugs as well as peptides and proteins (Vervaet and Byron, 1999, Brindley, 1999, Smyth, 2003, Ganderton et al., 2003, Marijani et al., 2007). HFAs provide a greener alternative to CFCs as propellants in these devices, however, their physicochemical properties have required extensive redevelopment of the CFC based product (McDonald and Martin, 2000). While CFCs are completely halogenated, HFAs are asymmetrical in that they have at least one unbalanced hydrogen atom (Byron and Blondino, 1996). The electronegative influence of fluorine on these molecules results in the hydrogen atom(s) becoming highly electropositive and therefore, susceptible to dipole-dipole interactions. Consequently, HFAs have considerably higher polarity than CFCs which is responsible for the obstacles associated with HFA formulation development (Clarke et al., 1993, Vervaet and Byron, 1999, Butz et al., 2002, Wu and da Rocha, 2007).

Surfactants were incorporated into CFC pMDIs for several reasons. In suspensions, surfactants have been used to stabilize the dispersion by reducing the electrostatic charges of the micronized drug (Johnson, 1996), help solubilise drug and prevent crystal growth during storage in solution formulations and valve lubrication (Vervaet and Byron, 1999). The solubility of the different surfactants in HFA 134a and 227ae is considerably lower than the concentration required to stabilize CFC suspensions (Byron et al., 1994, Smyth, 2003). Surfactants traditionally used in CFC-based pMDIs are not soluble in HFAs without the use of co-solvents (Smyth, 2003). However, the use of co-solvents, such as ethanol, is most likely incompatible with suspension formulations as drug solubility will also be promoted (Smyth, 2003). The resulting increase in drug solubility can promote partial drug dissolution and crystal growth due to Ostwald Ripening (Vervaet and Byron, 1999). This is a process where small particles (less energetically favoured) thermodynamically associate with larger particles (more energetically favoured), due to entropy favouring the dissolution of small particles. Therefore changing the aerodynamic size distribution of the dose (Vervaet and Byron, 1999). The consequence of this phenomenon is a product of limited stability due to poor dosing consistency and a decrease in the fine particle fraction as required for penetration of the drug into the deep lung. Thus, there is a need for surfactants which are significantly more soluble in HFA propellants. The effect of surfactants on emitted droplet size has been investigated by several groups. In work performed by Polli et al. the surfactant sorbitan trioleate decreased the mass median aerodynamic distribution (MMAD) of the CFC dexamethasone suspension when added to the formulation (Polli et al., 1969). A suspension of terbutaline in a CFC system containing sorbitan

trioleate surfactant was also shown to have little change in emitted particle size (Baeckstroem and Nilsson, 1988).

Reformulation of suspension aerosols in HFAs is of great current interest and may help the different problems encountered in suspension pMDI formulations. Typically, suspension aerosols will contain a mixture of micronized drug, a surfactant, a co-solvent, and propellant(s). A surfactant, such as oleic acid or lecithin helps to disperse the drug and lubricate the metering valve. A co-solvent, such as ethanol helps to solubilise the surfactants. A co-solvent may also help to disperse the drug and is required to form a drug/co-solvent concentrate in many manufacturing processes currently used for suspension formulations (Tzou et al., 1997).

6.1.1 Chapter Aims and Objectives

Budesonide, like beclomethasone dipropionate, has a significant solubility in replacement HFA propellants (23.13 μg/g and 29.85 for budesonide and BDP respectively in HFA-134a) (Jones et al, 2006, Traini et al, 2006). Therefore, stability with respect to particle size and morphology in the different HFA propellants must be determined in the presence of surfactants and co-solvents. This chapter will discuss the effect of three different mHFA media: mHFA alone, mHFA containing 2% (v/v) anhydrous ethanol as a co-solvent and finally mHFA containing 0.05% (v/v) oleic acid as a surfactant and 2% (v/v) anhydrous ethanol, on the behaviour of BDP and budesonide in the propellant. The effect of the different mHFA media on the morphology and the particle size of the APIs

will be determined using scanning electron microscopy (SEM). Following this, atomic force microscopy (AFM) will be used to study the surface topographical changes and the surface roughness (RMS) of the different APIs when exposed to the different mHFA media. Additionally, a laser diffraction technique was utilised to determine the mean particle size of the different APIs at different time points of storage in the mHFA media. From these data, it will be possible to apply the LSW theory and determine the rate of Ostwald ripening (K_{LSW}) (Chapter 1, Section 1.6.2.3).

6.2 Materials and Methods

All of the chemicals used were the same as the ones stated in Chapter 3, Section 3.2.1. The pMDI components were supplied by 3M drug delivery systems Ltd (Loughborough, UK).

6.2.1 Methods

6.2.1.1 Preparation of mHFA Based Media for Ripening Studies

To examine the effect of ethanol and oleic acid on the API ripening in a model propellant mHFA, the following solutions were used:

Anhydrous mHFA: This medium was used as a control environment in order to determine the coarsening behaviour of the API molecules in a model propellant. A 2.5 litre batch of mHFA was placed into a clean, dry Duran bottle (Duran,

Mainz, Germany). Approximately 100g of molecular sieves (5 Å pore diameter) were added to the bottle, to remove any trace of water from the solution. The bottle was sealed with a screw-lid and Parafilm (Alcan, Neenah, WI, US), and stored in a fridge at 4°C prior to use.

Anhydrous mHFA and 2% v/v Anhydrous Ethanol (mHFA EtOH): This was used as the first test environment to examine the influence of ethanol on API coarsening behaviour. 250 ml of anhydrous mHFA was taken from the 1 litre batch and placed into a clean, dry Duran bottle (Duran). 5.0 ml of anhydrous ethanol prepared in the same way was added to the mHFA using a glass pipette (SLS, Nottingham). Approximately 100g of molecular sieves (5 Å pore diameter) were added to the bottle, to remove any trace of water from the mixed solution. The bottle was sealed with a screw-lid and Parafilm (Alcan), and shaken vigorously by hand for 5 minutes followed by sonication in a sonic bath for 20 minutes. The solution was then stored in a fridge at 4°C for at least 48 hours prior to use.

Anhydrous mHFA with 2% v/v Anhydrous Ethanol and 0.05% v/v Oleic Acid (mHFA EtOH oleic acid): 489.75 ml of anhydrous mHFA was taken from the 1 litre batch and placed into a clean, dry Duran bottle (Duran). Exactly 10.0 ml of anhydrous ethanol prepared in the same way was added to the mHFA using a glass pipette (SLS, Nottingham). The bottle was sealed with a screw-lid and Parafilm (Alcan), and shaken vigorously by hand for 5 minutes followed by sonication in a sonic bath for 20 minutes. Following this, exactly 0.25 ml of oleic acid was added to the mixture. The bottle was again sealed with a screw-lid and

Parafilm (Alcan), and shaken vigorously by hand for 5 minutes followed by sonication in a sonic bath for 20 minutes. 100g of molecular sieves (5 Å pore diameter) were added to the bottle, to remove any trace of water from the mixed solution. The solution was then refrigerated at 4°C for at least 48 hours prior to use.

6.2.1.2 Isolation of BDP CFC-11 Clathrate

Anhydrous BDP was suspended in CFC-11 at a concentration of 1.67% w/w BDP in CFC-11. The same procedure as stated in Chapter 3, Section 3.2.2.1 was used to extract and store the clathrate crystals.

6.2.1.3 Preparation of APIs Compressed Discs for AFM Topographical Imaging

API compressed discs were produced using the same method utilized to produce KBr discs for IR-spectroscopy. The API powders (approximately 300 mg) were transferred into a mortar. Two stainless steel discs were removed from a desicator. The cutout hole was then filled with the powders and the second stainless steel disc was placed on top in the hydraulic press. The die assembly was left under vacuum for 2 minutes to remove air from the discs in a die cast IR press (Specadie, Specar Ltd, Kent, UK). The pressure was then increased to 15 tons for 5 minutes and then slowly released. The discs were then obtained by dismantling the two dies. A pumping movement was used to move the hydraulic

pump handle downward. The piston moved upwards until it reached the top of the pump chamber.

6.2.1.4 Preparation of API Propellant Suspensions for Particle Sizing

50 mg of each of budesonide, anhydrous BDP and BDP CFC-11 clathrates were suspended in 20 ml of each of the mHFA based media described in the section above in a dry vial for use in particle size determination. A small amount of molecular sieves was added to the suspension in order to keep the levels of water to a minimum. The suspensions were then vigorously shaken by hand followed by sonication in a sonic bath for 5 minutes. The solutions were used straight after the sonication.

6.2.1.5 Scanning Electron Microscopy (SEM)

SEM was used in order to determine the surface morphology and qualitative particle size range for the budesonide and BDP entities at different time points while in suspension. 250 µl of each of the suspension was pipetted onto a carbon stub at 1, 10, 20, 35, 60, 120, 360 minutes and 24 hours. The samples were then sputter coated with a thin layer of gold (20 nm thickness) in an argon atmosphere (50Pa) at 30 mA for 4 minutes for SEM analysis. SEM analysis (JEOL (UK) Ltd, Welwyn Garden City, UK) was carried out at an appropriate accelerating voltage (between 1 keV and 10 keV) and a spot size between 48nm and 62 nm. These parameters were varied for each sample in order to optimise each particular image.

6.2.1.6 Atomic Force Microscopy (AFM) – Topographical Imaging Acquisition

Each material was topographically imaged in order to determine the root mean square (RMS) roughness of each BDP and budesonide entity both in a dry environment and then when in continuous immersion in the different mHFA media as prepared above. Each sample was imaged using an EnviroScope (E-Scope) AFM (Veeco, Santa Barbara, USA) in contact mode using D-NPS cantilevers (Veeco, Santa Barbara, USA). The tests were conducted at ambient temperature (20°C) and less than 1 % relative humidity. A Triton Laboratory Instrument Control Application (Triton Technology, Keyworth, UK) controlled and maintained the humidity within the chamber. The compressed API discs were placed in a small petri dish then introduced in the humidity chamber of the E-scope AFM for imaging in both air and liquid to take place. Two different images in air at two different areas of the sample discs were taken in order to determine any topographical difference in the heights of the sample surface. A scan rate of 1.97 Hz was used over 20 µm x 20 µm scans. Once the images in air were acquired, 10 ml of each of the mHFA solutions were added to the petri dish, allowing complete immersion of the sample discs and the AFM tip in the liquid. A scan rate of 1.97 Hz was again used over 20 µm x 20 µm scans. The images were acquired from each of the API discs in continuous mode with an image being taken every 4 minutes and 30 seconds. The images were then used in order to generate the RMS roughness as previously reported in Chapter 5 which was calculated using software incorporated in the AFM system, via the following equation 6-1

$$R_{rms} = \sqrt{\frac{1}{n}\sum_{i=1}^{n} y_i^2} \qquad \textbf{Equation 6-1}$$

where n is the number of points in the topography profile, i is the asperities and y_i is the distance between the asperities.

6.2.1.7 Particle Size Determination Using Light Diffraction Technique

Particle size distribution of the different API suspensions prepared above were determine using a Coulter LS 230 laser light-scattering apparatus (Beckman-Coulter, Miami, FL) which uses the principle of laser diffraction. 500 µl of each API suspension was resuspended in each of the mHFA media (20 ml) prior to introduction into the fluid module. The amount of sample required was determined by the obscuration percentage of the laser beam through the sample cell, with the recommended range between 8 and 12%. The particle size distribution of the different APIs in mHFAs solution was measured in continuous stirring to prevent any sedimentation or agglomeration and using a Fraunhofer mathematical model to determine the size of the particles. Readings were taken at 1, 2, 3, 4, 5, 6, 7, 8, 9, 10, 15, 20, 25, 35, 45, 60, 75, 90, 120, 150, 180, 240, 300 and 360 minutes then at 22, 23 and 24 hours. The length of the measurements was of 30 seconds per run for each reading. A number of statistical summary parameters were generated, which mathematically describe the particle size distribution, including mean, median and standard deviations.

In order to determine the coarsening behaviour of the different pMDI suspensions, LSW theory was applied to the different API suspensions following equation 6-2

$$R^3(t) = K_{LSW} \cdot t + R^3(0)$$ (Snyder, 2001) **Equation 6-2**

where R is the radius of the particles, t is time and K_{LSW} is the rate of Ostwald ripening.

6.3 Results

6.3.1 SEM Results

6.3.1.1 Effects of the Different mHFA Media on Anhydrous BDP

Figure 6-1 shows SEM images of anhydrous BDP, suspended in mHFA, taken at different time points after storage. These images show changes that have taken place rapidly in the morphology of the micronised anhydrous BDP after being suspended in mHFA. The surface of the BDP crystals becoming smoother in appearance and having a more defined crystalline nature than those observed for micronized anhydrous BDP in Chapter 3, Section 3.3.1, Figure 3.1. BDP particles, which were extracted after one minute, have a particle size ranging from 2 to 4 µm (n=50) in size which corresponds to the same particle size observed for micronized anhydrous BDP. However, the different fractions

extracted at different time points from the mHFA BDP suspension showed certain differences related to the size and the

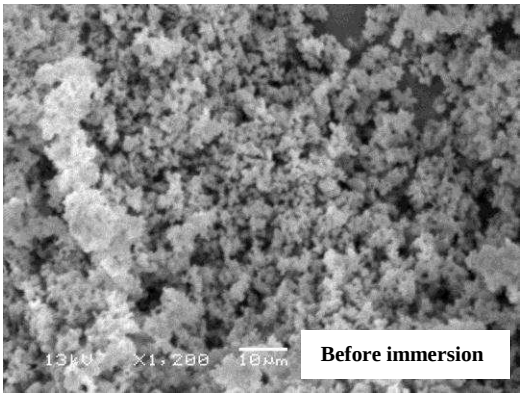

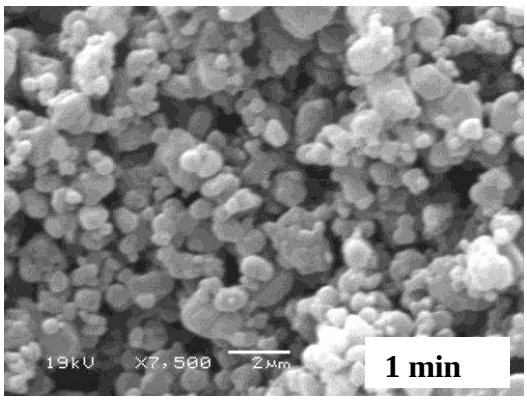

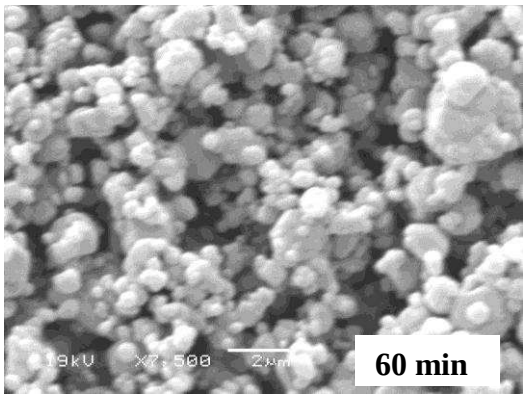

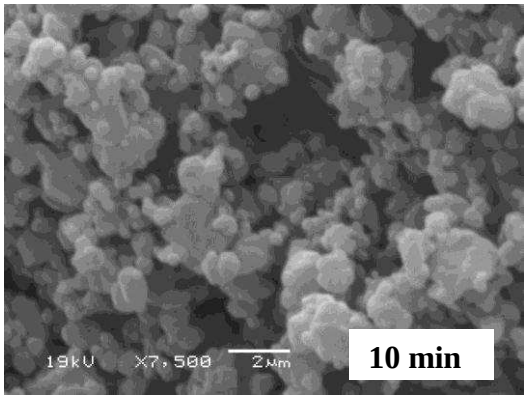

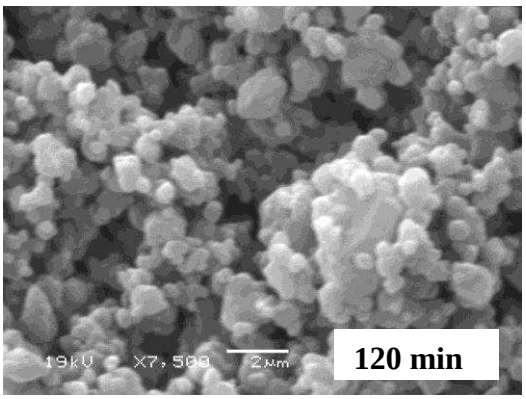

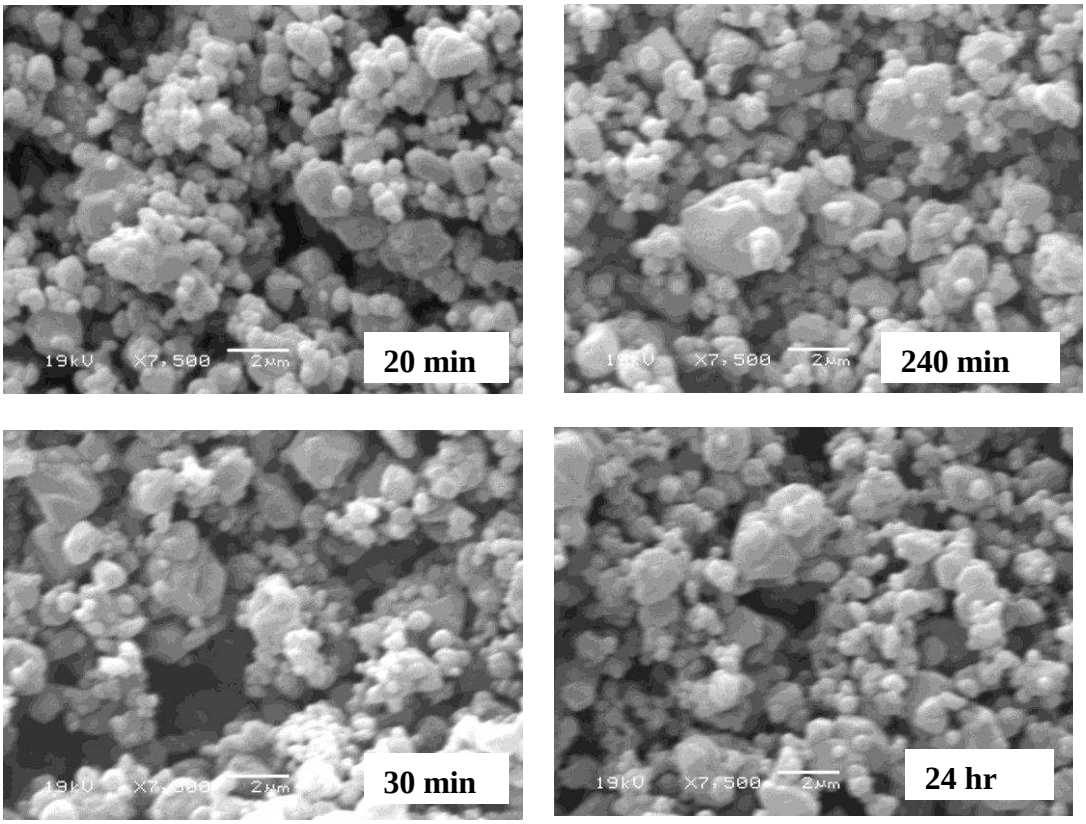

Figure 6-1: SEM images showing the effect of mHFA on anhydrous BDP at different time points.

morphology of these particles. Unlike, the particles that were extracted at the first minute, the particles extracted at a later storage time showed a number of small particle aggregates and attached to a larger one as seen in Figure 6-1 at 60 minutes of storage. The morphology of the particles also changes from a more rounded structure to more ordered particles with defined edges. As storage time increased, small particles seem to attach to the large ones and fuse to their surface. Furthermore, the appearance of larger particles of approximately 8 µm in size with smaller (2 µm) aggregated on their surface is more pronounced after 60 minutes and is observed throughout the experiments with a slight increase in the average particle size at each time point. It can also be observed that the

volume occupied by the particles have reduced which is due to a decrease in the number of particles in the suspensions.

The SEM images in Figure 6-2 show the effect of mHFA EtOH on anhydrous BDP particles. The results show a change in the morphology of the particles as seen in mHFA to a more regular shape which can indicate the formation of crystals. An average particle size of 2-4 µm (n=3) is observed during the first minutes of storage. However, as storage time increases, the surface of the particles changes quite rapidly which resulted in a change in the morphology of the particles from rounded to a more defined geometrical shape. Furthermore, the particles increased in size to around 20 µm after 60 minutes and continued to grow to reach a maximum of approximately 100 µm after 360 minutes with well defined geometrical shape.

The SEM images of anhydrous BDP suspended in mHFA EtOH oleic acid, which were taken at different time points after storage, are shown in Figure 6-3. The different crystal extracts at different time points of storage showed an increase in the average particle size and a change in the morphology of the crystals from spherical particles to well defined edges. The particles which exhibited a similar size range as observed with mHFA alone do not show a drastic change in particle size during the first two hours of storage. However, 360 minutes of the storage time showed a pronounced increase in size where the particles reached an average of approximately 100 µm as shown in Figure 6-3. No further growth of particle was observed after 24 hours as particle were of similar size to those observed at the 360 minute. It can also be observed from

both Figures 6-2 and 6-3 that the volume occupied by the particles has reduced which is due to a decrease in the number of particles in the suspensions. These results emphasise that EtOH and oleic acid do produce major change in terms of the size and morphology of particles compared to mHFA alone.

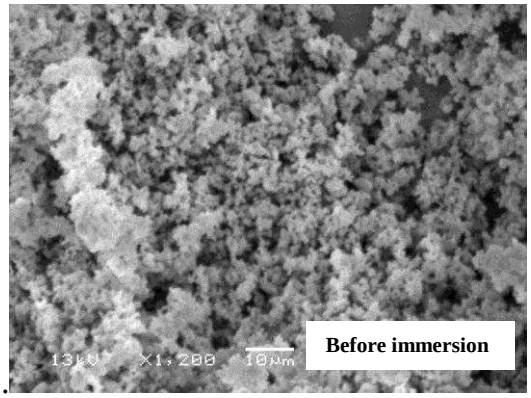

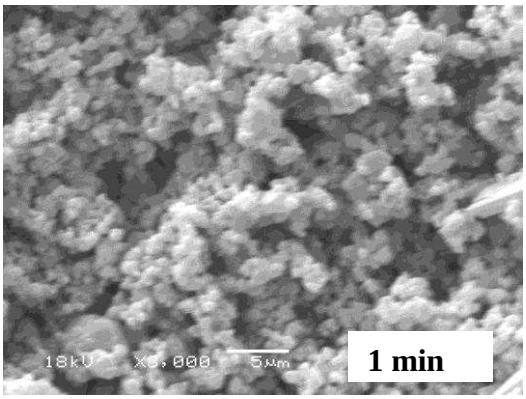

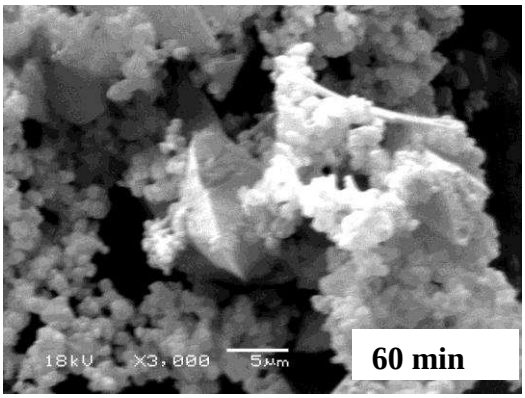

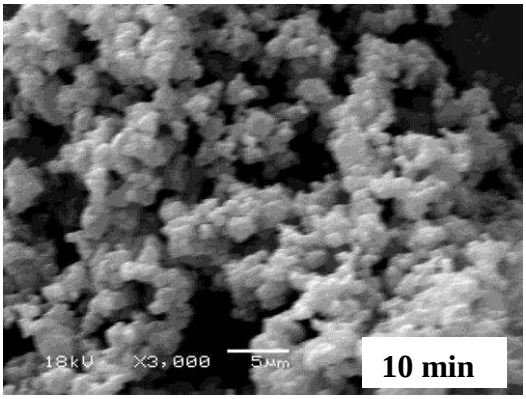

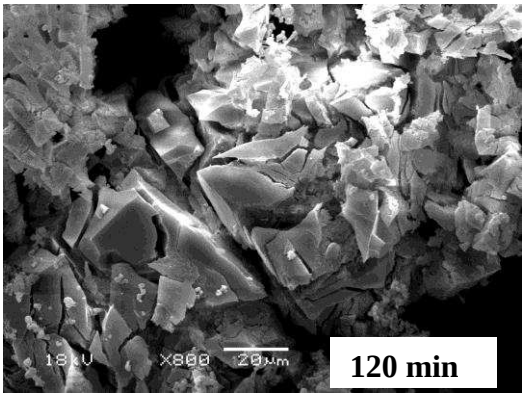

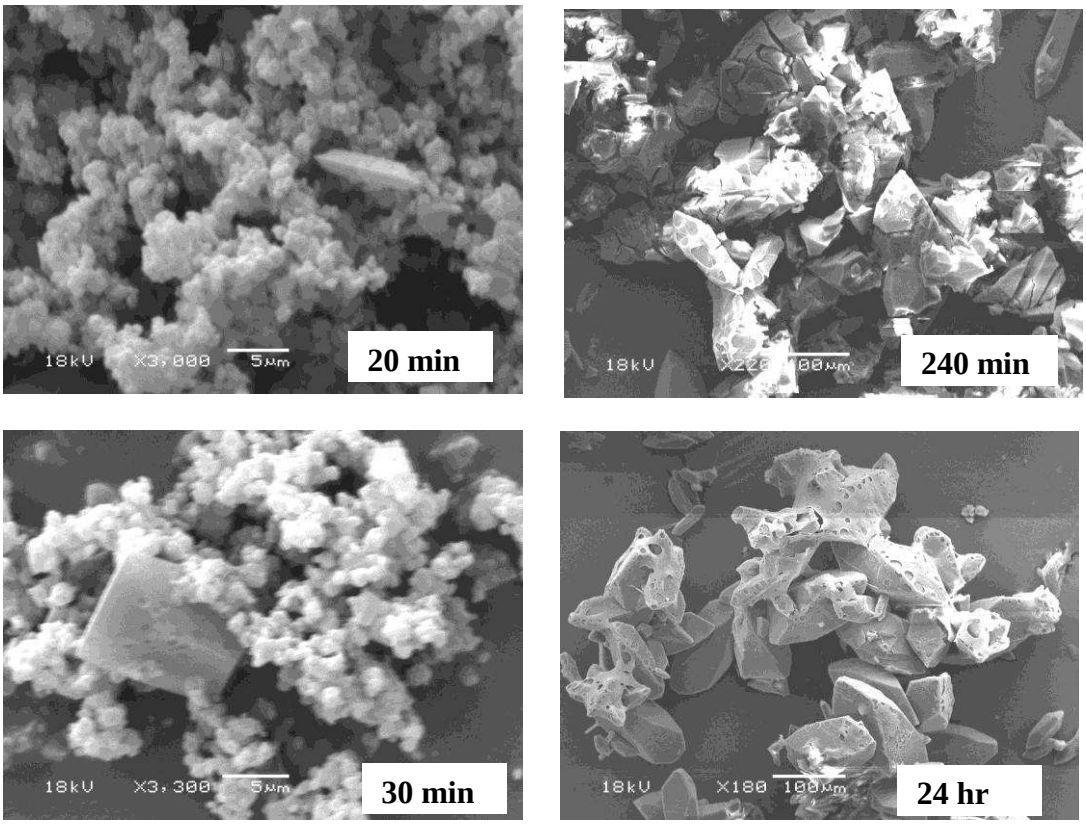

Figure 6-2: SEM images showing the effect of mHFA EtOH on anhydrous BDP at different time points.

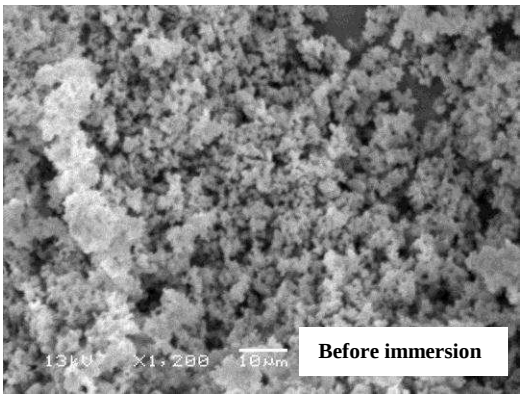

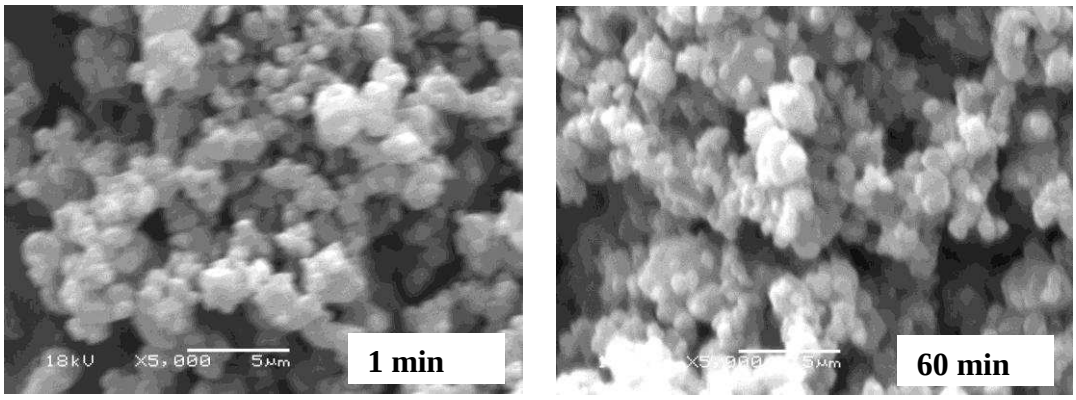

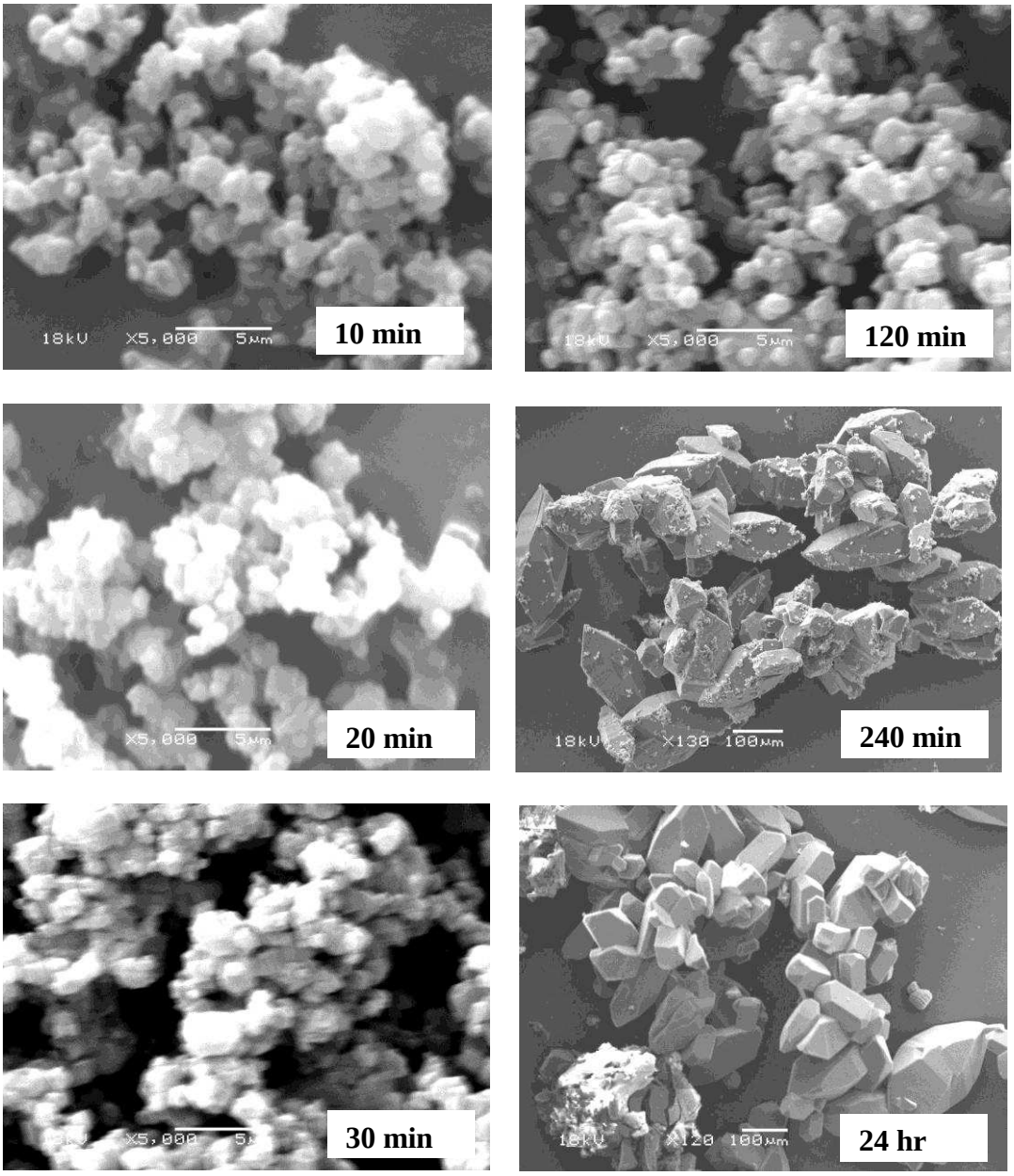

Figure 6-3: SEM images showing the effect of mHFA EtOH oleic acid on anhydrous BDP at different time points.

6.3.1.2 Effects of the Different mHFA Media on BDP CFC-11 Clathrates

The SEM images of BDP CFC-11 clathrates suspended in mHFA at different time points are shown in Figure 6-4. The overall structure of the BDP CFC-11 clathrate particles showed well defined crystals of a hexagonal shape as seen in Chapter 3, Section 3.3.1 and particle size of 60-70 µm. However, the extracted

crystals after 10 minutes in mHFA showed a decrease in the average size of the particles and a moderate change in their morphology where the structure of the particles changed from hexagonal shaped particles to a more disordered shape (Fig. 6-4). The average particle size observed was of approximately 30-40 µm. The decrease in the particle size and the changes observed in the morphology of

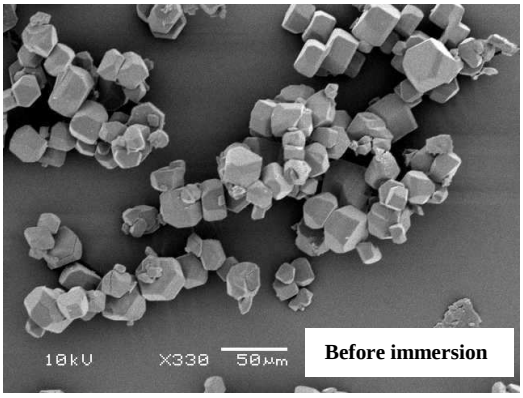

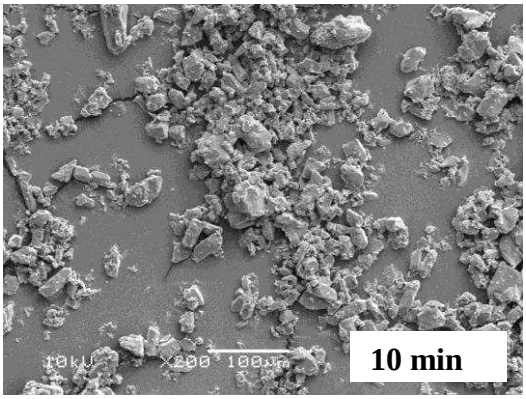

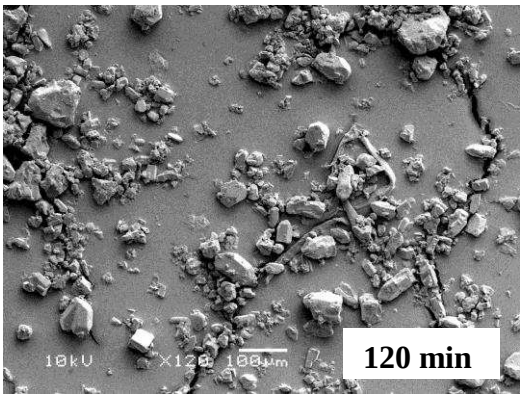

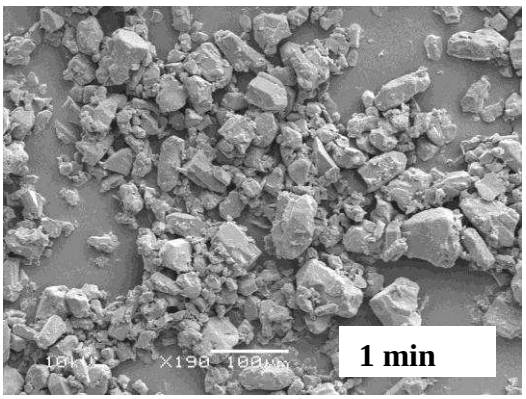

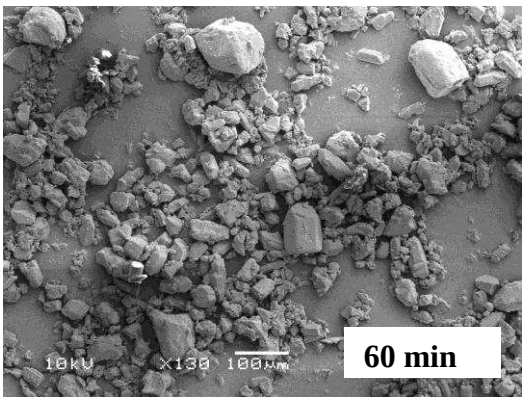

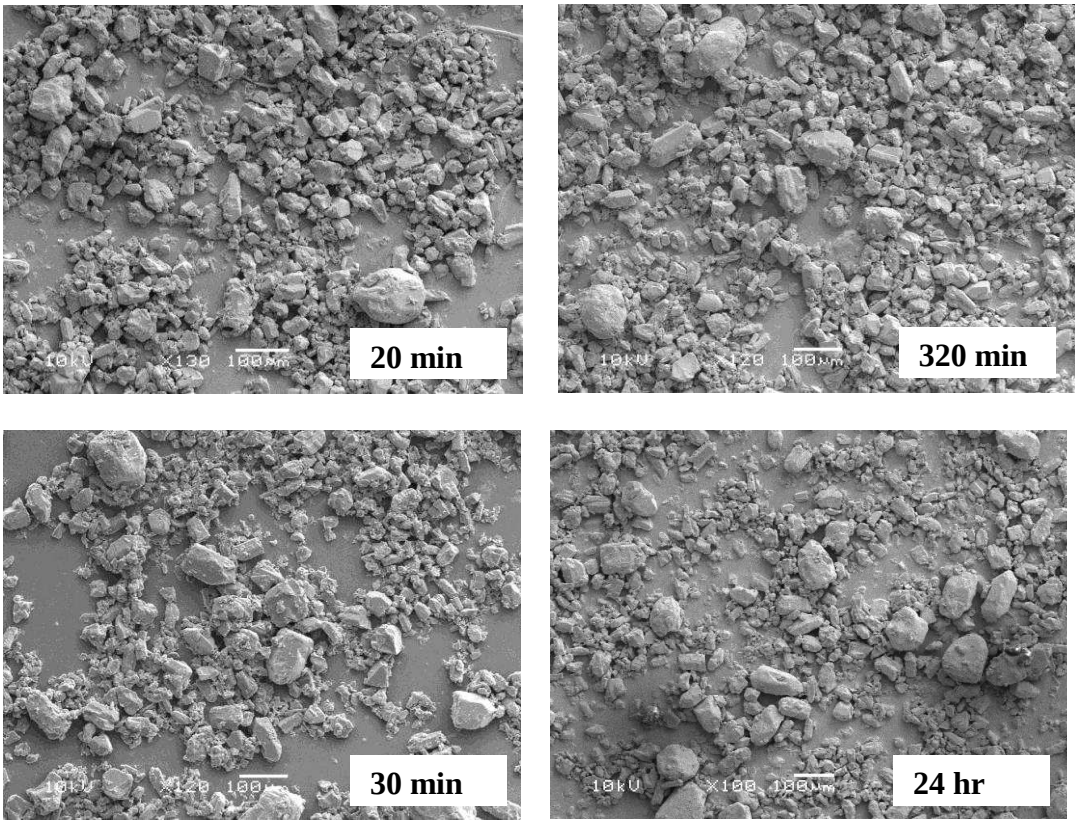

Figure 6-4: SEM images showing the effect of mHFA on BDP CFC-11 clathrates at different time points.

the BDP CFC-11 clathrate particles was seen at different time points until the particles reached the smallest size (of approximately 10-20 µm) with a stabilization of the particle size at around 30 minutes (Figure. 6-4). A moderate increase in the average particle size of the BDP CFC-11 clathrates is then observed after being extracted from the mHFA suspension from 20 µm to an average of 40 µm. This is associated with a change in the morphology of the particles from hexagonal to an elongated shape. As the storage time of BDP CFC-11 clathrate in mHFA increased to 360 minutes, the particles continued to increase in size until they reached an average size of around 35-40 µm associated with a decrease in the small particles that were described earlier. At 24 hours of

storage, the particles reached their maximum particle size of approximately 50 µm as shown in Figure 6-4.

In contrast, mHFA EtOH had a different effect on the BDP CFC-11 clathrate particles (Fig. 6-5), featured by the different morphology of BDP CFC-11 clathrates compared to the ones observed in mHFA. The clathrate crystals were slightly smaller in size (~ 20 µm) with an occasional loss of their hexagonal shape. During the first 60 minutes of storage time in mHFA EtOH, the SEM images of the BDP CFC-11 clathrate (Fig. 6-5) showed a decrease in particle size to an average of 10 µm. As the storage time increased, the images showed an increase in the particle size of the BDP-CFC-11 clathrates and the formation of hexagonal shaped crystals of approximately 80 µm in size.

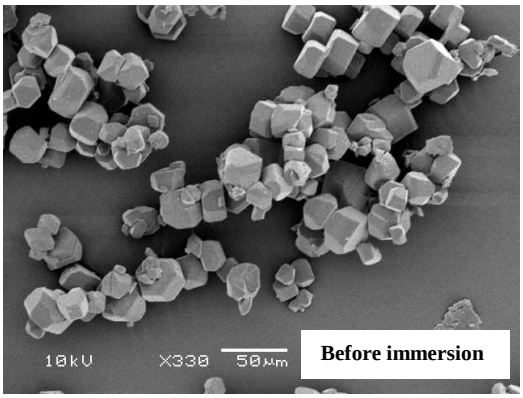

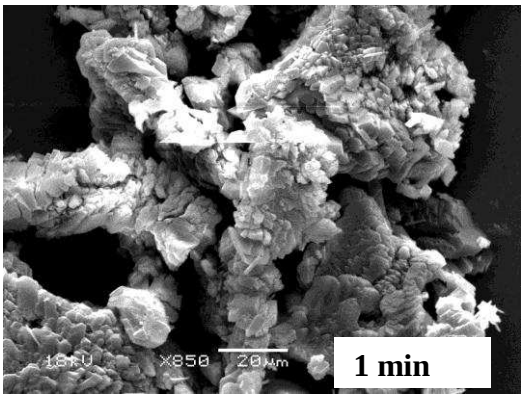

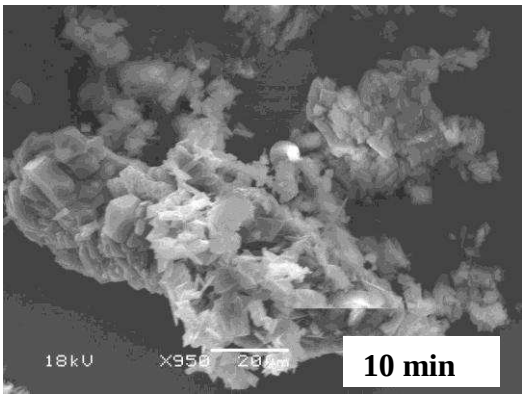

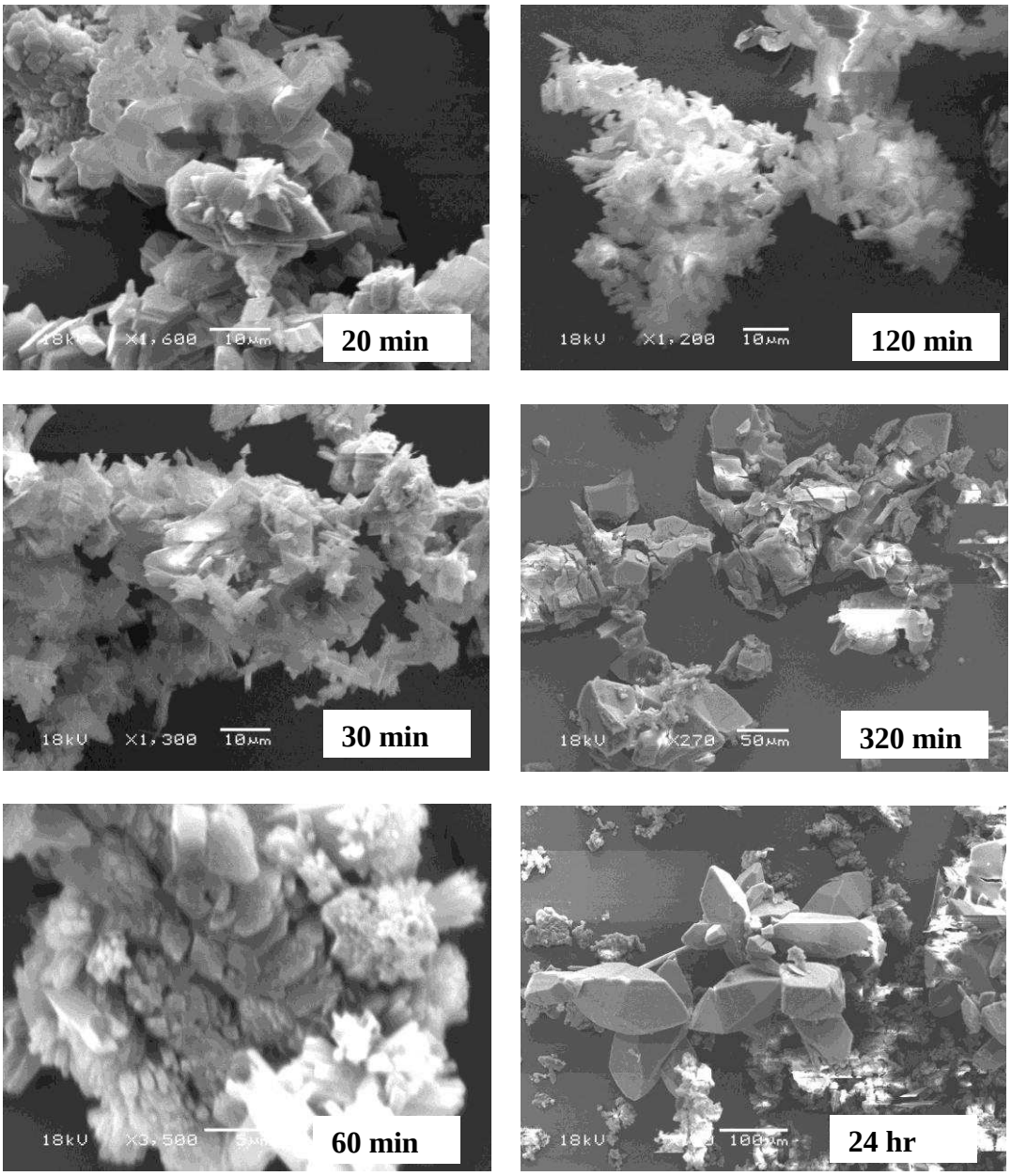

Figure 6-5: SEM images showing the effect of mHFA EtOH on BDP CFC-11 clathrates at different time points.

Concerning the results obtained for BDP CFC-11 clathrates in mHFA EtOH oleic acid (Fig. 6-6), the SEM images are comparable to the particles obtained by suspending BDP CFC-11 clathrates in mHFA EtOH. From the first minutes of suspending the BDP CFC-11 clathrates in mHFA EtOH oleic acid, a change in the surface of the clathrates is observed with small cracks at different faces of the

crystals are noticeable (Fig. 6-6). The particle size in the initial first minute of storage ranged between 30 and 40 µm, as observed previously. During the following 35 minutes, particles of BDP CFC-11 clathrate showed a similar pattern of changes as previously described with both mHFA and mHFA EtOH media where particles seem to collapse and form smaller particles in size (< 20 µm). However, the morphology of the particles observed in mHFA EtOH oleic acid after 120 minutes of storage time is different compared to the ones observed previously in the two other media. The particles show small cracks at their surface with more round than hexagonal shape as shown previously. The particles seem to have reached a maximum size of around 100 µm after 360 minutes of storage time.

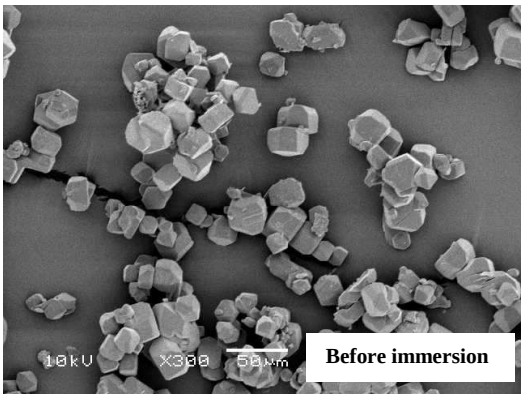

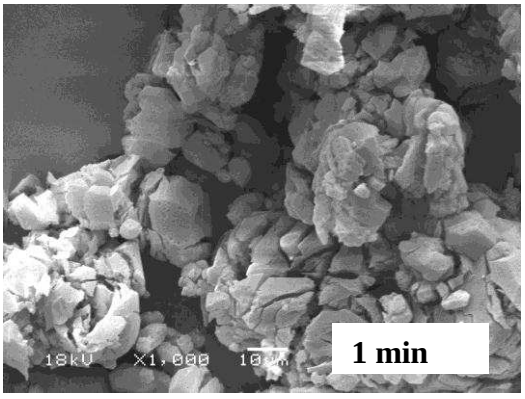

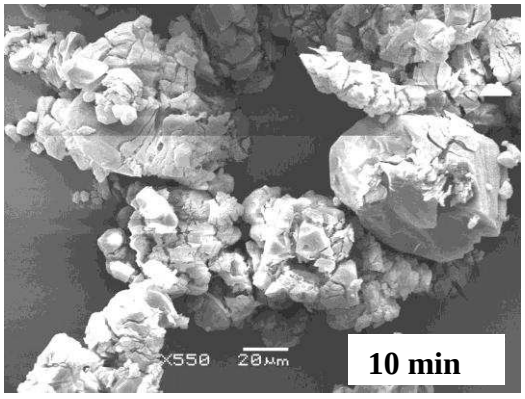

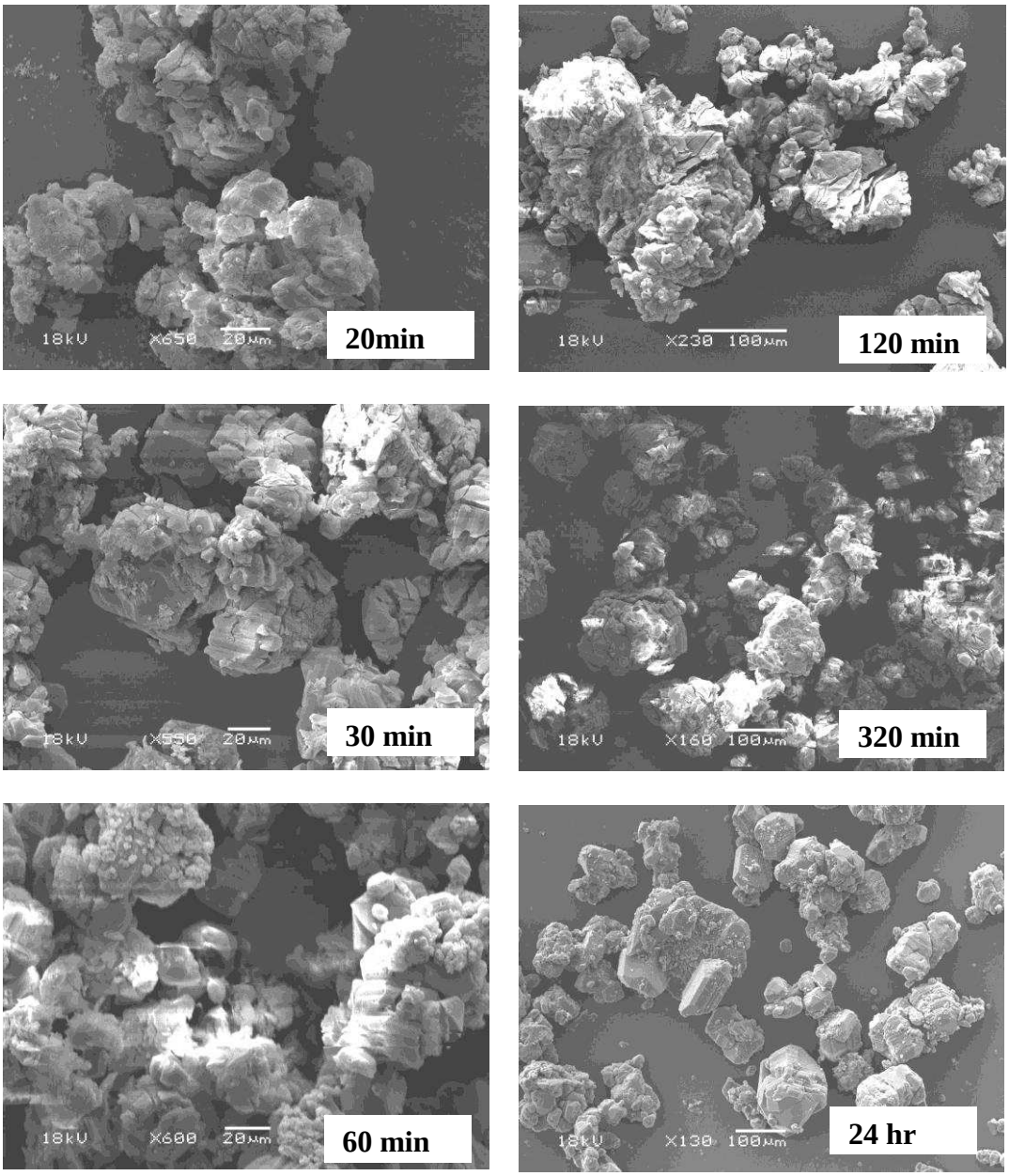

Figure 6-6: SEM images showing the effect of mHFA EtOH oleic acid on BDP CFC-11 clathrates at different time points.

6.3.1.3 Effects of the Different mHFA Media on Budesonide

Figure 6-7 shows the effects of different mHFA media on budesonide. The particles extracted after 1 minute of suspending budesonide in mHFA had a well defined structure with a particle size ranging between of 5-10 µm. However, some small rounded particles of approximately 1 µm or less can be observed

attached to the surface of the larger particles. After 10 minutes of storage time, budesonide particles showed a minor increase in the overall particle size of the sample and a small change in the size of the small particles that are still present at different storage times (Fig. 6-7).

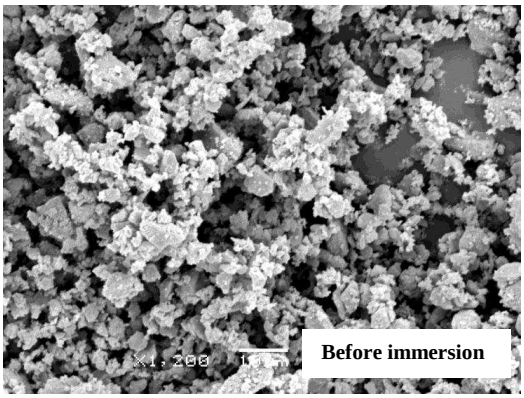

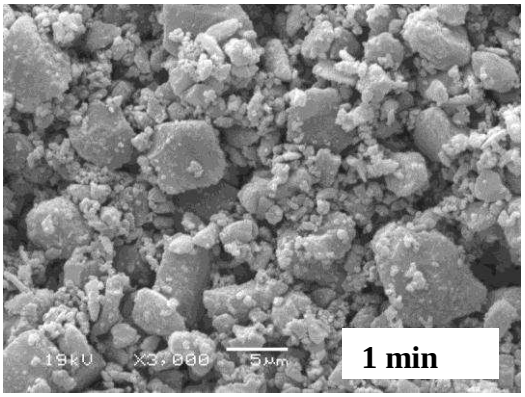

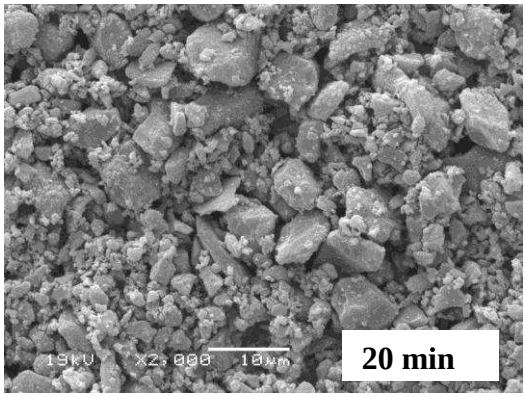

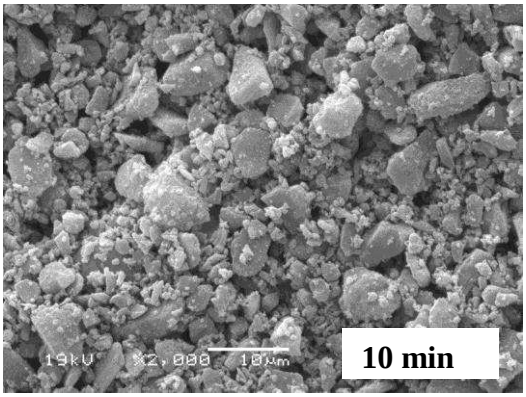

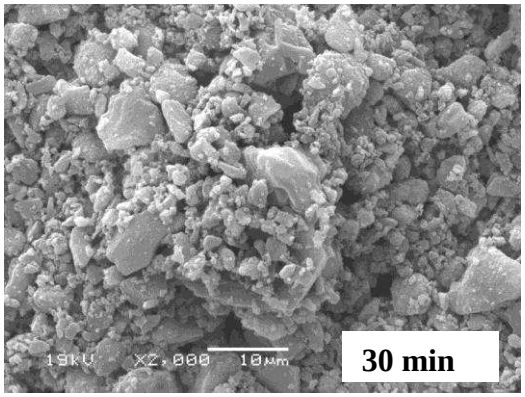

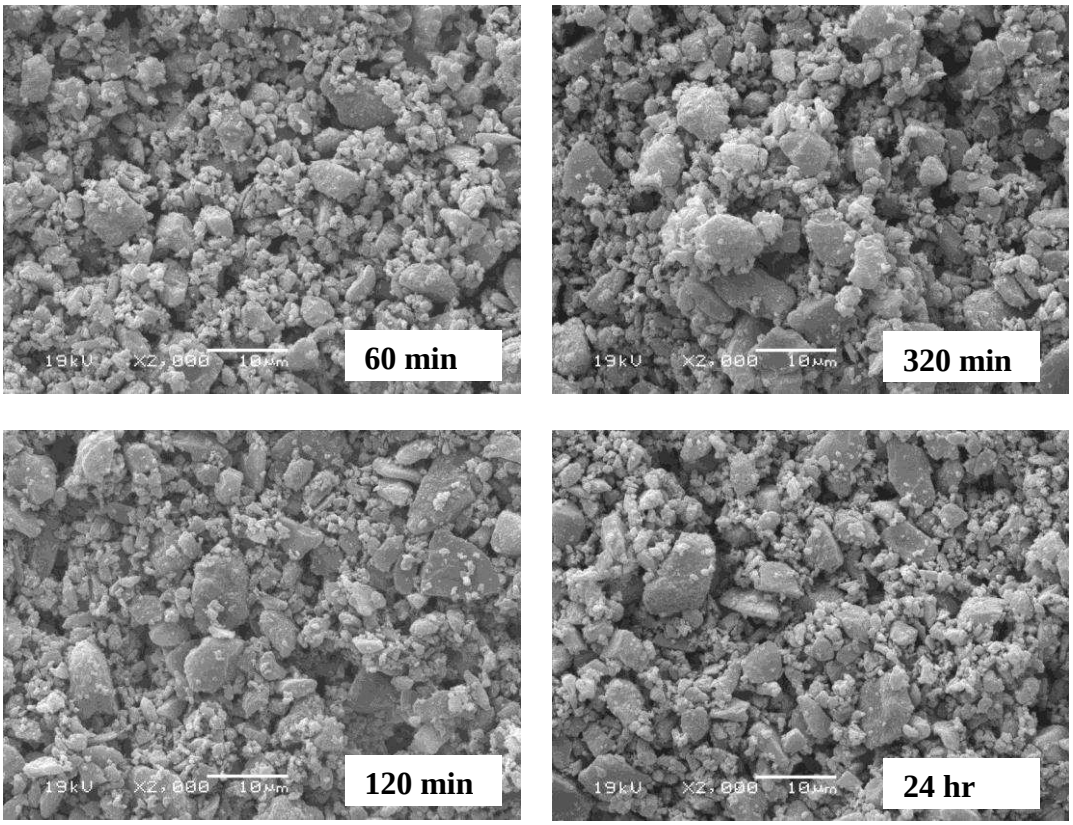

Figure 6-7: SEM images showing the effect of mHFA on budesonide at different time points.

By 60 minutes, the morphology of the particles changes to a more defined quasi-cubic shape with a particle size that ranged between 10-20 µm. The small particles of around 1-2 µm in size are still present at the surface of the larger ones and seem to be fusing to the surface of these latter (small asperities at the surface of the larger budesonide particles). By the end of the experimental storage time, the particle size of budesonide particles was around 10-25 µm with a well defined structure (Fig. 6-7). The presence of small budesonide particles was still evident.

In contrast, the effect of mHFA EtOH on the shape and morphology of budesonide particles showed similar results to those observed in anhydrous BDP mHFA EtOH suspension. The SEM images in Figure 6-8 show very little

variation in terms of changes in the morphology and particle size of budesonide particles in mHFA EtOH media. The particle size of budesonide was of approximately 10 µm, similar to the results obtained earlier in mHFA media. As the storage in the media increases, the particles show little increase in particle size and no major changes are observed in their morphology up to the 35 minute of storage. After 35 minutes, changes in the morphology of the particles to a more regular shape can be seen in Figure 6-5 at 60 minutes indicating the formation of crystals, where small budesonide particles seem to fuse together to form slightly larger particles, reaching a maximum size of approximately 20-25 µm after 360 minute of storage time and remained unchanged after 24 hours. Therefore, the particles in mHFA EtOH media showed a better stability in terms of the average particle size as observed by the size of the different budesonide particles by the end of the experimental time. This might be due to an increased solubility of budesonide in mHFA EtOH that leads to more stable particles.

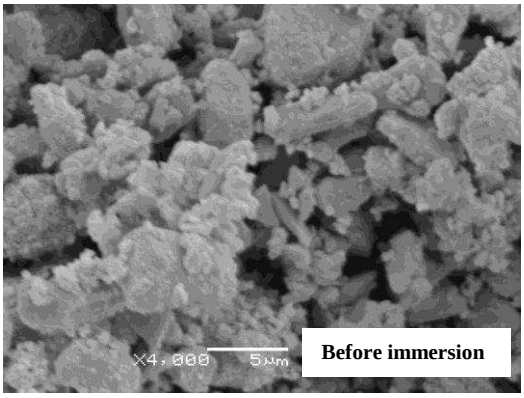

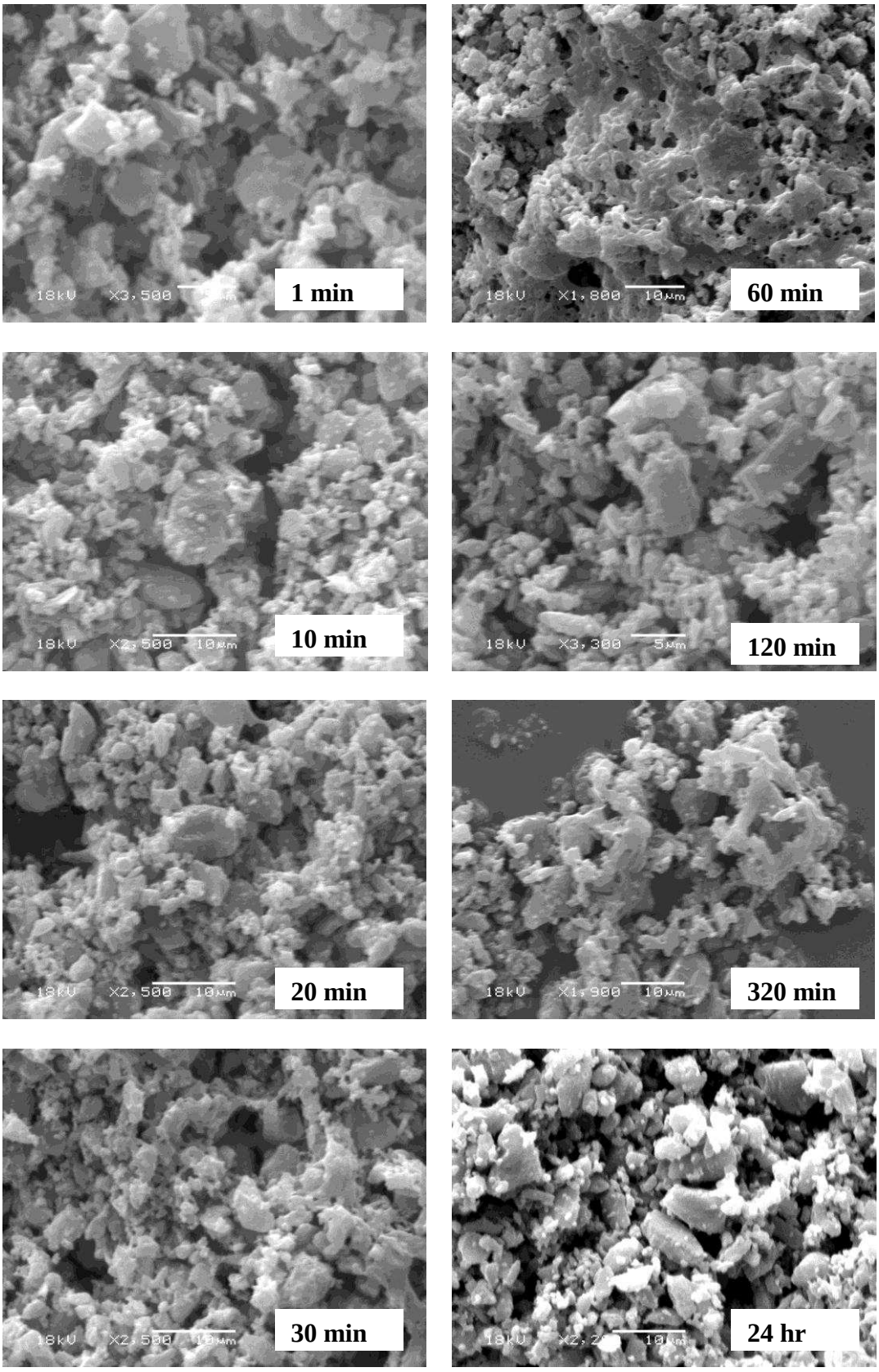

Figure 6-8: SEM images showing the effect of mHFA EtOH on budesonide at different time points.

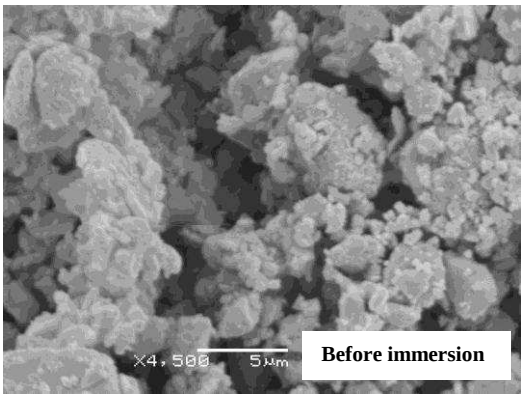
Before immersion

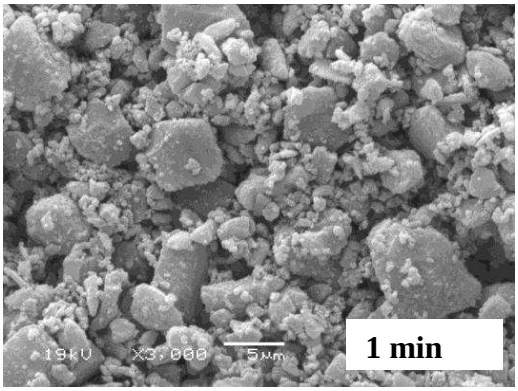
1 min

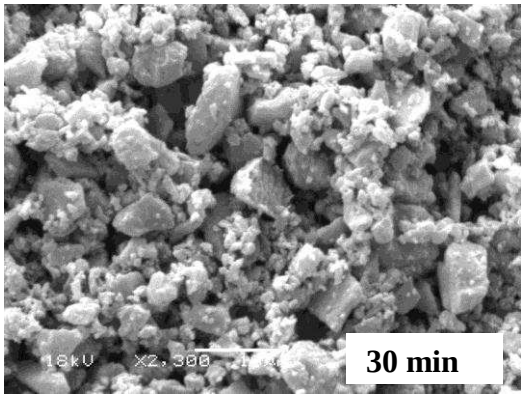
30 min

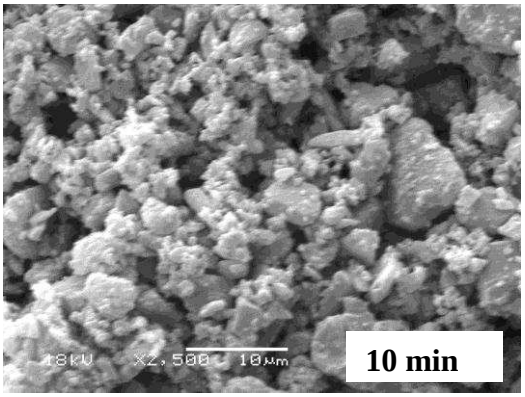
10 min

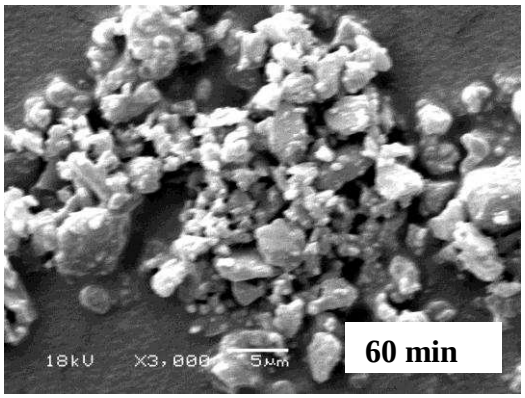
60 min

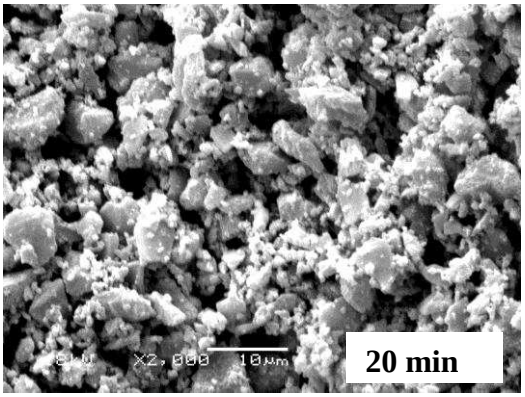
20 min

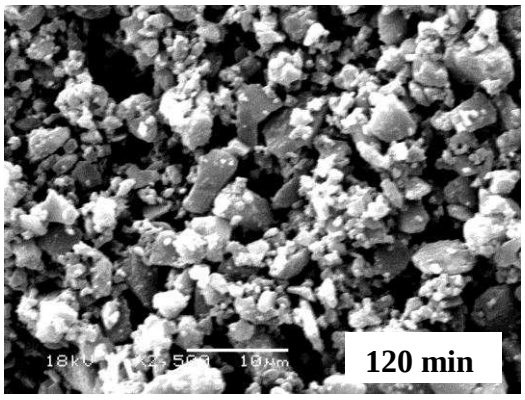
120 min

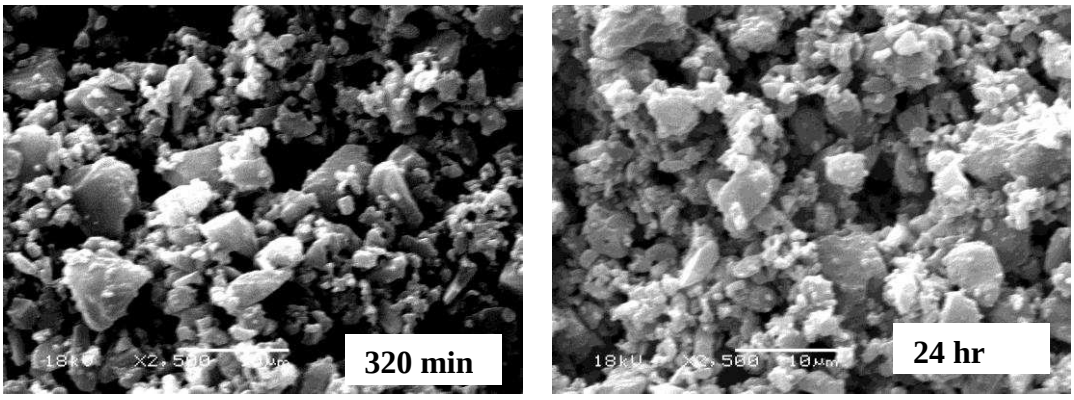

Figure 6-9: SEM images showing the effect of mHFA EtOH oleic acid on budesonide at different time points.

The results obtained for budesonide mHFA EtOH oleic acid suspension, shown in Figure 6-9, are comparable to the ones observed earlier in both mHFA and mHFA EtOH. Budesonide particles seem to form crystals a soon as they are suspended in mHFA EtOH oleic acid and have an average particle size of approximately 5 µm. During the first 60 minutes, a small change in the morphology of budesonide particles as well as their average particle size could be observed. The particles then approximately doubled in size. However, after 24 hours of storage time in mHFA EtOH oleic acid, budesonide particles still seem to be smaller than the particles observed in both mHFA and mHFA EtOH suspensions, previously described. From these results, oleic acid might have improved the stability of the suspension, as evidenced by the lower average particle size of the particles obtained.

6.3.2 AFM –Topographical Imaging Acquisition

6.3.2.1 Effect of the Different mHFA Media on the Anhydrous BDP

Anhydrous BDP discs were continuously imaged in mHFA alone for a period of 240 minutes and the AFM images obtained are presented in Figure 6-10. The images show a developing surface topography and these changes are observed until the end of the storage time. The AFM images indicate an active surface of the BDP disc i.e. structural rearrangement of the surface. At 1 minute, the surface of anhydrous BDP discs shows a reasonably flattened surface with very little variations and no defined particles (Fig. 6-10). The surface shows particles that are fused together which might be due to the pressure applied when forming the anhydrous BDP discs using the IR press. After a few minutes of immersion in mHFA media, it can be observed that the shape of the particles becomes more defined as seen in 5 minutes AFM image in Figure 6-10.

As time of immersion in mHFA media increased, the topography of the BDP disc is continuously changing where small particles are dissolving and other particles already present show an increase in diameter and height. At 240 minutes, most of the small particles that were present seem to have completely disappeared with only few still present and the largest particles having a maximum height of 2.4 µm and a maximum width of 5 µm.

The results obtained for anhydrous BDP disc immersed in mHFA EtOH media at different time points are shown in Figure 6-11. The AFM images show a large

surface activity where the surface topography and the height are continuously changing with time. As seen with mHFA alone, the AFM images in the initial first minute of mHFA EtOH contact with the surface of BDP, the surface show very little variation in terms of height with only small particles appearing that are closely packed together. However, after 5 minutes, the surface starts to show some variations as it can be observed that some small amount of material disappeared from the surface of the disc and other areas increased in size. This behaviour is noticeable and continuous until the end of storage time. The size of the particles increased to approximately 5.4 µm in diameter and 3.6 µm in height. The rate of these changes seemed to be more rapid than observed in mHFA as the most significant changes were observed as early as 20 minutes of exposure (Fig. 6-11).

In contrast, the topographical images obtained for BDP immersed in mHFA EtOH oleic acid (Fig. 6-12) show similar features to the ones observed earlier in

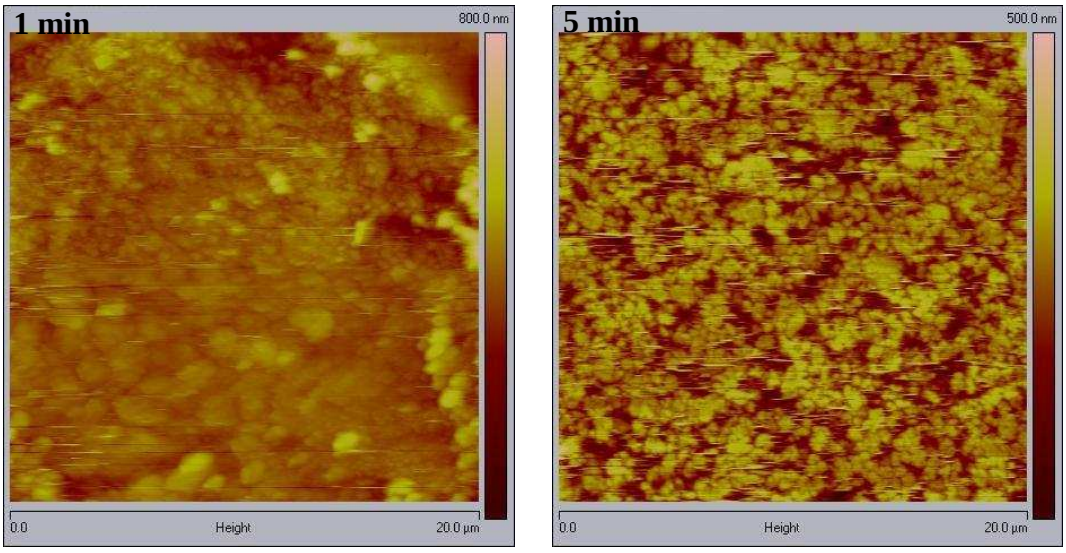

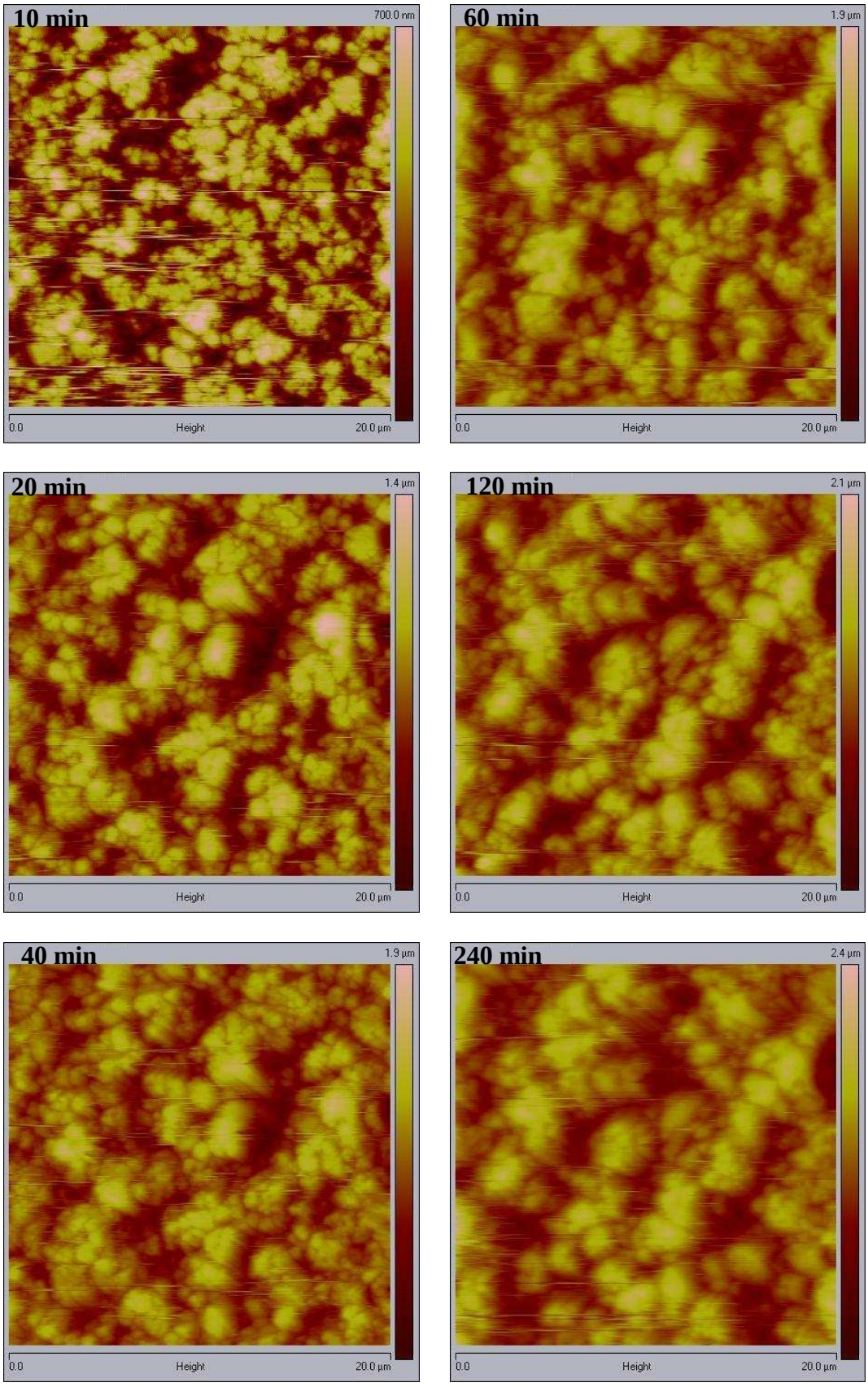

Figure 6-10: AFM images of anhydrous BDP in mHFA at various time points (scale; 20 µm x 20 µm).

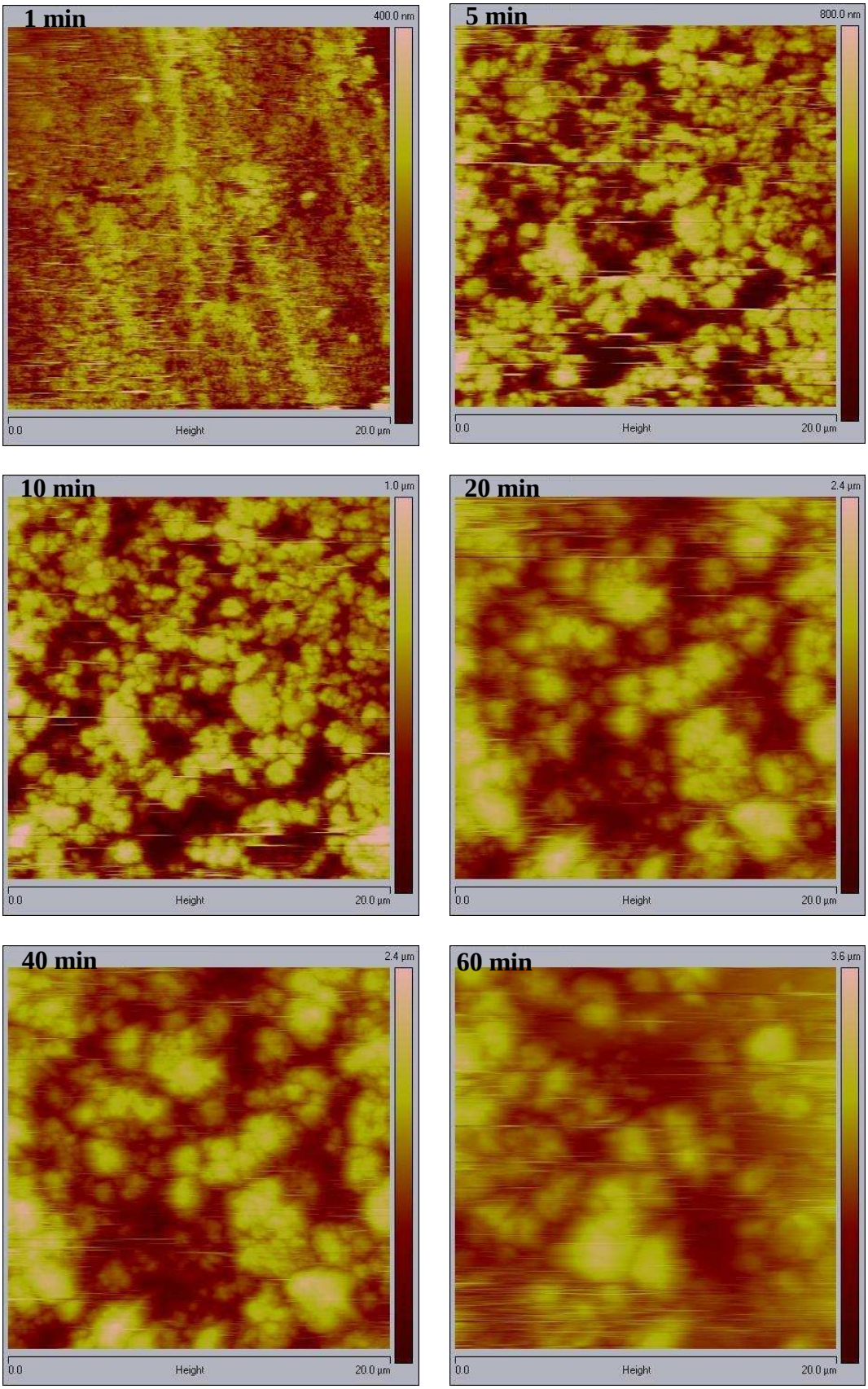
1 min
400.0 nm
0.0
Height
20.0 µm
5 min
800.0 nm
0.0
Height
20.0 µm
10 min
1.0 µm
0.0
Height
20.0 µm
20 min
2.4 µm
0.0
Height
20.0 µm
40 min
2.4 µm
0.0
Height
20.0 µm
60 min
3.6 µm
0.0
Height
20.0 µm

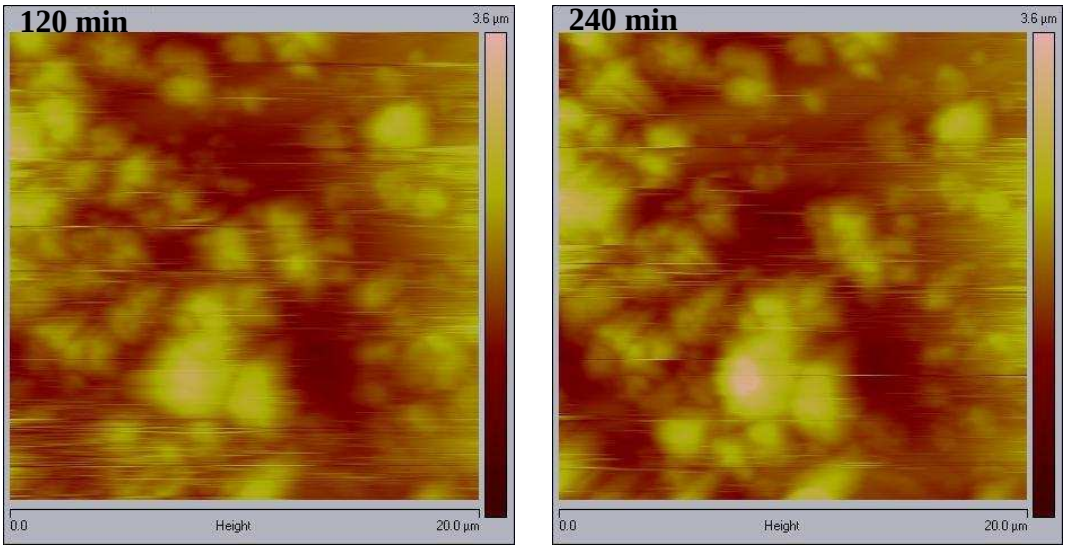

Figure 6-11: AFM images of anhydrous BDP in mHFA EtOH at various time points (scale; 20 µm x 20 µm).

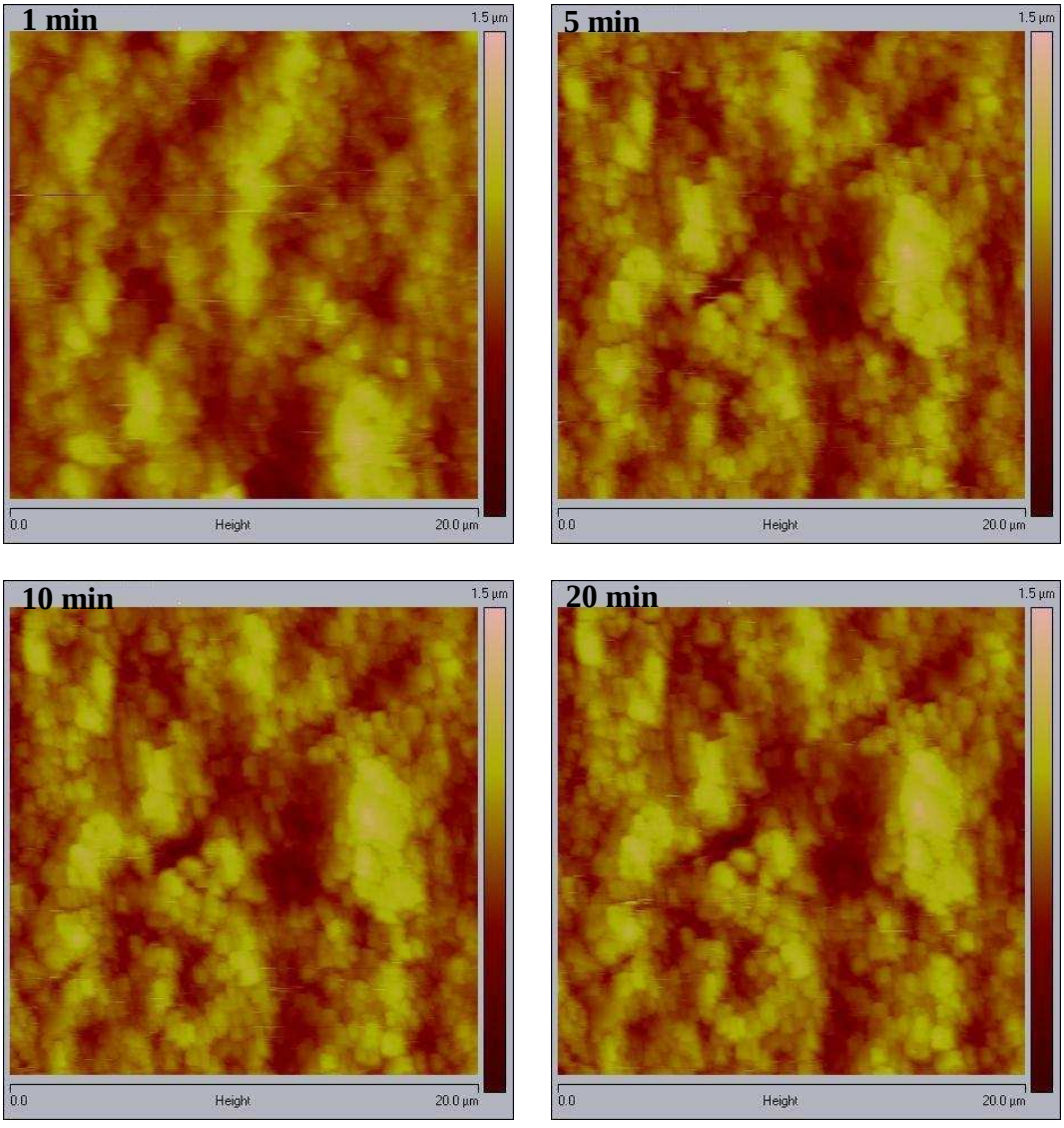

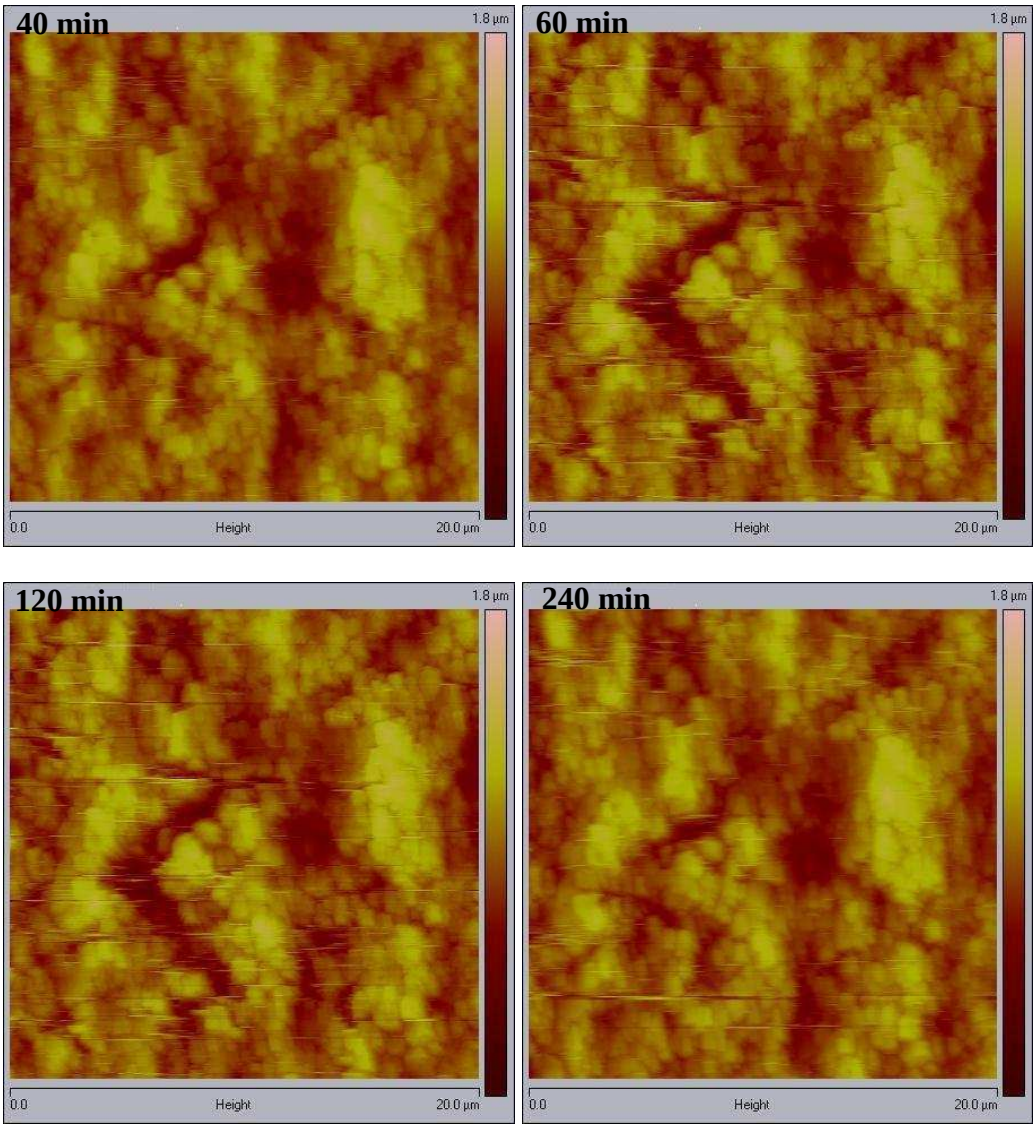

Figure 6-12: AFM images of anhydrous BDP in mHFA EtOH oleic acid at various time points (scale; 20 µm x 20 µm).

mHFA and mHFA EtOH. The surface of the BDP disc in mHFA EtOH oleic acid show some activity similar to that observed previously in the two other media. As immersion time in the media increases, the surface topography changes included the disappearance of small particles and the increase in the width and height of others. However, the rate of these changes seems to be extremely slow in mHFA EtOH oleic acid when compared to the other medium and seems to reach a steady state after 120 minutes of exposure

The different streaks observed in various AFM images of anhydrous BDP in Figures 6-10 to 6-12 are a result of the high surface activity of the anhydrous BDP where the dissolution occurring on the surface of the anhydrous BDP disc probably led to some very fine particles sticking to the tip leading to the sweeping artefact observed in the images.

In order to determine the effect of the media on the surface roughness, the RMS values obtained at each time point for each of the mHFA media were plotted against time allowing the effects of each media on the behaviour of anhydrous BDP to be studied. The results obtained are represented in Figure 6-13. RMS roughness values for BDP in the different mHFA media show a continuous increase which confirms the effects of the nature of media on the surface activity.

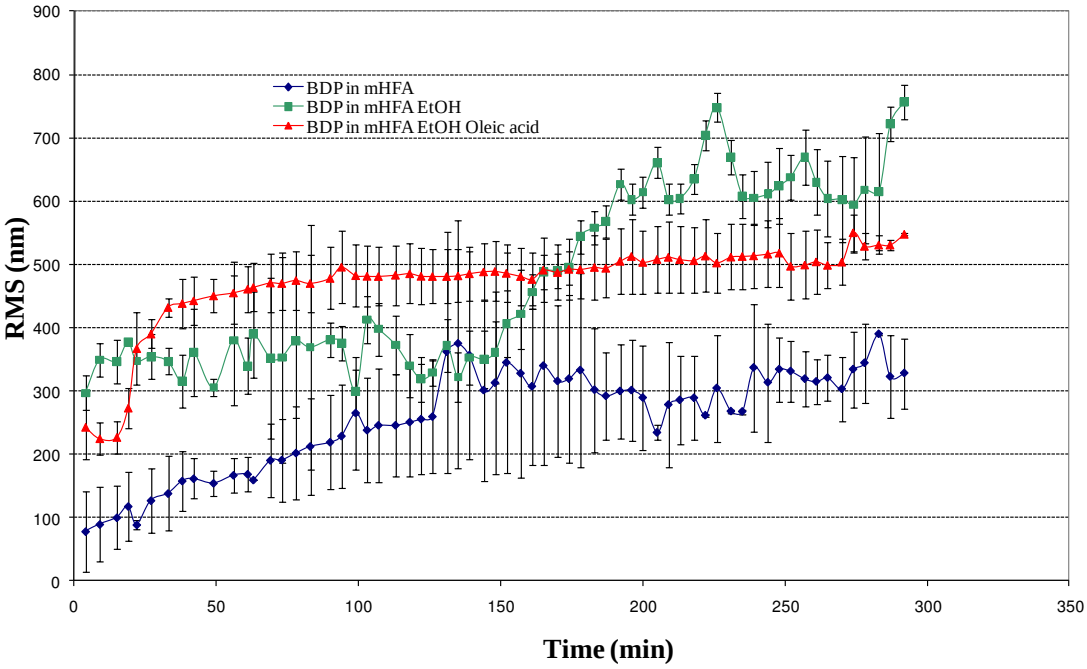

Figure 6-13: Effect of Different mHFA media on the RMS roughness of anhydrous BDP with time.

The surface of BDP is most affected by mHFA and mHFA EtOH as observed in Figure 6-13. The RMS values in mHFA EtOH oleic reached a steady state value quite rapidly and the percentage change in RMS was lower than in the other two media signifying that oleic acid might have provided some stability to the surface and led to a smaller surface activity compared to the ones exposed to mHFA and mHFA EtOH.

6.3.2.2 Effects of the Different mHFA Media on BDP CFC-11 Clathrates

The AFM images of BDP CFC-11 clathrates in the different mHFA media were taken at the surface of individual BDP CFC-11 particles due to their size (Fig. 6-

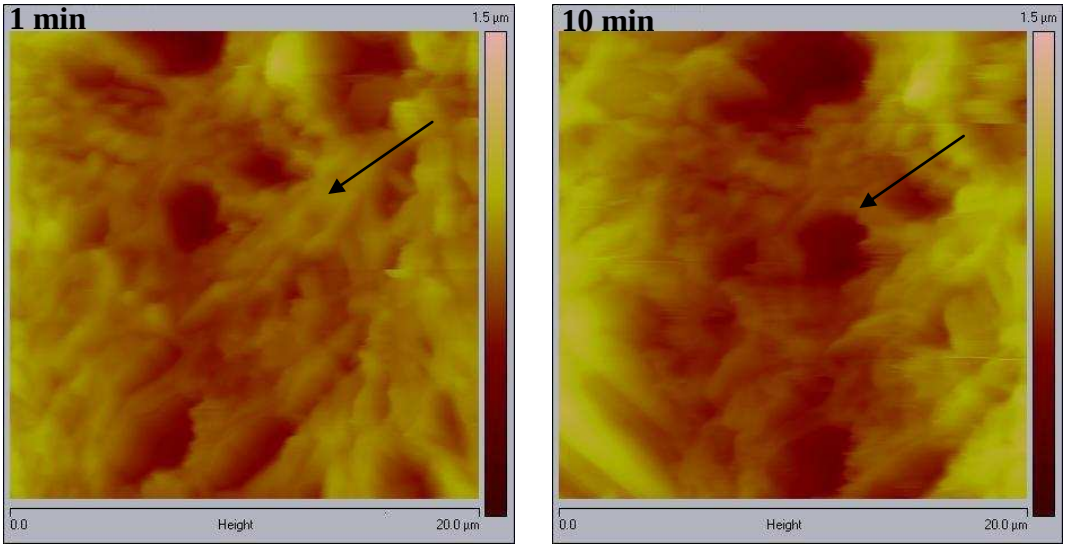

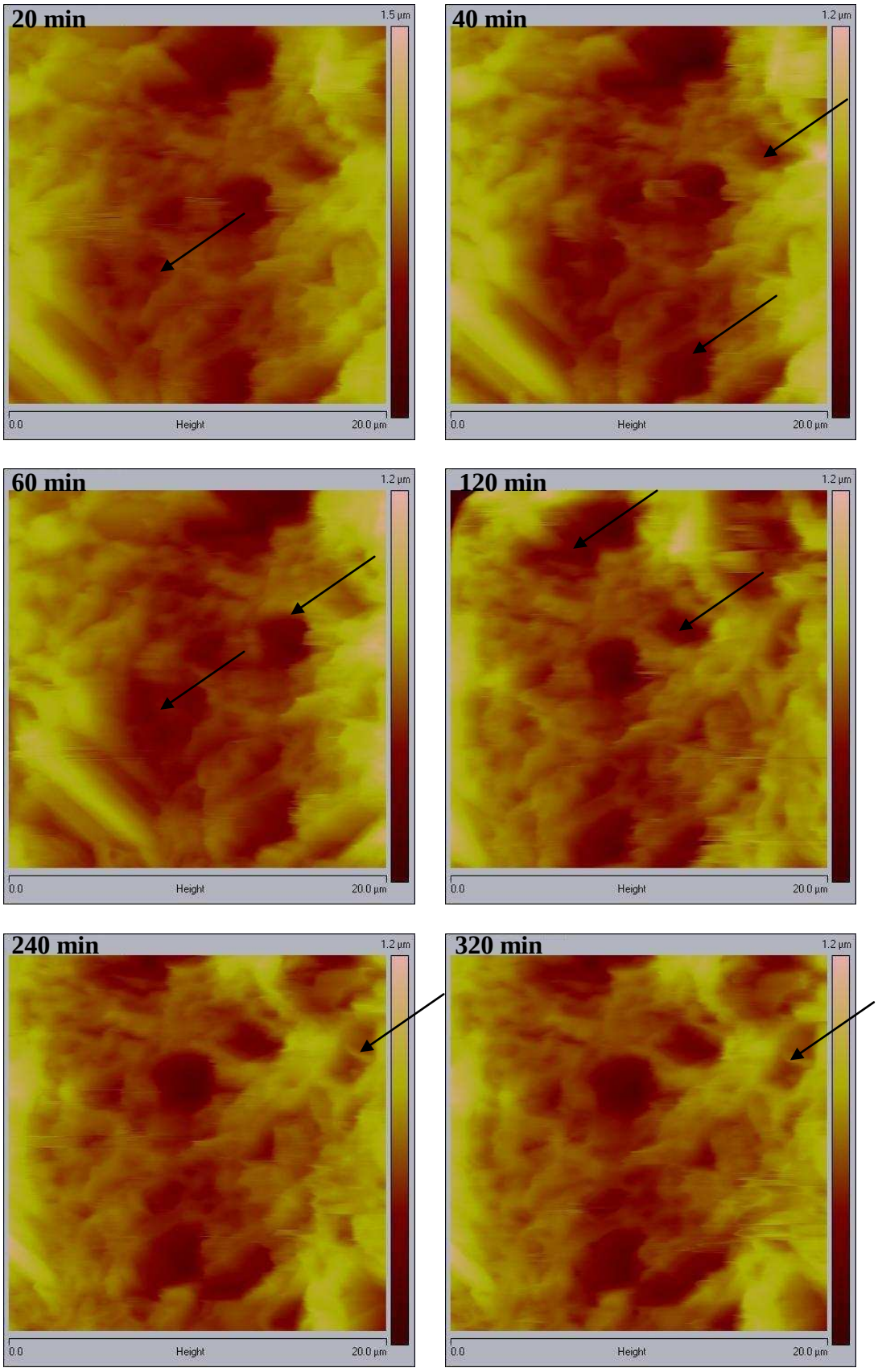

Figure 6-14: AFM images of BDP CFC-11 clathrates in mHFA at various time points (scale; 20 µm x 20 µm).

14). The AFM images were taking at different crystal faces of the BDP CFC-11 clathrates as these were large enough (40 µm) and hence the behaviour on a single BDP CFC-11 clathrate particle can be determined. The AFM images show the formation of small etch pits at the surface of the particle as soon as these are immersed in mHFA. As exposure time to mHFA increases, the surface of BDP CFC-11 clathrate particles change very gradually with more pits appearing and higher asperities present. These pits might be due to the gradual collapse of the particles in mHFA caused by the release of the CFC-11 present in the crystal structure or can be associated with the preferential dissolution of the clathrate at high energy sites that are related to the presence of defects and dislocations in the structure of the clathrates.

The same behaviour was observed when exposing BDP CFC-11 clathrate particles to mHFA EtOH and mHFA EtOH oleic acid as shown in Figures 6-15 and 6-16. The AFM images show that as soon as the particles are in contact with the two different media, small etch pitches appeared on the surface of the clathrates and their width increases gradually in relation with time of exposure to the media. However, the effect of both mHFA EtOH and mHFA EtOH oleic acid exhibited the most rapid change in the surface of the clathrates and an almost instant collapse in the structure. In both figures, it is noticeable that exposure time to the two different media is associated with an increase in the depth of the etch pits. Furthermore, the formation of small particles with an apparent size of about 1-2 µm at the surface of the BDP CFC-11 clathrates is evident, probably as a result of the crystal structure of the clathrate collapsing when exposed to the media, eventually leading to the release of the propellant from within the

channels inside the clathrate structure. As the collapse of the clathrate crystal leads to the formation of anhydrous BDP as discussed in Chapter 3, Section 3.3.5, the formation of a potentially small anhydrous BDP particle on the surface BDP CFC-11 particles is consistent with the data. Further DSC analysis of BDP particles after being suspended in mHFA showed no transition and hence confirms that the particles remained as anhydrous BDP (Figure 8-2 in appendix 2)

As for the AFM images of anhydrous BDP, RMS roughness of BDP CFC-11 clathrate surface were obtained for the different time points of exposure to the different mHFA media (Fig. 6-17). These results show that mHFA had a minor effect in terms of the changes observed in the RMS values, with a small increase in RMS at 50 minutes followed by a quasi-steady state level.

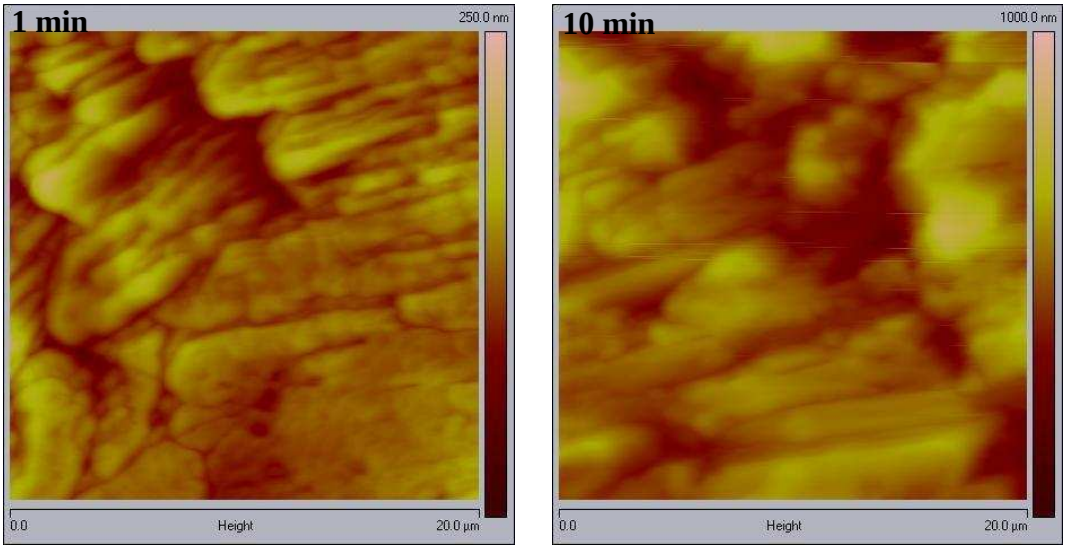

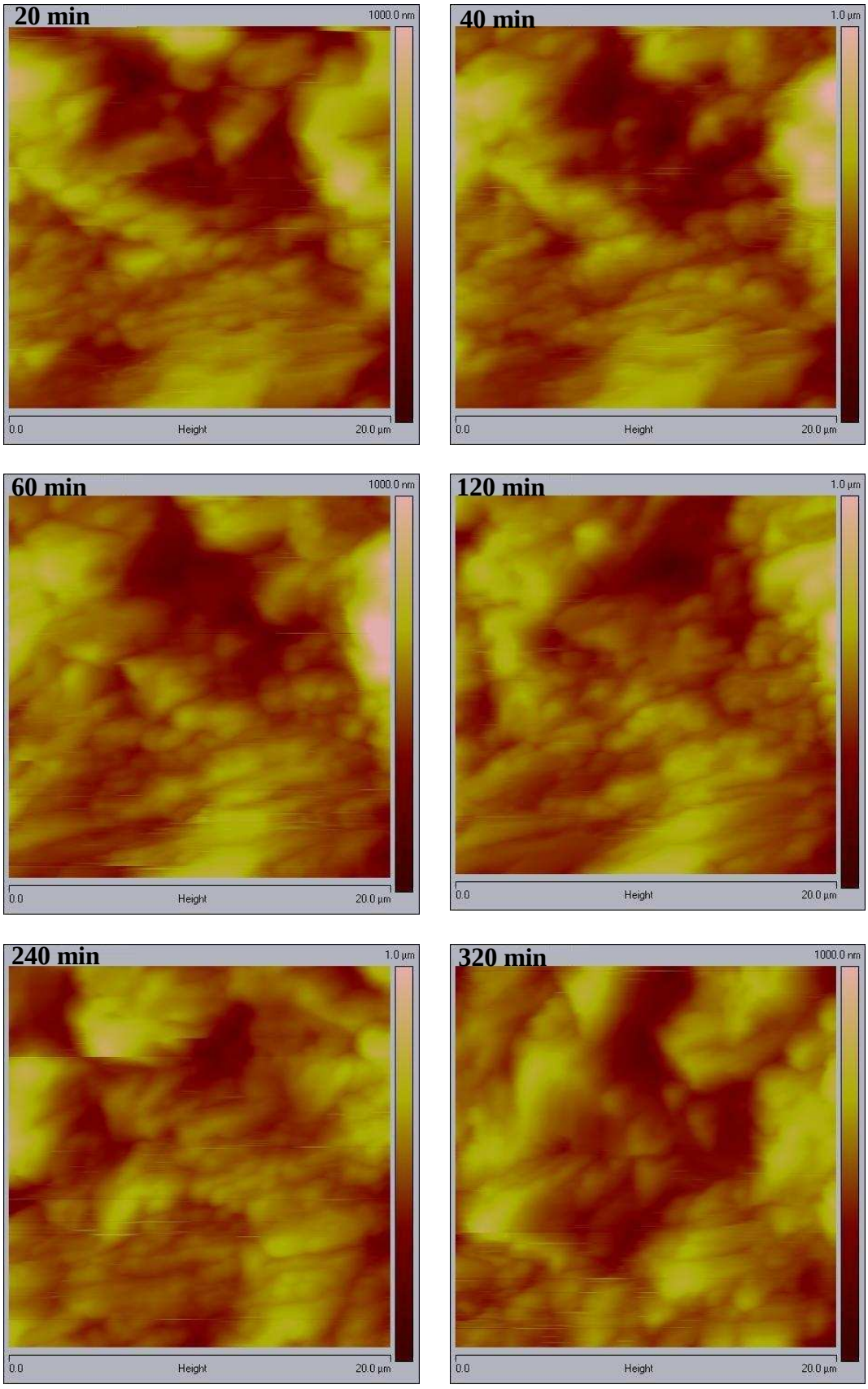

Figure 6-15: AFM images of BDP CFC-11 clathrates in mHFA EtOH at various time points (scale; 20 µm x 20 µm).

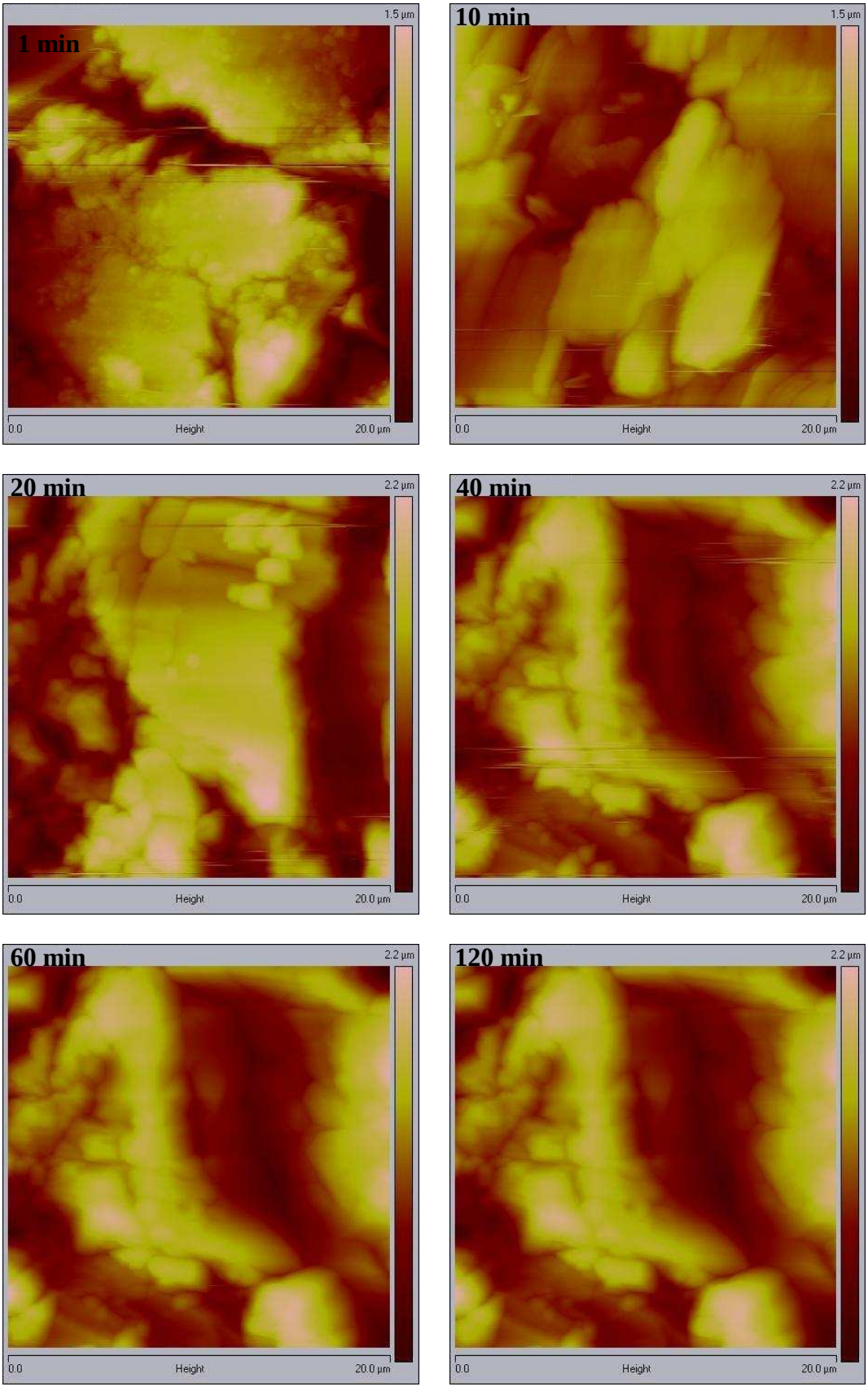
1 min
1.5 µm
0.0
Height
20.0 µm
10 min
1.5 µm
0.0
Height
20.0 µm
20 min
2.2 µm
0.0
Height
20.0 µm
40 min
2.2 µm
0.0
Height
20.0 µm
60 min
2.2 µm
0.0
Height
20.0 µm
120 min
2.2 µm
0.0
Height
20.0 µm

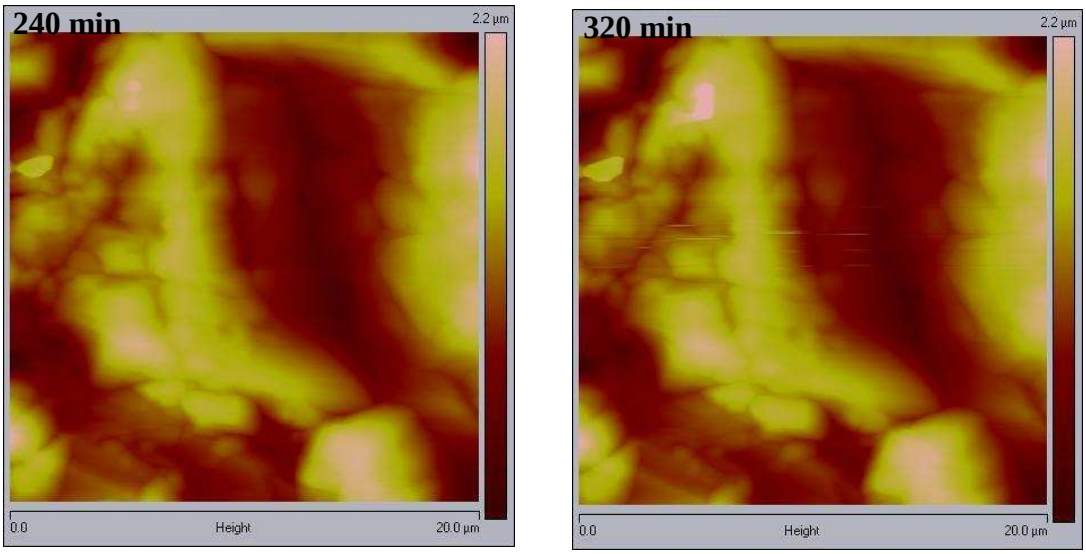

Figure 6-16: AFM images of BDP CFC-11 clathrates in mHFA EtOH oleic acid at various time points (scale; 20 µm x 20 µm).

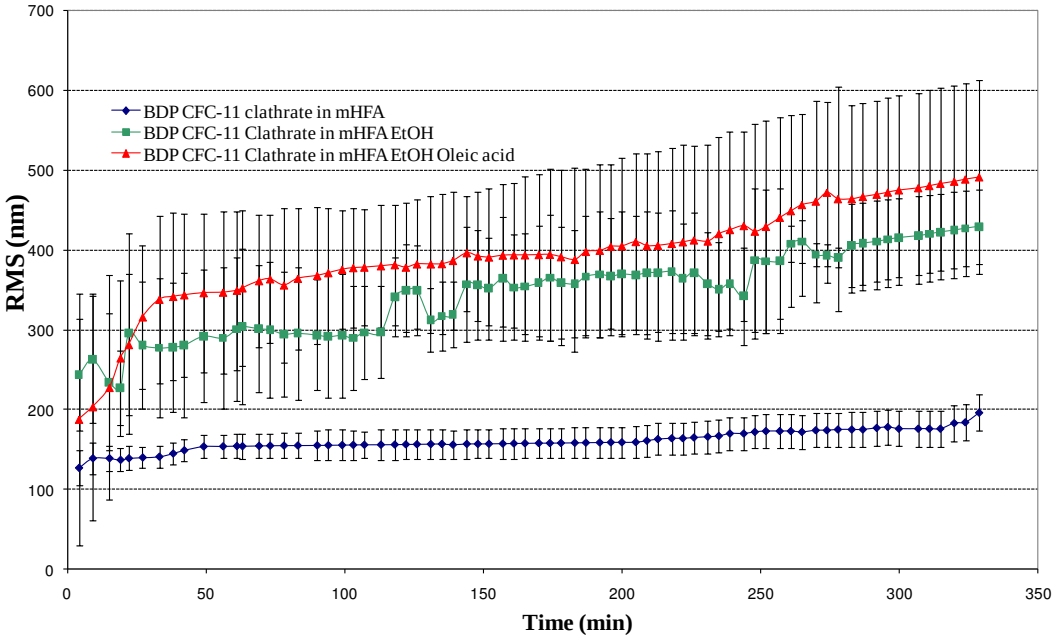

Figure 6-17: Effect of Different mHFA media on the RMS roughness of BDP CFC-11 clathrates with time.

A rapid increase in RMS values of BDP CFC-11 clathrate surface when exposed to mHFA EtOH and mHFA EtOH oleic acid agrees with the topographical images observed in Figures 6-15 and 6-16. A large increase in the roughness of the surface is more pronounced in the first 50 minutes of exposure, with a slower

but steady rate thereafter. This continuous increase in RMS when exposed to mHFA EtOH and mHFA EtOH oleic acid confirms the high surface activity of the clathrate and their potential change when exposed to different media. However, the addition of oleic acid does not seem to have a great influence on the behaviour of the clathrates due to the similarity of the results obtained from both mHFA EtOH and mHFA EtOH oleic acid.

6.3.2.3 Effects of the Different mHFA Media on Budesonide

The effects of different mHFA media on the budesonide particles at different time points of the immersion process was monitored over time by continuous AFM imaging to acquire different topographical images of the surface of budesonide discs. The images in Figure 6-18, show the changes associated with the immersion of budesonide in mHFA alone. These shows the surface of budesonide discs to be very flat with most of the particles aggregated and flattened together with various changes over the period of the study. However, at later stages of their exposure to mHFA, budesonide particles show an increase

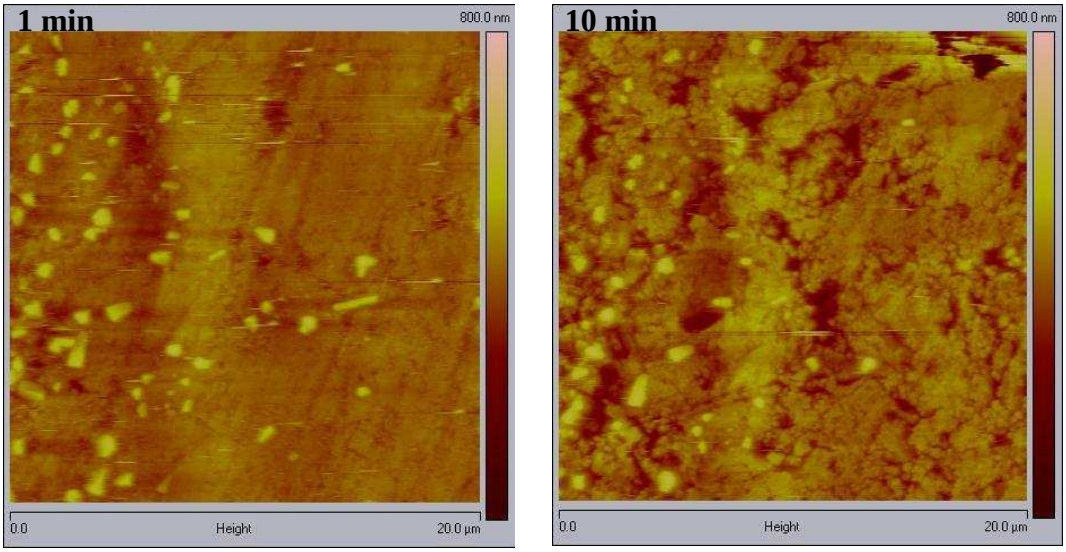

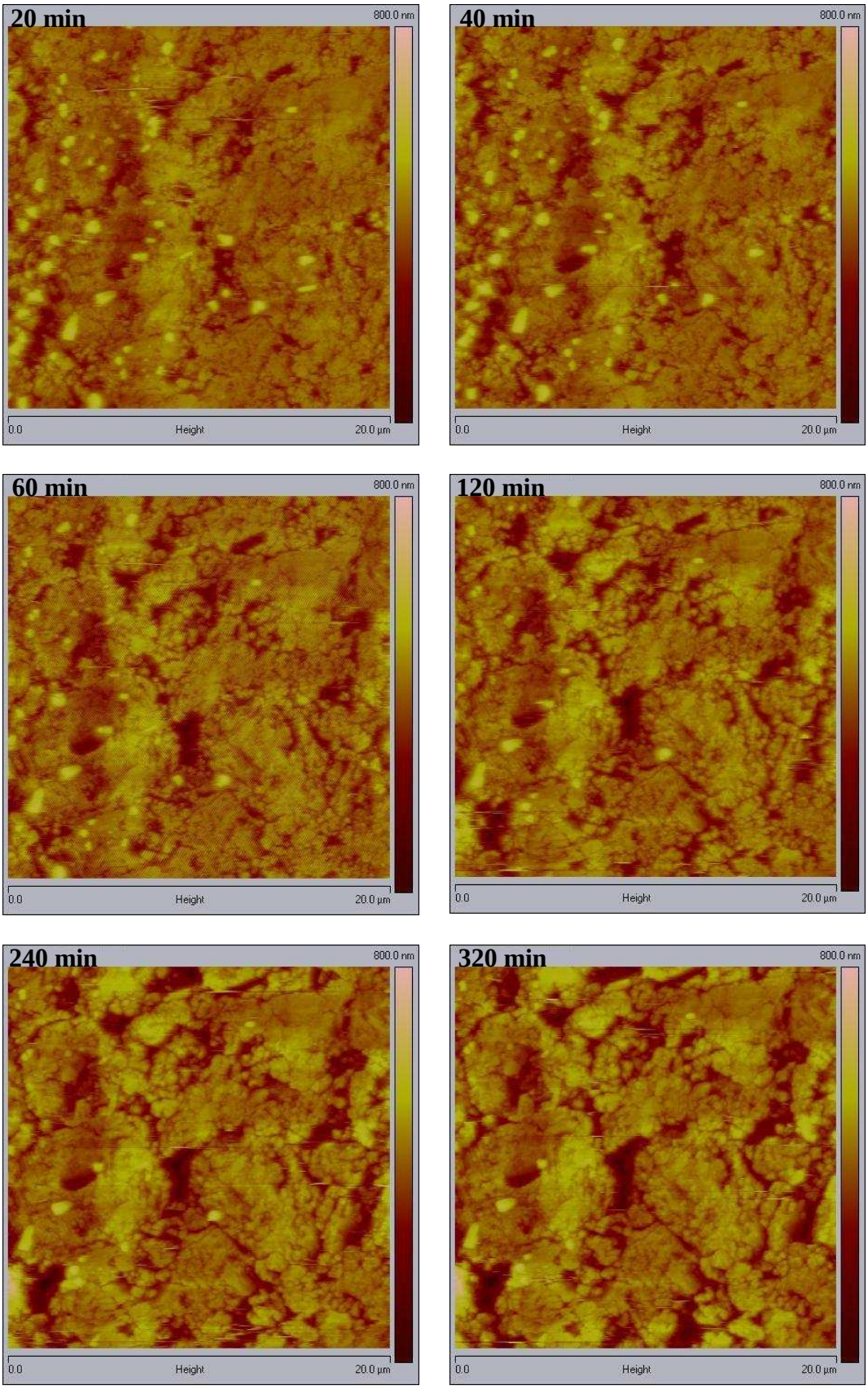

Figure 6-18: AFM images of budesonide in mHFA at various time points (scale; 20 µm x 20 µm).

in surface changes where some large asperities start to appear. Some small particles that were present on the surface of the budesonide disc at the start of the experiment significantly decreased in size by 120 minute of immersion and have disappeared by the end of the experimental period (i.e. 320 minutes). In addition, an increase in the height of various areas on the AFM images is observed, which might suggest the attachment of small particles to different parts of budesonide. This process is relatively rapid as changes in the height of budesonide particles are seen by the minute 5 of their exposure to mHFA media and continues over the experimental exposure time.

Following the exposure of budesonide discs to mHFA EtOH media, the topographical images show minimal variation in the surface over time (Fig. 6-19). An increase in the height of the disc surface is observed after 10 minutes with a steady state thereafter.

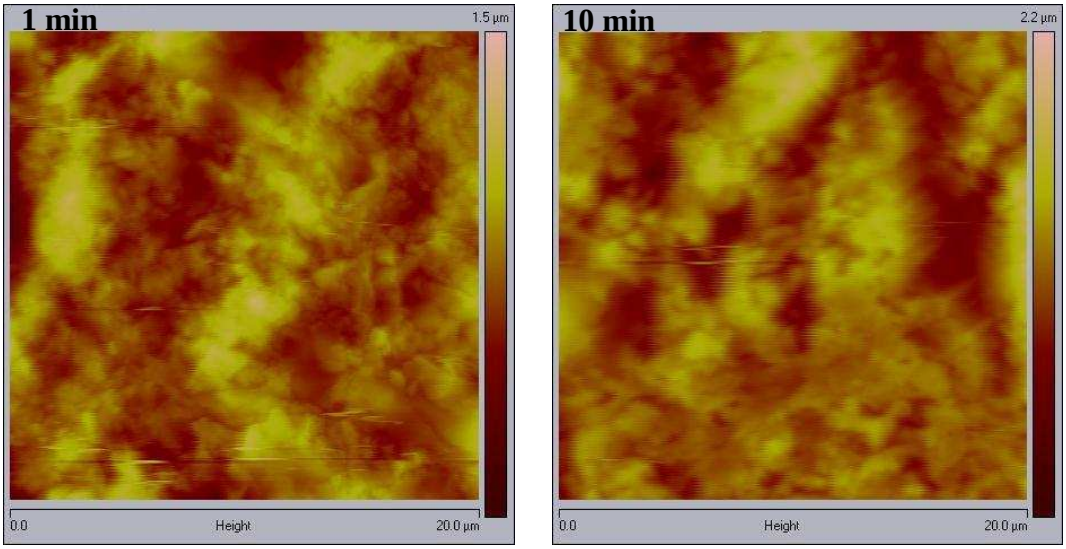

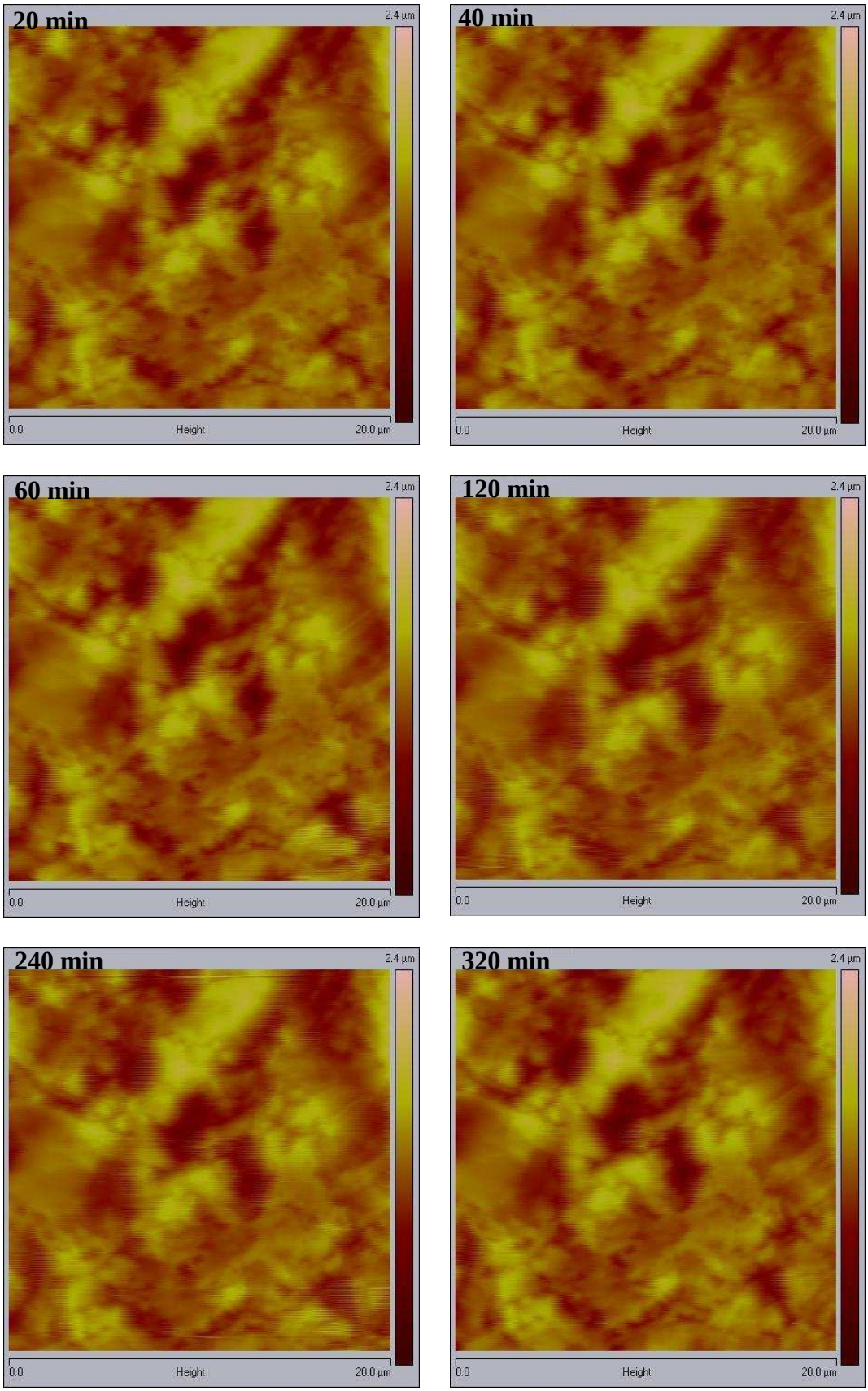

Figure 6-19: AFM images of budesonide in mHFA EtOH at various time points (scale; 20 µm x 20 µm).

Changes in the surface were relatively slow as only few asperities appeared over the surface area of the image, which is thought to be due to dissolution of the small particles. Further changes included the appearance of more rounded particles on the surface of the budesonide discs after 40 minutes of the exposure that might be due to the fusion of very small budesonide particles together to form larger ones. From these images, mHFA EtOH media seems to have a modest effect on the surface of budesonide.

Similarly, mHFA EtOH oleic acid caused no major changes to the surface topography of budesonide particles over the first 10 minutes (Fig. 6-20). However, some changes can be observed after 20 minute where larger asperities could be observed on the surface accompanied by the dissolution of certain parts of the particles. With longer exposure to mHFA EtOH oleic acid, the surface of the budesonide discs show slight variations in the associated topography as featured by a decrease in the height of some areas, possibly due to the dissolution

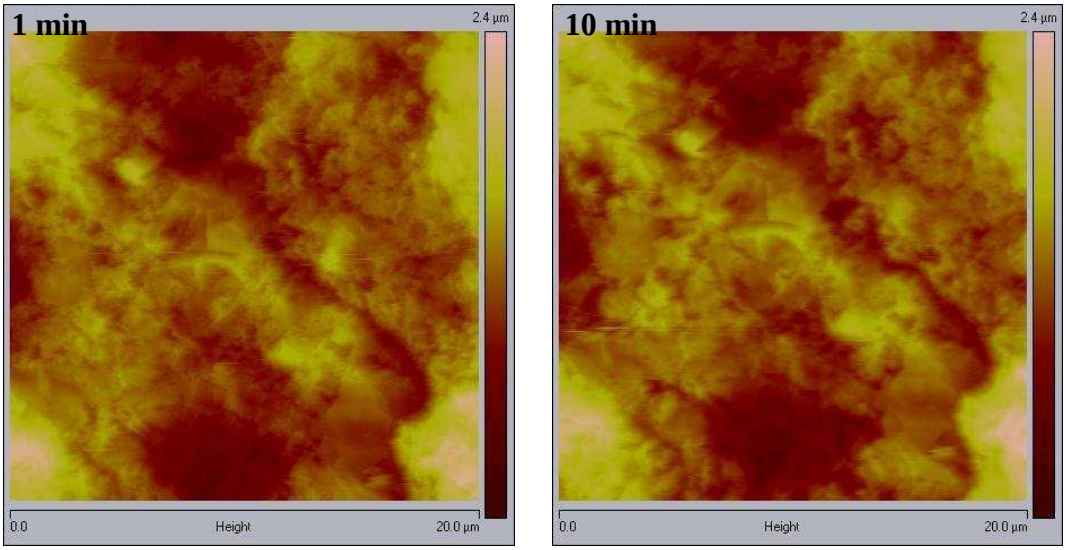

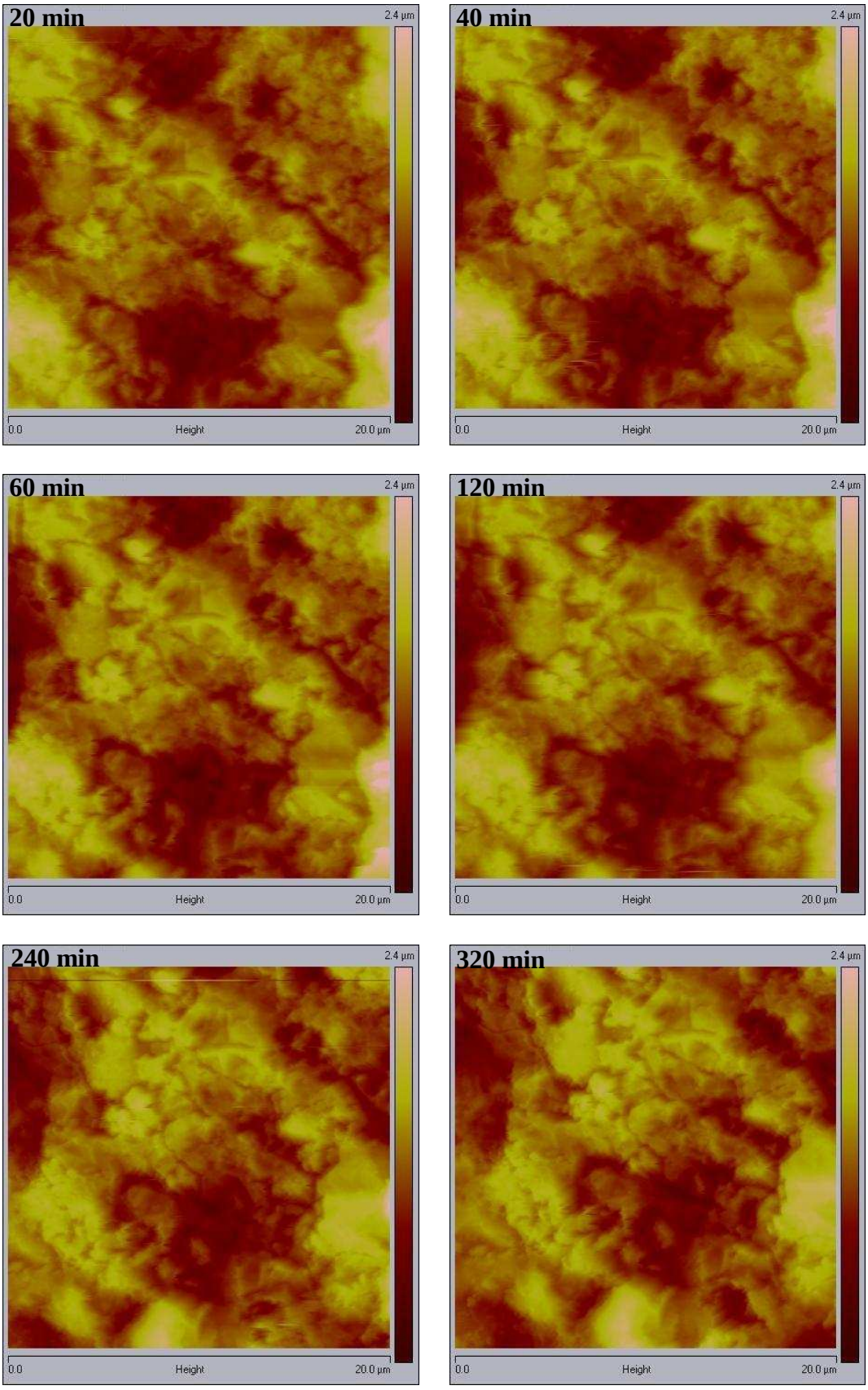

Figure 6-20: AFM images of budesonide in mHFA EtOH oleic acid at various time points (scale; 20 µm x 20 µm).

of some very fine particles, while others parts of the particles seem to have increased due to the localised merging of small particles to the surface.

In order to compare the surface roughness of the budesonide particles, which has been described previously with both anhydrous BDP and BDP CFC-11 clathrates, the RMS values of each of the different AFM images in the different mHFA media were obtained and plotted against time (Figure 6-21). The surface roughness of budesonide particles followed a similar pattern when immersed in all mHFA media with the highest increase being observed in budesonide mHFA

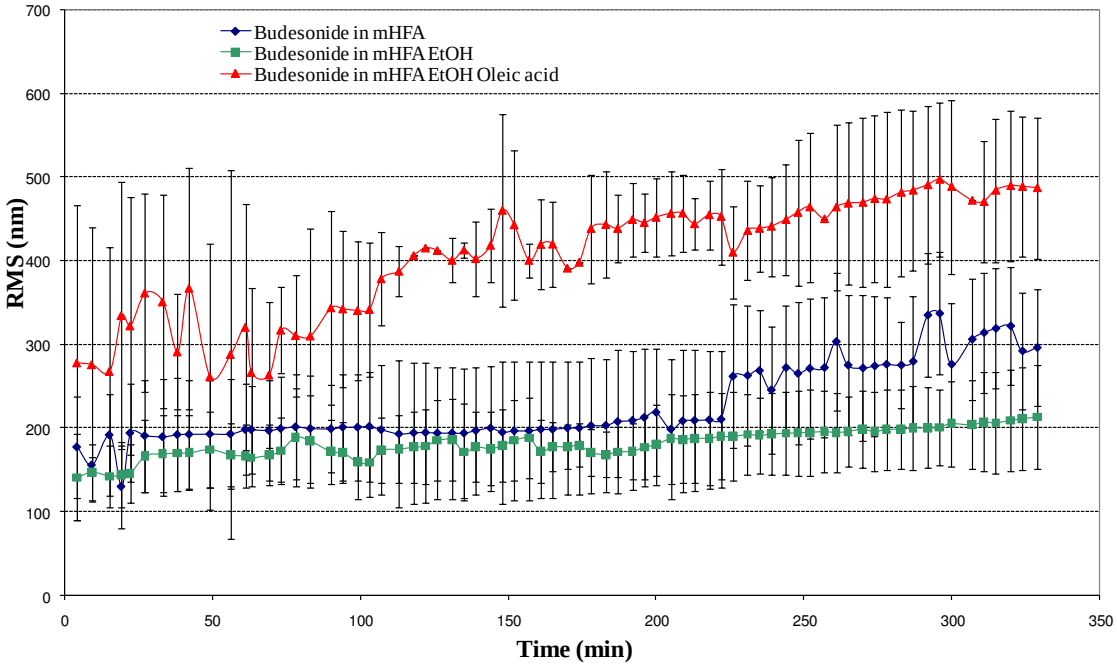

Figure 6-21: Effect of Different mHFA media on the RMS roughness of budesonide with time.

EtOH oleic acid. The pattern of changes included a minimal increase in the surface roughness of budesonide particles (in both mHFA EtOH and mHFA alone) reaching a steady state by 200 minutes which is maintained thereafter. This can be explained by the possible formation of slightly larger particles following the fusion of the smaller dissolved particles of budesonide to the

already existent particles leading to a noticeable change in the surface topography of the budesonide particles and an increase in surface roughness.

6.3.3 Effects of Different mHFA Media on the Particle Size of the Different APIs

The particle size of the APIs, when suspended in the different mHFA media, was determined using the LS Coulter to examine the effects of the propellant on the size of the particles and hence its effect on the overall formulation. The mean particle size of the different APIs used during this project was assessed at different time points of their storage in different mHFA. Results in Figure 6-22 describe changes in the particle size of anhydrous BDP, BDP CFC-11 clathrate and budesonide. The different APIs showed a similar pattern in terms of changes in the mean particle size in the different mHFA media over time, except for BDP CFC-11 clathrates (Fig. 6-22). The patterns observed for both anhydrous BDP and budesonide at different storage times in the different mHFA media exhibit three distinct phases where the mean particle size increase over time as shown in Figures 6-22A and 6-22C, respectively. An initial rapid increase in the mean particle size for both anhydrous BDP and budesonide in the three different media is observed from suspending the particles in the propellant during the first 45 minutes. A second phase is observed for both APIs with a slower rate in the change in the mean particle size from 45 minutes to around 400 minutes. The third phase is a steady state beyond 400 minutes where the mean particle size of both anhydrous BDP and budesonide in the different mHFA media remains constant.

When comparing the behaviour of anhydrous BDP in the different mHFA media it can be observed that the initial mean particle size in the three different media is similar ranging around 15 µm followed by a drastic change in the mean particle size of BDP as featured by an increase in size over time until reaching a steady state by 400 minutes (Fig. 6-22A). Anhydrous BDP suspended in mHFA alone showed the largest increase in the mean particle size where the particles reached a steady state at approximately 110 µm. The standard deviations seem to be relatively large for the different suspensions of the APIs in mHFA alone, possibly due to the high instability of the particles in these suspensions and the rapid kinetic changes occurring at different time points. Exposure of anhydrous BDP to both mHFA EtOH and mHFA EtOH oleic acid resulted in similar pattern of changes to those observed with BDP particles suspended in mHFA alone. However, the rate of changes in the average particle size in the initial phase was slightly lower than that observed in mHFA alone or mHFA oleic acid (Table 6-1). Moreover, exposure of BDP in mHFA EtOH medium was associated with a less significant change in the average particle size compared to BDP particles which were suspended in either mHFA alone or mHFA EtOH oleic acid. This is described by a slow increase in the mean particle size of BDP to approximately 30 µm which, unlike other media, had rapidly reached a steady state by the minute 120 of the storage time.

Suspensions of BDP CFC-11 clathrates in the different mHFA media, however, exhibited a different behaviour compared to the two other APIs especially during the first 20-45 minutes of storage time (Fig. 6-22B). Initially, changes included a relatively rapid reduction in the size of the particles which was more pronounced

for the clathrates that were suspended in mHFA alone, from 45 µm to approximately 2 µm-sized particles. The same behaviour was observed for BDP CFC-11 clathrates suspended in the other mHFA media where the particles were reduced in size from 45 µm to 14 µm and to 18 µm in mHFA EtOH and mHFA EtOH oleic acid, respectively.

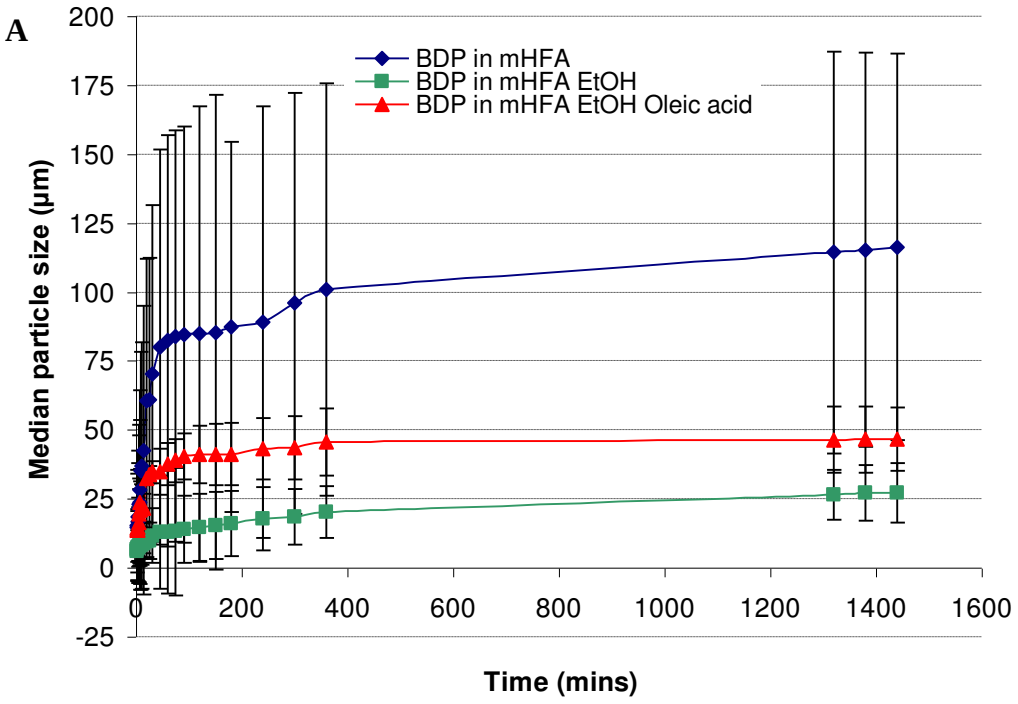

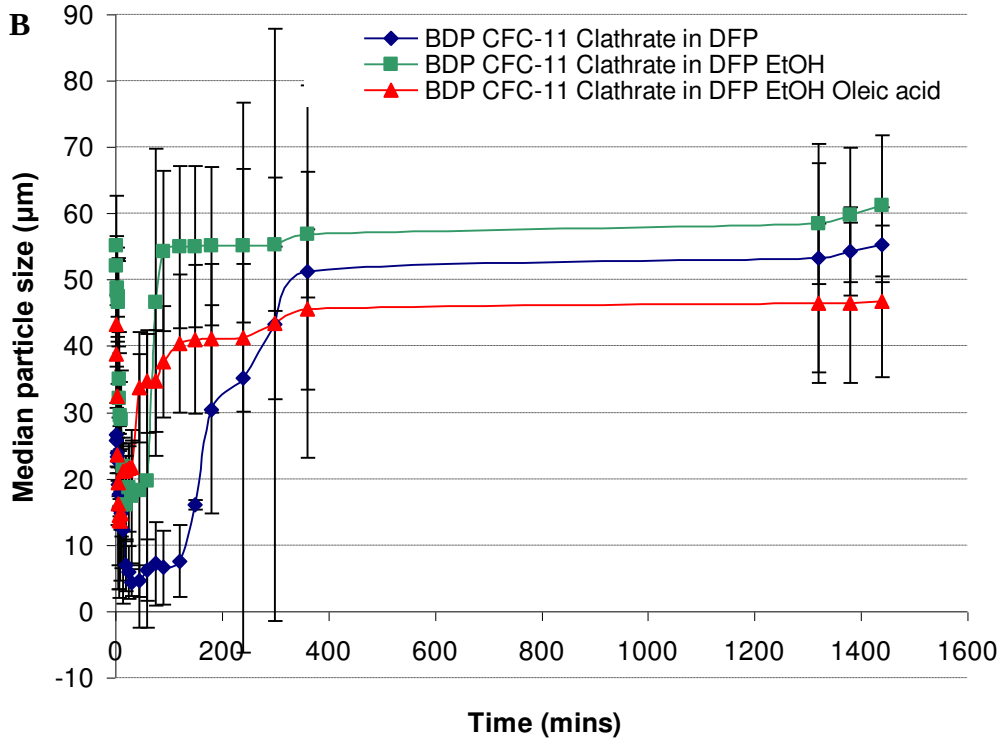

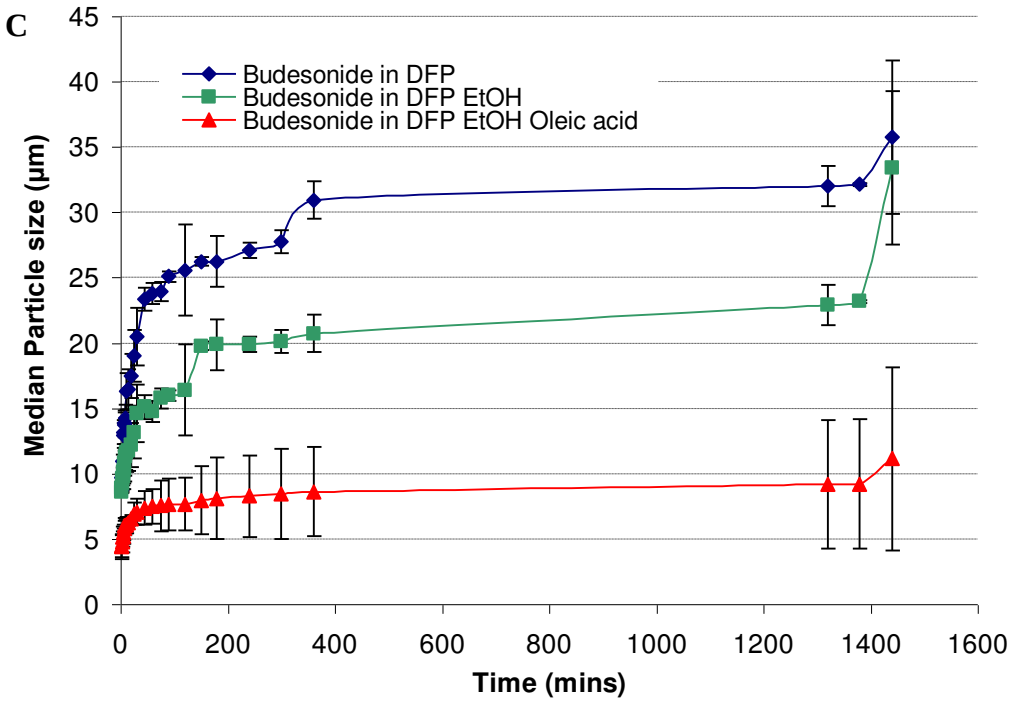

Figure 6-22: Effect of Different mHFA media on the mean particle size of **A-** anhydrous BDP, **B-** BDP CFC-11 clathrate and **C-** budesonide with time.

After the initial reduction in particle size, the particles reached a steady state and then followed a similar behaviour to the one observed with both anhydrous BDP and budesonide in the different mHFA propellant media. The steady state phase was longer for the BDP CFC-11 clathrates in mHFA alone lasting approximately 100 minutes before an increase in the mean particle size was observed (Fig. 6-22B).

The increase in the mean particle size of BDP CFC-11 clathrate was significantly different in the three different media with the highest rate being observed in mHFA alone and the lowest when the clathrates were suspended mHFA EtOH oleic acid. Finally, a stabilisation of the different BDP CFC-11 clathrates-suspensions was reached after approximately 400 minutes of storage allowing

particles to reach their largest average particle size of approximately 55 µm when suspended in mHFA EtOH, while clathrates which were suspended in mHFA alone or in mHFA EtOH oleic acid have reached a size of around 50 µm and 41 µm, respectively.

In contrast, budesonide particles when suspended in the different mHFA media exhibited comparable changes in the average particle size to those observed with anhydrous BDP as shown in Figure 6-22C. Similarities involved the three distinct phases occurring during the storage time. The mean particle size of budesonide increased from approximately 6 µm to 35 µm, 33 µm and 11 µm in mHFA, mHFA EtOH oleic acid and mHFA EtOH, respectively. The rate of the changes in the average particle size of budesonide was similar in mHFA and mHFA EtOH with a lower particle size being observed for budesonide suspended in the latter. Unlike suspensions made with mHFA and mHFA EtOH, mHFA EtOH oleic acid seems to have significantly reduced the average particle size of budesonide, allowing the particle size to rapidly reach a steady state around the minute 200 of the storage time.

Using data from the average particle size of the different APIs in the different mHFA media, the LSW theory was applied using equation 6-2 and results are presented in Figure 6-23. Applying the LSW theory on both anhydrous BDP and budesonide suspended in the different mHFA media, a linear relationship over the four different phases was observed where R^3 was linearly increased with time reaching a steady state during the last phase (Figs. 6-23 A and C respectively).

Table 6-1: Different coarsening rates (K_{LSW} (μm^3/min)) at different stages for anhydrous BDP, BDP CFC-11 clathrate and budesonide.

BDP

Time (mins)\Medium	K_{LSW} in mHFA	K_{LSW} in mHFA EtOH	K_{LSW} in mHFA EtOH Oleic Acid
0 - 45	3410.1	8.6628	838.81
45 - 240	235.92	3.0381	15.656
240 - 360	48277.1	3.0381	1374.2
360 - 1440	504.22	1.364	148.59

BDP CFC-11 Clathrate

Time (mins)\Medium	K_{LSW} in mHFA	K_{LSW} in mHFA EtOH	K_{LSW} in mHFA EtOH Oleic Acid
0 - 90	-98.138	-1146.8	-792.41
90 - 180	67.516	172.38	48.931
180 - 360	32.001	9.8238	7.6761
360 - 1440	2.5027	2.6134	0.8298

Budesonide

Time (mins)\Medium	K_{LSW} in mHFA	K_{LSW} in mHFA EtOH	K_{LSW} in mHFA EtOH Oleic Acid
0 - 35	42.02	7.3521	0.9928
35 - 240	5.2693	5.4622	0.352
240 - 1320	2.1062	0.4422	0.091
1320 - 1440	0.104	0.4422	0.091

The different phases had different slopes i.e. different rates of Ostwald ripening (Table 6-1). These results are in agreement with the ones obtained earlier in Figure 6-22, in which the mean particle size of the particles reaches a steady state in terms of the size. The largest increase in R^3 for both anhydrous BDP and budesonide was observed with the mHFA media alone, while both mHFA EtOH and mHFA EtOH oleic acid resulted in a lower R^3. Exceptionally, mHFA EtOH showed a significant reduction in the cubic radius of the particle size of anhydrous BDP compared to the two other media, whereas mHFA EtOH oleic acid produced the highest reduction in R^3 in budesonide.

However, applying the LSW theory on BDP CFC-11 clathrates suspended in the different mHFA media showed some differences compared to both anhydrous BDP and budesonide (Fig. 6-23B), highlighting two major phases:

- An initial phase where R^3 is reduced corresponding to the collapse of the BDP CFC-11 clathrate structure and the formation of smaller particles with lower R^3.
- A second phase in which a linear relationship of the increasing R^3 over time is similar to the other APIs. Three different phases are observed for the coarsening of BDP CFC-11 clathrates where the rate of each phase is gradually decreasing until reaching a steady state (Fig. 6-23B) and the rate of the coarsening is shown in Table 6-1.

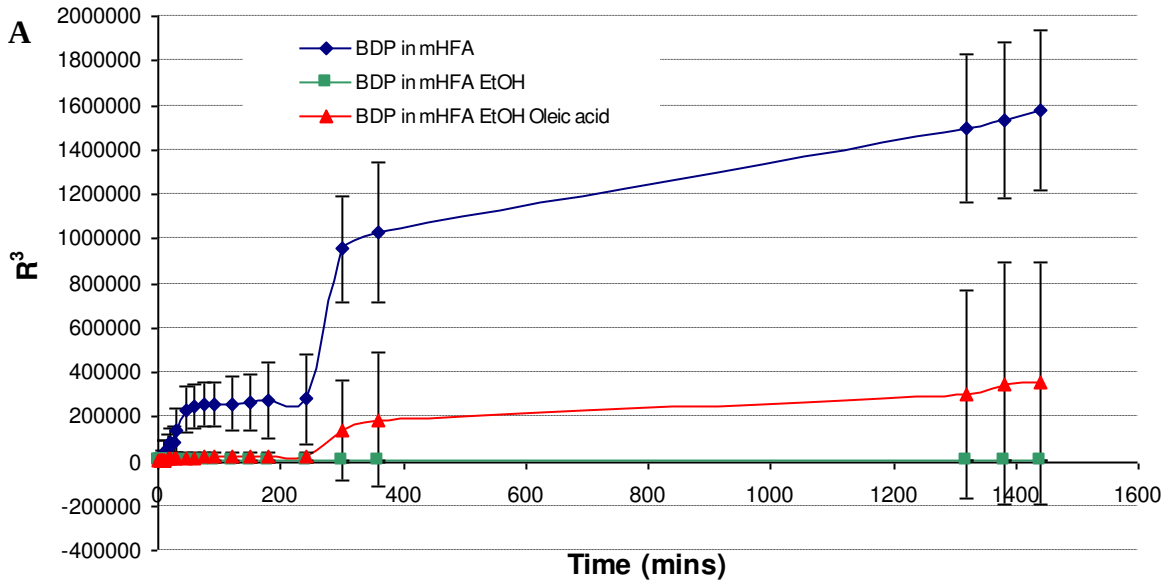

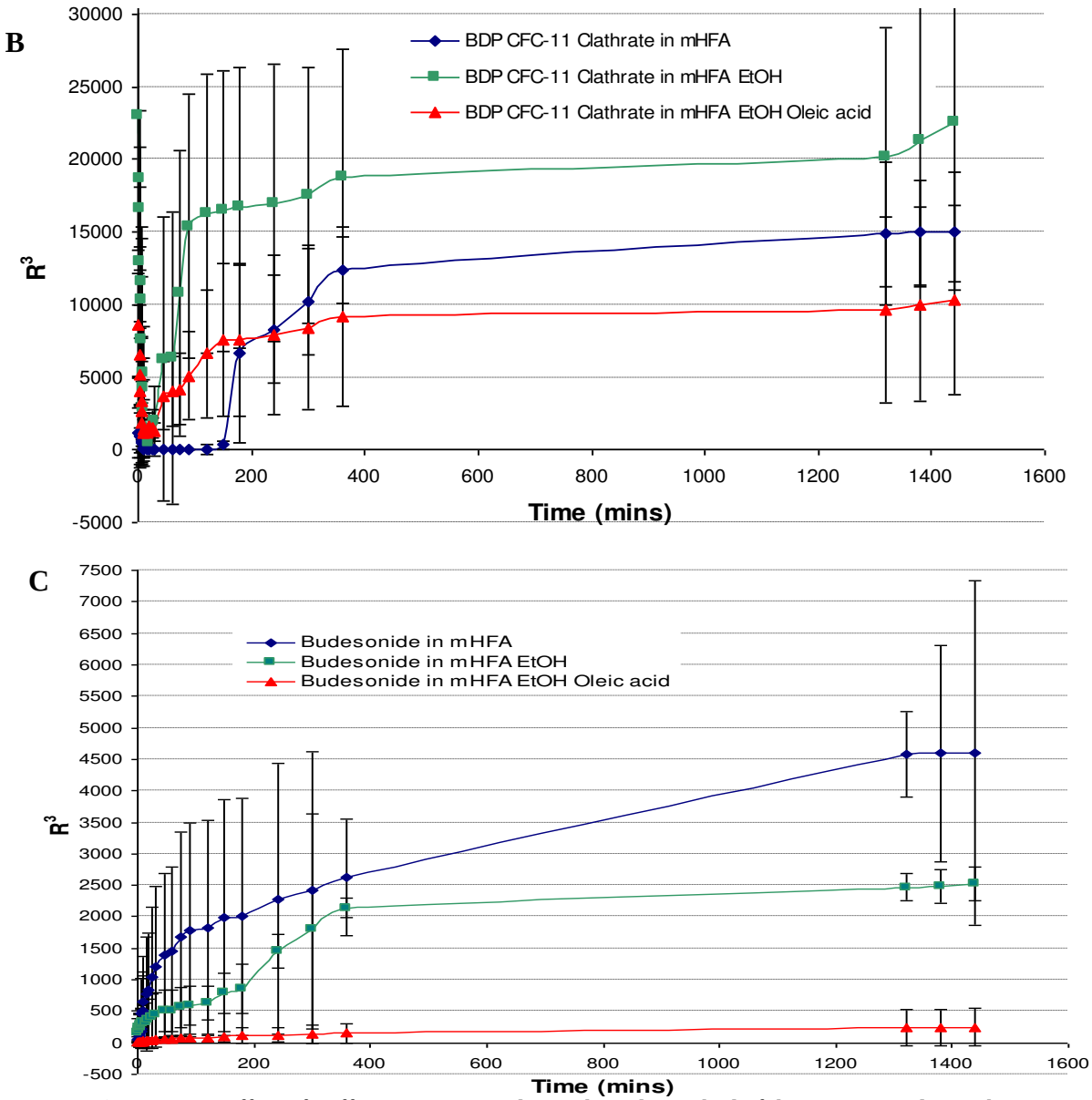

Figure 6-23: Effect of Different mHFA media on the radius cubed of the mean particle size by applying LSW theory of **A-** anhydrous BDP, **B-** BDP CFC-11 clathrate and **C-** budesonide with time.

6.4 Discussion

6.4.1 Effects of the Different mHFA Media on the Surface of the Different APIs

The SEM results showed, qualitatively, that the primary particle size of the suspended drugs was of 1-5 µm, 5-10 µm and 60-70 µm for anhydrous BDP,

budesonide and BDP CFC-11 clathrates respectively shortly after being suspended in the different mHFA media. BDP CFC-11 clathrates, showed a very significant reduction in the average particle size after being suspended in the different mHFA media. This reduction can be attributed to the collapse of the crystal structure as soon as these are immersed in a different media from their mother liquor. The collapse of the structure, led to the formation of a different BDP entity (anhydrous BDP) as discussed in Chapter 3, Section 3.3.5. The size of the particles formed was slightly larger in size than anhydrous BDP (~ 20 µm) and indicated high crystallinity. Evidence of a corresponding increase in the average drug particle size was observed for anhydrous BDP in the different mHFA media with time after being suspended in the different mHFA media. After an initial reduction during the first minutes of exposure to the different mHFA media, BDP CFC-11 clathrates followed a similar pattern to that observed for the other APIs. Budesonide showed a very small increase in particle size in the different mHFA media. However, the SEM images of budesonide in the different mHFA media revealed the presence of larger size particles at the end of the experimental storage time. The majority of the model propellant evaporates very rapidly. Thereafter, micronized drug particles may adhere together with surfactant in the case of the APIs suspended in mHFA EtOH oleic acid.

The continuous changes in the surface roughness of the different APIs can be explained by the high activity (i.e. rapid dissolution and changes on the surface topography as observed by AFM) of the surface due to the exposure to the different mHFA media. Both BDP and budesonide have increased solubility in

mHFA compared to the ozone depleting CFC propellants (Tzou et al., 1997). This will lead to some dissolution of particles at the surface of the two different APIs. The dissolution of the particles led to changes in surface topography and differences in height that will lead to an increased surface roughness. Furthermore, the small particles may attach to the larger more energetically favoured surface leading to an increase in height that is expressed by an increase in the RMS roughness. Furthermore, growth tends to occur at the edge of a particles rather than on the flat surface (Noboru et al., 1999). This was observed for both BDP and budesonide compared to the BDP CFC-11 clathrates. This may be attributed to the higher surface energy in these positions (Mullin, 2001). This could mean that particles with a rougher surface are likely to grow faster than those with a smoother surface.

The addition of ethanol showed mostly a higher surface roughness compared to the mHFA alone. Ethanol is used in order to solubilise the different surfactants in the propellants and also help to disperse the drug (Tzou et al., 1997). The addition of ethanol also increases the solubility of both APIs (Berry et al., 2003). Therefore, this may lead to an increased dissolution of the surface of the different APIs leading to more significant changes in surface roughness. The increase observed in surface roughness can be explained by the dissolution of very small fine particles at the surface of the APIs that will lead to changes an height and their corresponding attachment to larger particles already present at the surface forming more energetically favoured particles that have a greater size, and hence difference in the heights and RMS roughness values.

The addition of oleic acid to mHFA EtOH media reduced the rate of surface roughness changes compared to the other mHFA media. This can be attributed to the effect of the surfactant, oleic acid on the surface of the different APIs. Oleic acid would adhere to the surface of the API leading to an increased RMS roughness and providing more stability to the particles (James, 2009). The mechanism of this surfactant adherence to the APIs surface is most likely via the encapsulation of API particles by surfactant molecules in the solution, i.e. the hydrophilic head of the surfactant associating with the particle surface, leaving the hydrophobic tails to protrude into the highly hydrophobic bulk surfactant media. Therefore, this will lead to a lower surface activity.

6.4.2 Effects of the Different mHFA Media on Ostwald Ripening of the Different APIs

Size-dependent particle growth, in which larger particles grow more readily than smaller particles, has been observed for a number of suspension systems of low viscosity (White et al., 1976, Wey and Strong, 1977, Garside and Davey, 1980, Yushan et al., 1984, Jones et al., 1986, Sta´vek and Ulrich, 1994). For seed crystals in the size range of about 0.5 µm to 100 µm, a linear increase in particle growth with the size of the seed crystal has been observed (Garside and Davey, 1980, Yushan et al., 1984, Berry et al., 2003). These conditions exist in the present system because the particles were within the predicted size range. Based on the results obtained in the previous section, the increase in particle size in the different mHFA media can be attributed at least in part to the particle size of the suspended API.

The move to larger particle sizes is believed to occur as a result of the dissolution of the smaller particles (less energetically favoured) followed by the deposition of these on the existing particles (more energetically favoured) (Ostwald ripening) (Berry et al., 2004b). Size-dependent particle growth involves diffusion of the molecular growth units to the solid surface of the particle, followed by rate-limiting integration of these growth units onto the particle (Garside and Davey, 1980, Berry et al., 2003). According to the Ostwald ripening model, the proportion of nucleation sites would be greater on large particles compared with small particles (Garside and Davey, 1980, Berry et al., 2003). There was no strong evidence of new nuclei formation in this system. The formation of new nuclei tends to occur for relatively dilute systems in which the majority of particles are < 500 nm (Verdoes et al., 1992, Auer and Frenkel, 2001, Mullin, 2001). This process is unlikely to have occurred as most of the particles in the different systems studied in this chapter have particles in the micron range.

It has been found in HFA-based systems that there was an increase in API cohesiveness due to the tendency of the fluorocarbon propellant to self associate (Tzou et al., 1997, James, 2009). Therefore, a greater particle contact could result in particle growth through fusion of particle surfaces. This phenomenon could contribute to the enhanced particle growth of coarse material by the fact that larger surfaces are generally considered to have stronger interparticle forces, and these materials may also have surface properties that would lead them to be more prone to growth (Berry et al., 2003). Also, the effects of micronization of the APIs cannot be neglected as these results in particles that have a slightly higher

surface energy as demonstrated in Chapter 5 and hence may lead to more interactions between particles resulting in the formation of larger particles.

For suspension formulations, by altering the surface properties of a drug can promote drug aggregation and or particle growth and lead to an increase in the average particle size of the particles due to the addition of either co-solvents and/or surfactants (Berry et al., 2003). Ethanol is used as a co-solvent and is employed to dissolve the surfactant, which in this case results in an increased API solubility of more than 0.5% w/w as well as helping to disperse the drug in many manufacturing processes currently used for suspension formulations (Tzou et al., 1997). This level of solubility in the present system may be sufficient to provide the driving force for rate-limiting step for particle growth. As particles in the suspension dissolve, this will lead to the formation of a very fine particle with a reduced thermodynamic stability that would lead to the attachment to larger particles to form more thermodynamically energetically favoured particles.

The presence of surfactant (oleic acid) in the formulation, a long chain fatty acid, may aid in the stabilization of the drug surface. The adhesion of oleic acid to the drug surface could reduce the polarity of the drug, thus making it less likely to interact with the highly electronegative propellant medium. Factors that affect the surface energy of the particles (i.e., by steric or charge stabilization), including the addition of additives such as surfactants, have been shown to control their aggregation behaviour by inducing a decrease in their cohesiveness (Hickey et al., 1988, Eriksson et al., 1995, Blackett and Buckton, 1995, Bower et

al., 1996, Ranucci et al., 1990, Parsons et al., 1992, Tzou et al., 1997). Generally, these additives lead to reduced particle interaction and hence less particle-particle interaction leading to a lower rate of particle growth and result in a smaller average particle size within the formulation (Ranucci et al., 1990, Bower et al., 1996, Berry et al., 2004a).

6.5 Conclusions

This study showed that the particle size of the APIs in the pMDI suspension followed size dependent particle growth via Ostwald ripening and the LSW theory. This process involved the association of small thermodynamically unstable API particles with larger more energetically favoured particles. This association was shown by a linear increase in particle growth with the time. The level of solubility in the different systems was sufficient to provide the driving force for rate-limiting particle growth and thus the dominant step in the particle growth. However, as the storage time increases the rate of the coarsening decreases to reach an equilibrium and stability due to a decrease in the dissolution as small API particles disappear through their attachment to larger particles.

The use of APIs in mHFA propellant alone showed particle growth following LSW theory. This behaviour was due to an increased cohesiveness of the API particles when in contact with the propellant leading to instability of the formulation. However, the use of ethanol as a co-solvent and oleic acid as a surfactant within the pMDI formulation created more stable formulations. Even

though, ethanol showed an increase in the solubility of the different APIs in the pMDI formulation. However, the effect on the particle size showed a reduction in the mean particle size of the APIs when compared to the use of the APIs with propellant on its own. The use of a combination of both ethanol and oleic acid in the pMDI formulation produced an increase in the stability of the colloidal suspension and a decrease in the average particle growth as well as the rate of Ostwald ripening.

Since it is critical that the drug particle size of MDIs be tightly controlled, it is important that all factors that affect it be well understood and carefully evaluated as this can have an impact on aerodynamic particle size of the emitted aerosol is presented and hence on final product quality and effectiveness.

6.6 References

AUER, S. & FRENKEL, D. (2001) Suppression of crystal nucleation in polydisperse colloids due to increase of the surface free energy. Nature, 12**,** 773-779.

BAECKSTROEM, K. & NILSSON, P. G. (1988) Measurements of droplet size distributions from metered dose inhalers with different vapour pressures and contents of surfactant. Journal of Aerosol Science, 19**,** 1097 - 1100.

BERRY, J., KLINE, L., NAINI, V., CHAUDHRY, S., HART, J. & SEQUEIRA, J. (2004a) Influence of the valve lubricant on the aerodynamic particle size of a metered dose inhaler. Drug Development and Industrial Pharmacy, 30**,** 267-75.

BERRY, J., KLINE, L. C., HART, J. L. & SEQUEIRA, J. (2003) Influence of the storage orientation on the aerodynamic particle size of a suspension metered dose inhaler containing propellant HFA-227. Drug Development and Industrial Pharmacy, 29**,** 631-9.

BERRY, J., KLINE, L. C., SHERWOOD, J. K., CHAUDHRY, S., OBENAUER-KUTNER, L., HART, J. L. & SEQUEIRA, J. (2004b) Influence of the size of micronized active pharmaceutical ingredient on the aerodynamic particle size and stability of a metered dose inhaler. Drug Development and Industrial Pharmacy, 30**,** 705-14.

BLACKETT, P. M. & BUCKTON, G. (1995) A microcalorimetric investigation of the interaction of surfactants with crystalline and partially crystalline salbutamol sulphate in a model inhalation aerosol system. Pharmaceutical Research, 12**,** 1689-1693.

BOWER, C., WASHINGTON, C. & PUREWAL, T. S. (1996) Characterization of surfactant effect on aggregates in model aerosol propellant suspensions. Journal of Pharmacy and Pharmacology, 48**,** 337-341.

BRINDLEY, A. (1999) The chlorofluorocarbon to hydrofluoroalkane transition: the effect on pressurized metered dose inhaler suspension stability. Journal of Allergy and Clinical Immunology, 104**,** S221-6.

BUTZ, N., PORTE´, C., COURRIER, H., KRAFFT, M. P. & VANDAMME, T. F. (2002) Reverse water-in-fluorocarbon emulsions for use in pressurized metered-dose inhalers containing hydrofluoroalkane propellants. International Journal of Pharmaceutics, 238**,** 257–269.

BYRON, P. R. & BLONDINO, F. (1996) Pharmaceutically acceptable agents for solubilising, wetting, emulsifying, or lubricating in metered dose inhaler formulations which use HFC-227 propellant. The Center for Innovative Technology; Virginia Commonwealth University.

BYRON, P. R., MILLER, N. C., BLONDINO, F. E., VISICH, J. E. & WARD, G. H. (1994) Some aspects of alternative propellant solvency. RDD IV.

CLARKE, J. G., WICKS, S. R. & FARR, S. J. (1993) Surfactant-Mediated Effects in Pressurized Metered-Dose Inhalers Formulated as Suspensions. International Journal of Pharmaceutics, 93**,** 221-231.

ERIKSSON, P. M., SANDSTROM, K. B. & ROSENHOLM, J. B. (1995) The distribution of oleic acid between salbutamol base drug and different propellant blends. Pharmaceutical Research, 12**,** 715-719.

GANDERTON, D., LEWIS, D., DAVIES, R., MEAKIN, B. & CHURCH, T. (2003) The formulation and evaluation of a CFC-free budesonide pressurised metered dose inhaler. Respiratory Medicine, 97 Suppl D**,** S4-9.

GARSIDE, J. & DAVEY, R. J. (1980) Secondary contact nucleation: kinetics, growth and scale-up. Chemical Engineering Communications, 4**,** 393–424.

HICKEY, A. J., DALBY, R. N. & BYRON, P. R. (1988) Effects of surfactants on aerosol powders in suspension. International Journal of Pharmaceutics, 42**,** 267-270.

JAMES, J. (2009) The interaction of drug particles with materials employed in inhaled delivery devices. School of Pharmacy. Nottingham, University of Nottingham.

JOHNSON, K. A. (1996) Interfacial phenomena and phase behaviour in metered-dose inhaler formulations. IN DEKKER, M. (Ed.) Inhalation Aerosols. D.J.W. Grant ed. New York, Marcel Dekker.

JONES, A. G., BUDZ, J. & MULLIN, J. W. (1986) Crystallization kinetics of potassium sulfate in an MSMPR agitated vessel. AIChE Journal, 32**,** 2002-2009.

JONES, S. A., Martin, G. P. & Brown, M. C. (2006) Manipulation of beclomethasone–hydrofluoroalkane interactions using biocompatible macromolecules. Journal of Pharmaceutical Sciences, 95, 1060-1074.

MARIJANI, R., SHAIK, M. S., CHATTERJEE, A. & SINGH, M. (2007) Evaluation of metered dose inhaler (MDI) formulations of ciclosporin. Journal of Pharmacy and Pharmacology, 59**,** 15-21.

MCDONALD, K. J. & MARTIN, G. P. (2000) Transition to CFC-free metered dose inhalers - into the new millennium. International Journal of Pharmaceutics, 201**,** 89-107.

MULLIN, J. W. (2001) Crystallization, Butterworth.

NOBORU, S., MASAAKI, Y., AKIRA, S. & NORIAKI, K. (1999) Growth enhancement and liquid-inclusion formation by contacts on NaCl crystal. AIChE Journal, 45**,** 1153-1156.

PARSONS, G. E., BUCKTON, G. & CHATHAM, S. M. (1992) The use of surface energy and polarity determinations to predict physical stability of non-polar, nonaqueous suspensions. International Journal of Pharmaceutics, 83**,** 163-170.

POLLI, G. P., GRIM, W. M., BACHER, F. A. & YUNKER, M. H. (1969) Influence of formulation on aerosol particle size. Journal of Pharmaceutical Sciences, 58**,** 484-6.

RANUCCI, J. A., DIXIT, S., BRAY, R. N., JR. & GOLDMAN, D. (1990) Controlled flocculation in metered-dose aerosol suspensions. Pharmaceutical Technology**,** 68-74.

SMYTH, H. D. (2003) The influence of formulation variables on the performance of alternative propellant-driven metered dose inhalers. Advanced Drug Delivery Reviews, 55**,** 807-28.

SNYDER, V. A., ALKEMPER, J. AND VOORHEES, P.W. (2001) Transient Ostwald ripening and the disagreement between steady-state coarsening theory and experiment. Acta Materialia, 49**,** 699-709.

STA´VEK, J. & ULRICH, J. (1994) A possible new approach to the better understanding of crystallization kinetics. Crystal Research and Technology, 29**,** 465–484.

TRAINI, D. YOUNG, P. M., PRICE, R., & ROGUEDA, P. (2006) A novel apparatus for the determination of solubility in pressurized metered dose inhalers. Drug Development and Industrial Pharmacy, 32, 1159-1163.

TZOU, T. Z., PACHUTA, R. R., COY, R. B. & SCHULTZ, R. K. (1997) Drug form selection in albuterol-containing metered-dose inhaler formulations and its impact on chemical and physical stability. Journal of Pharmaceutical Sciences, 86**,** 1352-7.

VERDOES, D., KASHCHIEV, D. & VAN ROSMALEN, G. M. (1992) Determination of nucleation and growth rates from induction times in seeded and unseeded precipitation of calcium carbonate. Journal of Crystal Growth, 118**,** 401-413.

VERVAET, C. & BYRON, P. R. (1999) Drug-surfactant-propellant interactions in HFA-formulations. International Journal of Pharmaceutics, 186**,** 13-30.

WEY, J. S. & STRONG, R. W. (1977) Influence of the Gibbs–Thomson effect on the growth behaviour of AgBr crystals. Photographic Science and Engineering, 21**,** 248–252.

WHITE, E. T., BENDIG, L. L. & LARSON, M. A. (1976) The effect of size on the growth rate of potassium sulfate crystals. AIChE Symposium Series, 153**,** 41-47.

WU, L. & DA ROCHA, S. R. (2007) Biocompatible and biodegradable copolymer stabilizers for hydrofluoroalkane dispersions: a colloidal probe microscopy investigation. Langmuir, 23**,** 12104-10.

YUSHAN, R., QIU, T. & YUANMOU, Z. (1984) A study on the growth kinetics of small crystals of KCl. Process Technology Proceedings, 2**,** 289–292.

Chapter 7 Final Conclusions

7.1 General Introduction

At the start of this PhD project, a large number of studies had been undertaken in order to study the performance of different inhaled therapy systems. Most of these studies investigated the stability and particle interaction relevant to DPI formulation, while fewer studies were used to determine stability in pMDI formulations. With the release of the new HFA propellants as a replacement of the non-environmentally friendly CFCs, different HFA formulations have faced problems with the stability of different APIs and their interactions within a pMDI system. HFA and CFC propellants possess different physical and chemical properties and are generally poor solvents for many anti-asthma drugs and excipients currently used in pMDIs (McDonald and Martin, 2000). Thus the substitution to HFAs propellant changed the properties of some of the drugs delivered by CFC propellant systems and required reformulation of the drugs (Terzano, 2001). Furthermore, the APIs used in previous studies have been limited; typically salbutamol sulphate, formoterol fumarate. Few studies have considered the stability of corticosteroids (such as beclomethasone dipropionate and budesonide) that have potential use in pMDI systems. Hence, to the author's knowledge, while the crystal structure of the BDP co-solvent/propellant clathrate has been investigated, there is little information on the physico-chemical characteristics of the BDP co-solvent/propellant clathrates, their stability and their potential interactions within a pMDI system. Subsequently, the work in this

thesis sought to gain a better understanding of the effects of various formulation constituents on the solid-state of different APIs and their potential interactions within a pMDI system.

Different analytical techniques have been used on several studies to determine the solid state behaviour of APIs in pMDIs (Phillips and Byron, 1994). Thermal analysis techniques (including DSC and TGA) and X-ray diffractions have been used in order to determine any changes on the nature of the drugs in terms of polymorphism and/or introduction of amorphous material following manufacturing processes. AFM was also used in investigating the interaction between individual particles from inhaled therapy systems in order to determine the effect on the product performance (Ashayer et al., 2004, Traini et al., 2006, James et al., 2008). Furthermore, AFM was used as a tool to determine the effect of different media on the crystal behaviour of the drugs. Other techniques, such as light scattering techniques have been utilised for investigating particle growth and have been demonstrated on several relevant systems. However, most of these studies were determined in model propellants without the use of any additives such as co-solvents and/or surfactants. The effects of these different formulation excipients are crucial to the formulation stability and therefore the end performance of a pMDI system. The different techniques described allow for an early-stage detection of the suitability of use of different materials in combination with co-solvents and surfactants to obtain an optimal stability and performance.

Moreover, this study has purposely undertaken a single particle approach via AFM to understand the API interactions within a pMDI system. AFM provided single-particle force measurements which generated information that was then used to determine the corresponding surface energy of the different APIs. These results allowed the determination of the force of adhesion in situ following size reduction, between the API and a corresponding surface in relation to the surrounding medium relevant to the formulation of an API for inhalation therapy.

Generally speaking, most of the analytical techniques used in the different studies within this thesis require micrograms of material for analysis to characterise the different API and their combined use provide useful information about the solid-state of the API as well as the interactive nature of each material in a pMDI system. Therefore these approaches could allow for early-phase development of pMDI systems with new chemical entities since any API of interest in research and development would warrant the use of only small amounts of material. These techniques would also provide information about the nature of the new chemical entities and their potential interactions within a device.

Here, the relevant conclusions concerning the project will be outlined as well as overall comments based on the conclusions in relation to formulating an effective pMDI system with the environmentally friendly HFA propellants.

7.2 Physico-chemical Characteristics of Beclomethasone HFA Propellant Clathrates

In Chapter 3, BDP CFC-11 clathrate was produced as a model clathrate due to its stability by suspending BDP in CFC-11. This formation is due to BDP crystallizing with a channel structure forming a clathrate that allows the insertion of CFC-11 within its structure (Harris et al., 2003). The results obtained using different techniques showed an efficient growth of the clathrate with the different concentrations used for the study as well as successful inclusion of CFC-11 molecules into the BDP channels. The highest molar ratio of CFC-11 to BDP obtained with a 1.67% w/w BDP in CFC-11 was a 0.6:1 molar ratio. It has been shown that the presence of a stoichiometric relationship can be observed with increasing ratios of CFC-11 to BDP. The release of the propellant from the structure was induced by heating. This was proposed to be due to a structural rearrangement of the clathrate. It is understood that this structural rearrangement induces changes in the hydrogen bonding holding the clathrate from collapsing or decomposing that leads to the release of the propellant from the tunnels constituting the structure of the clathrate.

Chapter 4, an experimental approach based on DSC/TGA and XRPD showed evidence of the clathrate formation with HFA-134a and HFA-134/ethanol mixture. The crystals exhibited a transition when being heated to their melting point, which is considered to be due to the release of the HFA-134a and HFA-134a/ethanol from the channels constituting the crystal structure of the clathrate. The release of HFA-134 and ethanol is due to a structural rearrangement of the crystal structure releasing the propellant and the propellant/co-solvent leading to

the formation of anhydrous BDP. The use of ethanol/HFA-134a provides a more rigid structure of the channels and prevents the collapse and the release of both ethanol and the propellants from some channels at room temperature.

Anhydrous BDP and BDP HFA-134a/ethanol clathrate mixture showed a high stability from room temperature to approximately 71 ºC. A further increase in temperature leads to a transformation of BDP clathrate to the anhydrous form of BDP which was more stable at higher temperatures. This means that the formation of BDP HFA-134a/ethanol is quite stable at room temperature and that some clathrate channels retain both the solvent and the propellant to quite high temperatures. After 90 ºC, a similar behaviour to the one observed in anhydrous BDP followed, due to the increased vibration of the side chain of BDP molecules.

In contrast, no clathrate formation was seen for BDP HFA-227ae which is due to the increased solubility of BDP in this propellant and the formation of a solution formulation rather than a suspension. The formation of the monohydrate was observed when BDP was suspended in HFA-227ae/ethanol mixture confirming the disability of forming a clathrate from these latter.

The analysis of the different BDP HFA-227ae suspensions showed no formation of clathrates when anhydrous BDP was suspended in HFA-227ae and in HFA-227ae/ethanol mixture. The analysis showed the crystals of pure anhydrous BDP which is due to the increased solubility of BDP in HFA-227ae which does not allow further crystallisation at high pressure. The analysis showed that

anhydrous BDP was stable and its structure did not change as a function of temperature and hence no polymorphic transformation occurred. However, an increased vibration of different parts of the anhydrous BDP molecules especially the side chain showed some peak splitting starting at 84 ºC. These vibrations are due to very small effect induced by thermal expansion of the BDP molecule.

7.3 Effect of Size Reduction on API Surface Energy and Interactions in pMDI Systems

In chapter 5, the effect of formulation processing (particle size reduction) on surface energy and its subsequent effect on the adhesion of the particles on the different parts of a pMDI system was determined. It was possible to calculate the surface energy of the different material using single particle adhesion data determined using AFM. The surface free energies for anhydrous BDP (micronized), BDP CFC-11 clathrate (ball-milled for 2.5 hours) and the BDP CFC-11 clathrate (crystalline) were 47.5 ± 4.9 mJm^{-2}, 15.24 ± 1.26 mJm^{-2} and 11.27 ± 4.05 mJm^{-2} respectively. Force of adhesion results measured in a model propellant showed that BDP CFC-11 clathrates had a lower F_{adh} compared to anhydrous BDP with the different pMDI components studied and that size reduction of the BDP CFC-11 clathrate did not have any significant effect in terms of surface energy and F_{adh}.

The results generally suggest that the in situ formation of a clathrate in a propellant formulation is beneficial in terms of a reduction the force of adhesion with different pMDI components. This could have implications for future HFA formulation development with APIs that are prone to the formation of propellant

clathrates because BDP forms a clathrate with HFA 134a much more slowly (over a time scale of months) (Vervaet and Byron, 1999).

7.4 Effect of Ethanol and Oleic Acid on Beclomethasone Dipropionate, its Clathrate and Budesonide Coarsening Behaviour in pMDI Systems

In Chapter 6, the different studies undertaken showed that the particle size of the APIs in the pMDI suspension followed size dependent particle growth via Ostwald ripening and the LSW theory. This process involves the association of small thermodynamically unstable API particles with larger more energetically favoured particles. The level of solubility in the different systems was sufficient to provide the driving force for rate-limiting particle growth and thus the dominant step in the particle growth. However, as the storage time increased the rate of the coarsening decreased to reach an equilibrium and stability due to a decrease in the dissolution as small API particles disappear through their attachment to larger particles.

The use of APIs in mHFA propellant alone showed particle growth following LSW theory. This behaviour was due to an increased cohesiveness of the API particles when in contact with the propellant leading to instability of the formulation. Even though, ethanol showed an increase in the solubility of the different APIs in the pMDI formulation, the effect on the particle size showed a reduction in the mean particle size of the APIs when compared to the use of the APIs with propellant on its own. The use of a combination of both ethanol and oleic acid in the pMDI formulation produced an increase in the stability of the

colloidal suspension and a decrease in the average particle growth as well as the rate of Ostwald ripening.

Since it is critical that the drug particle size of MDIs be tightly controlled, it is important that all factors that affect it be well understood and carefully evaluated as this can have an impact on aerodynamic particle size of the emitted aerosol is presented and hence on final product quality and effectiveness.

7.5 Final Comments and Future Work Suggestions

The work undertaken in this thesis provides some insight into aspects of inhalation development techniques that have been utilized elsewhere. These approaches to obtaining an advanced understanding of the solid-state and the physiochemical characterization of drugs in HFA propellants as well as the potential interactions that may occur within a pMDI system.

The different findings obtained in Chapters 3 and 4 concerning the potential formation of clathrate crystallized from BDP with the different HFAs propellants have shown that these depend on the solubility of the API in the propellants and hence can be the driving force in formation of the clathrate. BDP crystallizes with a channel structure forming a clathrate with the propellant that allows the insertion of CFC-11/HFA-134a molecules. The structure is stabilized through hydrogen bonding. When BDP is suspended in a pMDI formulation containing CFC-11, rapid crystal growth occurs. This has been attributed to the association of BDP and CFC-11 to the formation of a clathrate. However, few weeks are

needed to the formation of the clathrate crystals in HFA-134a and no formation was observed in HFA-227ae after months of storage. The use of co-solvent in combination with HFA-134a showed a formation of a mixture of clathrate and monohydrate as well as remains of anhydrous BDP.

The force of adhesion and surface energy of the different API entities used in this thesis showed considerable changes following micronization, as seen in Chapter 5 and depending on the form of API (i.e. either solvate or clathrate). These results showed an increase in the surface energy and adhesion of the APIs to the different pMDI components following size reduction due to the release of the co-solvents and the propellants from within the crystals structures. Therefore it would be advisable to undertake a study similar to this one, with an emphasis on monitoring the changes in API interactions, as a function of material form and process-induced changes (i.e. polymorphism and amorphous material). Furthermore, it would be of great interest to screen for a variety of selected drugs that might be prone to clathrate formation in HFA-134a and 227 and if any mixture of solvates and clathrates can be obtained when used in pMDI formulations.

The investigations detailed in Chapters 6 clearly demonstrate that the addition of surfactant led to an increased stability of the pMDI formulation by decreasing the Ostwald ripening rate. The use of surfactants appears to diminish the large levels of adhesion and cohesion in these systems. Therefore the need of HFA-phillic surfactant should be taken into account when developing new HFA formulation and the effect of different surfactants with the potential use of co-

solvent must be taken into consideration. The use of different surfactants such as oligolactic acid which appeared to decrease these interactions more than oleic acid (James, 2009) could be performed in order to determine the potential benefits of these latter to the formulation. The addition of ethanol led to the formation of smaller particles over time compared to when the propellant were used on its own. However, it has been shown that ethanol increases the steric barrier between API particles which will results in compromising the colloidal stability of the formulation which ultimately may result in increased Ostwald ripening (James, 2009). Therefore, similar studies to the ones used in Chapter 6 could be performed using varying concentrations of ethanol.

AFM was used in order to determine its applicability in studying Ostwald ripening and surface activity of the different APIs in different media. The results obtained generally displayed large complexity and unexpected results due to different phenomena taking place simultaneously and the high and fairly rapid changes occurring to the surface after exposure to the media. Other techniques show a potential beneficial use in order to determine the effect of different HFA propellant effect on pMDI formulation including the use of laser diffraction techniques using a high pressure cell in order to determine the in situ effect of HFA formulation on particle size changes and Ostwald ripening.

There is little information on the quantification of surface roughness of particles as this is difficult to achieve especially in liquid media and when the size of the particles are in the micrometer dimensions (Heng et al., 2000). AFM can be used for evaluating the physical surface features of particles due to the direct

quantification of the surface textures of the particles and provides quantitative roughness values. However, this technique showed some limitations especially if the material shows considerable surface topographies and a high level of changes in liquid. Furthermore, some problems of this technique are due to the restricted movement of the cantilever on very rough sections of the samples. Laser profilometry is a technique used to determine surface's profile in order to quantify its roughness. This technique offers a rapid and reliable way of performing surface roughness measurements (Adi et al., 2008). It involves scanning the object through the Z axis in non contact mode, using white light and measuring the interference fringes (degree of coherence) at each pixel in the image (Kuwamura and Yamaguchi, 1997). The advantage of optical profilometry is rapid collection of 3D topographical data without the risk of changing the material. This technique has been used to assess APIs for use in dry powder inhalers as shown by studies by Podczek (Podczeck, 1998), Adi (Adi et al., 2008) and (Narayan and Hancock, 2005) and shows potential in studying the surface roughness changes following the suspension of APIs in HFA propellants and the effect of different HFA media on the APIs surface characteristics.

To conclude, the work in this thesis has detailed the use of surface analytical techniques to better understand the interactive properties of API and any transformation (i.e. polymorphism or process induced transformation) following their subsequent formulation in a pMDI system. These different studies provide different parameters that might influence the performance of a pMDI system and provide different information to the formulator to use for each API in order to develop an optimised pMDI system.

7.6 References

ADI, S., ADI, H., CHAN, H. K., YOUNG, P. M., TRAINI, D., YANG, R. & YU, A. (2008) Scanning white-light interferometry as a novel technique to quantify the surface roughness of micron-sized particles for inhalation. Langmuir, 24**,** 11307-12.

ASHAYER, R., LUCKHAM, P. F., MANIMAARAN, S. & ROGUEDA, P. (2004) Investigation of the molecular interactions in a pMDI formulation by atomic force microscopy. European Journal of Pharmaceutical Sciences, 21**,** 533-43.

HARRIS, J. A., CARDUCCI, M. D. & MYRDAL, P. B. (2003) Beclomethasone dipropionate crystallized from HFA-134a and ethanol. Acta Crystallographica Section E, 59**,** 1631-1633.

HENG, P. W., CHAN, L. W. & LIM, L. T. (2000) Quantification of the surface morphologies of lactose carriers and their effect on the in vitro deposition of salbutamol sulphate. Chemical and Pharmaceutical Bulletin (Tokyo), 48**,** 393-8.

JAMES, J. (2009) The interaction of drug particles with materials employed in inhaled delivery devices. School of Pharmacy. Nottingham, University of Nottingham.

JAMES, J., CREAN, B., DAVIES, M., TOON, R., JINKS, P. & ROBERTS, C. J. (2008) The surface characterisation and comparison of two potential sub-micron, sugar bulking excipients for use in low-dose, suspension formulations in metered dose inhalers. International Journal of Pharmaceutics, 361**,** 209-21.

KUWAMURA, S. & YAMAGUCHI, I. (1997) Wavelength scanning profilometry for real-time surface shape measurement. Applied Optics, 36**,** 4473-82.

MCDONALD, K. J. & MARTIN, G. P. (2000) Transition to CFC-free metered dose inhalers - into the new millennium. International Journal of Pharmaceutics, 201**,** 89-107.

NARAYAN, R. & HANCOCK, B. C. (2005) The influence of particle size on the surface roughness of pharmaceutical excipient compacts. Materials Science and Engineering a-Structural Materials Properties Microstructure and Processing, 407**,** 226-233.

PHILLIPS, E. M. & BYRON, P. R. (1994) Surfactant promoted crystal growth of micronized methylprednisolone in trichloromonofluoromethane. International Journal of Pharmaceutics, 110**,** 9-19.

PODCZECK, F. (1998) Evaluation of the adhesion properties of salbutamol sulphate to inhaler materials. Pharmaceutical Research, 15**,** 806-8.

TERZANO, C. (2001) Pressurized metered dose inhalers and add-on devices. Pulmonary Pharmacology and Therapeutics, 14**,** 351-66.

TRAINI, D., YOUNG, P. M., ROGUEDA, P. & PRICE, R. (2006) The use of AFM and surface energy measurements to investigate drug-canister material interactions in a model pressurized metered dose inhaler formulation. Aerosol Science and Technology, 40**,** 227-236.

VERVAET, C. & BYRON, P. R. (1999) Drug-surfactant-propellant interactions in HFA-formulations. International Journal of Pharmaceutics, 186**,** 13-30.

Appendices

Appendix 1

XPS Results

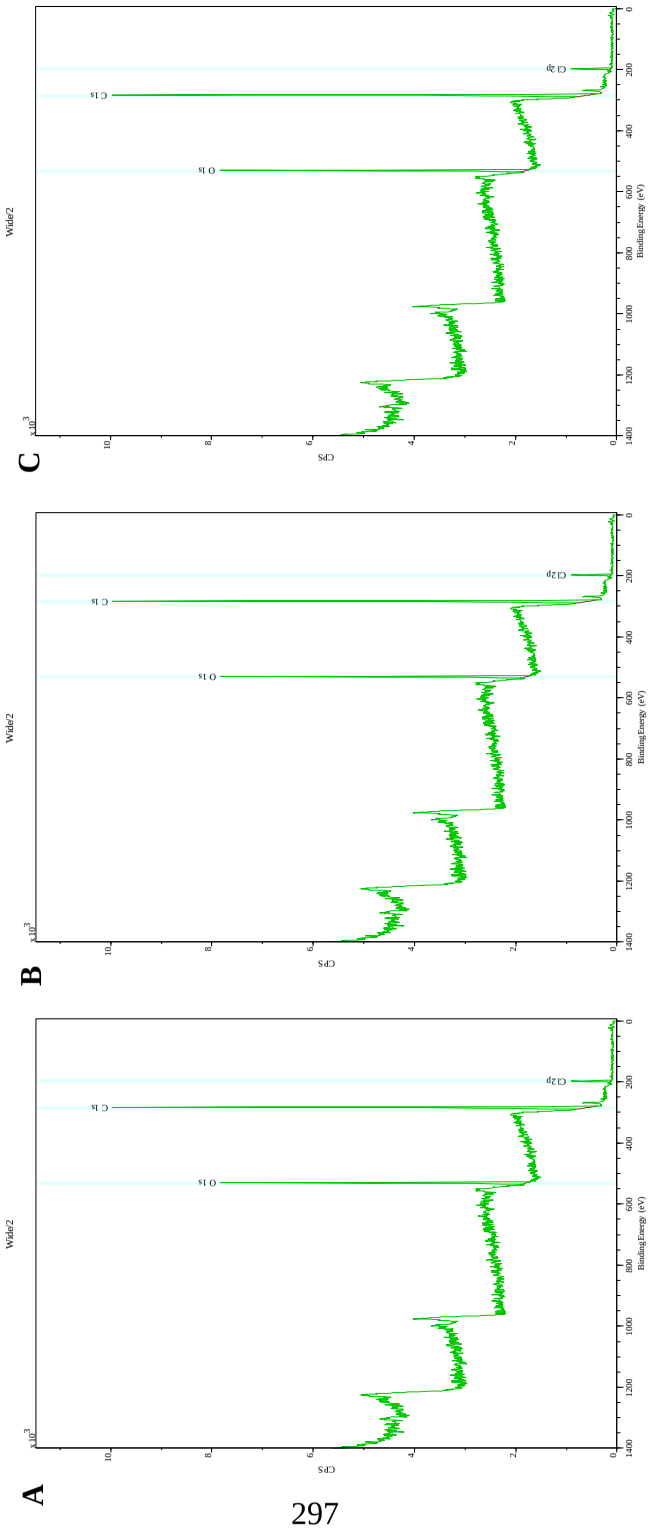

Figure 8-1: Wide survey scans of A- BDP HFA-227ae, B- BDP EtOH HFA-134a and C- BDP EtOH HFA-227ae crystals as obtained by XPS.

Appendix 2

DSC Results

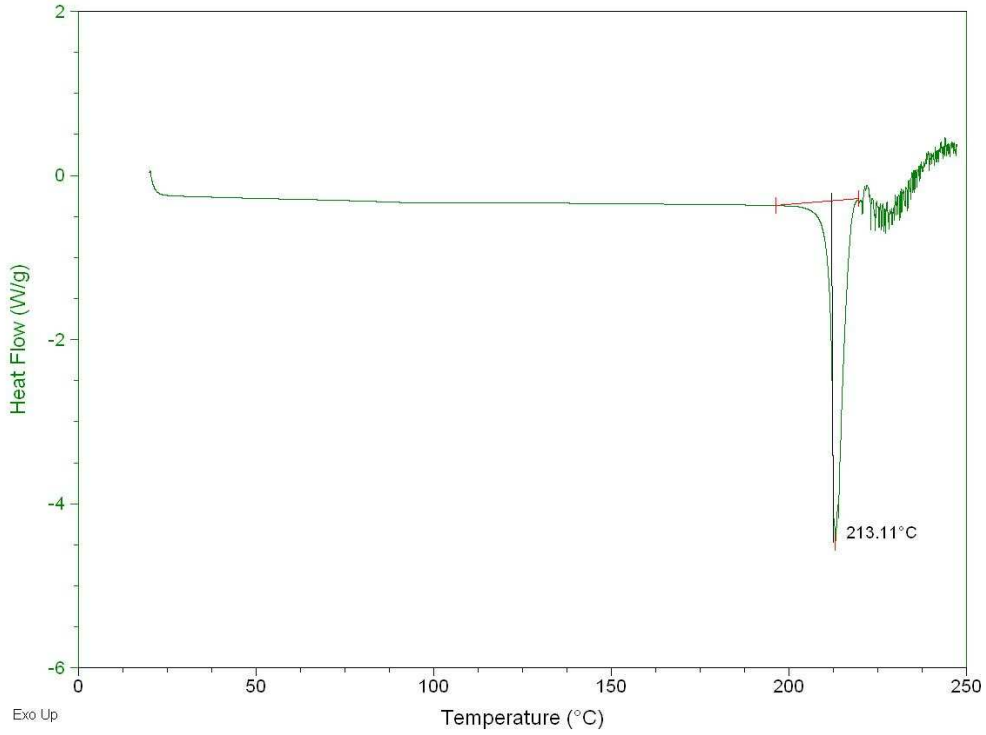

Figure 8-2: DSC curve of anhydrous BDP particles after being suspended in mHFA. All samples were heated from 20˚C to 250˚C at 10˚C/min.